INFORMATION TO USERS

This manuscript has been reproduced from the microfilm master. UMI films the text directly from the original or copy submitted. Thus, some thesis and dissertation copies are in typewriter face, while others may be from any type of computer printer.

The quality of this reproduction is dependent upon the quality of the copy submitted. Broken or indistinct print, colored or poor quality illustrations and photographs, print bleedthrough, substandard margins, and improper alignment can adversely affect reproduction.

In the unlikely event that the author did not send UMI a complete manuscript and there are missing pages, these will be noted. Also, if unauthorized copyright material had to be removed, a note will indicate the deletion.

Oversize materials (e.g., maps, drawings, charts) are reproduced by sectioning the original, beginning at the upper left-hand corner and continuing from left to right in equal sections with small overlaps.

Photographs included in the original manuscript have been reproduced xerographically in this copy. Higher quality 6" x 9" black and white photographic prints are available for any photographs or illustrations appearing in this copy for an additional charge. Contact UMI directly to order.

Bell & Howell Information and Learning
300 North Zeeb Road, Ann Arbor, MI 48106-1346 USA

UMI®
800-521-0600

UNIVERSITY OF OKLAHOMA

GRADUATE COLLEGE

ON THE FORMATION OF VERTICAL VORTICES IN THE ATMOSPHERE

A Dissertation

SUBMITTED TO THE GRADUATE FACULTY

in partial fulfillment of the requirements for the
Degree of

Doctor of Philosophy

By

KATHARINE MARIE KANAK

Norman, Oklahoma

1999

UMI Number: 9949692

Bell & Howell Information and Learning Company
300 North Zeeb Road
P.O. Box 1346
Ann Arbor, MI 48106-1346

ON THE FORMATION OF VERTICAL VORTICES IN THE ATMOSPHERE

A Dissertation APPROVED FOR THE
SCHOOL OF METEOROLOGY

BY

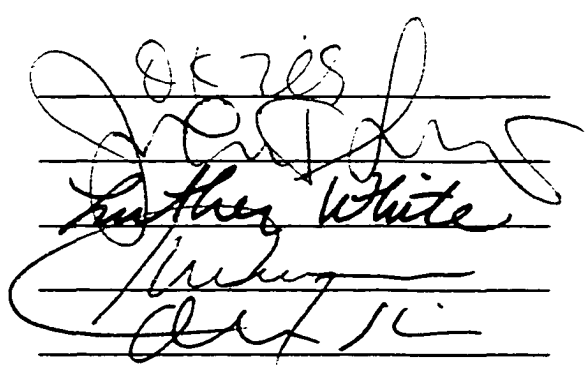

ACKNOWLEDGMENTS

The author wishes to gratefully acknowledge her major professor and mentor, Professor Emeritus, Douglas K. Lilly. It is truly an honor to be one of his Doctoral students. The author is very grateful to him for his guidance and encouragement and will benefit from his teaching for the rest of her career. The author also wishes to thank her co-advisor, Dean John T. Snow. She is very grateful for the many career development opportunities he has made available to her. She also appreciates his astute scientific suggestions that have guided her research.

The author gratefully acknowledges her other Doctoral committee members: Professor Alan Shapiro, for many interesting and helpful discussions, Professor Kelvin Droegemeier for helpful suggestions and encouragement and Professor Luther White of the Department of Mathematics.

Lastly, she would like to thank her Husband, Parents, Brother, her dear Grandmother, and all her family for their support and encouragement, and especially for the opportunity to pursue her education. She would like to thank her friends for their support and friendship. Thanks are also extended to the Faculty and Staff of the OU-School of Meteorology for all of their assistance.

Specific Acknowledgments for Chapter 2: This Chapter is dedicated to the memory of Professor Tzvi Gal-Chen. Many thanks are extended to Professor Tzvi Gal-Chen, Dr. Robert Davies-Jones, Ms. Limin Zhao, Ms. Yvette Richardson, Professor Alan Shapiro, and Professor Brian Fiedler for helpful comments. This work has been made possible by the support of NSF through the Center for the Analysis and Prediction of Storms (CAPS), grant ATM94-19599.

Specific Acknowledgments for Chapter 3: The author wishes to thank the following for various means of contributions to this research: Funding and/or resources for this research were provided by NSF ATM-9727150, Professor Peter Lamb/CIMMS, Professor Ken Crawford / OCS, NASA-Space Grant Fellowship, OU Graduate College, OU School of Meteorology, Center for the Analysis and Prediction of Storms (CAPS), and The National Severe Storms Laboratory (NSSL). Numerical computations were performed on the Cray-J90 at the OU Environmental Computing Application Systems (ECAS). Katharine M. Kanak, Jerry Straka, and Josh Wurman obtained the 3 cm radar observations. Andrew Crook and others from the National Center for Atmospheric Research (NCAR) coordinated acquisition of the MCLASS sounding. Thanks also to Alan Shapiro, for many helpful discussions, and to Jerry Straka for encouraging the author to write the numerical model. The following are acknowledged for interesting and helpful discussions: Professor Kerry Emanuel, Dr. Robert Davies-Jones, Dr. Andrew Crook, Mr. Jerry Brotze, Dr. Jeffrey Trapp, Professor Brian Fiedler, Dr. Lance Leslie and Dr. Yefim Kogan.

TABLE OF CONTENTS

LIST OF TABLES

LIST OF ILLUSTRATIONS

Chapter 3

Appendix B

ABSTRACT

This dissertation reports on two semi-independent studies of rotating atmospheric convection.

The first is an analytical investigation of the linear stability and structure of convection in a mean circular shear. The study is intended to complement the classical theoretical work of Asai and to extend the Lilly and Davies-Jones Beltrami solutions to consider the effects of buoyancy on disturbance helicity. The method of normal modes is used to analyze the Boussinesq equations with periodic lateral boundary conditions and free-slip, rigid vertical boundary conditions. The most unstable modes are found to be transverse to the shear vector at the channel center. At small Richardson numbers, the most unstable modes are highly helical with helicity obtained from the mean flow, but disturbance helicity decreases rapidly for Richardson numbers greater than unity.

The second study is a numerical investigation of the formation of vertical vortices in the convective boundary layer. In Nature, these vortices are typically made visible by the presence of dust or other particulates. Observations indicate that such vortices may be occurring, even in the absence of visible tracers. For example, MacPherson and Betts point out instrument observations of invisible boundary layer vertical vortices over a boreal forest. If boundary layer vertical vortices are therefore ubiquitous in the atmosphere, they may play an important role in boundary layer transports and evolution. However, these convective vertical vortices have not often been pointed out in laboratory or numerical simulations. Large-eddy simulations of convection, in the absence of imposed

mean wind or other sources of angular momentum, are performed for the purpose of investigating boundary layer vertical vortex formation. The simulations are designed to resolve boundary layer convective cells and embedded smaller-scale horizontal circulations. Simulated vertical vortices form rather readily at the vertices of polygonal convective rings, where updrafts are locally maximized. Although they have larger horizontal scale, these vortices have vertical structure similar to observed dust devils. The results indicate that boundary layer vertical vortices can form in the absence of surface or temperature inhomogeneities or imposed sources of angular momentum. In at least one case that is examined, the boundary layer height is elevated in the vicinity of a vortex. Possible mechanisms for vertical vortex formation are discussed.

Chapter 1

Introduction

Of principal interest to many meteorologists is the answer to the question, "How does an updraft begin to rotate and become an atmospheric vortex?" Observations suggest that there are many ways in which this can occur, most requiring both a source of buoyancy and a source of vorticity. The co-location of these results in a helical or columnar vortex. Assuming a source of buoyancy is provided, some of the vorticity generating processes might be categorized into the following cases: 1) direct generation of vertical vorticity associated with the existence of a horizontal shear zone; 2) vorticity generated by the interaction of convection and a mean wind shear; or 3) vorticity generated in convection in the absence of means winds. The first case is fairly straightforward and may be the primary mechanism for landspouts (Brady and Szoke 1989) and some dust devils (Barcilon and Drazin 1972). The more dynamically intriguing cases 2) and 3) are examined in this dissertation.

This dissertation describes two studies of rotating atmospheric convection. The first is an analytical investigation of the linear stability and structure of convection embedded in a mean shear flow with a circular hodograph, which was performed as a contribution to the classical theory. The second study consists of a numerical investigation of the formation of vertical vortices in the convective boundary layer. The background for these studies will now be described.

The interaction of a convective updraft with a mean wind shear has been used to explain the formation of rotating thunderstorms and has often been

studied using two idealized mean wind profiles. The first is a unidirectional vertical wind shear (speed shear), or straight hodograph, and the second is a wind shear turning at a constant rate with height (directional shear), or circular hodograph. A characteristic of disturbances in a circular mean shear is that streamwise vorticity is available to a disturbance updraft from its inception, in contrast to the case of unidirectional mean shear. Thus, linear dynamics enable the immediate rotation of an updraft and nonlinear forcing enhances this process. A nonlinear analytical solution exists in the form of a Beltrami flow (a solution in which the vorticity vector is parallel with the velocity vector). However, the Beltrami solution is not very relevant to atmospheric flows, since it does not involve buoyancy or dissipation. The linear equations permit the examination of buoyancy effects on the helical nature of the solutions.

Many analytical studies of convection mean wind shears have been performed, (e.g., Asai 1970 a, b, 1972) but none have considered the special case of a *circular* hodograph for linear stability analysis. Thus, the linear stability and structure of convection in a circular mean shear is examined and constitutes the first study reported in this dissertation. However, the emphasis is not as much on the stability properties of the flow, as on the helical characteristics of the preferred solutions. The method of normal modes is used for the Boussinesq equations and inviscid-nondiffusive solutions are emphasized. The vertical boundary conditions are rigid, free-slip and conducting, while lateral conditions are periodic. The stability results show two regimes that are separated by negative Richardson Number of approximately unity; a buoyancy (shear) dominated regime is characterized by growth rates that depend (do not depend) strongly on negative Richardson Number. The geometry of the preferred

solution is a two-dimensional roll, transverse to the mean shear vector at the center of the channel. For the case of a circular hodograph, disturbance helicity (a measure of the covariance of the velocity and vorticity vectors) can be obtained from the mean helicity and is proportional to the shear generation of kinetic energy. The relative helicity (normalized helicity) is reduced where buoyancy effects are maximized. However, the preferred solutions are highly helical.

Convection in a *unidirectional* mean shear has been studied numerically, as well as analytically, and has been applied to the formation of rotating thunderstorms. The second study described in this dissertation was initially motivated by unanswered questions regarding the role of moisture in the nonlinear updraft splitting process that takes place for moist supercellular convection in unidirectional mean wind shear. In such a mean shear, linear theory can explain the generation of two vertical vorticity centers that straddle an updraft center and lie in a plane perpendicular to the mean shear vector. However, nonlinear processes based on pressure gradient forces are required to explain the subsequent propagation of the updraft region, lateral to the mean shear vector, that results in the co-location of the updraft and a vertical vorticity center.

Prior work has implied that this nonlinear propagation process might be intrinsically related to the presence of moisture and related phase changes in the flow. In particular, Wu (1990) examined the disturbance helicity forcing terms for numerical simulations of supercell thunderstorms in both unidirectional and circular mean wind shears. She found that in the unidirectional (circular) mean shear, disturbance helicity was forced most strongly by the buoyancy (helicity

exchange) term[1]. She concluded that for supercell thunderstorms that form in unidirectional mean shear, the source of buoyancy forcing of disturbance helicity is the cold pool, formed by evaporatively cooled downdraft air. Originally it was thought that the formation of this cooled downdraft was responsible for the splitting of the original updraft. Dust devil vortices are notably independent of moisture processes and may form in essentially unidirectional boundary layer shear (Maxworthy 1973). The generation of rotation for dry thermal convection must differ somewhat from that of supercells.

Nevertheless, numerical simulations have showed that the nonlinear splitting process can take place with only parameterized latent heat release (Rotunno and Klemp 1982, hereafter RK82) and/or with the water-loading and evaporation processes turned off (Rotunno and Klemp 1985). To take this a step further, I performed a *completely dry*, coarse resolution, numerical simulation of a buoyant thermal rising in a unidirectional mean shear without any parameterization of latent heat release. The base state stratification was neutral and set to 300 K. A summary of the simulation parameters in shown in Table 1.1. (More details on the numerical model are given in Chapter 3 and Appendix A.)

Gridpts	Δx	Δy	Δz	Δt	θ_o	xr =yr	zr	Pr	Wind Shear
26x26x 26	1000 (m)	1000 (m)	500 (m)	6 (s)	3.5 (°C)	10 (km)	1.5 (km)	0.33	As in RK82

Table 1.1. Summary of simulation parameters.

[1] However, the buoyant forcing of disturbance helicity is similar in concept to the stretching of vorticity by divergence. The effect can only occur if there is some vorticity initially. Thus, another source of disturbance helicity is required for convection in unidirectional mean shear. Lilly (1994, unpublished) suggested that pressure forcing, although it vanishes globally, can locally produce disturbance helicity. Once produced, buoyancy effects act strongly to enhance the helicity of the disturbance.

It was found that the original updraft apparently does still split into two local updraft maxima, (Fig. 1.1a) and that these updraft centers are associated with vertical vorticity extrema (Fig. 1.1b). A Y-Z cross-section of the perturbation pressure (Fig. 1.1c) shows two low pressure centers on the flanks of the updraft, (as in Schlesinger 1980). These results provide evidence that something like the supercell mechanism may be operating for dust devils that may form in unidirectional wind shears in the absence of moisture processes.

However, Rotunno and Klemp (1985) found that updraft splitting did not occur without the rain process if the dynamic forcing was too weak. Many observational investigators have reported that the optimal conditions for dust devil formation include very light or calm winds (< 5 m s^{-1}, e.g., Sinclair 1969). This leaves the question of the formation of vertical vortices (e.g., dust devils) in weak winds and dry environments unexplained.

Despite the fact that the initial updraft split into two local updraft centers (Fig. 1.1a), subsequent lateral propagation was minimal and may require a mean temperature stratification (other than neutral) that promotes the preference of an updraft over a downdraft in the vicinity of the low pressure centers on the updraft flanks (Fig. 1.1c). (This issue is discussed in more detail in Chapter 3.) Since there was not much lateral propagation for the case of a single convective element in a unidirectional mean shear, it also seemed possible that the formation of dry dust devil-type vertical vortices might be dependent on the mutual interaction of nearby convective elements (e.g., Shapiro and Kogan 1994) or other dynamic processes, perhaps even in the absence of mean winds.

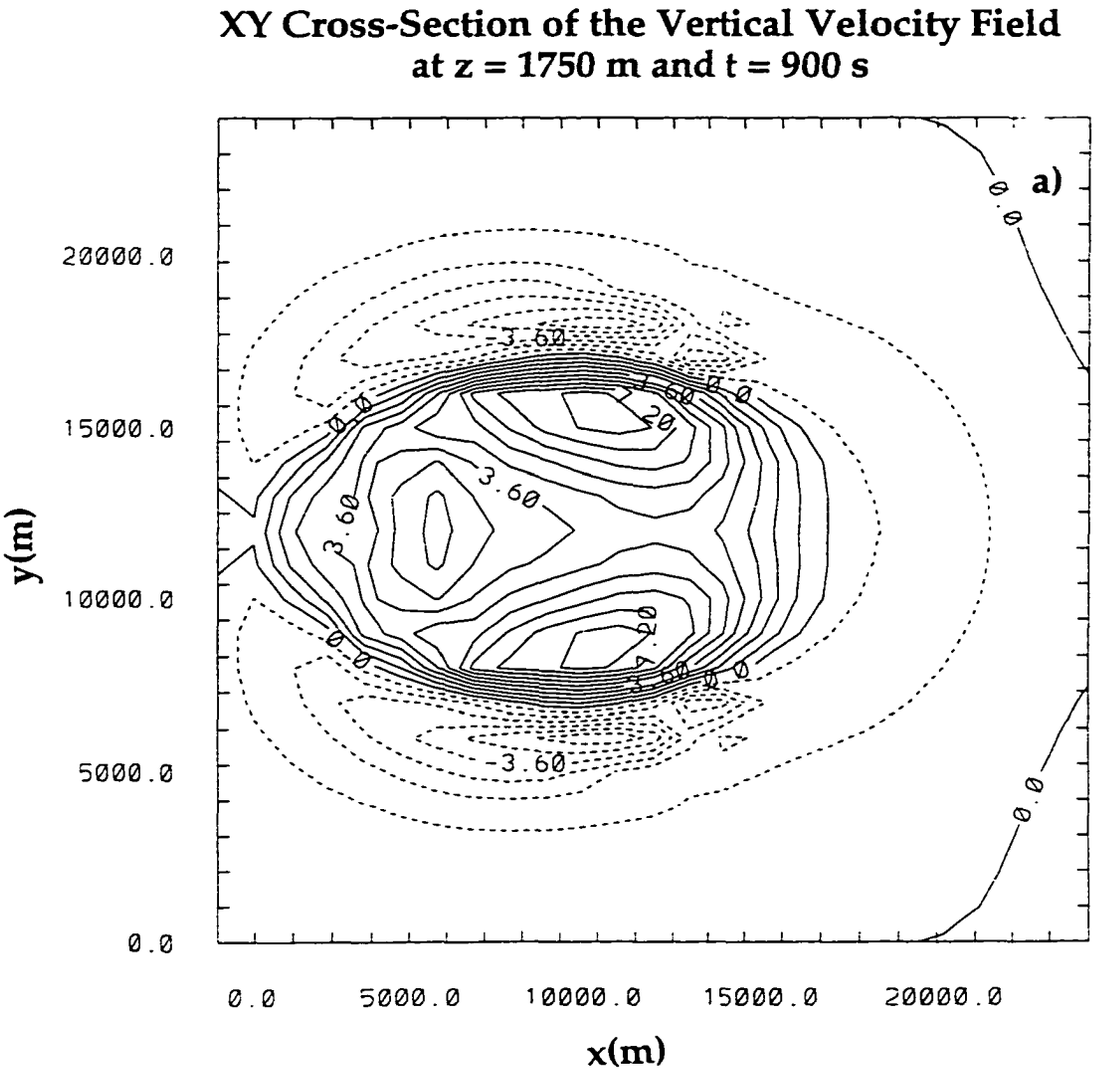

Fig. 1.1. (a) X-Y Cross-section of the vertical velocity at z = 1750 m and t = 900 s. Contours from –5.4 to 8.1 with interval 0.9 m s^{-1}.

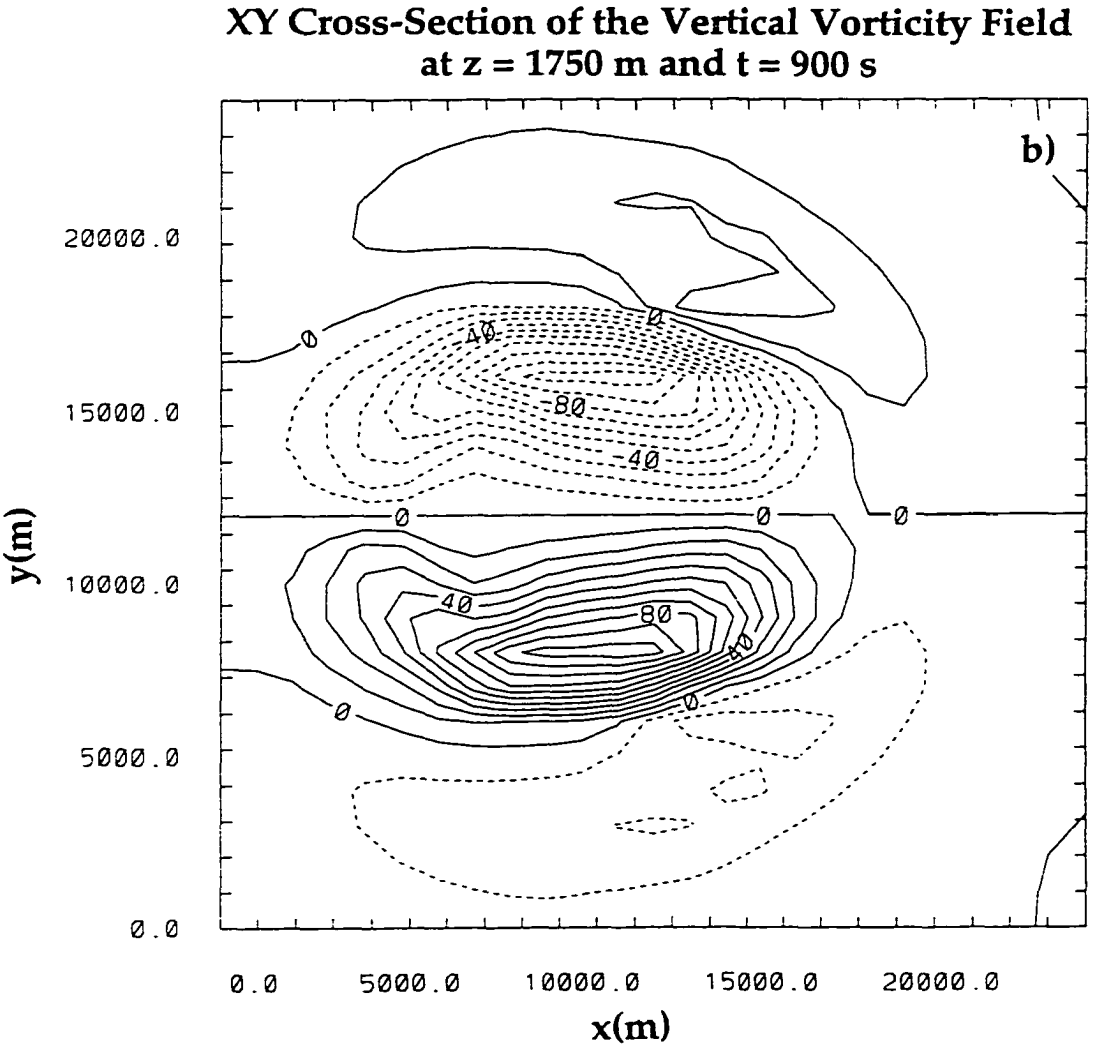

Fig. 1.1. *(continued).* (b) X-Y Cross-section of the vertical vorticity at z = 1750 m and t = 900 s. Contours from –0.01 to 0.01 with interval 0.001 s^{-1}. Labels scaled by 10000.

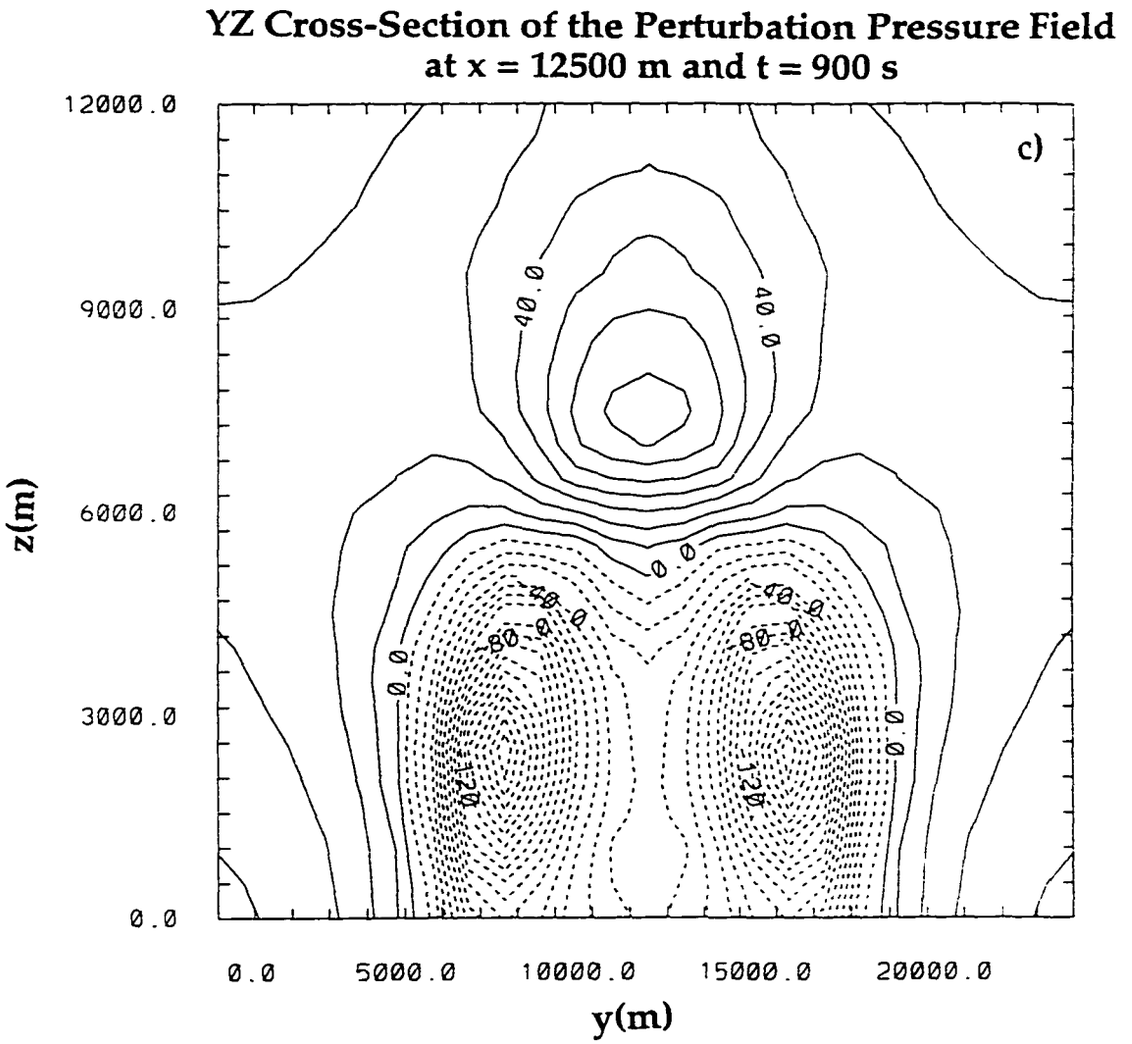

Fig. 1.1. *(continued)*. (c) Y-Z Cross-section of the perturbation pressure at x = 12500 m and t = 900 s. Contours from -180 to 70 with interval 10 Pa.

The mechanism for vertical vortex formation in the absence of mean winds is especially intriguing, since this has not often been pointed out in prior laboratory or numerical simulations of Rayleigh-Benard-type convection. Thus, it was chosen as the topic of investigation and constitutes the second study of rotating convection reported in this dissertation. After selecting this as the specific topic of interest, other questions such as, "What is the source of vorticity for these vortices?" and "Are vertical vortices more efficient transporters of heat and momentum in convective boundary layers than nonrotating convection?" became apparent. To address these and the question of vertical vortex formation in the absence of means winds or other imposed sources of angular momentum, Large Eddy Simulations (LES's) of the Convective Boundary Layer (CBL) have been performed. A desired consequence of this work is that the ubiquity and importance of rotating convection to boundary layer and convective-scale meteorology might be established.

Chapters 2 and 3 present the backgrounds, methodologies, results, discussions, and summaries for the analytical study of convection in a mean circular shear and for the numerical study of convective boundary layer vortices, respectively. Chapter 4 contains a summary of the dissertation.

Chapter 2

The Linear Stability and Structure of Convection in a Circular Mean Shear

An article published in the *Journal of Atmospheric Sciences*

1996, Volume 53, pages 2578-2593.

Chapter 2

The Linear Stability and Structure of Convection in a Mean Circular Shear

2.1 Background

Observations and numerical simulations have shown that both shear and buoyancy are important ingredients in the formation and maintenance of supercell thunderstorms and that there may be some optimal combination of both that is most conducive to severe rotating thunderstorms (e.g., Rasmussen and Wilhelmson 1983 and others). Buoyancy is critical to the initial formation of the convective storm and remains an principal energy source in the subsequent storm evolution (e.g., Weisman and Klemp 1982; Rotunno and Klemp 1982; and others). Wind shear is believed to provide an equally important source of storm energy (Lilly and Jewett 1990) and is also a source of rotation for storms through the tilting of horizontal vorticity (e.g., Browning and Landry 1963; Barnes 1968; Davies-Jones 1984; and Rotunno and Klemp 1985).

Helicity, the covariance of the velocity and vorticity vectors in a flow, characterizes severe storm structure and, when present in the mean flow, helps determine storm rotation potential and the origins of updraft rotation (Lilly 1982, 1986a,b; Davies-Jones 1984, 1985). Strongly curved mean wind hodographs are often observed to be associated with the formation of rotational storms (e.g., McCaul 1993). This study is largely motivated by that association.

The effects of wind shear on convection and the associated rotation-generating mechanisms have often been studied through the use of two idealized mean wind profiles. One is unidirectional shear, represented by a straight line

hodograph, and the other is a constant wind speed flow, represented by a circular hodograph with wind direction turning at a constant rate with height. Of course, observed wind profiles are never as simple as these idealized profiles but sometimes approach them. A typical wind profile associated with severe thunderstorms in the Southern Plains has a curved region in the lower troposphere surmounted at higher levels by a nearly unidirectional shear profile (Maddox 1976).

2.1.1. Unidirectional shear

The unidirectional shear idealization was used in the earliest Klemp and Wilhelmson (1978a) simulations of supercell-like storms and was also used in their simulation of an observed storm that split repeatedly to form a line of storms (Wilhelmson and Klemp 1981). The vorticity vector for a vertically shearing mean flow is always to the left of and normal to the shear vector. If an incipient storm updraft moves with the mean flow at some level, it lifts and draws in vortex tubes from both sides to produce vertically oriented vortices on either side of the updraft. Looking down the shear vector from above, the right (left) side of the updraft will acquire counterclockwise (clockwise) rotation. However, if the updraft begins to propagate in a direction transverse to the mean shear vector, air parcels in the inflow may be assumed to originate from the region in the direction of propagation and to possess vorticity parallel to that component of motion, that is, streamwise vorticity. The flow then becomes

helical in a coordinate frame tied to the updraft and the updraft develops a vortex at or near its center.

This sequence evidently starts with a process of updraft splitting. In the numerical simulations by Klemp and Wilhelmson (1978b), storm splitting appeared to be associated with the formation of a central rain-filled downdraft. Rotunno and Klemp (1982) found, however, that splitting can occur, although somewhat more slowly, without the presence of a downdraft. The main factor in the splitting process appears to be the nonlinear production of vertical pressure gradients on both the right and left flanks of the updraft (Schlesinger 1980). Midlevel pressure minima are attributed to rotation at midlevels that induces low pressure on the updraft flanks according to a diagnostic pressure equation in which the Laplacian of pressure is given by the difference between the square of the vorticity vector and the square of the deformation tensor.

A similar argument using dynamically induced pressure gradients has been made to explain discontinuous propagation of an updraft transverse to the mean shear vector (Rotunno and Klemp 1985). The formation of low pressure to the right and left of the main updraft promotes new updraft growth and thus transverse propagation of the storm system. Lilly (1986b) used concepts of vorticity generation and exchange, rather than pressure field generation, to obtain essentially similar results.

Klemp and Wilhelmson (1978b) showed, from a similar pressure field analysis, that hodograph curvature leads to enhancement of the half of a splitting storm on the concave side of the hodograph. Rotunno and Klemp (1982) extended this analysis and also showed that a pressure gradient relevant to propagation develops in the direction of the local shear vector. For a

unidirectional shear hodograph, this results in air rising in front of a storm and descending to its rear, and helps explain updraft penetration through a capping inversion.

The generation of vortices lateral to an updraft in a shear can be described by linear dynamics, but the feedback processes which produce a rotating updraft are inherently nonlinear. All linear analyses of convection in a unidirectional shear have shown that, for large negative Richardson number, the most unstable modes are rolls oriented downshear. For such modes, the shear neither contributes to nor penalizes the convective dynamics, although it does allow transfer of horizontal kinetic energy to the disturbance. All or nearly all laboratory experiments conducted in broad channels at small to moderate Rayleigh numbers support those results. Thus there is currently no satisfactory connection between those experiments and observed supercell storm phenomena.

2.1.2. Circular shear

In the circular hodograph case, rotation may develop in a convective updraft without a precedent storm split if the storm propagation vector lies within the circle since the mean vorticity must then always contain a component along the inflow vector and, thus, is helical. Partially circular hodographs are often associated with the development of supercell storms, which by definition contain rotation about a vertical axis. Numerical simulations in a circular (Lilly 1982) or semicircular (Weisman and Klemp 1982; Droegemeier et al. 1993)

hodograph environment have shown that a single rotating storm may develop, not as the result of a split, provided the magnitude of the shear is sufficient, as measured by a "bulk Richardson number" (as in Weisman and Klemp 1982). The environments of the well-studied Del City tornadic storm (e.g., Klemp et al. 1981) and the hurricane-generated tornadic storms studied by McCaul (1993) are represented by nearly circular hodographs. For both cases numerical simulations have been rather successful.

The mechanism for updraft rotation in a circular hodograph is simple and has been demonstrated using linear theory by Lilly (1982) and Davies-Jones (1984). A linearized vertical vorticity equation for a Boussinesq, incompressible flow can be written as

$$\frac{\partial \omega_3}{\partial t} + \bar{u}_i \frac{\partial \omega_3}{\partial x_i} = \bar{\omega}_i \frac{\partial u_3}{\partial x_i}, \tag{2.1}$$

where $\bar{u}_i$ and $\bar{\omega}_i$ are horizontal means of the horizontal velocity and vorticity vectors, respectively, and u_3 and ω_3 are disturbance quantities. For a circular hodograph where $\bar{u}_1 = -M\cos(\lambda x_3)$ and $\bar{u}_2 = M\sin(\lambda x_3)$, the right-hand side is proportional to the advection of vertical velocity; that is,

$$\bar{\omega}_i \frac{\partial u_3}{\partial x_i} = \lambda \bar{u}_i \frac{\partial u_3}{\partial x_i}, \tag{2.2}$$

so that a steady-state linear solution can exist with $\omega_3 = \lambda u_3$. For clockwise curvature where $\lambda > 0$ positive vorticity is generated upwind of the updraft and

negative vorticity downwind. Since the parcels of air coming into the updraft possess positive vorticity, the updraft will acquire cyclonic rotation.

Steady-state solutions of the inviscid Boussinesq equations of motion and continuity for the circular mean hodograph exist in the form of Beltrami flows of arbitrary amplitude (Lilly 1982, 1986b; Davies-Jones 1985). A flow that has perfect correlation everywhere is a Beltrami flow, defined by $\omega_i = \lambda u_i$, where λ is traditionally called the "abnormality," but may be interpreted as a wavenumber. The abnormality may not be constant, but if it is, the flow is also called Tkal. A mean circular hodograph is a Tkal flow. Here we shall neglect the subcategory distinction and call all Beltrami flows simply "Beltrami." The sum of two flows that are individually Beltrami flows remains Beltrami only if λ is the same for both (Truesdell 1954, 177). Such flows may appear quite different in geometrical structure but may be combined in any ratio and any amplitude. For present purposes, we consider the circular hodograph flow (horizontal velocity components varying only with height) to be the "mean" state, with small amplitude, three-dimensional "disturbances" superimposed on it. If both flows are Beltrami, however, the distinction between mean and disturbance is arbitrary.

A time-dependent solution for the viscous case was given by Shapiro (1993), which is similar to Beltrami flow but decays. Although the Beltrami solution is dynamically almost trivial, it nevertheless contains the same updraft-vortex linkages described above. The Beltrami solution is, however, apparently not maintainable in the presence of buoyancy effects. This can be seen from

examination of the steady-state inviscid Boussinesq vorticity equation, which may be written as

$$\frac{\partial}{\partial x_j}\left(u_j\omega_i - u_i\omega_j - \varepsilon_{ij3}b\right) = 0, \tag{2.3}$$

where b is the buoyancy. In a Beltrami flow the first two terms in parentheses must vanish, but this can only occur if the buoyancy is horizontally uniform. The nature of disturbances embedded in a buoyantly unstable Beltrami mean flow can, however, be examined within the linear framework.

2.1.3. Asai's studies

Asai (1970a,b) found that for unstable stratification in unidirectional shear, the preferred instability for large shear is somewhat incompatible with that for large buoyant instability. The most unstable modes for large shear (small positive or negative Richardson number) exhibit roll axes perpendicular to the mean shear vector. For a strongly buoyant mean state (large negative Richardson number) the preferred roll axes are aligned parallel to the shear vector, for which the growth rates are identical to those without shear. Thus, Asai concludes that the shear acts to inhibit convection. He and others consider cases where the shear vector turns with height (e.g., Asai 1972; Wu et al. 1992), but to our knowledge none have considered the special case of circular shear for a linear stability analysis. The current study may be considered an extension of

Asai (1972), but the emphasis is less on the disturbance stability than on the structure of the eigenmodes.

In section 2 we describe the methodology, section 3 gives the results of the analysis, and the conclusion is presented in section 4.

2.2. Methodology

A linear stability analysis is carried out to determine the stability properties and structure of growing disturbances in a circular mean shear. The method of normal modes is used to find the eigenvalues utilizing the linear Boussinesq equations with or without viscosity and in neutral or unstable stratification.

2.2.1. The mean state

The incompressible Boussinesq equations are linearized about a mean wind state characterized by a circular hodograph, which is linearly unstable even in the unstratified case, due to points of inflection in the profile. The equations are cast in Cartesian coordinates, where x and y are the horizontal directions and z is the vertical (note that where summation notation is used, $1 = x$, $2 = y$, and $3 = z$ direction). The mean density is assumed to vary linearly in the z

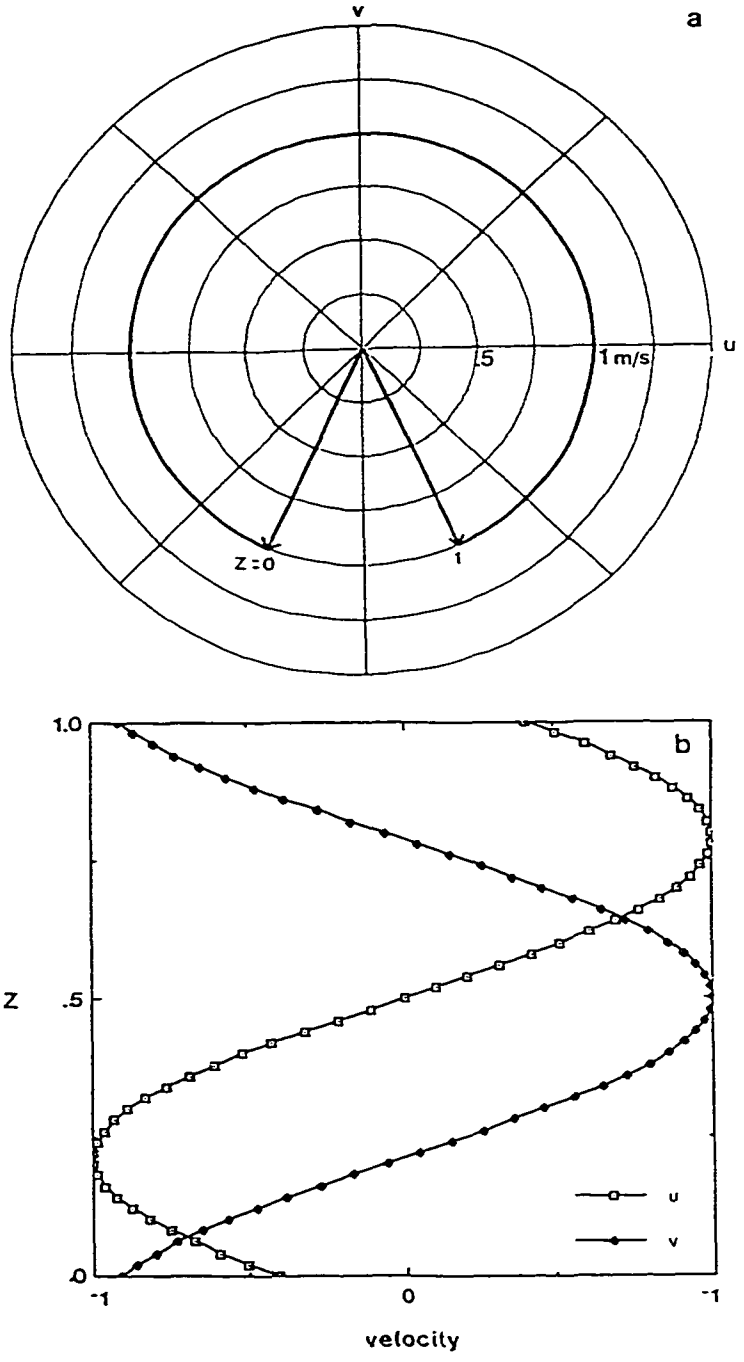

Fig. 2.1. (a) Mean-wind hodograph with veering wind with height and (b) profiles of the mean wind components.

direction only. The mean horizontal velocity is prescribed in the form used by Lilly (1986b):

$$\bar{u} = M\sin\left[\lambda\left(z-\frac{h}{2}\right)\right], \qquad \bar{v} = M\cos\left[\lambda\left(z-\frac{h}{2}\right)\right], \tag{2.4}$$

where $\bar{u}$ is the mean velocity in the x direction, $\bar{v}$ is the mean velocity in the y direction; M (=1 in our system, which is made dimensionless) is the radius of the hodograph. For most of our calculations we have chosen λ, the angular extent of the mean flow hodograph and also its dimensionless wavenumber, to be $\pi\sqrt{3} \approx 5.44$, or about 312°. Note that Lilly (1986b) found an analytical solution for this mean flow to which the current solutions may be qualitatively compared. (Also note that, in general, the solutions for the full circle hodograph were found not to vary significantly from those of the 312° hodograph.) The mean hodograph is shown in Fig. 2.1a. The mean vertical velocity $\bar{w}$ is zero. Points of inflection in are evident in the u and v component profiles of the mean flow, which are shown in Fig. 2.1b.

The rationale for the choice of λ is the following. We wish to allow formation of a Beltrami disturbance with the same abnormality as that of the mean flow. If the disturbance vertical wavenumber is not the same as the mean Beltrami flow, then the possibility of a Beltrami disturbance and comparison with the analytical solutions of Lilly (1986b) is precluded. This requires that the square of the vector wavenumber of the disturbance be the same as λ; that is,

$$\lambda^2 = \bar{k}_z^2 = k_x'^2 + k_y'^2 + k_z'^2, \tag{2.5}$$

where the disturbance wavenumbers are denoted by primes and the mean by an overbar. Thus, the vertical wavenumber of the mean flow $\bar{k}_z$ must be greater than the vertical wavenumber of the disturbance k_z', which for our rigid upper and lower boundary conditions is π or greater. Thus the limit for infinite horizontal wavelength is a half-circle hodograph (Davies-Jones 1985). For a cubic disturbance having horizontal half-wavelengths equal to the domain depth,

$$\lambda^2 = \frac{\pi^2}{L_x^2} + \frac{\pi^2}{L_y^2} + \frac{\pi^2}{L_z^2} = 3\pi^2. \tag{2.6}$$

Note that the total horizontal wavenumber for the disturbance Beltrami flow is then

$$k' = \sqrt{k_x'^2 + k_y'^2} = \sqrt{2\pi}. \tag{2.7}$$

Thus, for disturbances with one horizontal dimension of variability the mean flow wavelength is $\sqrt{2}$ times the domain depth.

2.2.2. The disturbance equations

The linearized Boussinesq disturbance equations are given by

$$\left(\frac{\partial}{\partial t}+\bar{u}_j\frac{\partial}{\partial x_j}-\nu\frac{\partial^2}{\partial x_j^2}\right)u_i'+u_3'\frac{d\bar{u}_i}{dx_3}+\frac{\partial\pi'}{\partial x_i}-\delta_{i3}b'=0, \tag{2.8}$$

$$\left(\frac{\partial}{\partial t}+\bar{u}_j\frac{\partial}{\partial x_j}-\kappa\frac{\partial^2}{\partial x_j^2}\right)b'+N^2u_3'=0, \tag{2.9}$$

and

$$\frac{\partial u'}{\partial x_i}=0, \tag{2.10}$$

where u_i''s are the disturbance velocities in the x, y, and z directions. The buoyancy frequency is given by

$$N^2=-\frac{g}{\rho_o}\frac{d\bar{\rho}}{dz}. \tag{2.11}$$

The pressure variable is defined by $\pi=p'/\rho_o$, where ρ_o is the reference density. The buoyancy variable is denoted by $b'=-g\rho'/\rho_o$, ν is the kinematic viscosity coefficient, and κ denotes the thermal diffusivity.

All disturbance equations are made dimensionless by scaling by the domain depth h, a characteristic velocity scale (the mean wind speed) U, and the buoyancy change over the depth of the domain $\Delta b=-N^2h$, where we have set $N^2=-1$. The Reynolds number Re, Prandtl number Pr, and Richardson number

Ri are defined as: $\mathrm{Re} = Uh/\nu$, $Ri = (h\Delta b)/U^2$ and $\mathrm{Pr} = \nu/\kappa$. The Rayleigh number Ra is given by $Ra = -\left(h^3 \Delta b\right)/(\nu\kappa) = -\mathrm{Pr}\, Ri\, \mathrm{Re}^2$.

Wave solutions for the disturbance quantities are assumed in the form

$$A' = \hat{A}(z)\exp\left[i\left(k_x x + k_y y\right) + \sigma t\right], \tag{2.12}$$

where $\hat{A}$ denotes the amplitude of any of u', v', w', b', ζ', and π'. The positive real part of σ is the amplification growth rate of the disturbance. The horizontal wavenumber in the x (y) direction is k_x (k_y). Upon substitution of (2.12) into (2.8)-(2.10), we first eliminate $\hat{U}$ and $\hat{V}$, and then the pressure variable and the following system of two equations and two unknowns, $\hat{W}$ and $\hat{B}$, is obtained:

$$\left\{\left[\sigma + i\left(k_x \bar{u} + k_y \bar{v}\right) - \mathrm{Re}^{-1}\left(\frac{d^2}{dz^2} - k^2\right)\right]\left(\frac{d^2}{dz^2} - k^2\right)\right\}\hat{W} - i\left(k_x \frac{d^2\bar{u}}{dz^2} + k_y \frac{d^2\bar{v}}{dz^2}\right)\hat{W} + k^2 Ri\hat{B} = 0, \tag{2.13}$$

and

$$\left[\sigma + i\left(k_x \bar{u} + k_y \bar{v}\right) - \mathrm{Pr}^{-1}\,\mathrm{Re}^{-1}\left(\frac{d^2}{dz^2} - k^2\right)\right]\hat{B} - \hat{W} = 0, \tag{2.14}$$

where k is the horizontal wavenumber, $k^2 = k_x^2 + k_y^2$. The vertical vorticity amplitude is obtained using

$$\left[\sigma + i\left(k_x\bar{u} + k_y\bar{v}\right) - \mathrm{Re}^{-1}\left(\frac{d^2}{dz^2} - k^2\right)\right]\hat{Z} = -i\left(k_x\frac{d\bar{v}}{dz} - k_y\frac{d\bar{u}}{dz}\right)\hat{W}. \tag{2.15}$$

The remaining velocity amplitudes are then found according to the following equations:

$$\hat{U} = ik^{-2}\left(k_y\hat{Z} + k_x\frac{d\hat{W}}{dz}\right) \tag{2.16}$$

and

$$\hat{V} = -ik^{-2}\left(k_x\hat{Z} - k_y\frac{d\hat{W}}{dz}\right). \tag{2.17}$$

The upper- and lower-disturbance boundary conditions are assumed to be rigid and free slip. In addition, the buoyancy at the upper and lower boundaries is held constant so that

$$\hat{W} = \frac{d^2\hat{W}}{dz^2} = \frac{d\hat{U}}{dz} = \frac{d\hat{V}}{dz} = \hat{B} = 0 \quad \text{at} \quad z = 0 \quad \text{and} \quad 1. \tag{2.18}$$

The ordinary differential equations, (2.13) and (2.14), and the boundary conditions, (2.18), are approximated by finite-difference equations and then written in the form of an eigenvalue problem. The maximum real part of the eigenvalue is selected and is the growth rate of the most unstable disturbance, while the corresponding eigenvectors are the disturbance amplitudes. The number of vertical levels is $n = 50$ unless otherwise stated. The procedure is very similar to that described in the appendix of Asai (1970a) except for the use of an

improved eigenvalue solver. Therefore, we will not repeat all the details here, but refer the reader to Asai (1970a). The newer GVCCG (IMSL library routine) eigenvalue solver computes all the eigenvalues and eigenvectors of a generalized complex eigensystem. The routine uses the LZ algorithm (Kaufman 1975) which is based on the QR algorithm. It does not require matrix inversion and, therefore, may be more appropriate for ill-conditioned systems. The LZ algorithm is also more efficient for use with complex matrices.

2.2.3. Energy and helicity budgets

Helicity density, hereafter helicity, is formally defined as the scalar product of velocity and vorticity, $h = u_i \omega_i$, where u_i is the velocity vector and ω_i is the vorticity vector. The development of helicity in an updraft-containing disturbance can be examined through the use of the linearized-disturbance helicity equation. First, we write the disturbance vorticity equation, which is obtained by taking the curl of (2.8):

$$\left(\frac{\partial}{\partial t} + \overline{u}_j \frac{\partial}{\partial x_j} - \nu \frac{\partial^2}{\partial x_j^2} \right) \omega_i' + u_3' \frac{\partial \overline{\omega}_i}{\partial x_3} - \overline{\omega}_j \frac{\partial u_i'}{\partial x_j} - \omega_3' \frac{\partial \overline{u}_i}{\partial x_3} - \varepsilon_{ij3} \frac{\partial b'}{\partial x_j} = 0. \qquad (2.19)$$

Multiplication of (2.8) by u_i', cross-multiplication of (2.8) and (2.19) by ω_i' and u_i', and taking the horizontal mean result in the kinetic energy and helicity equations, respectively,

$$\left(\frac{\partial}{\partial t}-\nu\frac{\partial^2}{\partial x_3^2}\right)\frac{\overline{u_i'^2}}{2}+\overline{u_i'u_3'}\frac{d\overline{u}_i}{dx_3}+\frac{\partial\left(\overline{\pi' u_3'}\right)}{\partial x_3}-\overline{b'u_3'}=-\nu\overline{\left(\frac{\partial u_i'}{\partial x_j}\right)^2}\,, \tag{2.20}$$

I II III IV V VI

and

$$\left(\frac{\partial}{\partial t}-\nu\frac{\partial^2}{\partial x_3^2}\right)\overline{u_i'\omega_i'}+2\overline{u_i'u_3'}\frac{d\overline{\omega}_i}{dx_3}+\frac{\partial}{\partial x_3}\left(\overline{\pi'\omega_3'}-\overline{\omega}_i\overline{u_i'u_3'}\right)-2\overline{b'\omega_3'}=-2\nu\overline{\left(\frac{\partial u_i'}{\partial x_j}\frac{\partial\omega_i'}{\partial x_j}\right)}. \tag{2.21}$$

I II III IV V VI

The horizontally averaged disturbance helicity is $\overline{u_i'\omega_i'}$. Terms III in both (2.20) and (2.21) represent the exchange of energy or helicity between the disturbance and the mean state and will be referred to as the "exchange" terms. Terms IV in both equations represent vertical transport of energy and helicity between levels. There is, however, the possible removal or generation of helicity at the boundary by the pressure term. In the helicity equation, it contains a momentum flux term and is somewhat arbitrary since the exchange term could be written in a form that removes it. Terms V represent the source of energy and helicity due to buoyancy effects. Lilly (1986b) speculatively defined a potential helicity that, like potential energy, exchanges with the disturbance helicity. Terms VI of both equations are denoted as "dissipation." For helicity, that term may not necessarily decrease the magnitude of total helicity, but it does so for each wavenumber considered separately.

Equations (2.20) and (2.21) can be expressed in terms of the wave spectral variables. From (2.15) it can be shown for the inviscid nondiffusive case that the

product of $\hat{Z}\hat{B}^*$, where an asterisk denotes the complex conjugate, is imaginary so that the vorticity buoyancy product [term V of (2.21)] identically vanishes.

Wu (1990) evaluated helicity budgets for simulated storms in mean-shearing environments. She found that the exchange term is nearly zero for a unidirectional shear case, with disturbance helicity generated mostly by the buoyancy term, in perhaps surprising agreement with linear theory. For the numerically simulated Del City storm, with a roughly circular hodograph, the principal source of disturbance helicity is transfer from the mean state (Wu et al. 1992). Droegemeier et al. (1993) also showed transfer of helicity from a mean state with a semicircular hodograph to a simulated convective storm.

We define the disturbance *relative* helicity (RH) to be the horizontally averaged correlation between vector velocity and vorticity, or the mean cosine of the angle between them. It is, therefore, a function of the vertical coordinate z:

$$RH(z) = \left(\frac{\overline{u_i' \omega_i'}}{\left(\overline{u_j'^2 \omega_i'^2} \right)^{1/2}} \right). \tag{2.22}$$

Some insight can be obtained by assuming that the momentum flux, term III of (2.21), can be adequately parameterized by an eddy viscosity assumption; that is,

$$\overline{u_i' u_3'} = -K \frac{d\overline{u}_i}{dx_3}. \tag{2.23}$$

Then term III may be written as

$$K\frac{d\overline{u}_i}{dx_3}\frac{d\overline{\omega}_i}{dx_3}. \tag{2.24}$$

The derivative product is a mean-state form of $(\partial u_i/\partial x_j)(\partial \omega_i/\partial x_j)$, also occurring on the right-hand side of (2.21), which has been termed "superhelicity" by Hide (1989). This quantity bears the same relationship to helicity as does enstrophy to kinetic energy. Superhelicity is proportional to helicity for a circular mean hodograph but otherwise can be determined algebraically or graphically from the mean flow hodograph. It can be shown that a vertical integral of superhelicity is not particularly sensitive to discontinuities in the vorticity. It is, however, very sensitive to loops in the hodograph. As a measure of mean-disturbance helicity exchange potential, the mean-state superhelicity might be considered an improvement on helicity itself because it is independent of the frame of reference. Its significance for this purpose depends, however, on the momentum flux being downshear so that disturbance energy is obtained from the mean state. This is generally found to be true for isolated three-dimensional convective elements (Lemone 1984; Lilly and Jewett 1990), but not necessarily for quasi-two-dimensional squall line convection (Lemone 1983). Emanuel (1994) and Lilly (1986a) have found that the irrotational horizontal velocity components feed energy from disturbance to mean state, with the opposite being true for the nondivergent components.

Whether or not (2.23) is a particularly useful relationship for a given flow field, the helicity exchange terms, term III in (2.21), are proportional to those for energy exchange if the mean flow is Beltrami.

In addition, Davies-Jones showed that vertically integrated helicity is proportional to the area of the figure bounded by the hodograph and the wind vectors at its bottom and top. Thus, for a closed hodograph it is proportional to the total area within it, and this remains true within any reference frame. The more nearly closed a hodograph is, the less sensitive helicity is to the reference frame.

2.3. Results and Discussion

2.3.1. Unstable modes and phase speeds

Unless otherwise specified, the results are for inviscid and nondiffusive equations, with varying Richardson number and wavenumbers. The most interesting results are almost independent of Reynolds and Rayleigh numbers, provided these are large enough to allow instability. Where finite Reynolds and Rayleigh numbers are considered, the Prandtl number is always assumed unity.

Figure 2.2 shows the growth rate as a function of k_y and k_x for neutral stratification $Ri = 0$. The preferred solution, wavenumber ≈2.7, has roll axes aligned with the y axis ($k_y = 0$), thus perpendicular to the mean shear vector at the center of the channel in the x direction. We will call this the transverse

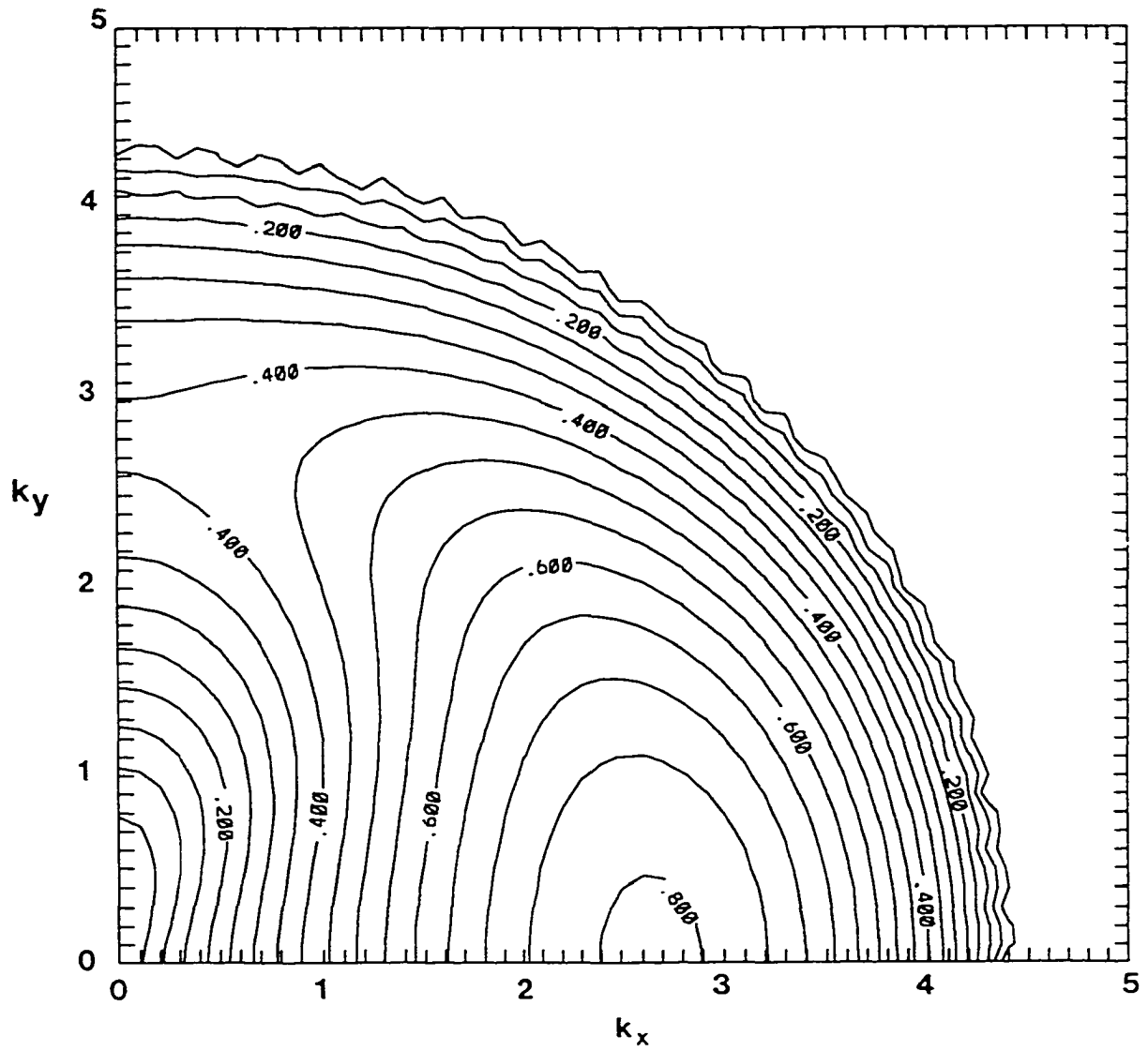

Fig. 2.2. Growth Rate contours as a function of k_y and k_x for Ri = 0 and $n = 90$. Minimum value is 0.0 and maximum value is 0.8. Contour interval is 0.05.

mode, with $k_x = 0$ identified as the longitudinal mode. Asai (1970b, 1972) found that such a transverse instability was dominant for other types of mean shear profiles at small $-Ri$. Here significant growth also occurs, however, for all other orientations at about the same total wavenumber, due to shear in the other directions.

Our disturbance solutions are thus obtained as periodic rolls having only one horizontal dimension of variability, although the roll orientation may be varied arbitrarily with respect to the mean flow. Many severe storms are, and the Lilly-Davies-Jones Beltrami flow solution can be, fully three-dimensional. Since linear disturbance solutions may be combined arbitrarily, it is possible to obtain three-dimensional disturbances, of either square or rectangular planform, by combining pairs of roll disturbances. Each member of these pairs must, however, have the same growth rate. While this procedure adds no new information to the individual modal solutions, it facilitates comparisons with the more nonlinear phenomena. The propagation velocity of the synthesized three-dimensional disturbances becomes the mean of its two components and, thus is normal to two of the rectangular faces of its planform.

The direction of propagation of the most unstable solution is perpendicular to the wavefronts and thus will be in the x direction (Fig. 2.2). Figure 2.3 shows the magnitude of the propagation velocity plotted as a function of k_x versus k_y, also for $Ri = 0$. Values greater than $k = 4.3$ are not plotted since these values are near the stability boundary, where the most unstable mode is difficult to identify. The propagation speed of the wave of most unstable

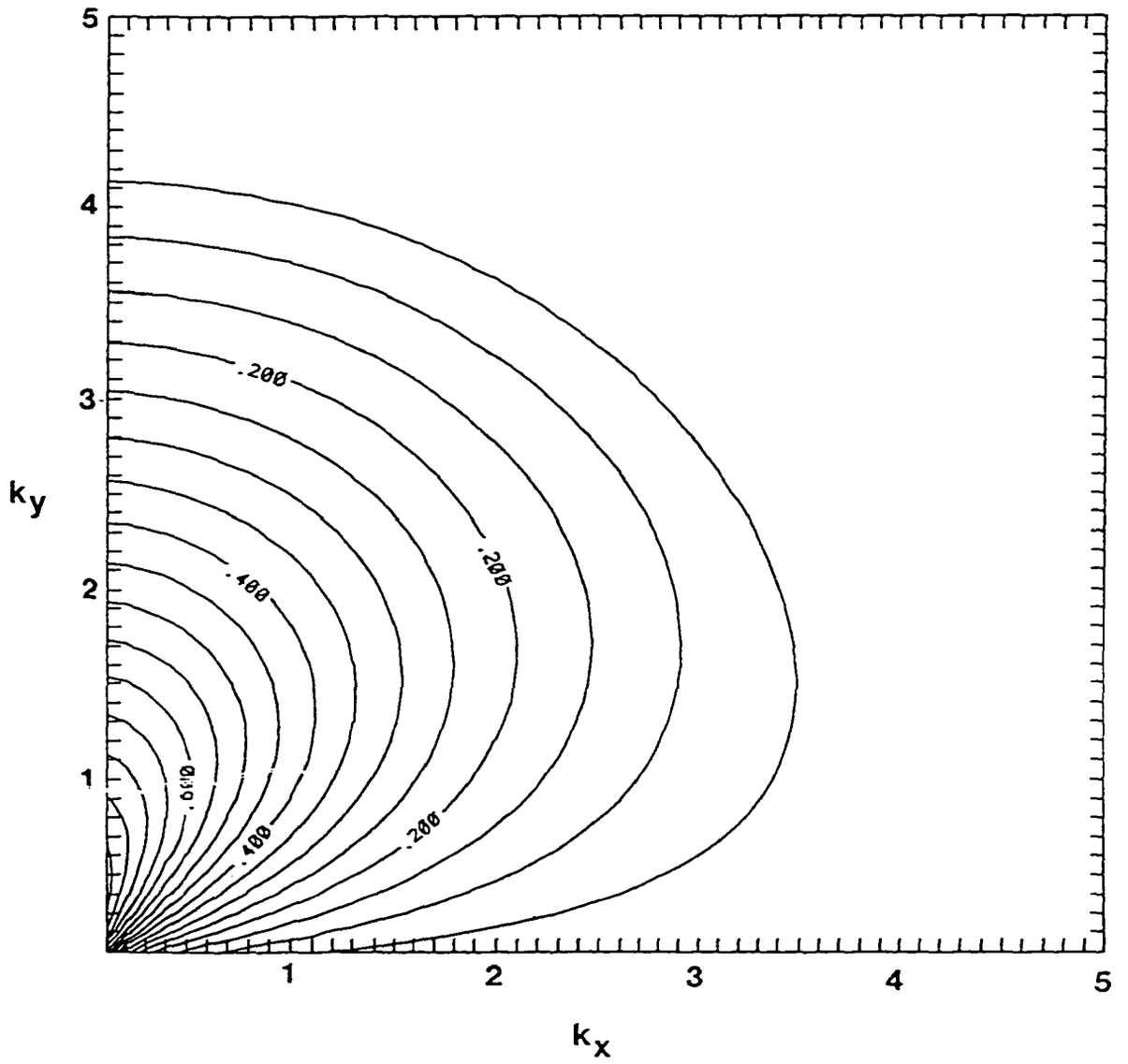

Fig. 2.3. Magnitude of the phase velocity vector plotted as a function of k_x and k_y. Contour interval is 0.05. Minimum value is zero, and maximum value is 0.8; Ri = 0 and $n = 50$. Values for $k > 4.3$ are not plotted.

solution geometry ($k_x > k_y$) is a minimum, while the less unstable solutions propagate at greater speeds (e.g., $k_x > k_y$ will propagate in the y direction).

Figure 2.4 presents the growth rate for inviscid flow as a function of -Ri and k, with $k_y = 10^{-3}$. The values 10^{-3} are used for numerical convenience but may be considered as nearly zero. Thus, if we envision Fig. 2.2 as extending out of the page for variable Ri, this figure represents a vertical cut approximately along the k_x axis. The figure shows a monotonic increase of growth rate with increasing $-Ri$. This result appears to differ from that of Asai (1970a), who found two regions of instability separated by $-Ri = 0.1$, and a preference for longitudinal modes for negative Ri larger than that. A more accurate comparison of his results and ours shows, however, that they are not significantly different. The mean flow Asai (1970b) uses for his "case a" is similar to our v component, with points of inflection above and below the centerline. Figure 2.5a shows growth rates for this case with finite diffusion and viscosity as in Asai's (1970b) Fig.2. The approximate wavenumber amplitude of maximum growth rate $k = \sqrt{8}$ is very close to our wavenumber of maximum instability. The best comparison comes if Asai's wave direction is chosen along the mean shear, that is, in the x direction. Figure 2.5b shows growth rate as a function of wavenumber and $-Ri$, recalculated by us for this situation, with $k_y = 10^{-3}$. The comparison with Fig. 2.5a is qualitatively good. However, we have a separation of instabilities at about $-Ri = 1.0$ and our growth rates are larger because our maximum shear is greater than that of Asai.

Asai's (1970b) Fig. 3 is presented here as Fig. 2.6, showing growth rates plotted against all three dimensionless numbers for $k_x = k_y = 2$. The peaks of the

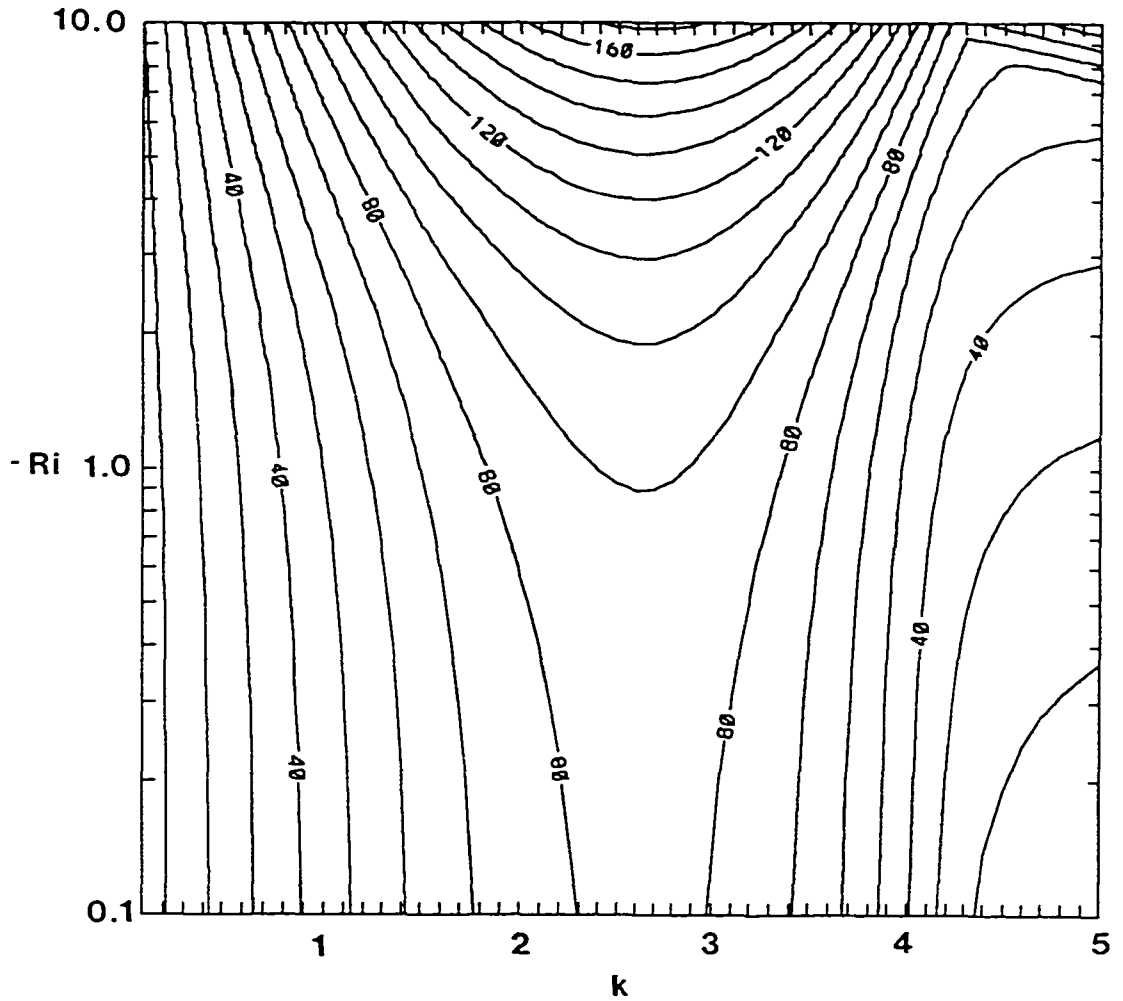

Fig. 2.4. Inviscid growth rate (x100) as a function of horizontal wavenumber and negative Richardson Number for $k_y \approx 0$ and $n = 50$. Minimum value is 0.001, maximum is 1.701, and the contour interval is 0.1.

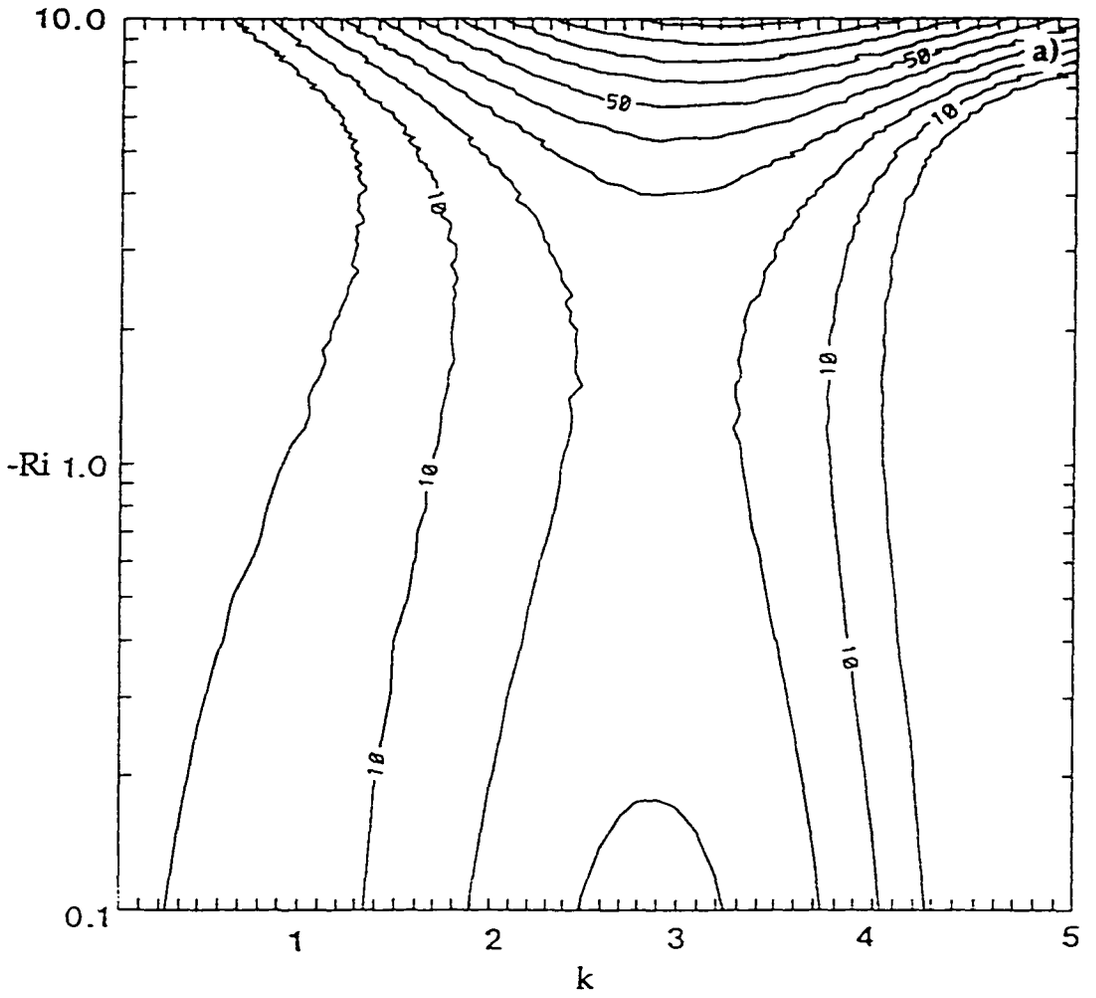

Fig. 2.5. (a) Growth rate (x100) as a function of horizontal wavenumber and negative Richardson Number for $k_y = 0$, Ra = 10^4, variable Re, and $n = 50$. Minimum value is 0.001, maximum is 1.201, and the contour interval is 0.1.

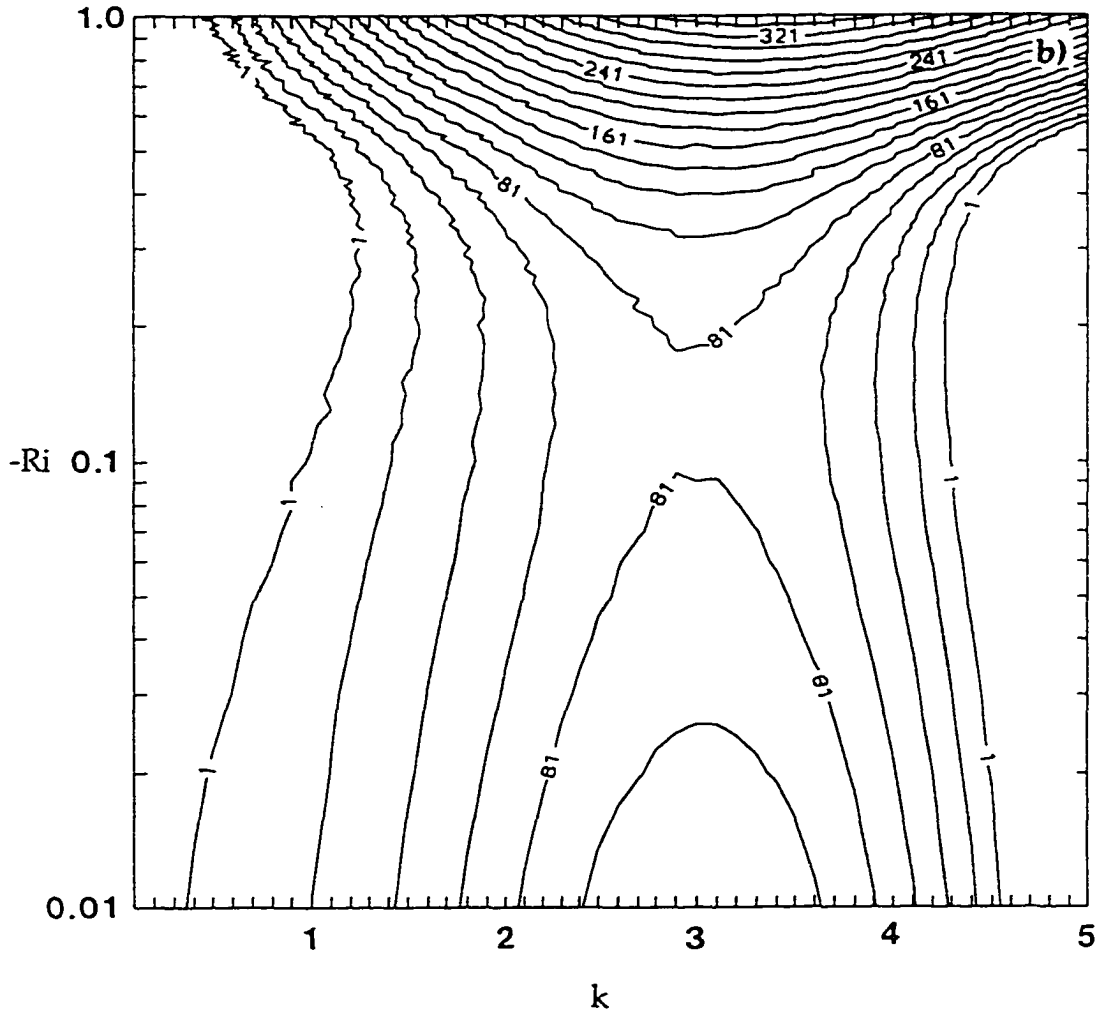

Fig. 2.5. *(continued).* (b) Growth rate (x100) as a function of horizontal wavenumber and negative Richardson Number for Asai's Case (a) as in Fig. 2 of Asai (1970b) except $k_y \approx 0$, and n=50. Minimum value is 0.001, maximum is 1.701, and the contour interval is 0.1.

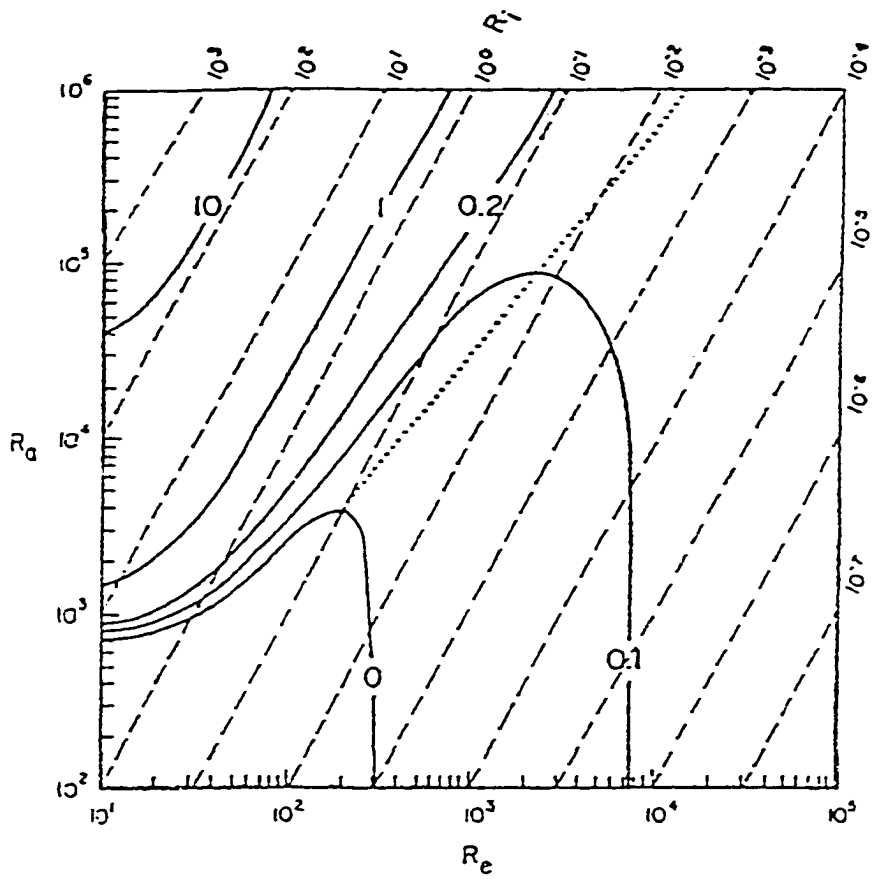

Fig. 2.6. Figure 3 of Asai (1970b). Stability diagram for case (a) in which $k_x = k_y = 2$ are adopted. Solid lines indicate amplification rates against the Rayleigh number Ra and the Reynolds number Re. Slanting dashed line illustrates the respective Richardson number Ri. Dotted line connecting a minimum amplification rate for a given value of Ra separates the thermal instability domain from the inertial. (Adapted from the *J. Meteor. Soc. Japan.*)

$\sigma = 0$ and 0.1 curves illustrate Asai's principal point that the existence of a mean shear suppresses the onset and growth of convective instability if Re and Ri are varied holding Ra constant. On the other hand, if negative Ri is increased with Re held constant, corresponding to vertical lines in Fig. 2.6, the growth rate increases monotonically. Thus, there is no suppressing effect of convection on shear-dominated modes, and the latter are steadily transformed into the former. Our inviscid results can be considered to lie infinitely far to the upper right of the curves in Fig. 2.6. On Fig. 2.7 we show plots of growth rate against Richardson number, similar to Fig. 2.4, but for $\mathrm{Re} = 10^3$. There is very little difference between Figs. 2.4 and 2.7 except that the growth rates are a little smaller for the finite Re cases. This shows that our inviscid results are qualitatively similar to those holding Re constant and provides grounds for us to concentrate on the inviscid solutions. The shape of the growth rate curves on the upper right of Fig. 2.4 indicates a second maximum at larger wavenumber. This corresponds to the well-known result that growth rate is maximum for infinite wavenumber in an inviscid nondiffusive fluid. This result is of no physical interest here and is ignored.

Figure 2.8 (from Asai 1970b, Fig. 7) shows the variation of growth rate with the wave vector direction for six values of Ri, and Fig. 2.9 shows a similar plot for several values of negative Ri from our results. By use of a transformation like that leading to the Squire theorem for pure shear flow, it can be shown that Fig. 2.8 is a remapping of data along the $Ra = 10^4$ line of Fig. 2.6. The transformation consists of a rescaling of the dimensionless velocity field and Re by the factor k_x / k. The results allow an improved interpretation of Fig. 2.8. For

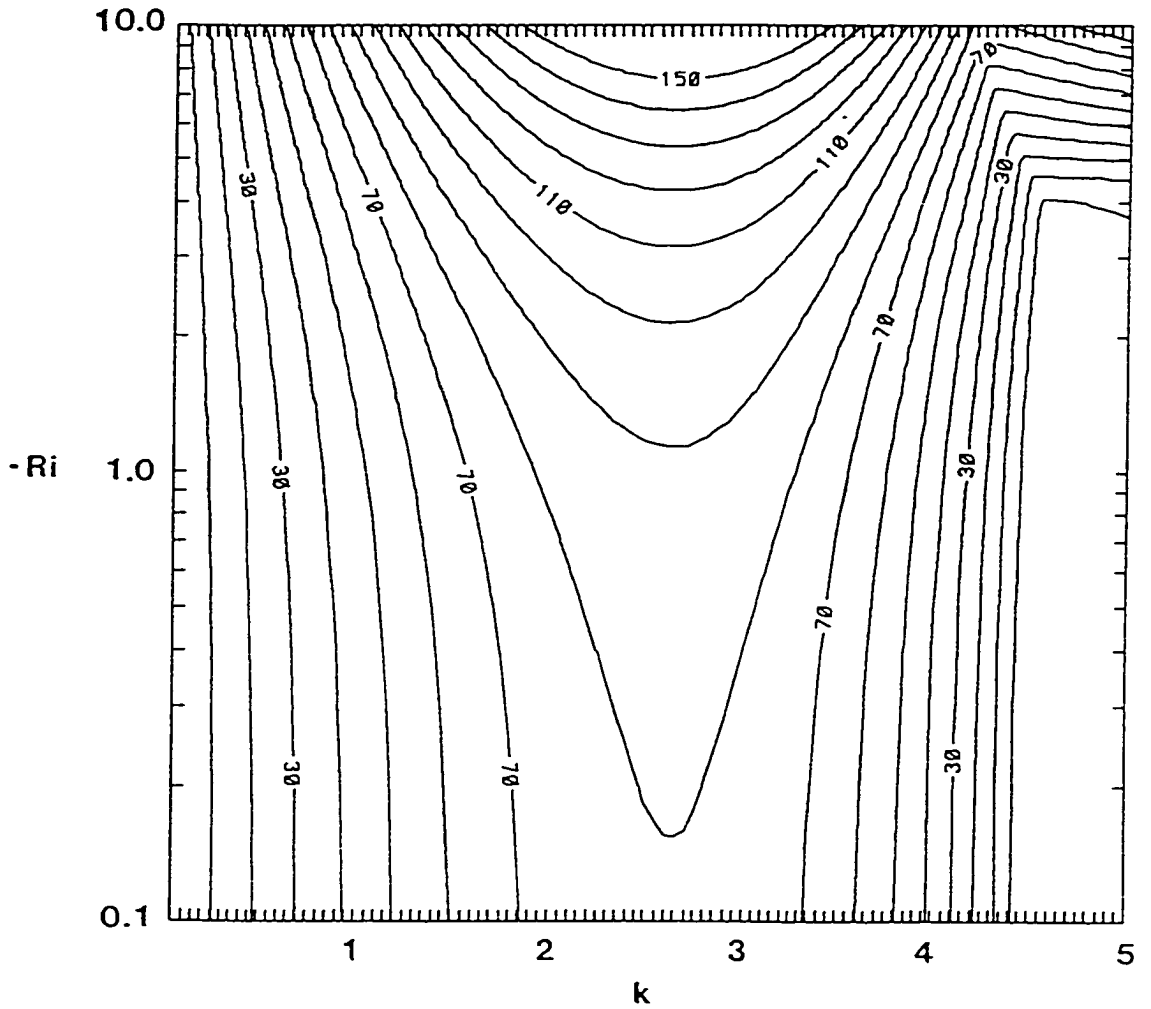

Fig. 2.7. Growth rate (x100) as a function of horizontal wavenumber and negative Richardson number for Pr = 1.0, Re = 10^3, $k_y \approx 0$ and $n = 50$. Minimum value is 0.001, maximum is 1.701, and the contour interval is 0.1.

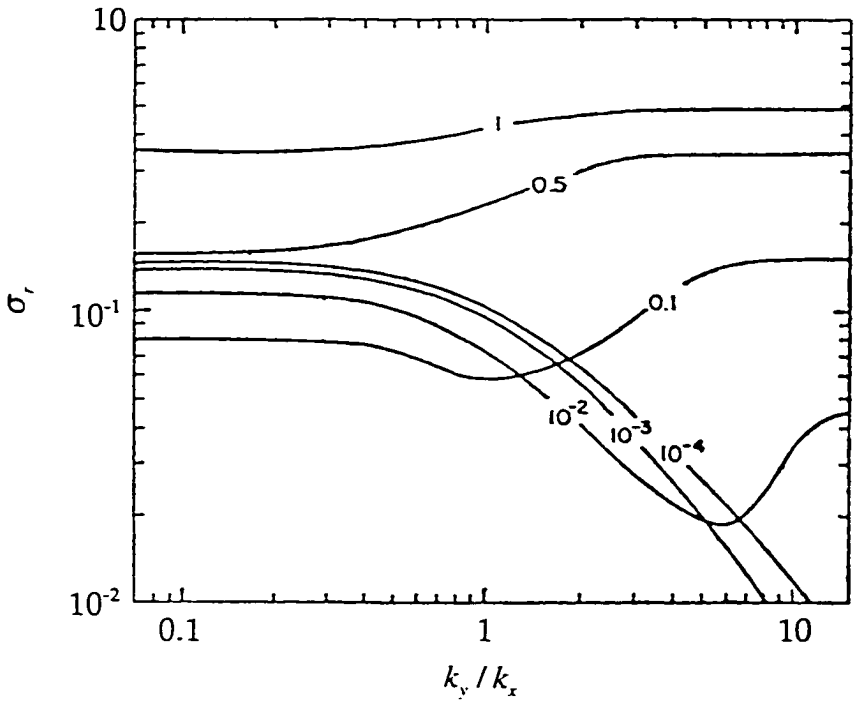

Fig. 2.8. Figure 7 for case (a) of Asai (1970 b). Variations of amplification rates with the ratio between the wavenumber in the x and y directions k_y / k_x for different values of Ri. Here Ra = 10^4 and $k = 2\sqrt{2}$ are assumed. (Adapted from the *J. Meteor. Soc. Japan.*)

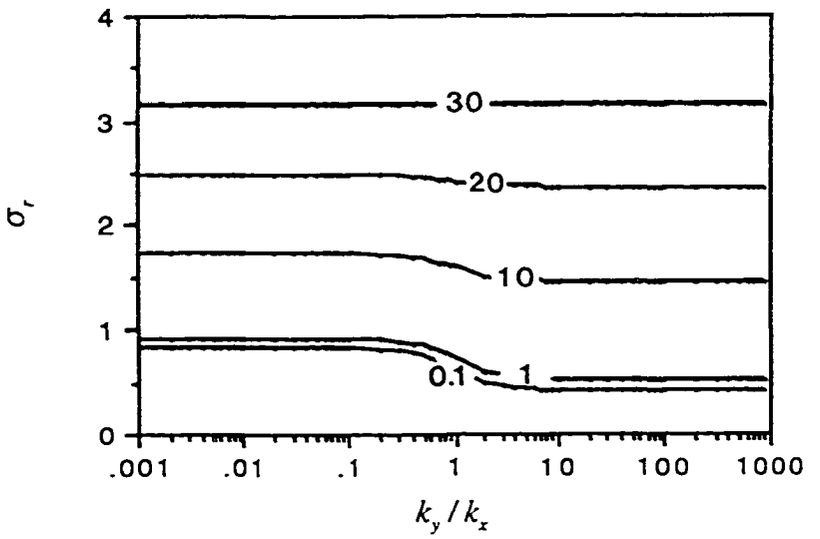

Fig. 2.9. Inviscid Growth rate vs k_y / k_x for $k = 2.7$ and various values of -Ri.

$-Ri$ less than the value where the dotted line crosses $Ra = 10^4$, about 0.2, the Squire theorem holds; that is, the growth rate is always greater for the wave vector parallel to the shear direction than for oblique wave vectors (sometimes called a three-dimensional mode, in this case $k_y \neq 0$). For larger $-Ri$ the Squire theorem no longer holds, and the longitudinal wave vector is most unstable.

A comparison between Figs. 2.8 and 2.9 suggests a different behavior of our and Asai's results, with transverse modes preferred in all our results except at large $-Ri$, where the growth rate is nearly isotropic. This comparison may also be somewhat misleading. For Asai's unidirectional shear, rotation of the wave vector changes the amplitude, but not the shape, of the shear seen in its direction. For our case that rotation does not change the amplitude of the mean shear but changes its vertical location. For what we call the transverse mode, the point of inflection and the strongest mean shear along the wave number vector occur at the center of the channel, while for the longitudinal mode two maxima occur closer to the edges. The preference for transverse modes at large $-Ri$ occurs because their energy transfer from the mean flow is more positive (or less negative) than that for the longitudinal modes.

2.3.2. Eigenvector fields and helicity calculations

The vertical resolution necessary to obtain a consistent eigenvalue is dependent on the particular parameter choices. At larger wavenumbers, at least 35 vertical levels were required to achieve a consistent growth rate with further

increases in resolution. Based on these results, $n = 50$ was chosen for all eigenvector calculations.

The linear eigenvector solutions are of arbitrary amplitude but, for comparisons, are here normalized by requiring the total integrated disturbance kinetic energy to be unity. The eigenvector fields associated with the inviscid Beltrami solution at $k = \sqrt{2}\pi$ and $k_y \approx 0$ are shown in Figs. 2.10a,b and are essentially identical to those presented by Lilly (1986b). The modes are convective rolls with longitudinal jets at the circulation centers, which are located at the midlevel, $z = 0.5$. The streamfunction for $k_y \approx 0$ (Fig. 2.10a) is plotted in place of u', and is defined such that $\partial\psi'/\partial z = u'$ and $\partial\psi'/\partial x = -w'$. The streamfunction in the $x - z$ plane is given by

$$\nabla^2\psi(x,z) = \left(\frac{\partial^2}{\partial x^2} + \frac{\partial^2}{\partial z^2}\right)\psi(x,z) = \frac{\partial u}{\partial z} - \frac{\partial w}{\partial x} = \eta, \tag{2.25}$$

where η is the y component of vorticity. The dimensionless, transformed streamfunction equation is then

$$\frac{d^2\hat{\Psi}}{dz^2} - k_x^2\hat{\Psi} = -ik_x\hat{W} + \frac{d\hat{U}}{dz}. \tag{2.26}$$

The v' velocity is simply proportional to ψ' and is not shown. The disturbance kinetic energy is shown in Fig. 2.10b. The kinetic energy and helicity exchange, terms III in (2.20) and (2.21), are proportional.

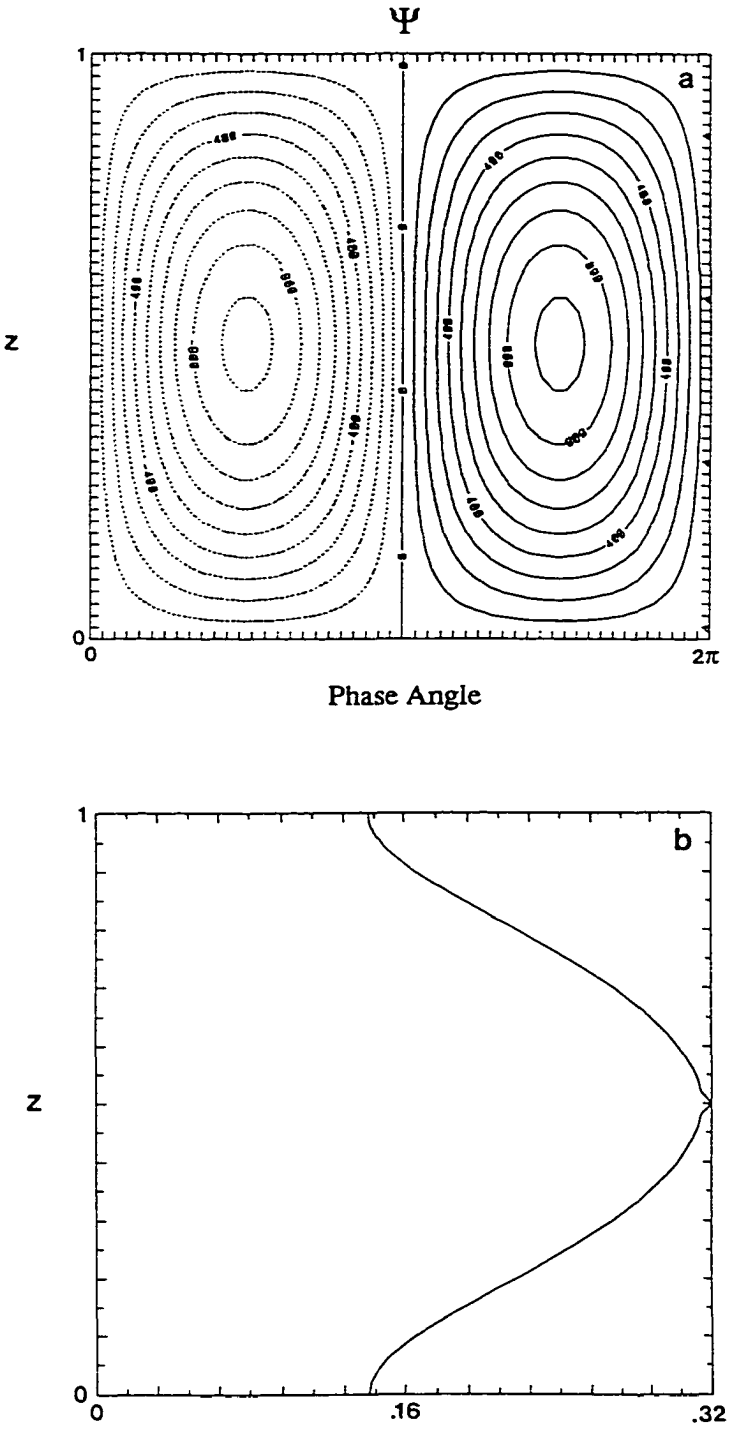

Fig. 2.10. Vertical Structure of the Beltrami perturbation solution for Ri = 0, $k = \sqrt{2}\pi$, and $k_y \approx 0$. Eigenvector fields are plotted as a function of dimensionless height (ordinate) and phase angle (abscissa). (a) Perturbation streamfunction; labels are scaled by 10 000. Minimum is -0.09 and maximum is 0.09 with contour interval of 0.01. (b) Profile of perturbation kinetic energy.

We exhibit, in Figs. 2.11-2.13, results for three amplifying mode cases: one (case I) at wavenumber $\sqrt{2}\pi$, that of the Beltrami flow, and two (cases II and III) at wavenumber 2.7, close to the fastest growing modes. Cases I and III are evaluated for $Ri = -0.1$, for which energy exchanged with the mean shear flow is expected to dominate, and case III is evaluated for $Ri = -10.0$, where buoyancy forcing is expected to dominate. In each of Figs. 2.11-2.13, the vertical velocity, buoyancy, v velocity, streamfunction in $x-z$ plane, the helicity and relative helicity, and kinetic energy source terms, are shown in six panels. All the results are for inviscid, nondiffusive equations and $k_y \approx 0$.

Figure 2.11 shows the eigenvector fields for case I, for which, from Fig. 2.4, the growth rate is ≈ 0.2. The velocities, stream function, kinetic energy source terms, relative helicity and helicity profiles are all similar to those of the Beltrami solution except near the midlevel, where a thin buoyant region appears, and the gradients of horizontal velocity are very sharp. The v velocity vanishes at the midlevel point. Also a slight phase shift appears between the upper and lower halves of the domain. The sharp gradients suggest that the eigenvector is not fully resolved in that vicinity and may be nearly singular. Figures 2.11a (w') and 2.11b (b') show that positively (negatively) buoyant fluid mostly coincides with rising (sinking) motion. Thus potential energy feeds the disturbance, principally near the midlevel, where the temperature extrema are located. From the slight slope of the streamlines and the apparent negative correlation between $u' (= \partial\psi'/\partial z)$ and w', mean kinetic energy is also being transferred to the disturbance in the midlevel region. Thus, the mean flow also transfers helicity to the disturbance in the midlevel region, even though that is where the helicity

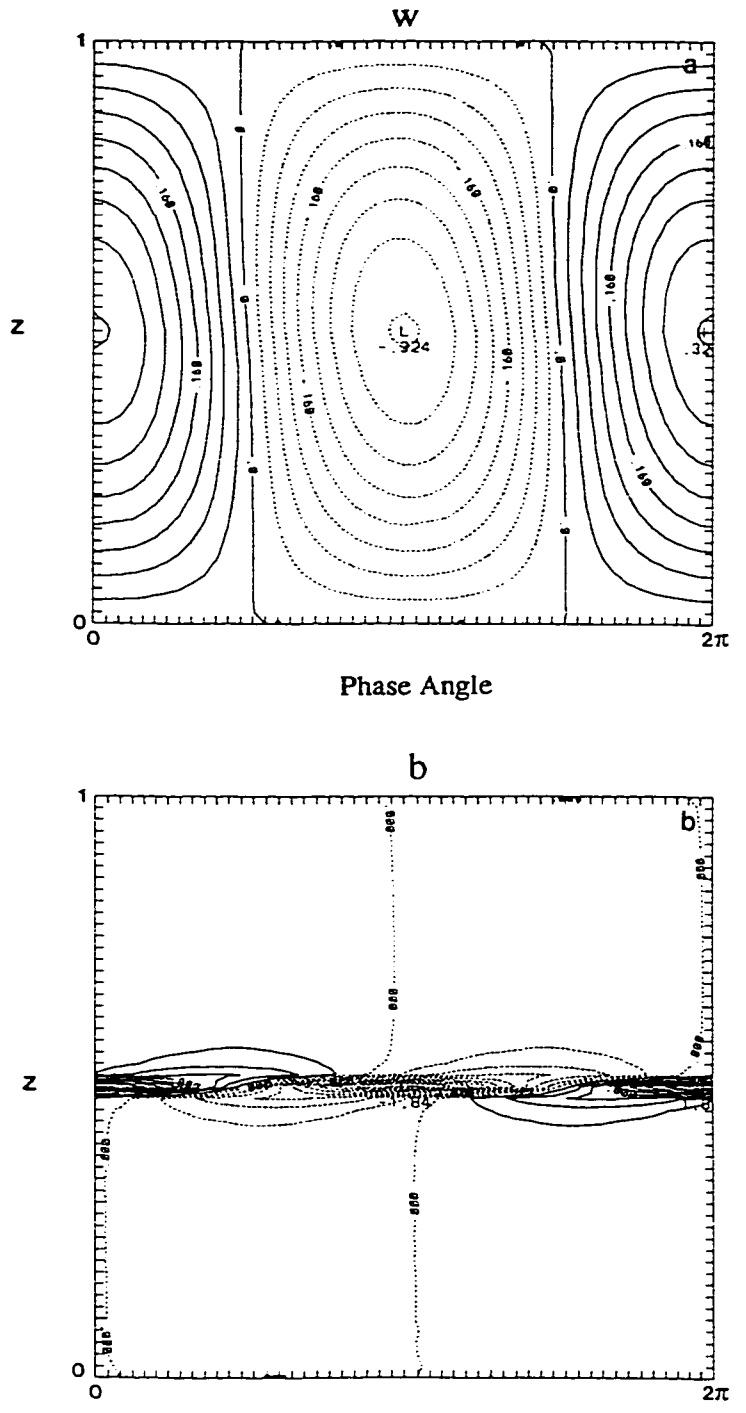

Fig. 2.11. Eigenvector fields for case I. The parameters are Ri = -0.1, $k_y \approx 0$, $k = \sqrt{2}\pi$, and $n = 50$. (a) Vertical velocity with contour interval of 0.04. (b) Buoyancy with contour interval of 0.2.

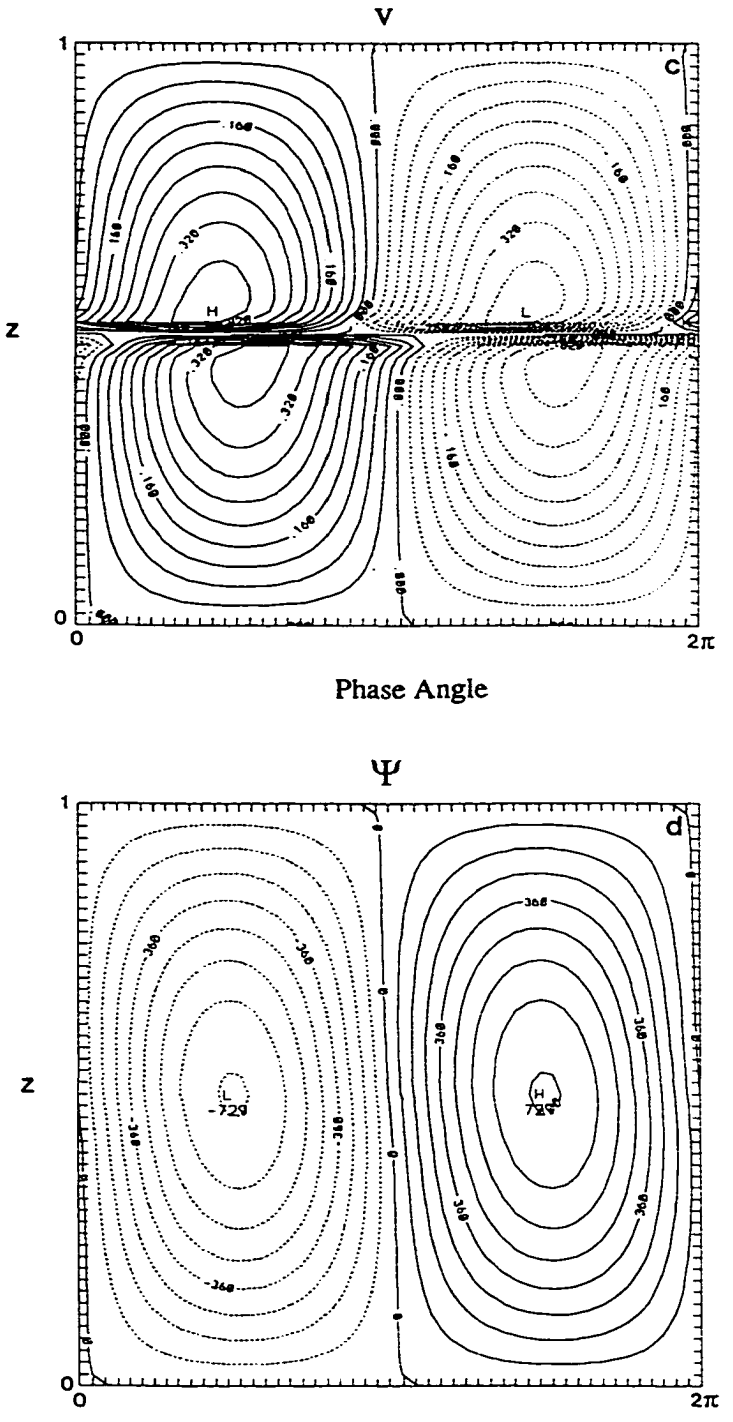

Fig. 2.11 *(continued)*. (c) Velocity in the y direction with contour interval of 0.04. (d) Streamfunction (x10 000) in $x-z$ plane with contour interval of 0.009.

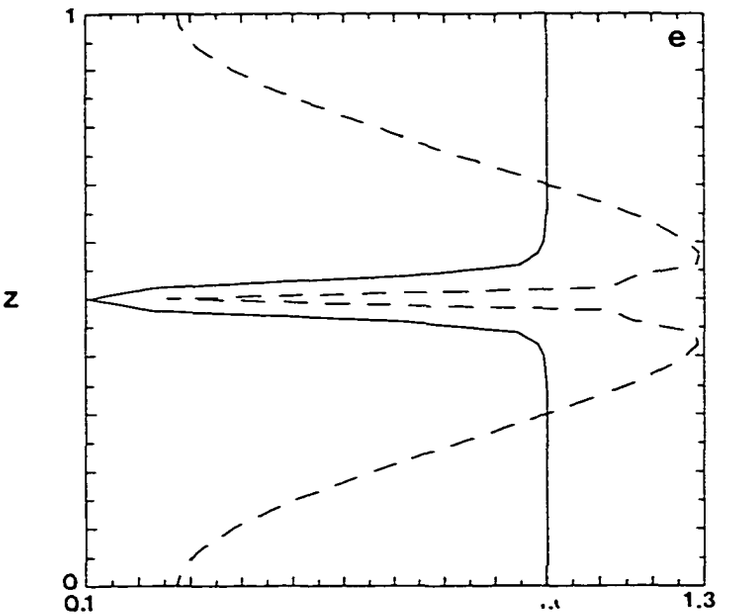

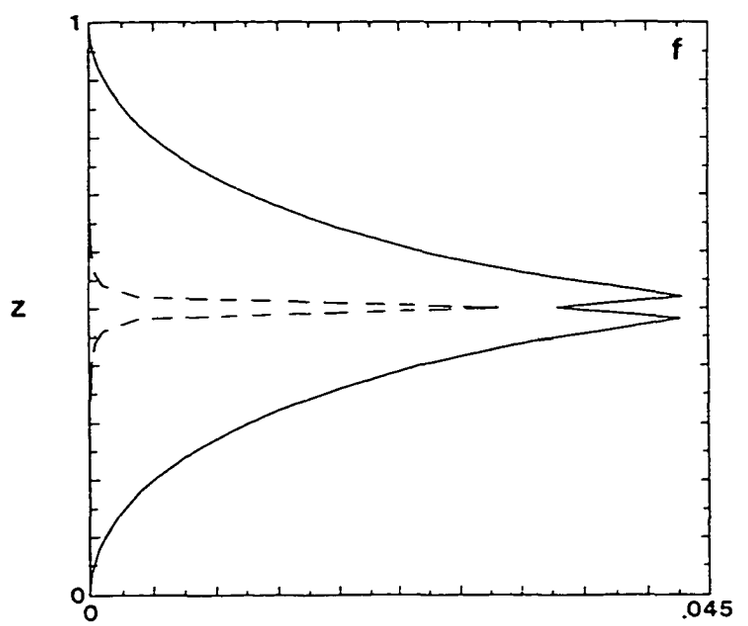

Fig. 2.11 *(continued)*. (e) Relative helicity (solid) and helicity (dashed) profiles. (f) Kinetic energy exchange (solid) and buoyancy (dashed) term profiles.

nearly vanishes (Fig. 2.11e). These conclusions are confirmed by the kinetic energy budget (Fig. 2.11f). These curves show that the maximum exchange of disturbance energy from the mean flow is nearly twice as large as the maximum buoyancy generation and extends over a much deeper region.

Figures 2.12 (case II) and 2.13 (case III) show the same fields as Fig. 2.11, but for wavenumber $k = 2.7$, which is near that of maximum growth rate. In case II, disturbance kinetic energy is obtained from the mean flow and relative helicity is highest in the upper and lower portions and lowest in midlevels where buoyancy is maximized. In case III, the buoyancy flux is strongly positive, the u momentum flux appears to be downgradient, and the v momentum flux is strongly so. This helps account for the continued positive enhancement of shear forcing to instability. The vertical integral of the energy exchange is, from Fig. 2.13f, about equal to the energy obtained from buoyancy. Where shear generation of kinetic energy is large, helicity is generated (Figs. 2.12e,f and 2.13e,f). The helicity is reduced over a larger depth, which is associated with increased buoyancy effects over the domain. Yet, relative helicity values are near or greater than 0.9 for a significant portion of the depth for both cases.

Table 2.1 summarizes the growth rates, the normalized values of integrated energy conversions, and the vertically averaged relative helicity for each of the three cases discussed above. The association of the conversion of potential energy to kinetic and low relative helicity values is notable (previously deduced by Davies-Jones 1984). These values were obtained by taking simple vertical means of the profiles from Figs. 2.11-2.13.

We now show a few more figures to summarize the helicity results. The globally averaged inviscid disturbance relative helicity [(2.22)] has been plotted

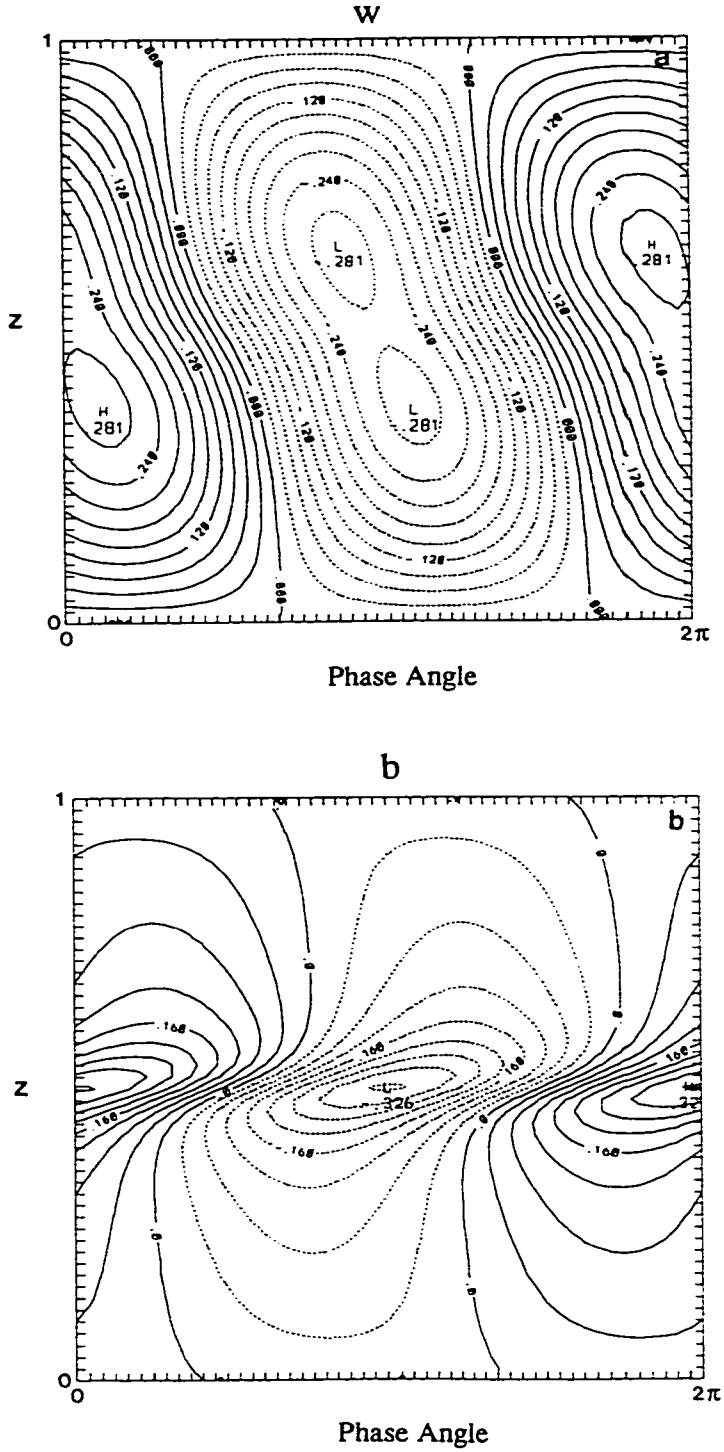

Fig. 2.12. Eigenvector fields for case II. The parameters are Ri = -0.1, $k_y \approx 0$, $k = 2.7$, and $n = 50$. (a) Vertical velocity with contour interval of 0.03. (b) Buoyancy with contour interval of 0.04.

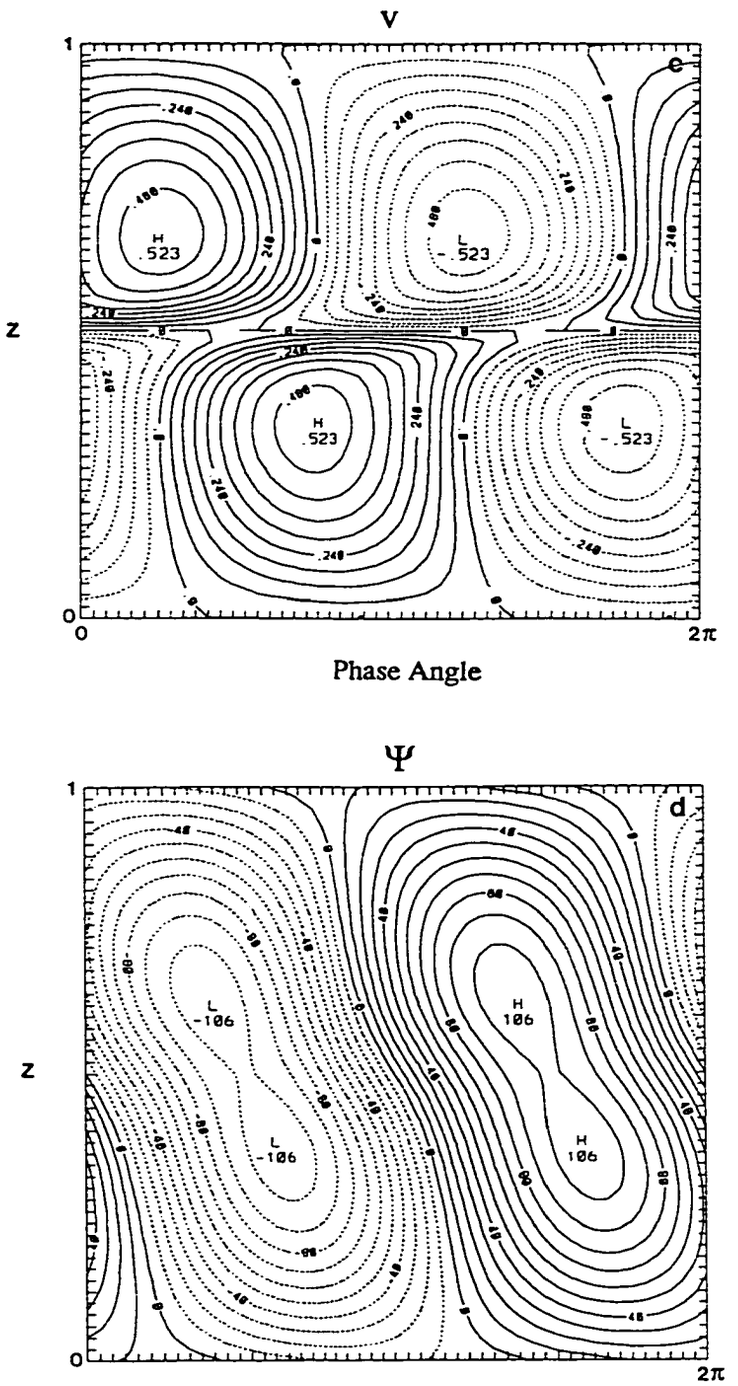

Fig. 2.12 *(continued)*. (c) Velocity in the y direction with contour interval of 0.06. (d) Streamfunction (x1000) in $x-z$ plane with contour interval of 0.01.

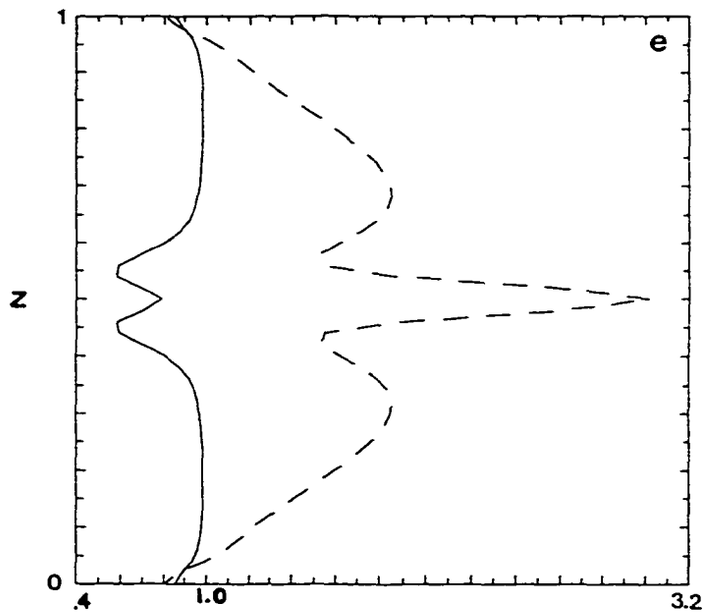

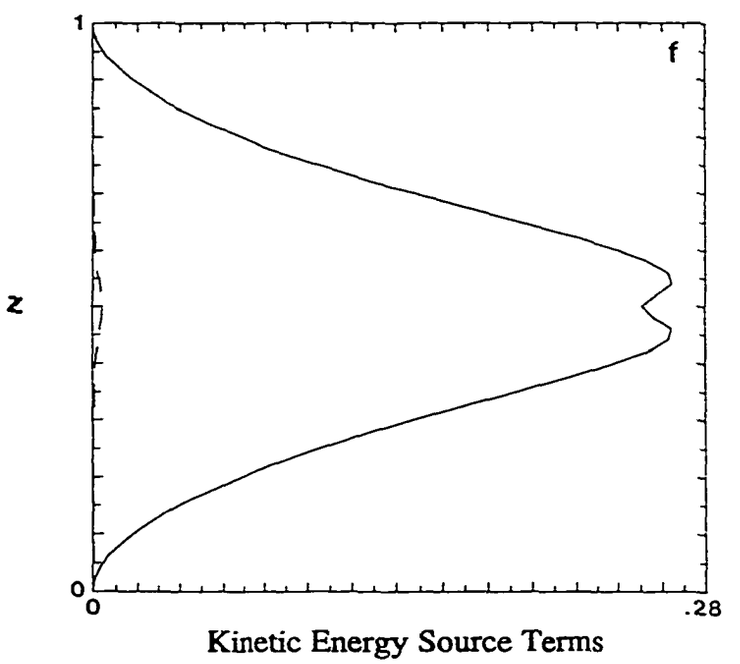

Fig. 2.12 *(continued)*. (e) Relative helicity (solid) and helicity (dashed) profiles. (f) Kinetic energy exchange (solid) and buoyancy (dashed) term profiles.

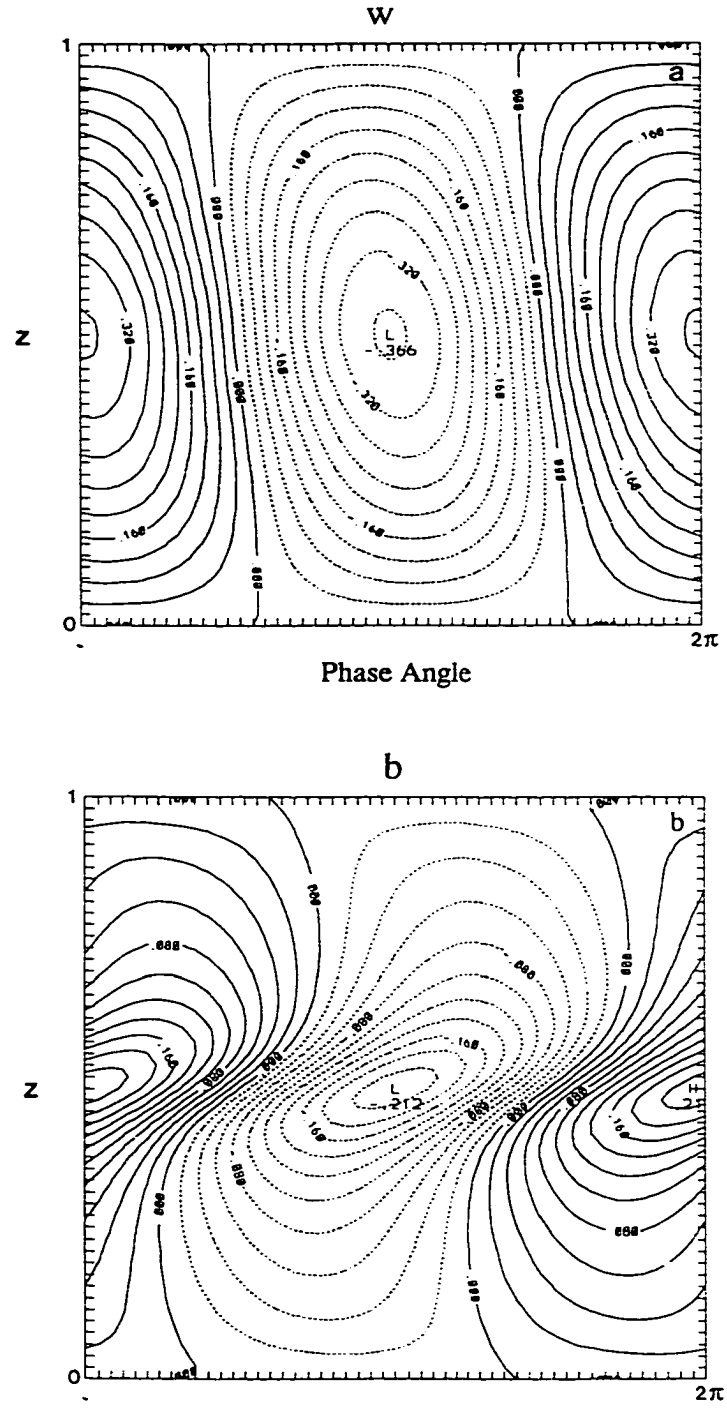

Fig. 2.13. Eigenvector fields for case III. The parameters are Ri = -10.0, $k_y \approx 0$, $k = 2.7$, and $n = 50$. (a) Vertical velocity with contour interval of 0.04. (b) Buoyancy with contour interval of 0.02.

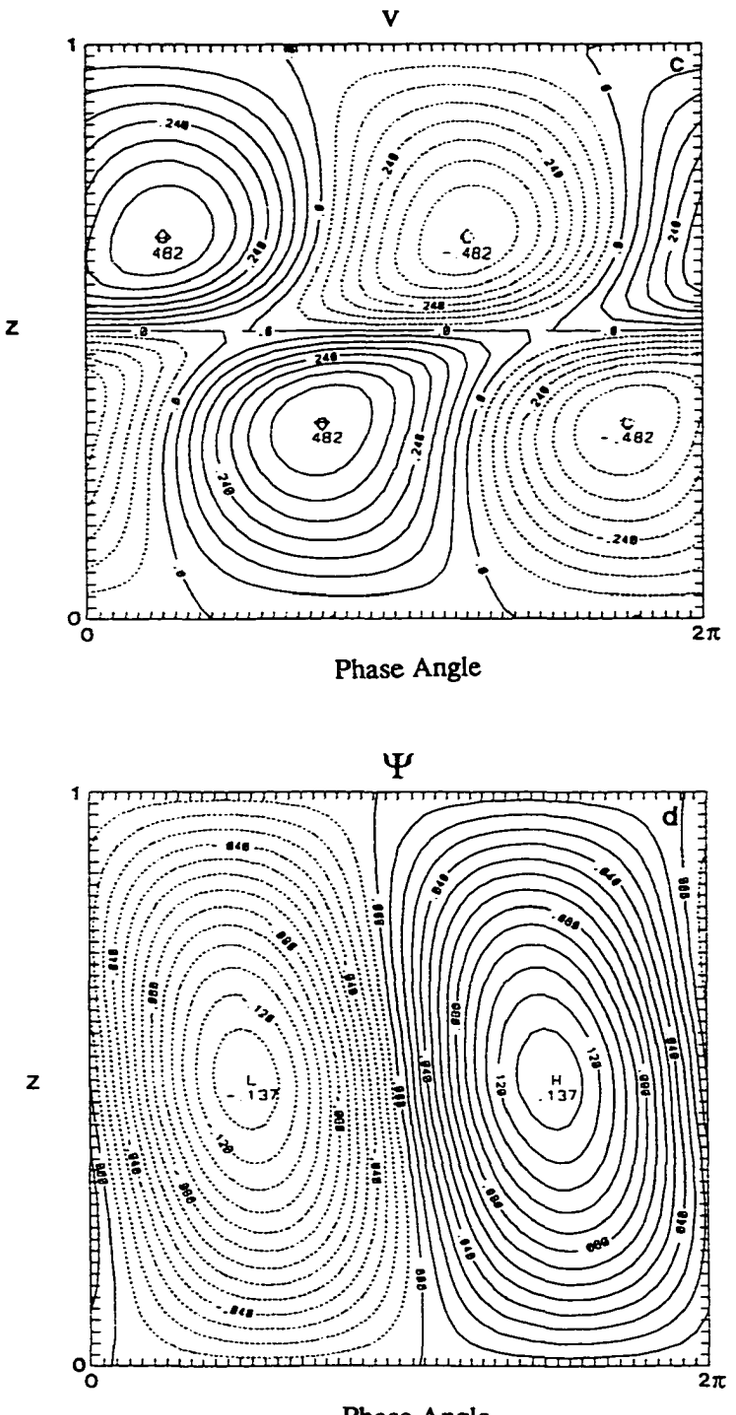

Fig. 2.13 *(continued)*. (c) Velocity in the y direction with contour interval of 0.06. (d) Streamfunction in $x-z$ plane with contour interval of 0.01.

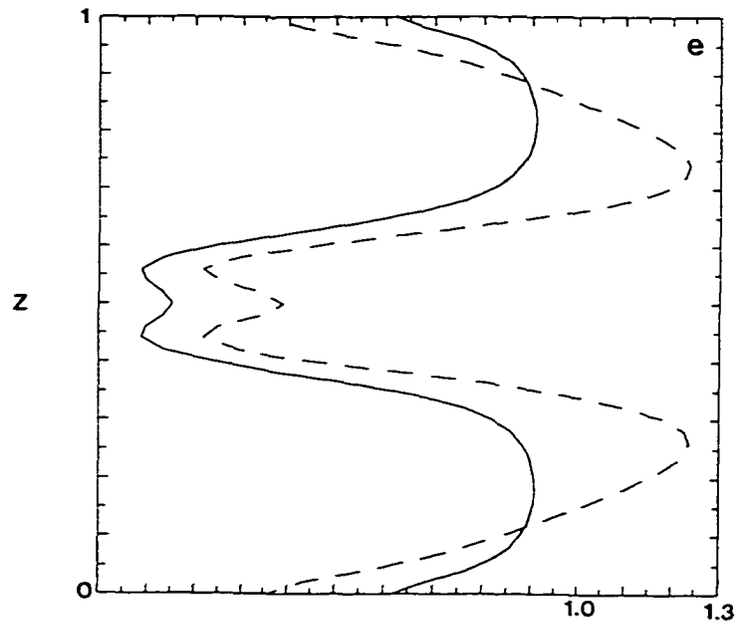

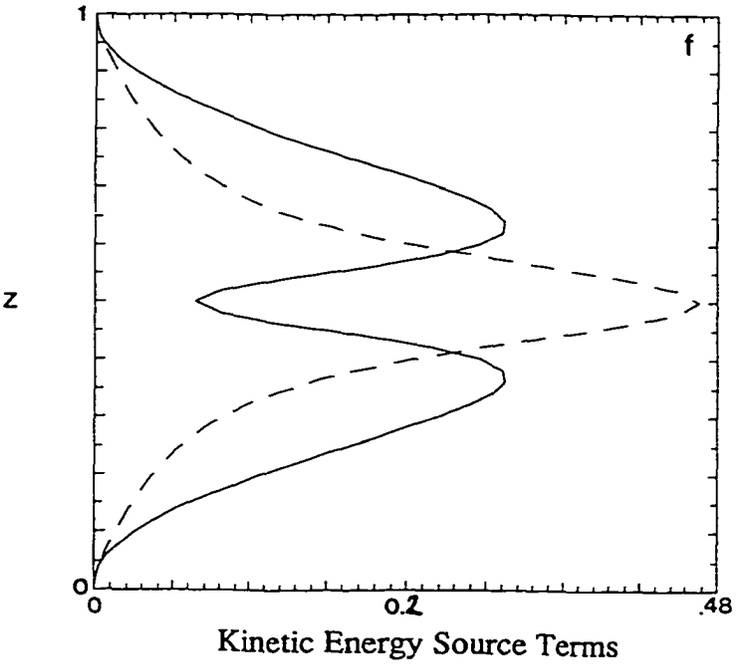

Fig. 2.13 *(continued)*. (e) Relative helicity (solid) and helicity (dashed) profiles. (f) Kinetic energy exchange (solid) and buoyancy (dashed) term profiles.

	Case I	Case II	Case III
-Ri	0.1	0.1	10.0
k	$\sqrt{2}\pi$	2.7	2.7
Growth Rate	0.2	0.85	1.7
PE->DKE	0.00081	0.00078	0.10356
MKE-DKE	0.01210	0.11806	0.12398
Overall RH	0.93714	0.89608	0.65140

Table 2.1. Identification of the three specific cases examined. For each case, the magnitudes of the energy conversions and vertical mean of relative helicity are presented.

as function of k and $-Ri$ and is shown in Fig. 2.14. The relative helicity is mostly independent of Ri for the shear regime (smaller values of $-Ri$) for the smaller wavenumbers plotted. There is also a small maximum near the Beltrami wavenumber for the smallest $-Ri$. As the Richardson number approaches zero, the relative helicity does in fact approach unity and the Lilly-Davies-Jones Beltrami analytical solution is recovered. The relative helicity drops off rapidly in the thermal regime as $-Ri$ is increased. The maximum relative helicity occurs for the zero wavenumber but is still large at the wavenumber of maximum growth. Figure 2.15 is the same as Fig. 2.14 but with finite viscosity and diffusivity as in Fig. 2.7. The effect is a decrease in the average relative helicity for the largest and smallest wavenumbers, increase in the relative helicity for small and moderate $-Ri$, and maintenance of the maximum near the Beltrami wavenumber.

Note that the globally averaged relative helicity values (Fig. 2.14) that correspond to the three cases are substantially lower than the simple vertical profile means shown in Table 2.1. If we consider case I as an example, Fig. 2.11e shows that the RH is highest away from the midlevel. But most of the energy is located at midlevel. The simple vertical mean cannot represent this phenomenon but, instead weights each vertical level equally. In the global average given by (2.22), the levels where there is more energy are weighted more heavily in the average. As a result, the average RH using the global average is smaller than the average RH using a simple vertical mean of the RH profile. The analytical solution of RH unity for the Beltrami parameters is approached more closely for small $-Ri$ using the simple vertical mean. This result suggests the need for a more sophisticated helicity statistic.

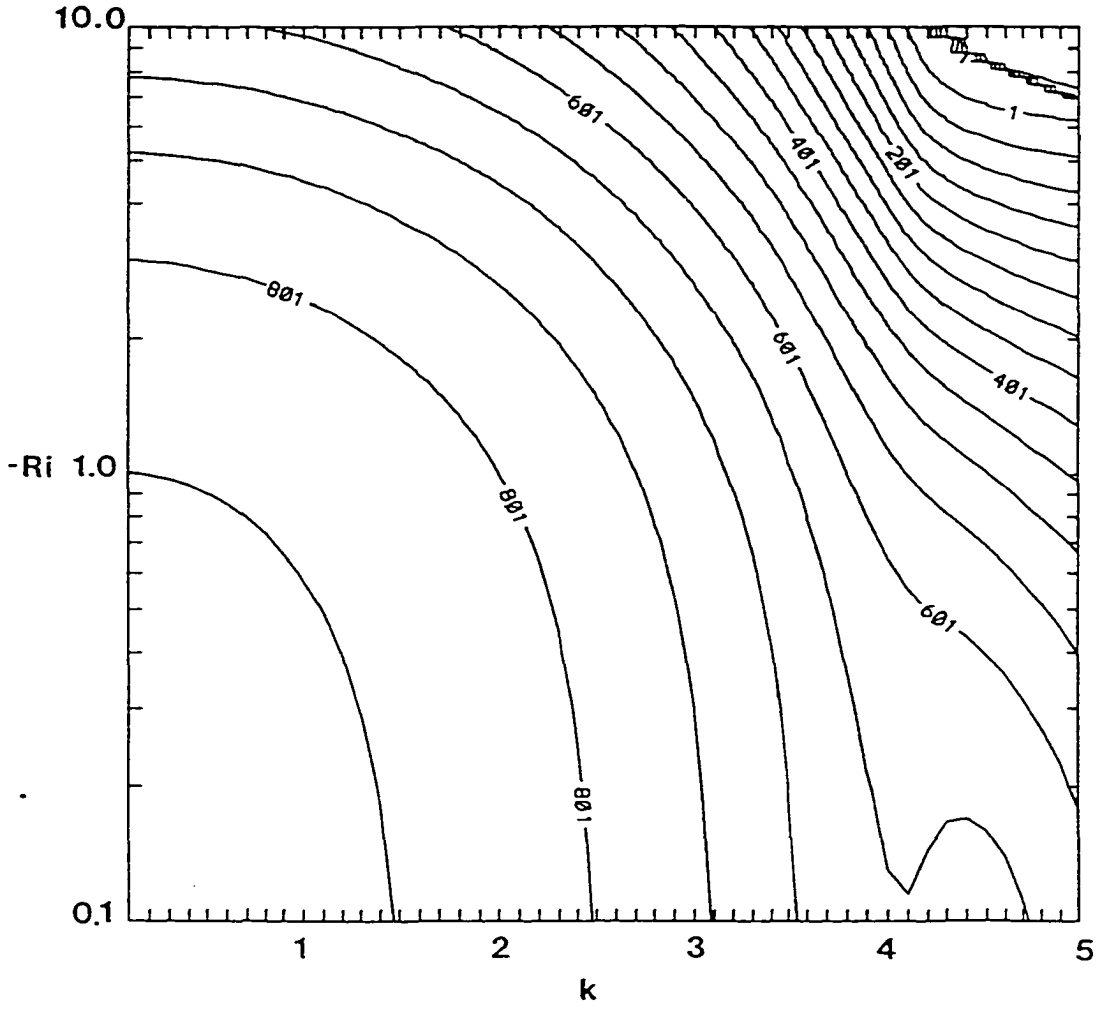

Fig. 2.14. Perturbation relative helicity contours (x1000) as a function of Richardson number and horizontal wavenumber for $k_y \approx 0$ and $n = 50$ for the inviscid case. Minimum is 0.001, maximum is 0.851, and contour interval is 0.05.

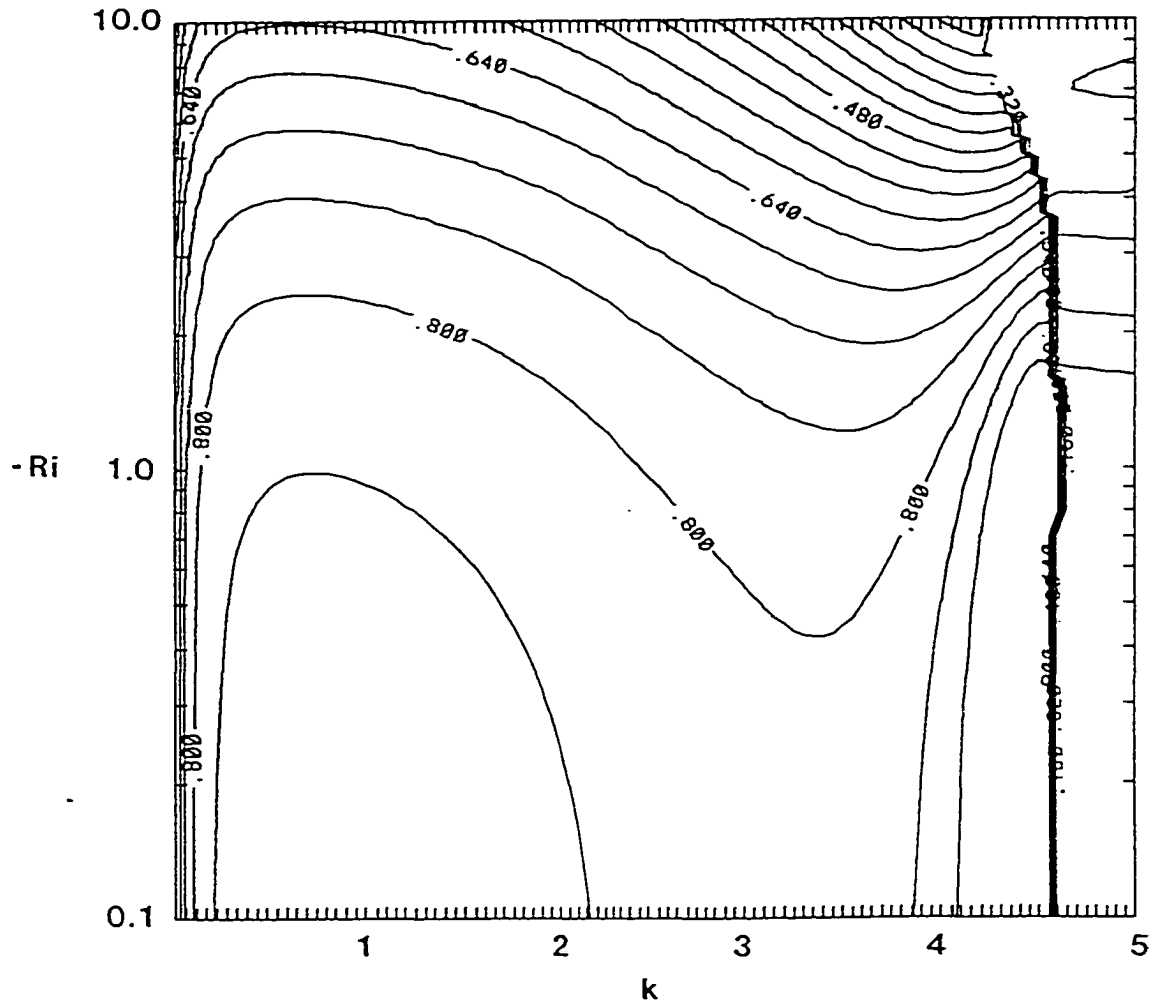

Fig. 2.15. Perturbation relative helicity contours (x1000) as a function of Richardson number and horizontal wavenumber for $k_y \approx 0$, $n = 50$, Re = 10^3 and Pr = 1.0. Minimum is 0.001, maximum is 0.851, and contour interval is 0.05.

Last, the dependence of globally averaged inviscid relative helicity [(2.22)] on the preferred disturbance geometry is plotted in Fig. 2.16. For $Ri = -0.1$, RH is greatest for transverse rolls, which are also the most unstable geometry. For the thermally dominated flow ($-Ri = 10.0$), the relative helicity is considerably reduced and shows only slight dependence on orientation angle. Upon comparison of Fig. 2.16 and Fig. 2.9, it is clear that the wave orientation of the most rapidly growing modes tends to have nearly the highest relative helicity.

2.4. Summary

The stability and structure of convection in a circular mean shear is investigated using the method of normal modes. The results may be considered an extension of Asai's work for the special case of a circular hodograph with emphasis on the eigenvector characteristics. In addition, the effects of buoyancy on helical flows are examined in order to build on the Lilly-Davies-Jones analytical Beltrami solutions. The effects of viscosity on the disturbance characteristics are determined to be small, and inviscid solutions are emphasized.

The preferred disturbance solutions are obtained as essentially two-dimensional periodic rolls for small and moderate Richardson numbers and are transverse to the shear vector at the center of the domain depth. For large negative Richardson numbers, the most unstable solution is nearly independent of orientation angle. It is possible to obtain fully three-dimensional solutions by combining pairs of solutions provided they have the same growth rates.

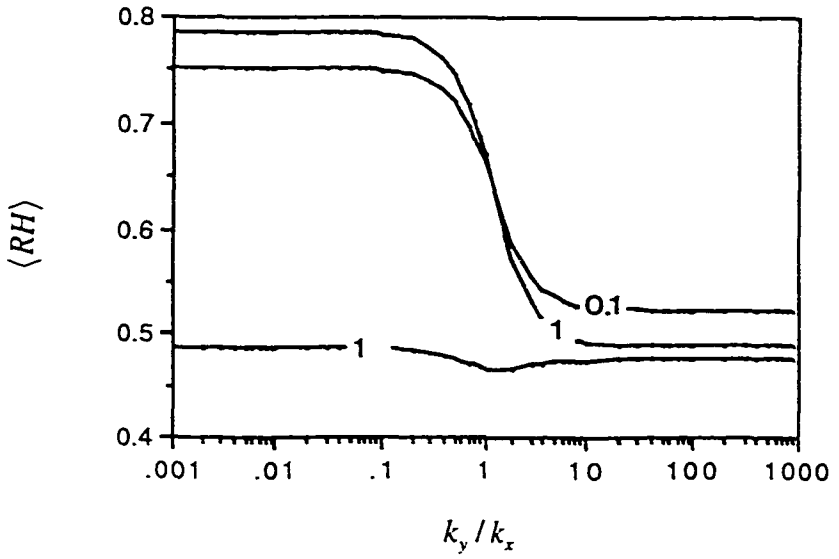

Fig. 2.16. Globally averaged inviscid perturbation relative helicity vs k_y / k_x for various -Ri and $k = 2.7$.

Two stability regimes, one dominated by buoyant effects and one dominated by shear effects, are evident for this hodograph and are qualitatively similar to the regimes presented by Asai (1970b). The thermal (shear) regime is characterized by dependence (independence) of both growth rate and globally averaged relative helicity on changes in Richardson number. The helicity and kinetic energy properties for three cases, summarized in Table 2.1, were examined. It was found that disturbance helicity is obtained from the mean flow and is minimized in regions where buoyancy is largest. However, the relative helicity values for the preferred solutions were near or greater than 0.9 for significant portions of the depth, even for larger negative Richardson numbers. Within the linear context, helicity cannot be generated by buoyancy {for the inviscid nondiffusive case that the vorticity buoyancy product [term V of (2.21)] identically vanishes}, but with a curved hodograph helicity generation is proportional to energy transfer from the mean flow. Furthermore, growth rate and disturbance relative helicity are strongly correlated (cf. Figs. 2.2. and 2.12, 2.4 and 2.13).

The concept of superhelicity is introduced as a measure of the mean-disturbance helicity exchange potential and is independent of reference frame. In addition, we point out that the more nearly closed a hodograph is, the less sensitive helicity is to the reference frame.

The results of this study are intended to complement previous theoretical work on the dynamics of rotating thunderstorms. The extension of these results to such nonlinear features is inherently limited by the idealized assumptions of dry, absolutely unstable flow. Nevertheless, the results add insight into the

dynamics of updrafts in curved shear flows. Future work might include extending the analysis to consider a mean stratification characterized by conditional instability.

Chapter 3

The Formation of Vertical Vortices in the Convective Boundary Layer

Based on an manuscript submitted to the

Quarterly Journal of the Royal Meteorological Society

July 1999

Chapter 3

The Formation of Vertical Vortices in the Convective Boundary Layer

3.1. Background

This Chapter reports on of a study of atmospheric boundary layer vertical vortices. These vortices are typically manifest as dust devils although there is evidence that they exist with some frequency in the absence of visible flow tracers (e.g., MacPherson and Betts 1997). The dust devil is one of the smaller-scale members of the broad spectrum of columnar atmospheric vortices, which includes tornadoes, waterspouts, landspouts, cold air funnels, steam devils, and firewhirls. The dust devil is distinguished from tornadoes and waterspouts by its independence of water vapor condensation. This may be partly a matter of verbal definition, however, since some of the weaker shear line or gust front vortices made visible by condensation may be dynamically similar to some dust devils (e.g., Bluestein 1985; Brady and Szoke 1989). In addition, Wakimoto and Wilson (1989) describe cases where dust whirls have formed beneath cumulus convection and eventually evolved into non-supercell tornadoes. Whether the dust devil is dynamically simpler than the moist vortices remains uncertain, since it is embedded in a strongly heated boundary layer, which provides unique complexities.

3.1.1 Observations of dust devils and their environments

Optimal conditions for dust devil formation apparently include light to moderate wind conditions and a large superadiabatic lapse rate near the surface, with the latter reported by Ryan and Carroll (1970) to be up to 9000 times the dry adiabatic lapse rate for dust devil environments in the Mojave Desert. From Prandtl mixing length theory, such conditions would be associated with large sensible heat flux, which can be forced by strong solar heating on a dry surface. Another possible source of large heat flux is cold air flowing over a warm surface. Sinclair (1969) cites Grant (1949) for an example of a dust devil that formed in the sub-Arctic with 60°F surface temperature. Cold funnels, vertical vortices associated with shallow convection, (Hess et al. 1988) may also occur in such conditions.

Many investigators have asserted that dust devils are not observed for low-level ambient windspeeds greater than some value, for example, five meters per second (Webb 1963; Sinclair 1969). Morton (1966) states that wind speeds greater than seven to ten meters per second will break up the dust devil.

In a field observation study in the Mojave Desert, Carroll and Ryan (1970) used a "vorticity meter," consisting of four low-density spheres at the ends of two mutually perpendicular one meter rods, to measure vertical vorticity in the environment of dust devils. They found good correlation between the sign of vorticity from the meter and the sense of rotation of observed dust devils.

In laboratory and numerical simulations of ordinary thermal convection, vertical vortices have not often been observed except in the presence of basic vertical vorticity (Barcilon and Drazin, 1972) or some other well-defined source

of angular momentum. Most of those were done at relatively low Rayleigh number (Ra), 10^6 or less. However, from numerical simulations of Rayleigh-Benard convection at Ra = 4×10^7 and greater, involving so-called "hard" turbulence, Cortese and Balachandar (1993) observe vertical vortices without a mean flow. Mason (1989) presented CBL, LES results that indicated the presence of vertical vortices, but these were not discussed. In an earlier laboratory simulation of convection with uniformly heated boundaries, no mean flow, and Ra $\approx 10^9$, Willis and Deardorff (1979) observed many transient rotating plumes at the vertices between three convective cells. From these results, they concluded that dust devils may form in the absence of surface temperature or roughness inhomogeneities.

The intensity of dust devils can be as great as that of small tornadoes. There have been reports of significant damage to houses (McGinnigle 1970) and windows broken (Cooley 1971) by dust devils. Wind speeds recorded as a dust devil passed over a meteorological recording station were as high as 41 m s^{-1} (Ives 1947). A more typical value of measured tangential wind speed in a dust devil is about 15 m s^{-1} (Sinclair 1973). Dust devil diameters range between 10's of cm and 30 m and heights range from a few meters to 1000 m or more (Sinclair 1964). Hess and Spillane (1990) report dust or grass, associated with dust devil circulations, that was visible at heights of 1500-2400 m.

Regarding dust devil rotation and translation, there appears to be no preferential direction of rotation except for the very largest diameter dust devils, where there may be some preference for cyclonic rotation (Durward 1931; Flower 1936; Sinclair 1965). However, a very large multi-vortex dust devil, observed by Fujita (1971), was anticyclonic and embedded in a mesoscale anticyclone.

Sinclair (1969) observed that most dust devils translate in a direction that is within 45 degrees of the mean wind direction. Flower (1936) and Maxworthy (1973) observed that cyclonic dust devils appear to move to the right of the mean wind and anticyclonic ones to the left. Most dust devils are reported to move continuously and at a speed nearly equal to that of the mean wind.

3.1.2 Dynamics of dust devil formation

Sources of both buoyancy and vorticity are necessary for dust devil existence. While the source of buoyancy undoubtedly lies in the superadiabatic layer near the surface that is present in the environments of most observed dust devils, the source of vorticity remains the principal issue of debate (Maxworthy 1973).

Ambient vertical vorticity sources have been proposed, based on the pre-existence of horizontal shear zones (Barcilon and Drazin 1972), as well as the direct generation of vertical vorticity by flow past elevated topography (Sinclair 1969; Hallet and Hoffer 1971) or smaller obstacles, such as buildings (Ives 1947). Vertical vorticity may also be generated by tilting of ambient horizontal vorticity, such as that associated with mean wind shear (Maxworthy 1973), differential surface heating (inferred from the results of Snow and McClelland 1990), sea breeze circulations (McGinnigle 1970) or other mesoscale features, or turbulence (Busse 1972). Several authors (e.g., Carroll and Ryan 1970; Willis and Deardorff 1979; Cortese and Balachandar 1993; Shapiro and Kogan 1994) have proposed or provided evidence that larger scale convective circulations that are not initially

rotational can generate vertical and/or tiltable horizontal vorticity. Some of these proposed mechanisms for the generation of vertical vorticity and coaxial updrafts will now be described.

3.1.2.1 Concentration of ambient vertical vorticity

This is the most straightforward mechanism. If net circulation exists around the perimeter of some area, buoyant convection within that area will concentrate the circulation and increase the local vorticity by stretching. There is no obvious reason to assume that the initiation of penetrative convection will be favored in such a region, but once it is established, rotational or helical stabilization and increased efficiency may favor its maintenance and growth. If this is the case, the presence of vortical boundary layer flows may play an important role in heat and momentum transports in the boundary layer, and consequently in convective initiation.

3.1.2.2 Convective tilting of mean flow horizontal vorticity

This concept, although proposed earlier, became accepted as the source of rotation of supercell convective storms after the seminal numerical experiments of Klemp and Wilhelmson (1978). This mechanism has been frequently explained and illustrated (e.g., Lilly 1982, 1999; Davies-Jones 1984; and Klemp 1987) and is the generally accepted source of midlevel rotation for supercell convective storms. An updraft rising through an environment with a mean vertical shear develops a pair of counter-rotating vertical vorticity centers on

either side of the updraft center relative to the mean shear vector. A schematic illustration of this process, from Klemp (1987), has been reproduced here as Fig. 3.1. This evolution is quite general, based on linear theory, but extended to nonlinear conditions by potential vorticity concepts (Rotunno and Klemp 1985). In the case of a shear vector changing direction with height (curved hodograph), Rotunno and Klemp (1985) showed that the vortex on the concave side of the hodograph is favored in amplitude. For a circular or nearly circular hodograph, it appears that only one vortex is formed, centered approximately coincidentally with the updraft axis (Lilly 1986; Kanak and Lilly 1996).

The explanation of the observed coincidence of supercell updraft and vortex centers is somewhat complex and perhaps not yet fully established, and its applicability to dust devils is uncertain. One accepted concept is that if an updraft can be induced to propagate with a component lateral to the mean shear vector, then the vortex generation continues to the center of the updraft, which also becomes the vortex center. At least two different mechanisms have been proposed to explain such lateral motion.

In the presence of a mean wind near the surface, it is often observed that the movement of the base of a dust devil vortex lags behind its propagation aloft, so that it is fairly strongly tilted near the surface, becoming upright aloft. Maxworthy (1973) invoked the Biot-Savart Law, which shows that for a curved vortex, each segment generates a flow which advects other segments, leading to vortex propagation in the direction of the vortex flow on the inside of the curve. (A classical example is the propagation of a smoke ring.) From this reasoning, a

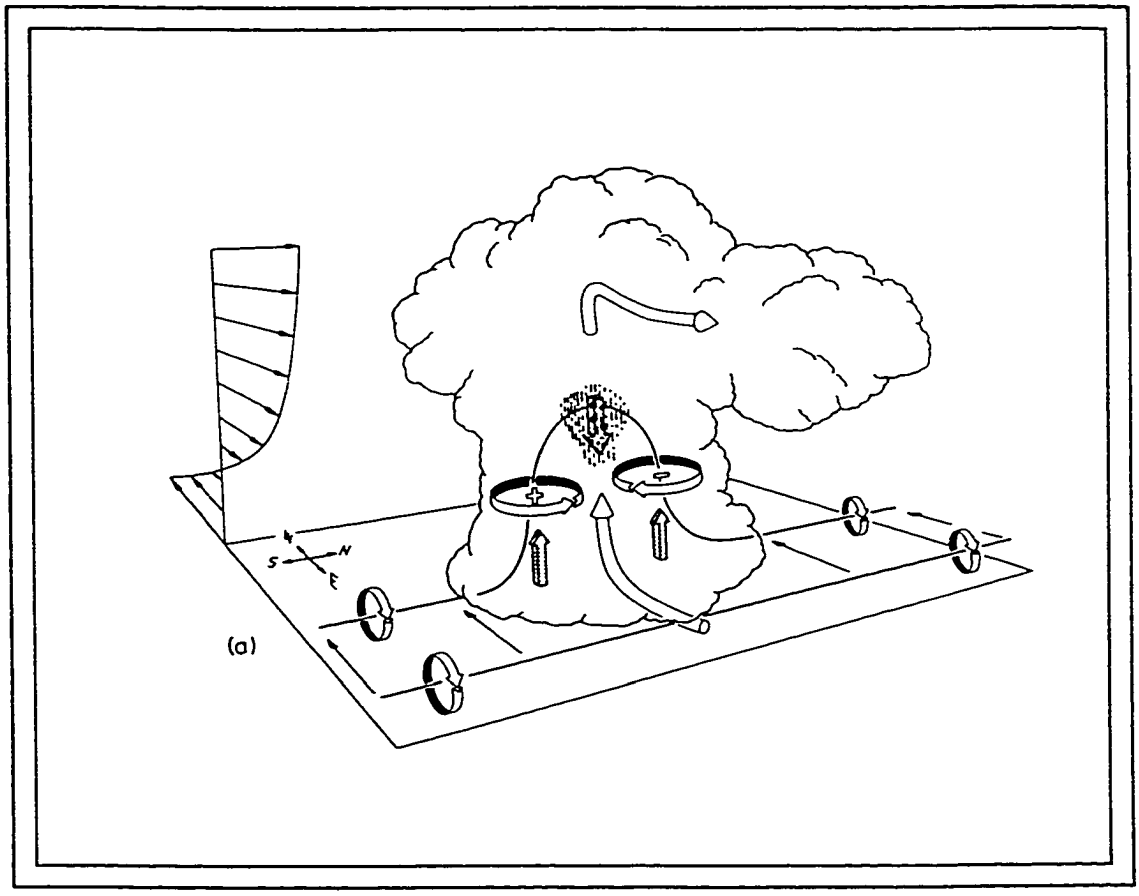

Fig. 3.1. From Klemp (1987). Illustration of the development of rotation within a simulated thunderstorm through vortex-line tilting. In the early stage, a vortex pair forms from tilting of the horizontal vorticity associated with the mean shear. (Adapted from *Ann. Rev. Fluid Mech.*)

cyclonic (anticyclonic) vortex will have an induced motion to the right (left) of the mean shear vector, in agreement with Maxworthy's field observations.

Rotunno and Klemp (1982) carried out an analysis, based on the pressure field, of updraft motion in simulated supercell flows that has been generally accepted. The vortex tilting mechanism predicts maximum vorticity where the product of updraft amplitude and mean shear is the largest, which is always above the surface. A maintained vortex center is necessarily a low-pressure center. Thus a vertical pressure gradient develops and accelerates flow toward the pressure minimum. Rotunno and Klemp did not clearly point out, however, that downward acceleration is predicted above the vortex maximum. While it is possible for an updraft to accelerate into the vortex center, attain its maximum strength there and decelerate above it, it seems equally possible for a downdraft to originate at higher levels, attain its maximum strength at the vortex center, and decelerate below it. This would seemingly cause an updraft to be repelled by a vortex. Such an event is seldom, if ever, observed in convective storms. The reason is probably conditional instability (Lilly 1999). An updraft becomes saturated and rises with positive buoyancy to high levels, while a downdraft is and remains dry, and consumes kinetic energy as it descends.

Since a dust devil does not normally involve conditional instability, the supercell mechanism for updraft migration may not apply. On the other hand, in a boundary layer heated from below the static stability is normally negative in about the lower half of the mixed layer and slightly positive above that. Thus, if a vortex is formed by tilting of vorticity in the middle of the mixed layer, an updraft may be expected to migrate into it or generate within it.

3.1.2.3 Generation of vertical vorticity without a mean shear

Individual convective circulation cells are well-defined sources of horizontal (azimuthal with respect to the updraft centers) vorticity, although the horizontal flow field at a given level is irrotational. Cortese and Balachandar (1993) propose that near the edges and intersections of convective cells, vertical and horizontal shear may occur randomly and then be concentrated by small-scale convective updrafts. A similar concept may explain the results of Willis and Deardorff (1979).

Carroll and Ryan's (1970) interpretation of their vorticity meter data is that the "environmental" vorticity that they measure is produced by convective cell circulations. They conclude this based on observations taken over flat topography in the absence of obvious mesoscale wind patterns. They state that convective downdrafts diverge as they impinge on the ground surface and that they typically do so in an asymmetric fashion with respect to the updraft centers, perhaps due to minor surface inhomogeneities and/or momentum brought down from upper levels. The latter process would require the presence of a mean flow aloft. Areas of local shear would then be produced that might result in vertical vorticity centers on the periphery of each convective element.

A related but different way in which the interaction of convective updrafts could result in the production of vertical vorticity is presented by Shapiro and Kogan (1994). In numerical simulations of merging convective clouds, they find horizontal vorticity to be formed in rings around each updraft. Whenever two or more convective circulation cells interact, the horizontal vortex lines are advected upward at slower rates on the sides of the updrafts which are closest to each

other. In this way the horizontal vorticity is tilted and vertical vorticity centers of opposite signs are produced on the periphery of merging convective cells. This mechanism could be applicable to the applicable to the dust devil environment through the interaction of neighboring thermals and the associated convective circulations. However, it would have to be modified to represent the open cell convection that is characteristic of that environment. A subsequent process for the co-location of these vorticity centers with updrafts is also required.

The interaction of boundary layer convective scale circulations, as well as the tilting of mean vertical shear, could explain the generation of vertical vorticity above the ground in dust devil environments. However, as in the case for tornadogenesis, a mechanism must exist to explain the presence of vertical vorticity near the ground for dust devil formation. Several tornado generation mechanisms have been proposed and to varying extents justified by numerical simulation results. For example, Davies-Jones (1982) argues that a downdraft must be present to tilt horizontal vorticity into the vertical near the ground for tornadogenesis to occur. Walko (1993) adds that downdraft tilting and subsequent convergence must both occur for tornadogenesis. It is not obvious whether or not these theories are applicable to dust devils. Within the dust devil environment, however, wind shear and buoyancy both have extreme maxima at the surface. This suggests that significant tilting could occur within the first few meters above ground, and a vortex generated that low could be linked to the surface by turbulent transfer.

This last case, of vertical vortex formation in the absence of mean winds, is the dynamical regime chosen for study in this dissertation.

3.1.3 Energetics and mechanism

The potential energy of the superadiabatic layer near the surface of dust devil environments clearly provides energy for formation and maintenance of the dust devil (Flower 1936; Battan 1958; Sinclair 1969; Ryan and Carroll 1970; Emanuel 1988). Emanuel (1988) asserts that the source of energy for the dust devil is the thermal disequilibrium between the surface and the overlying air, which is the same as that for hurricanes. He also suggests that the dust devil may be maintained in a similar fashion as the hurricane; that is, by a feedback process between the vortex circulation and surface heat fluxes. Sinclair (1969) comes to a similar conclusion by suggesting that vortex translation permits the dust devil to continuously acquire new potential energy sources. He explains the observed decrease in dust devil activity directly following a maximum in occurrence, as due to depletion of the superadiabatic layer, which must recover before dust devil frequency can again increase. The occasional existence of stationary vortices must indicate a strong continuing source of buoyant energy.

A variety of mechanistic theories of dust devil vortex formation have been proposed and are here described briefly without comment.

The optimality of high surface heat flux and low mean wind requires that the Monin-Obukhov length (MO) must be small. Based on the analytical solution for a plane sink vortex, Webb (1963) derives a condition for vortex formation requiring that MO be small.

Similarly, Deardorff (1978, cited by Hess and Spillane 1990) suggests that a necessary condition for dust devil formation is that -h / MO be on the order of 100 or more, where h is the height of the convective boundary layer. Hess and Spillane (1990) suggest that -h / MO need only be greater than 50.

Fitzjarrald (1973) proposed that there exists an optimal combination of buoyancy and vorticity (Richardson Number) for the formation of dust devils. This is perhaps similar to the optimal bulk Richardson numbers found for supercell thunderstorms by Weisman and Klemp (1982).

Goody and Gierasch (1974) regard the non-rotating plume and the dust devil as triggered by the same process but evolving into one or the other based on the ambient thermal and dynamical conditions. They suggest that this transition is accomplished by the suppression of turbulence by rotation at the edge of the plume, which results in the contraction of the plume and the concentration of ambient angular momentum. They derive a condition for the transformation of a nonrotating thermal plume to a vortex based on the ambient vorticity and Brunt-Vaisala frequency.

Kaimal and Businger (1970) proposed that vertical stretching at the back edge of the plume concentrates vorticity, and if it is of sufficient magnitude will transform a non-rotating plume into a dust devil. They provide an example of a plume, which had a large enough value of vorticity to be considered to be in a "transition" stage.

Emanuel (1988) adds that a vortex will spin up only if the inflowing air converges through a deep enough layer that frictional dissipation of the initial angular momentum is overcome.

3.1.4 Heat and momentum transport by dust devils

Dust devils may be significant transporters of heat and momentum in the atmosphere (e.g., Kaimal and Businger 1970; Smith and Leslie 1976). If rotating thermals rise higher than non-rotating thermals (Porch 1974), they may control growth of the boundary layer, which would be important to boundary layer parameterizations. Observational studies by Sinclair (1969) and Kaimal and Businger (1970) suggest that this may be true.

Kaimal and Businger (1970) performed a single case study comparison of a non-rotating thermal plume and a dust devil, observed at two levels on a tall tower. They found that the dust devil transported more heat and momentum at both levels considered (5.66 and 22.6 m) than the nonrotating plume. Sinclair (1969) reports that the heights of dust columns in dust devils are usually less than 600 m but, in desert conditions with deep mixed layers, the thermal updrafts associated with them are observed to extend as high as 4500 m.

Businger (1972) asserts that dust devils transport ten times as much heat and momentum as non-rotating plumes. In contrast, however, Goody and Gierasch (1974) suggest that plumes are much more efficient transporters of heat

and momentum. Apparently, they conclude this from observations of the upper-level diameters of the plume and dust devil.

The dynamic rationale for increased convective efficiency by dust devils was provided by Ludlam and Scorer (1953), who proposed that rotation in a dust devil inhibits mixing in an ascending updraft. Andre and Lesieur (1977) concluded from turbulence closure studies that helical structures are less dissipative than non-helical flow structures. Lilly (1986) proposed that this concept applies to rotating convective storms and may be partly responsible for their high energy and durability.

In summary, the following questions motivate this study of convective boundary layer vortices: 1) Is vorticity generated by the larger scale convective circulations (Cortese and Balachandar 1993)? 2) Can the proposed vorticity generating mechanisms of Shapiro and Kogan (1994) and Carroll and Ryan (1970) be applied to dust devil formation? 3) Is vortex formation favored at the vertices of open cellular convective patterns (e.g., as in Willis and Deardorff 1979; Hess and Spillane 1990; Cortese and Balachandar 1993)? 4) Do dust devils transport more heat and momentum than non-rotating thermals? 5) Is this is so, is the height of the boundary layer determined largely by the existence of vertical vortices?

3.2 Methodology

3.2.1 Numerical model description

A fully three-dimensional, nonhydrostatic numerical model has been developed specifically for this research and is called "KANSAS" (KANak's System for Atmospheric Simulation). The model integrates the advective form of the supercompressible equations for dry fluid motion (Anderson et al. 1985; Droegemeier and Wilhelmson 1987; Droegemeier and Davies-Jones 1987).

The supercompressible system consists of prognostic equations for five dependent variables: perturbation pressure, potential temperature, and three Cartesian velocity components, u, v, and w. The mass continuity equation is used in deriving a prognostic equation for perturbation pressure. Each variable can be considered to be comprised of base state, perturbation, and subgrid-scale (SGS) contributions. The base state satisfies the hydrostatic and ideal gas equations.

3.2.1.1 Dynamical framework

The compressible equations for buoyant convection in a Cartesian coordinate system may be written as

$$\frac{\partial u_i}{\partial t} = -u_j \frac{\partial u_i}{\partial x_j} - \frac{1}{\rho}\frac{\partial p}{\partial x_i} - \delta_{i3} g + F_i \quad , \tag{3.1}$$

$$\frac{\partial \theta}{\partial t} = -u_j \frac{\partial \theta}{\partial x_j} + D_\theta \quad , \tag{3.2}$$

and

$$\frac{\partial \rho}{\partial t} = -\frac{\partial (\rho u_j)}{\partial x_j}, \tag{3.3}$$

where u_i are the three Cartesian velocity components, p is pressure, g is gravity, θ is the potential temperature, ρ is the density, $F_i = F_{is} + F_{if}$ and $D_\theta = D_{\theta s} + D_{\theta f}$ represent the sub-grid turbulent mixing terms and numerical filtering terms. This fully compressible system permits both acoustic and gravity wave solutions.

Since the thermodynamic quantities vary more rapidly in the vertical than the horizontal, they may be written as a sum of a base state variable which is a function of z only and a perturbation from the base state,

$$\theta = \bar{\theta}(z) + \theta'(x, y, z) \tag{3. 4}$$

and

$$p = \bar{p}(z) + p'(x, y, z). \tag{3. 5}$$

Upon substitution of (3.4) and (3.5), use of the base state hydrostatic equation, and the neglect of terms containing products of perturbations, (3.1) is written as

$$\frac{\partial u_i}{\partial t} = -u_j \frac{\partial u_i}{\partial x_j} - \frac{1}{\rho}\frac{\partial p'}{\partial x_i} - \delta_{i3}\frac{\rho'}{\bar{\rho}}g + F_i, \tag{3.6}$$

and the equation of state can now be written

$$\frac{\rho'}{\bar{\rho}} = \frac{p'}{\bar{p}}\frac{c_v}{c_p} - \frac{\theta'}{\bar{\theta}} \tag{3.7}$$

This unapproximated, fully compressible, prognostic system [(3.2), (3.3), and (3.6)] is preferred. However, the computationally stable timestep is severely restricted by the presence of acoustic wave solutions. In order to circumvent this disadvantage, approximations which eliminate sound waves, such as the anelastic approximation, are often used. However, the anelastic system requires the diagnostic solution of an elliptic equation for the pressure variable, which can be computationally intensive. An alternative to the anelastic system is the supercompressible form of the equations, in which the sound wave propagation speed is artificially reduced by adding a term to the continuity equation and thus exaggerates the compressibility. The result is a prognostic equation for perturbation pressure, which may be derived by taking the substantial derivative of (3.7) and using (3.3),

$$\frac{\partial p'}{\partial t} = -\bar{c}_s^{\,2}\frac{\partial(\bar{\rho}u_i)}{\partial x_i}. \tag{3.8}$$

Note that other forcing terms for pressure have been neglected since they are small (Klemp and Wilhelmson 1978). In (3.8), the speed of sound wave propagation is defined as

$$\bar{c}_s^{\,2} = \frac{c_p}{c_v} R\bar{T} \,. \tag{3.9}$$

and is reduced to 150 m s^{-1}. Two possible interpretations of the reduction in sound speed are that either the gas constant of the fluid is reduced, or that the definition of absolute zero is reduced.

The equations of motion (3.6) may now be rewritten as

$$\frac{\partial u_i}{\partial t} = -u_j \frac{\partial u_i}{\partial x_j} - \frac{1}{\rho}\frac{\partial p'}{\partial x_i} + \delta_{i3} g\left(\frac{\theta'}{\bar{\theta}} - \frac{p'}{\bar{p}}\frac{c_v}{c_p}\right) + F_i \tag{3.10}$$

From the supercompressible system, eqns. (3.2), (3.8), and (3.10), the anelastic system is recovered as c_S approaches infinity (Anderson et al. 1985). By comparing the supercompressible solution to the anelastic solution, Anderson et al. (1985) find good agreement when the sound speed is chosen to be greater than or equal to twice the speed of the fastest advection velocity. While the timestep for the supercompressible system must be about half of the anelastic timestep, the overall computational efficiency is still increased since the solution of the diagnostic pressure equation is not required. As in the anelastic system, this approximation results in the non-conservation of mass, but this effect is small as

long as the sound speed is specified properly (Droegemeier and Davies-Jones 1987).

3.2.1.2 Subgrid turbulence parameterization

A modified first-order Smagorinsky turbulence closure (Lilly 1962; Smagorinsky 1963) is used to represent SGS turbulent diffusion. The term F_i in (3.10) is the sum of the subgrid turbulent mixing terms and a numerical filter. Using the prime symbol here to denote SGS quantities, the subgrid mixing terms F_{is}, may be written as the gradient of the turbulent fluxes,

$$F_{is} = -\frac{\partial\left(\overline{u_i' u_j'}\right)}{\partial x_j}. \tag{3.11}$$

The turbulent fluxes may be parameterized in terms of the resolvable scale (unprimed quantities) deformation tensor, D_{ij},

$$-\overline{u_i' u_j'} = \tau_{ij} - \frac{1}{3}\delta_{ij}\tau_{kk}, \quad \text{where} \quad \tau_{ij} = K_m\left\{\left(\frac{\partial u_i}{\partial x_j} + \frac{\partial u_j}{\partial x_i}\right) - \frac{2}{3}\delta_{ij}\frac{\partial u_k}{\partial x_k}\right\}. \tag{3.12}$$

Similarly for (3.2), the subgrid mixing of potential temperature is parameterized as,

$$D_{\theta s} = -\frac{\partial\left(\overline{u_i\theta'}\right)}{\partial x_i} = -\frac{\partial}{\partial x_i}\left(K_h \frac{\partial\theta}{\partial x_i}\right) = -\frac{\partial H_i}{\partial x_i}. \tag{3. 13}$$

The eddy mixing coefficients are K_m and K_h in (3.12) and (3.13), respectively.

The modified Smagorinsky (Lilly 1962; Smagorinsky 1963) expression is used to determine K_m,

$$K_m = (k\Delta)^2 \sqrt{\left[\max\left(|D_{ij}|^2 - \frac{N^2}{\mathrm{Pr}}, 0\right)\right]}. \tag{3. 14}$$

[The formulation is similar to that used in the ARPS model (Xue et al. 1995) at the Center for Analysis and Prediction of Storms (CAPS)]. The empirical constant, k, is assigned to be 0.21 (Deardorff 1972). Pr is the Prandtl Number. The grid-scale measure is denoted by Δ and in nearly isotropic turbulence (grid scales similar in all directions) may be found using

$$\Delta = \sqrt[3]{(\Delta x \Delta y \Delta z)}. \tag{3. 15}$$

For dry, unsaturated motions, the Brunt-Väisälä frequency N^2 is

$$N^2 = \frac{g}{\theta}\frac{\partial\theta}{\partial z}. \tag{3. 16}$$

The eddy diffusivity K_h in (3.13) is found from

$$K_h = K_m / P_r. \tag{3.17}$$

3.2.1.3 Numerical Filters

An artifice of numerically integrated solutions is the spurious growth of short-wavelength modes and of nonlinear instabilities. In order to compensate for this, a model option for the use of a non-physical second- or fourth-order numerical filter is available. The fourth-order filter term for momentum is

$$F_{if} = -K_D \frac{\partial^4 u_i}{\partial x_j^4}. \tag{3.18}$$

For potential temperature the fourth-order filter term is

$$D_{\theta f} = -K_D \frac{\partial^4 \theta}{\partial x_j^4}. \tag{3.19}$$

The coefficient K_D is found from the relation, $K_D \Delta t / \Delta x^4 = 0.0025$ (Klemp and Wilhelmson 1978).

When the fourth-order filter is used, the filter cannot be evaluated at two or less gridpoints from any boundary. Therefore, a second-order filter

$$F_{if} = K_D \frac{\partial^2 u_i}{\partial^2 x_j} \tag{3. 20}$$

and

$$D_{\theta f} = K_D \frac{\partial^2 \theta}{\partial^2 x_j} \tag{3. 21}$$

is used for points near the boundary. No filtering is applied on the boundary.

In addition to the computational mixing terms, a Rayleigh damping filter (Klemp and Lilly 1978) may be applied to a layer near the top boundary to damp upward-propagating wave disturbances and to prevent wave reflection off of the top boundary. This filter is applied only to perturbation quantities so that the base state values are not affected. The form of this filter for velocity is

$$F_{if} = \nu(z)\left[u_i - \bar{u}\right], \tag{3. 22}$$

and for potential temperature

$$F_{i\theta} = \nu(z)\left[\theta - \bar{\theta}\right], \tag{3. 23}$$

where,

$$\nu(z) = \begin{cases} 0.0 & z < z_D \\ \nu_o \sin\left(\dfrac{\pi[z - z_D]}{2[z_T - z_D]} \right) & z \geq z_D \end{cases} . \qquad (3.24)$$

The height of the top boundary is z_T and the lowest height at which Rayleigh damping is applied is z_D. This distance between z_T and z_D is typically 1/3 to 1/4 of the total domain depth. The e-folding time scale of damping at z_T is $1/\nu_o$.

3.2.1.4 Boundary conditions

KANSAS has several options for boundary conditions. The vertical boundaries may be rigid, such that the normal velocity must vanish, or periodic boundary conditions may be used. In the lateral directions, the boundaries may be rigid, symmetric, periodic, or have open (radiative) boundary conditions (Klemp and Wilhelmson 1978) of the form

$$\frac{\partial u_i}{\partial t} = -(u_j + c_{g,}) \frac{\partial u_i}{\partial x_j} \quad , \qquad (3.25)$$

and

$$\frac{\partial \theta}{\partial t} = -(u_j + c_g)\frac{\partial \theta}{\partial x_j}, \tag{3. 26}$$

where c_g is the speed of the dominant gravity-wave mode and is positive or negative depending on the boundary and associated direction of outflow. The value of c_g is determined by estimating $(Nz_T)/\pi$, where N is the square root of the Brunt-Väisälä frequency. Equations (3.25) and (3.26) are applied only to the normal advection terms. For other variables, normal derivatives at the boundaries are computed using one-sided differences, and are lagged in time for computational stability. For variables that are not normal velocities, the outflow conditions do not include c_g. For the case of inflow, $u_j + c_{gj} = 0$ at the boundary, since there is no flow information available outside the domain boundaries. Finally, the subgrid scale fluxes normal to a lateral boundary or the top boundary are set to zero. Fluxes at the lower boundary are described next.

3.2.1.5 Parameterization of the surface fluxes

The representation of surface fluxes of heat and momentum are important in modeling the heated boundary layer. The surface fluxes are prescribed using the bulk aerodynamic formulae, first proposed by Taylor (1916),

$$\left(\overline{u_i u_j}\right)_{sfc} = C_D |u_i| \left(u_{j\,sfc} - u_{j_1}\right), \tag{3. 27}$$

and

$$\left(\overline{u_i'\theta'}\right)_{sfc} = C_e|u_i|\left(\theta_{sfc} - \theta_1\right). \tag{3.28}$$

Surface fluxes are incorporated through the mixing terms. In particular, they are used as the lower boundary conditions for velocity through the stress tensor, and for θ in the vertical gradient of H_i in (3.13). An option also exists for specifying a constant temperature at the lower boundary.

The supercompressible equations are cast on a Cartesian Arakawa C-grid and velocity variables are integrated using a second-order, quadratic conserving spatial discretization scheme, the "box" scheme (Kurihara and Holloway 1967), and the centered-in-time leapfrog temporal scheme. Either the box scheme with centered timestep or a sixth-order flux conservative Crowley scheme (Tremback et al. 1987) with a forward timestep can be used to prognose potential temperature. In addition, a monotonic flux corrector (Leonard 1991; Straka, personal communication), a high-order operator that guarantees monotonicity, can be used with the 6th-order Crowley scheme for potential temperature. A time-splitting scheme (Klemp and Wilhelmson 1978) is implemented so that the sound wave terms are integrated on a smaller timestep and the advective terms on a larger timestep for greater computational efficiency. An Asselin time filter (Asselin 1972) is applied to prevent solution decoupling. Further details of the discretization of the model equations are given in the Appendix A. Results for model validation tests are shown in Appendix B.

3.2.2 Numerical experiment design

It is challenging to adequately resolve and simulate both the boundary convective circulation cells and the concentration of angular momentum into a dust devil-type vortex itself. The smallest scales of motion that need to be represented are the diameter of a dust devil vortex and the Monin-Obukhov (MO) length scale, which are typically of similar magnitude based on observational data, such as that in Hess and Spillane (1990). (They report the average dust devil diameter is approximately twice the MO length). Horizontal and vertical resolution should be sufficient to resolve these in order to properly represent the vortex (probably requiring mesh spacing on the order of a few meters). At the larger end, the size of the simulation domain required to represent the likely scale on which vortex formation processes occur will depend on the actual sources of angular momentum. Therefore, both small vertical and horizontal resolution, on the order of the Monin-Obukhov length (few meters to ~60 m for dust devil environments), and a large domain size that would accommodate the simulation of multiple convective circulation cells (few km) are desirable. Table 3.1 presents some selected values of reported MO lengths for dust devil environments, dust devil diameters, and the number sampled, from prior observational and theoretical studies. Where possible, the larger values of MO associated with gust front or density current vortices has been omitted in order to conservatively estimate the required numerical resolution.

Researchers	Diameter	| Obukhov Length |	Numbers of dust devils in sample
Ryan & Carroll (1970)	up to 100m avg 8-10m	>10 m	Many
Lamberth (1966)	1-30 m		Many (3 mnths of obs)
Sinclair (1969)	< 3 m to > 30 m		Many
Smith & Holmes 1961	150 m		1 (Radar)
Fujita (1971)	30-40 m		1
Crozier (1970)	11-63 m		10
Deardorff (1978) Thy	1-50 m	10 m	
Hess & Spillane (1990)	7-34 m	14.4-51.2 m	Many

Table 3. 1: Dust devil Diameters and Monin-Obukhov Lengths

For practical considerations, the task has been divided into two separate simulations of different domain sizes and resolutions, only the first of which is addressed in this dissertation. The first focuses on the role of convective cell patterns in the formation of vertical vortices. The purpose here is to resolve the convective cell circulations and not necessarily dust devil-scale vortices. Finer resolution would resolve many more complicated features in the flow and make the task of identifying the role of larger-scale convective circulations in vortex formation more difficult. The second simulation will be designed to focus on the dynamics and maintenance of dust devil-scale CBL vertical vortices and will require much finer resolution.

Thus, a Large Eddy Simulation (LES) of the convective boundary layer, *without imposed mean wind shears or other sources of angular momentum*, has been performed (hereafter, "SIM1"). Some of the simulation input parameters were selected based on observational data of dust devils and the environments in which they form, which was collected on the afternoon of 27 June 1995, near Denver Colorado using a 3 cm mobile Doppler radar (Kanak 1996, informal presentation). In the early afternoon, radar reflectivity of a polygonal-type

convective pattern was observed. Subsequently, the environment and circulation of a dust devil were scanned with the radar. The circulation represented by the radar image (Fig. 3.2) was approximately 1.5 km wide and was visually associated with the occurrence of a dust devil. The actual dust devil diameter appeared to be much smaller. It may be surmised that the dust devil was embedded in the larger-scale radar-sampled circulation. The circulation persisted on the radar screen for about 20 minutes, while the visually observed dust devil moved over a vegetated surface and disappeared from sight after about five minutes.

With these observations in mind, an attempt was made to numerically simulate such larger-scale convective circulation cells, and the "parent" circulation of the dust devil. Therefore, a horizontal resolution of 35 m in both the x and y directions was selected and a domain size of 3 km x 3 km x 2.1 km was prescribed. The vertical grid resolution was stretched so that Δz near the bottom (top) of the domain was about 10 m (80.3 m). The time step was chosen to be 0.1 s.

For simplicity, the model surface pressure was set to 1000 mb and the surface height was set equal to zero meters. The initial base state potential temperature profile (Fig. 3.3) was dry adiabatic from the surface up to 900 m and a stable layer with lapse rate -0.003 K m^{-1} was prescribed above 900 m. This choice was based on an atmospheric sounding, which was taken near the occurrence of the observed Denver dust devil. The sounding exhibited a nearly dry neutral lapse rate up to about 550 mb and light and variable winds throughout the boundary layer depth. No mean wind was imposed in the numerical simulation.

Fig. 3.2

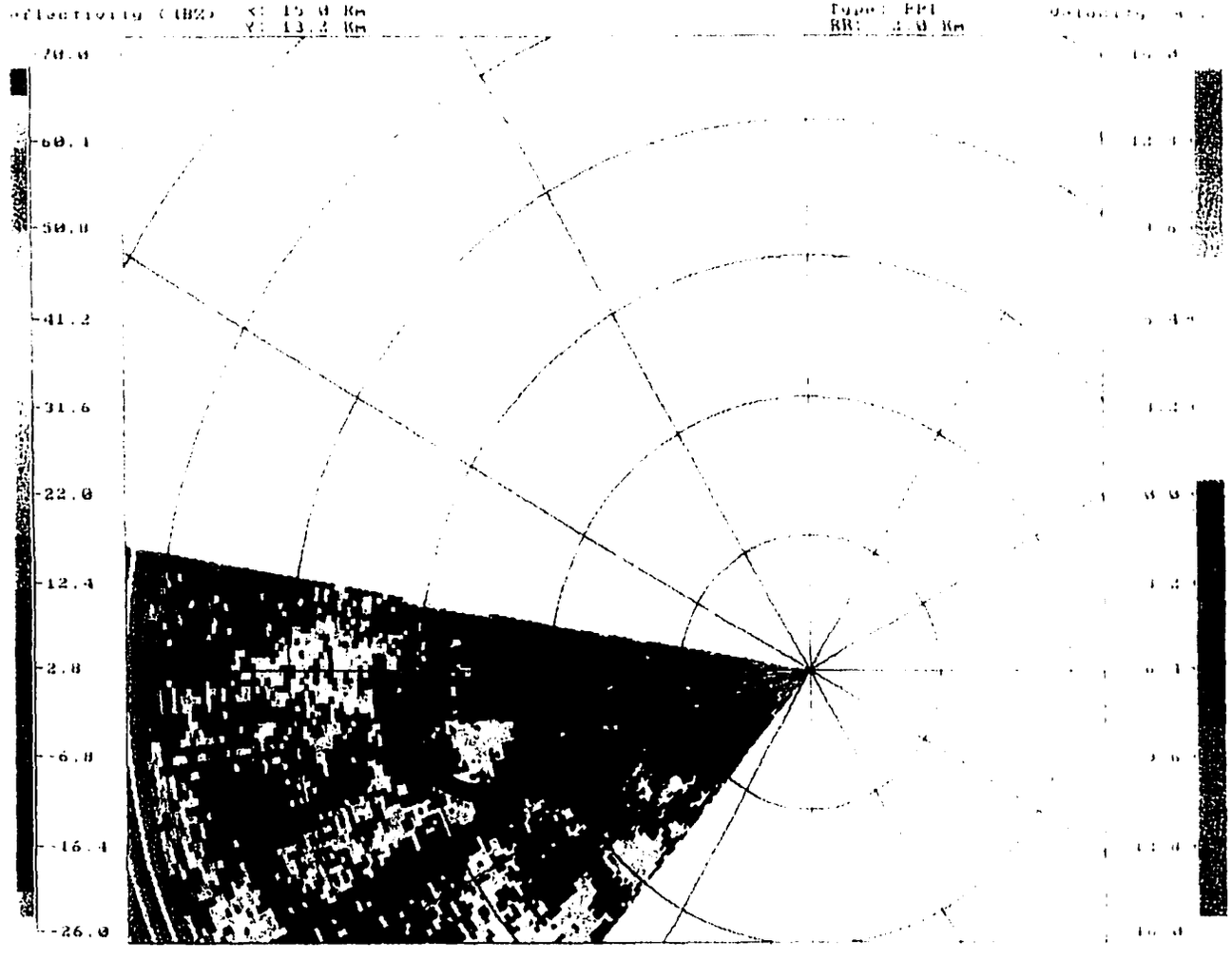

Fig. 3.2. Doppler velocity from 3 cm mobile Doppler radar collected at 2104 UTC 27 June 27 1995 near Denver International Airport. The range rings are 2 km apart. The anticyclonic circulation is located approximately five kilometers from the radar. The maximum outbound velocity is about 8 m s^{-1} (in orange) and the maximum inbound velocity is about 9.0 m s^{-1} (in purple). The circulation region spans about 1.5 km. A dust devil was visibly observed in approximately the same location as the radar indicated circulation. The circulation persisted on radar for about 15 minutes after the dust column passed over a vegetated field and was no longer visible to the eye.

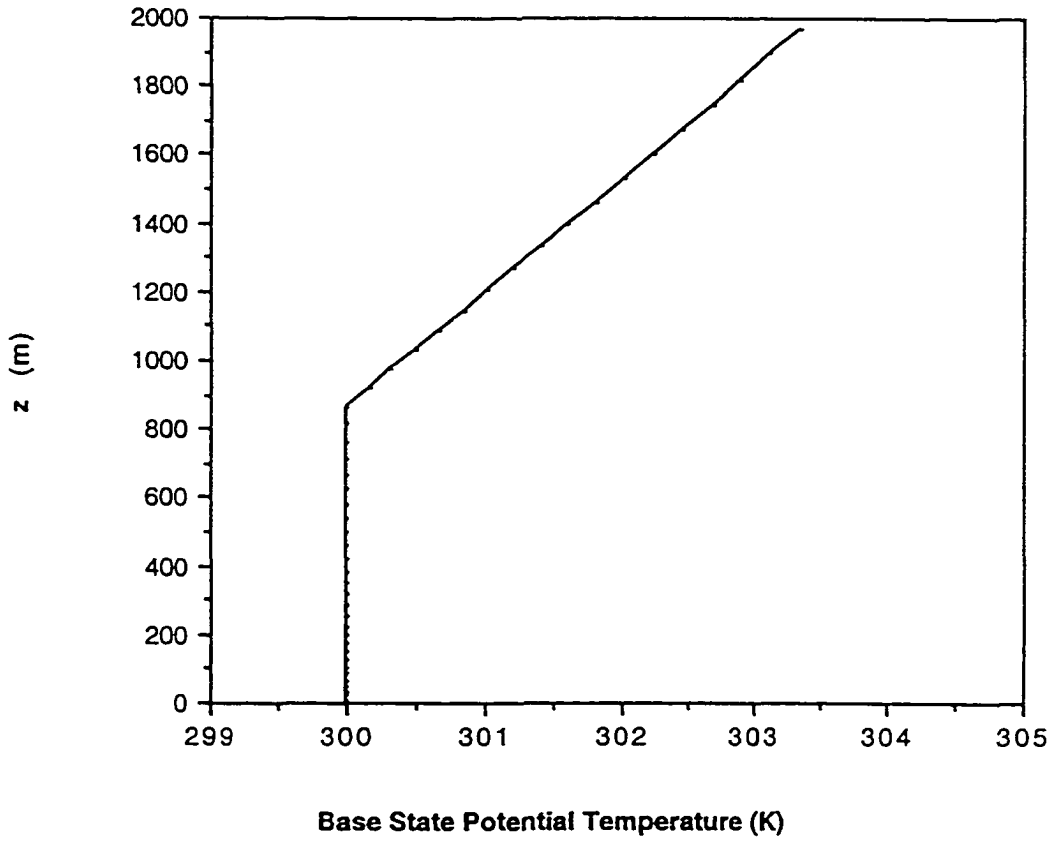

Fig. 3.3. Initial base state potential temperature as a function of height.

The prescribed initial disturbance condition was like that of Nieuwstadt et al. (1991; hereafter, N91) for a convective boundary layer LES:

$$\theta = \theta_o + 0.1r\left(1 - \frac{z}{z_{il}}\right)T_* \quad \text{and} \quad w = \begin{cases} 0.1r\left(1 - \frac{z}{z_{il}}\right)w_* & z < z_{il} = 0.844 z_{io}, \\ 0 & z > z_{il} \end{cases} \tag{3.29}$$

where $T_* = 0.041K$, $w_* = 1.46$ ms^{-1}, $z_{io} = 1.6$ km, $u = v = 0$, and $r(x, y)$was a random number uniformly distributed between -0.5 and 0.5. In the initial condition and some of the results that follow, convective scalings have been used:

$$w_* = \left(\frac{g}{T_o} Q_s z_i\right)^{1/3} \quad \text{and} \quad T_* = \frac{Q_s}{w_*} \tag{3.30}$$

A constant heat flux of 0.24 K m s^{-1} was designated at the lower boundary [as in Moeng and Sullivan (1994) for a highly convective boundary layer]. The Rayleigh damping layer was used above $z = 1500$ m. The ratio of K_h / K_m was set to 2.5 ($K_m = 0.4K_h$) on the grounds that in an initially isotropic flow, the generation of stress is reduced 60% by the pressure-velocity correlation, while that of a scalar is not (Deardorff 1972 cites Lilly, personal communication). The box scheme was used for the velocity and potential temperature equations. Lateral boundary conditions were periodic. The fourth-order filter was used in the horizontal directions to inhibit the growth of numerically generated small-scale instabilities.

A summary of the basic simulation parameters is provided in Table 3.2.

Gridpts	L_x	L_y	L_z	Δx	Δy	Δz_{sfc}	Δz_{top}	Δt	T_{total}	Pr	Q_*
86x86x	3	3	2.1	35	35	10.5	80.3	0.1	~2.0	0.4	0.24
48	(km)	(km)	(km)	(m)	(m)	(m)	(m)	(s)	hrs		Kms^{-1}

Table 3.2. Summary of simulation parameters for SIM1.

3.3 Results

3.3.1 Time series and Statistics

Selected statistical calculations are presented as a means of demonstrating that the current simulation has properties typical of a convective boundary layer.

A time series of the domain averaged subgrid- and resolved-scale kinetic energy is shown in Figs. 3.4 a and b, respectively. The curves indicate that the simulated turbulence has become quasi-stationary by time t ~ 2000 s.

The simulated boundary layer height is estimated to be at about 1200 m. Using this value, a convective turnover time according to $t_* = z_i / w_*$ is found to be about 570 s, where w_* is calculated to be about 2.11 m s^{-1}. The simulation is carried out for a total of about 13 turnover times, or about two hours.

Figures 3.5 a and b shows the horizontally averaged resolved-scale potential temperature and the resolved-scale vertical velocity at t = 2400 s, respectively.

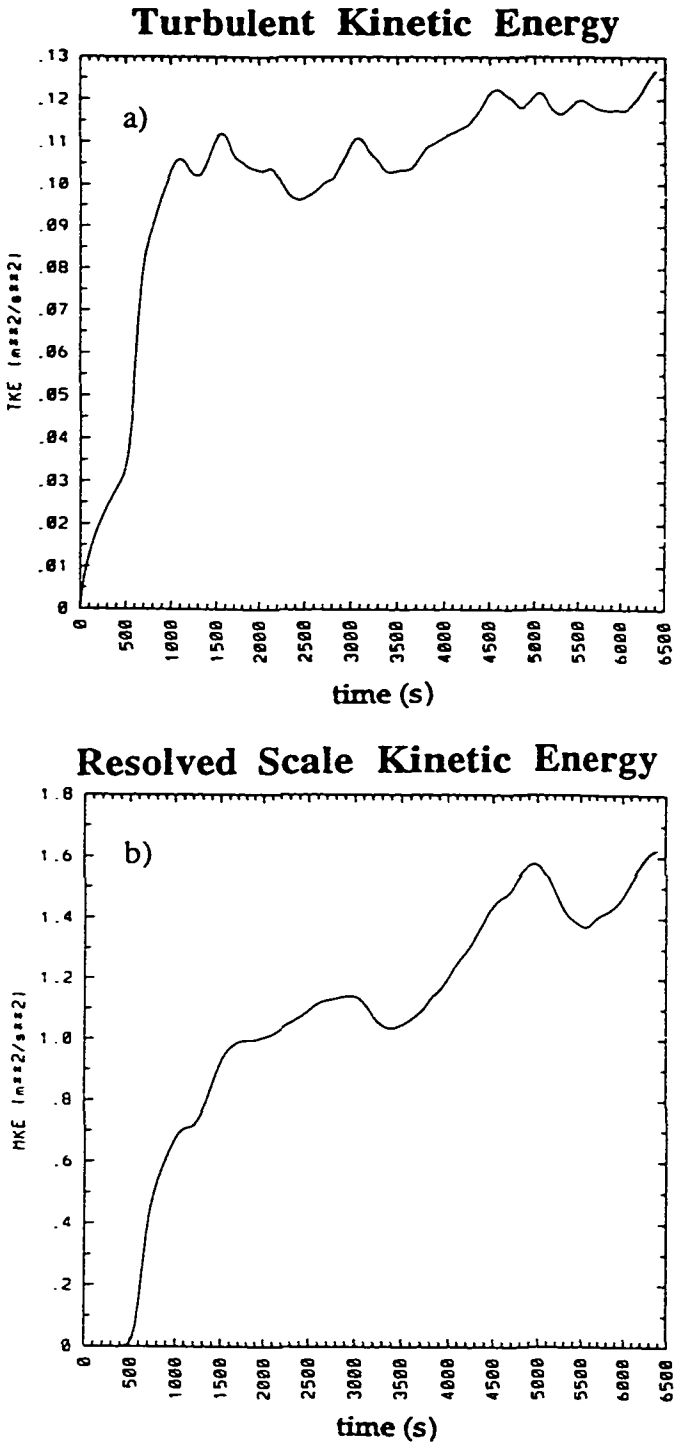

Fig. 3.4. Domain averaged (a) turbulent kinetic energy (m^2 s^{-2}) and (b) resolved-scale kinetic energy (m^2 s^{-2}) as a function of time (seconds).

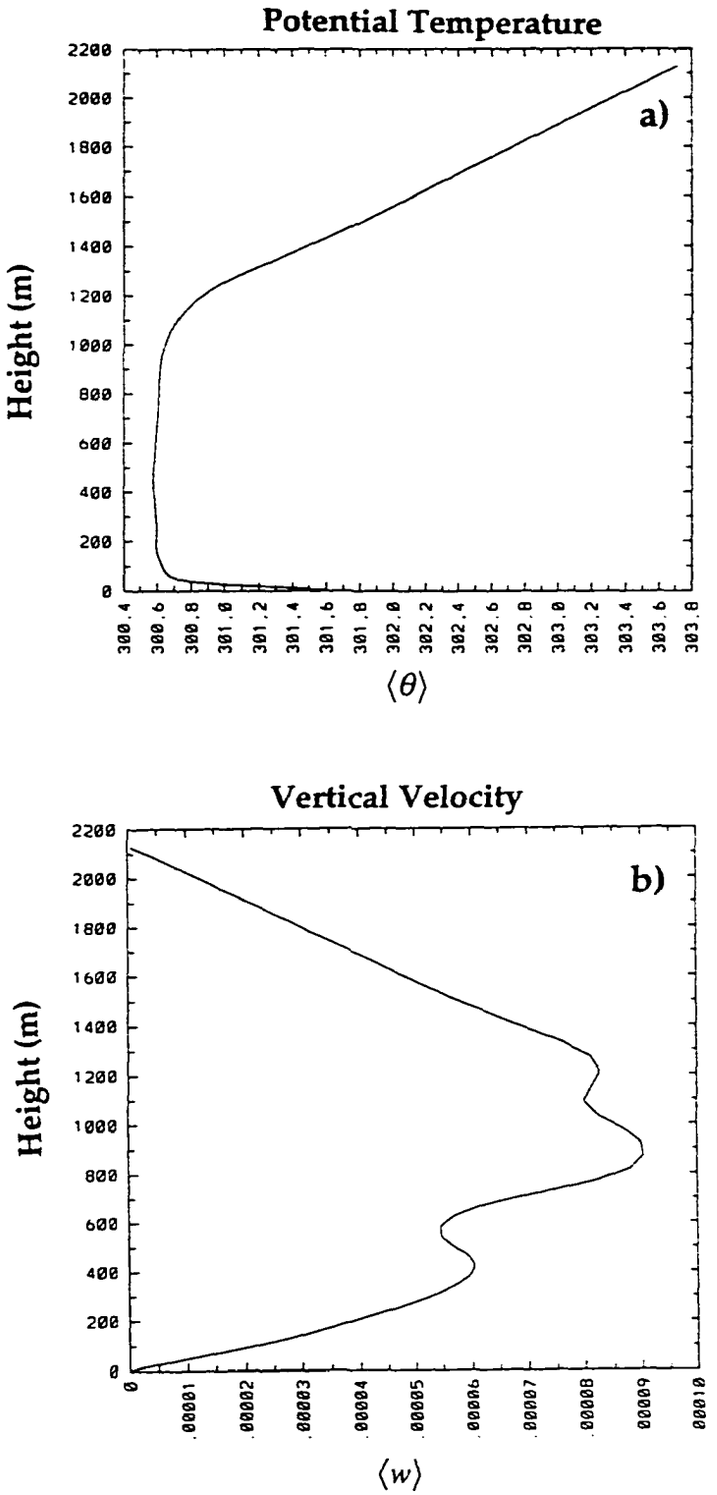

Fig. 3.5. Horizontally averaged profiles at t= 2400 s of: (a) resolved-scale potential temperature, $\langle\theta\rangle$; and (b) resolved-scale vertical velocity, $\langle w\rangle$.

These mean profiles are nearly constant over most of the depth of the boundary layer, which indicates that convection is efficient at transporting heat and momentum away from the lower boundary where the constant heat flux is prescribed. The sharpness of the inversion is not well represented by the turbulence closure. This is likely due to the lack of any modification of the mixing length near the inversion (e.g., as in N91). This issue is discussed further below.

Figures 3.5 c-f shows profiles of horizontally averaged statistical quantities that are averaged over 600 seconds (about 1 t_* , as in N91) for the period spanning t = 1800 s to t = 2400 s. The total (resolved-scale plus SGS) potential temperature flux (Fig. 3.5 c) is nearly linear throughout the boundary layer depth, which is consistent with a constant heating rate and the stationarity of the turbulence (N91) for the time averaging period. There is a slight departure of the profile from linearity near the surface. In preliminary tests with increased grid resolution this effect was amplified. This phenomenon can again be attributed to the fact that the mixing length in the subgrid turbulence closure is not modified near the surface (or for changes in static stability). Ideally, the eddy length scale should be proportional to the distance above the surface and this is often enforced in LES's. The maximum negative heat flux near the inversion is located at about z = 1150 m, which can be defined as the top of the boundary layer (Moeng and Sullivan 1994 and others).

The maximum in the total (resolved-scale plus SGS) vertical velocity fluctuation variance profile (Fig. 3.5 d) occurs at about z = 400 m and this value is in good agreement with other LESs of the convective boundary layer (e.g., N91).

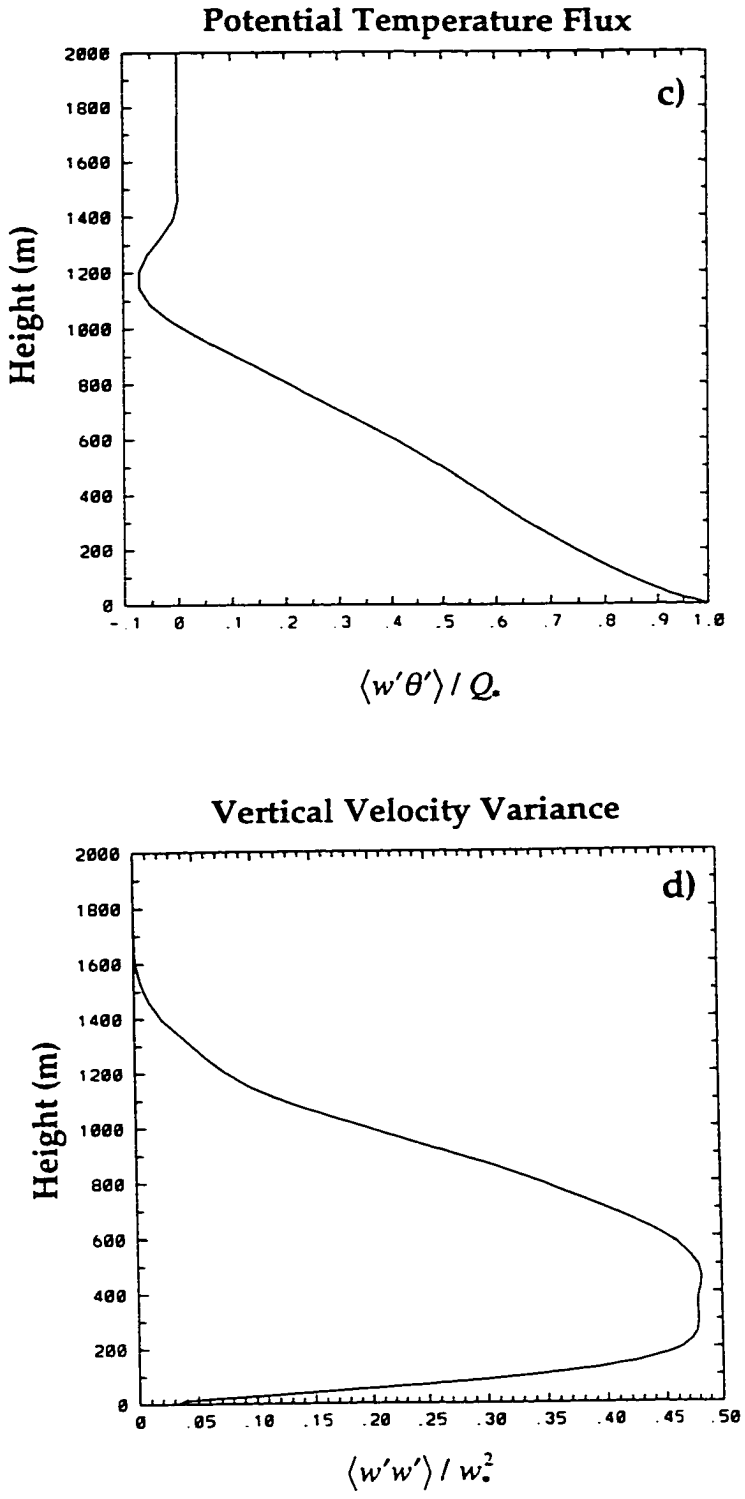

Fig. 3.5. *(continued)*. Horizontally averaged and temporally averaged (over the period of t = 1800 s to t = 2400 s) profiles of: (c) total (resolved-scale plus subgrid-scale) potential temperature flux, $\langle w'\theta' \rangle / Q_*$; and (d) total (resolved-scale plus subgrid-scale) vertical velocity fluctuation variance, $\langle w'w' \rangle / w_*^2$.

The resolved-scale third moment of the vertical velocity fluctuation profile (Fig. 3.5 e) indicates a maximum in the upper mixed layer due to the presence of non-equal areas of updrafts and downdrafts. In other words, there exist broad weak downdrafts and strong narrow updrafts on a given horizontal plane in the simulated convective boundary layer. Figure 3.5 f shows the vertical velocity fluctuation skewness (resolved-scale only). As with other LES's, the skewness increases in the upper part of the mixed layer, which is inconsistent with observations. Moeng and Rotunno (1990) offer an explanation for the LES results given a heated boundary layer, characterized by a typical mean potential temperature profile that is constant through the boundary layer and overlain by an inversion. Near the heated surface, irregular polygonal rings of upward motion exist, while at the inversion, only the most vigorous updrafts extend to that height. Updrafts impinging on the inversion lose their kinetic energy and as a result only weak and broadly distributed returning downdrafts exist among the updrafts in the upper mixed layer. This would explain the increase in skewness at these levels. Furthermore, Lemone (1990) suggests that, due to domain size and periodic lateral boundary conditions, LES's may not be able to fully represent gravity wave interaction with the boundary layer that would reduce the skewness near the inversion. In addition, Agee and Gluhovsky (1999) state that the discrepancy may be caused by the limited domain sizes of LES's, which eliminate the representation of larger-scale motions. To test this idea, they filtered observational data to remove the larger-scale flow components and found the skewness of the filtered observations to be more comparable with that of LES's.

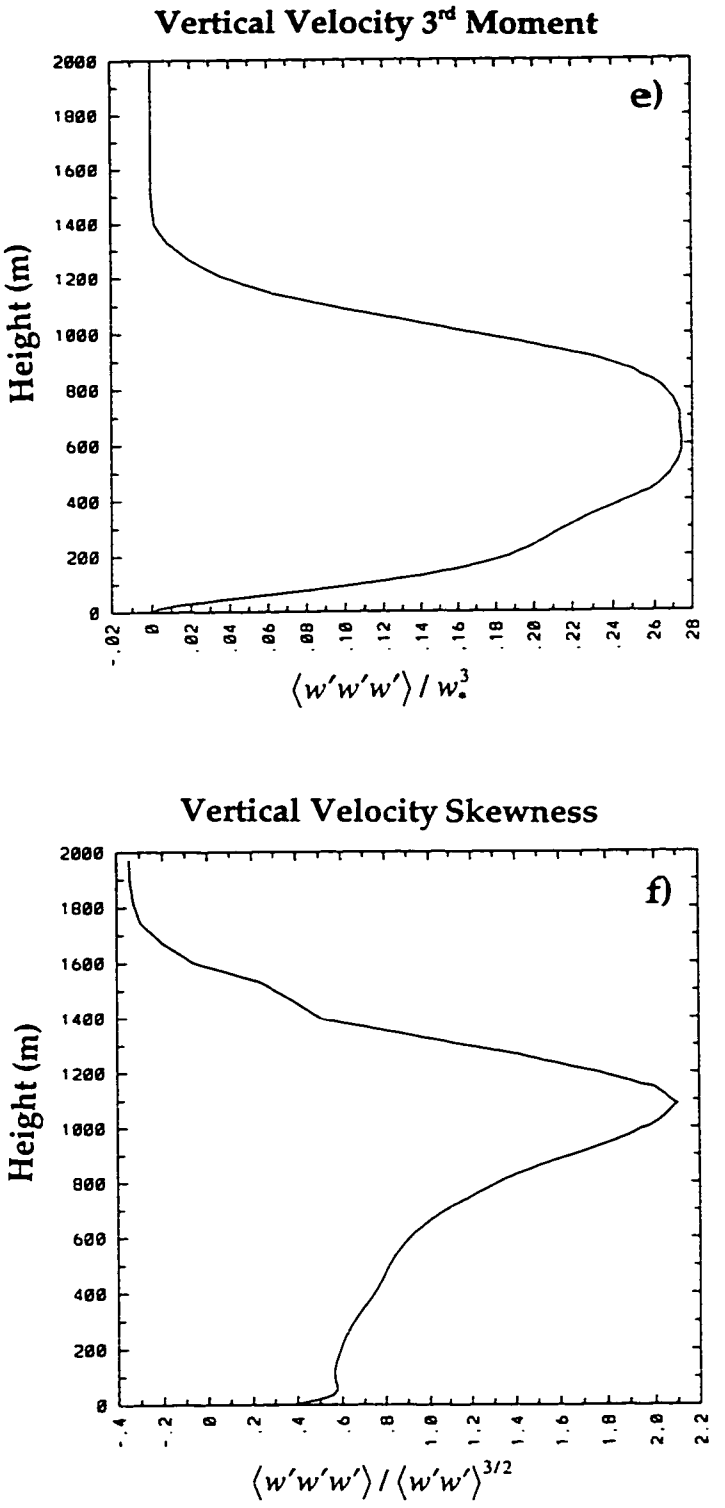

Fig. 3.5. *(continued)*. Horizontally averaged and temporally averaged (over the period of t = 1800 s to t = 2400 s) profiles of: (e) Resolved-scale third moment of the vertical velocity fluctuation, $\langle w'w'w' \rangle / w_*^3$; and (f) skewness of the vertical velocity fluctuation, $\langle w'w'w' \rangle / \langle w'w' \rangle^{3/2}$.

3.3.2 Flow fields

Some sample cross-sections of flow fields for selected times are now presented. The total variables are contoured (rather than deviations from horizontal means, which are often plotted in LES results).

3.3.2.1 Convective Cells

The transient behavior of the flow (simulation times prior to quasi-stationary turbulence) exhibits some interesting features. The evolution is characterized by broadening of the convective cell diameters (also documented by Fiedler and Khairoutdinov 1994; Dörnbrack 1997; and others). Horizontal cross-sections of vertical velocity show this effect nicely. (Cell broadening can also be identified in the potential temperature fields.) Figures 3.6 a-d shows the horizontal cross-sections of vertical velocity at z = 5.3 m at t = 600 s, t = 1000 s, t = 1400 s, and t = 2800 s. The most rapid cell broadening occurs between these times. In the first few hundred seconds of simulation, the vertical velocity field is characterized by small "bubbles" in which updraft and downdraft regions are of about the same size, d ~ 300-400 m (Fig. 3.6 a). At t = 1000 s the cell shapes are more rectangular and are about 300-600 m in horizontal scale (Fig. 3.6 b). After t = 1400 s, (Fig. 3.6 c) the flow is clearly composed of polygonal convective elements (or convective rings) that broaden from about 750 m to 1.5 km by 2800 s (Fig. 3.6 d). Dörnbrack explains the broadening process as a result of a large-scale drift in which streaming motions, in one direction near the lower boundary

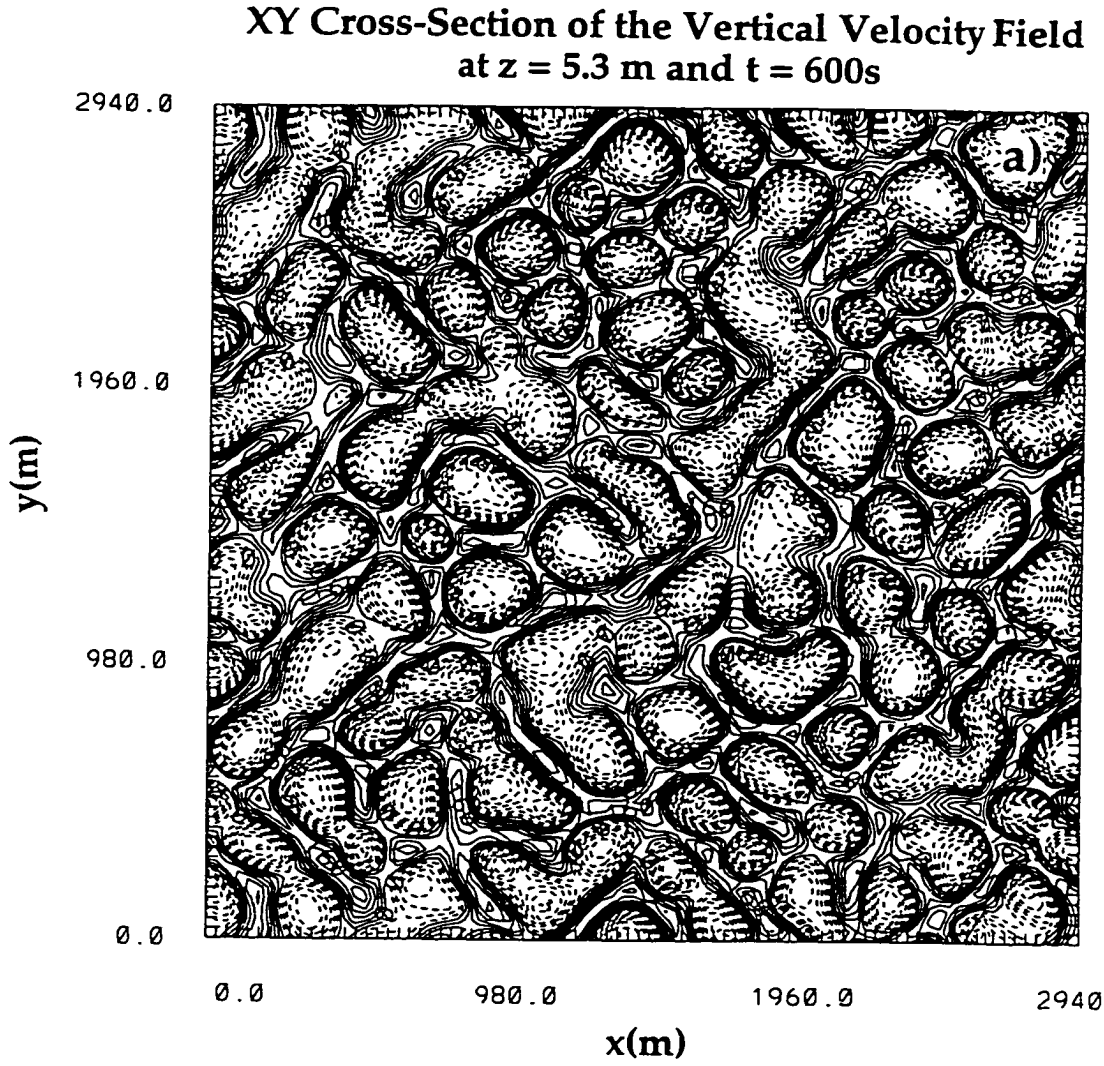

Fig. 3.6. (a) X-Y Cross-sections of the vertical velocity at z = 5.3 m and t = 600 s. Contours from -0.32 to 0.28 with interval 0.04 m s^{-1}.

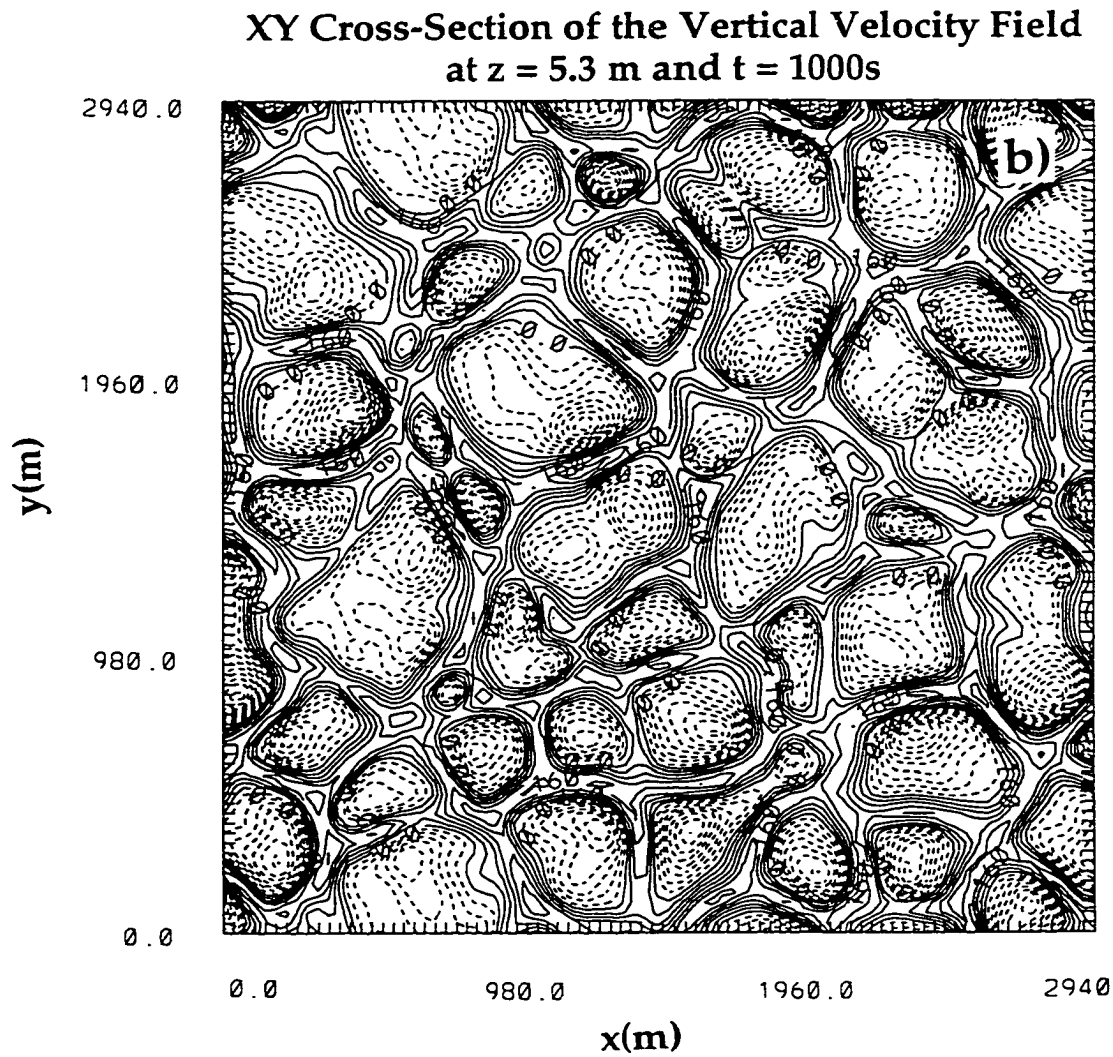

Fig. 3.6. *(continued).* (b) X-Y Cross-sections of the vertical velocity at z = 5.3 m and t = 1000 s. Contours from -0.4 to 0.24 with interval 0.04 m s^{-1}.

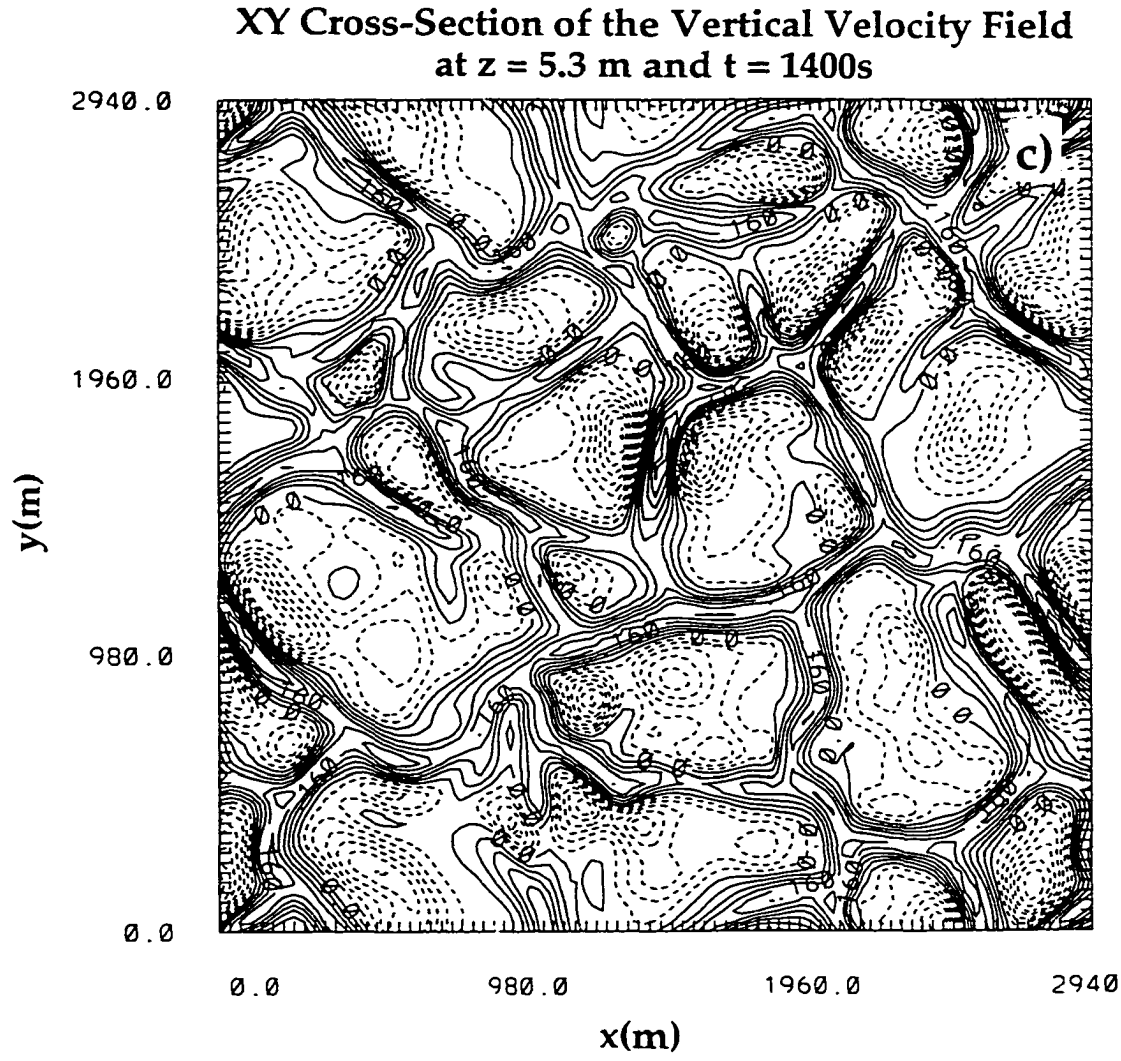

Fig. 3.6. *(continued)*. (c) X-Y Cross-sections of the vertical velocity at z = 5.3 m and t = 1400 s. Contours from -0.36 to 0.28 with interval 0.04 m s^{-1}.

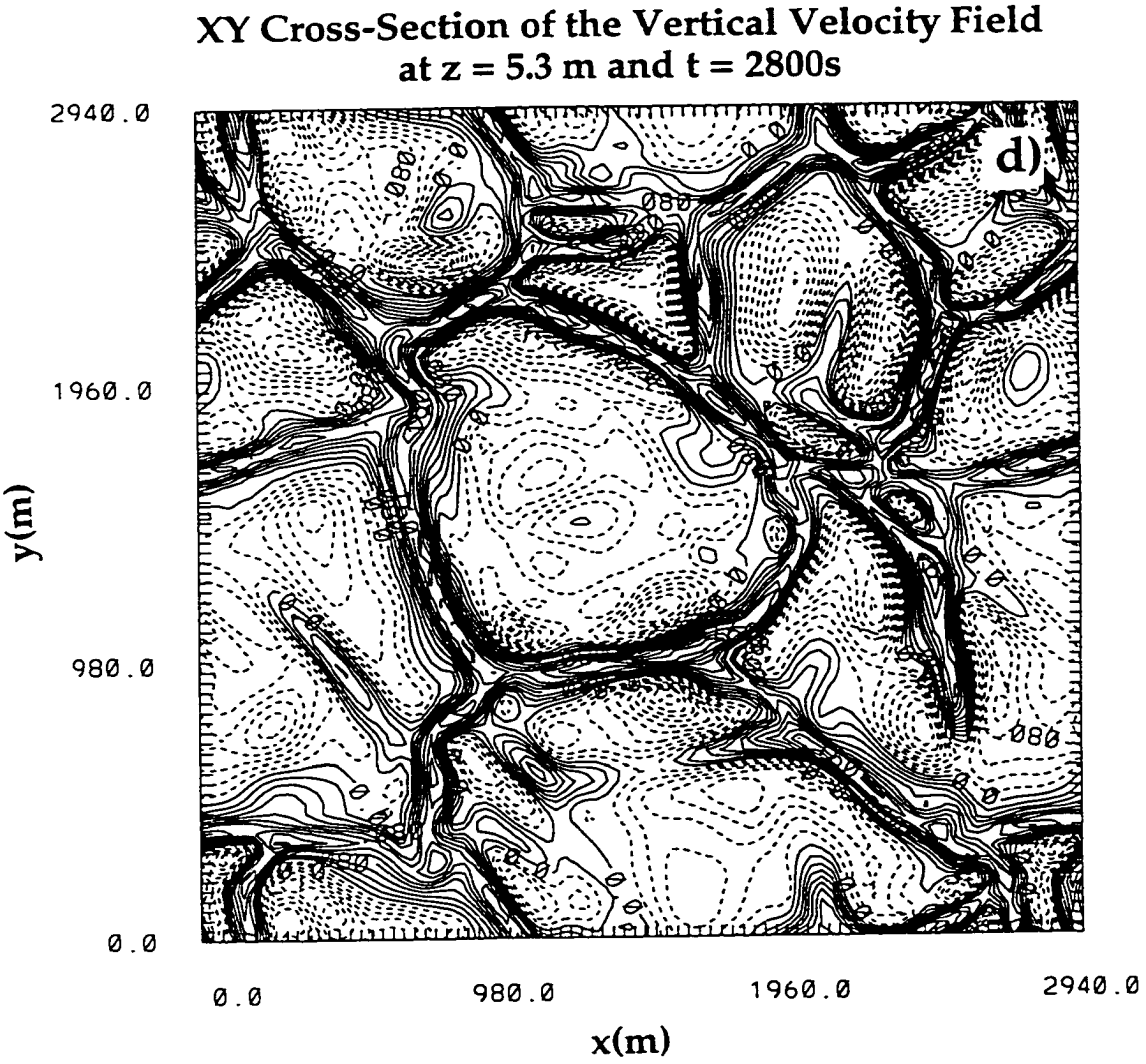

Fig. 3.6. *(continued)*. (d) X-Y Cross-sections of the vertical velocity at z = 5.3 m and t = 2800 s. Contours from -0.22 to 0.22 with interval 0.02 m s^{-1}.

and the opposite direction near the upper boundary, create a large-scale shear that acts in two directions. The shear acts to separate thermals at the mid-levels, which results in cell broadening. A similar argument is made for updraft broadening (or merging) in storm environments by Kogan and Shapiro (1996), where they suggest that mutual advection is the responsible mechanism.

Although the cells are changing size with time, their spatial dimensions are fairly consistent with the planforms of turbulent convection in the laboratory experiments of Willis and Deardorff (1979, with Ra = 10^9 and Re = 1200). The convective circulations, simulated by Willis and Deardorff (1979) and observed by Webb (1984), are shown schematically in a Figure presented in Hess and Spillane (1990) and it is reproduced here as Fig. 3.7. Willis and Deardorff report a rather stationary cell pattern that has average open cell diameter of 1.2 h ± 0.2 h, where h is the depth of the laboratory tank. If h is taken to be about 1200 m (approximate height of the mixed layer) for the current simulation, downdraft diameters would be expected to be about 1.4 km, which is supported by Fig. 3.6d. Willis and Deardorff also found updraft widths of $h/5$ (= 240 m would be predicted for the current simulation) and updrafts widths are found to be about 210 m at t = 2800 s.

Schematic Diagram of Convective Flow Patterns

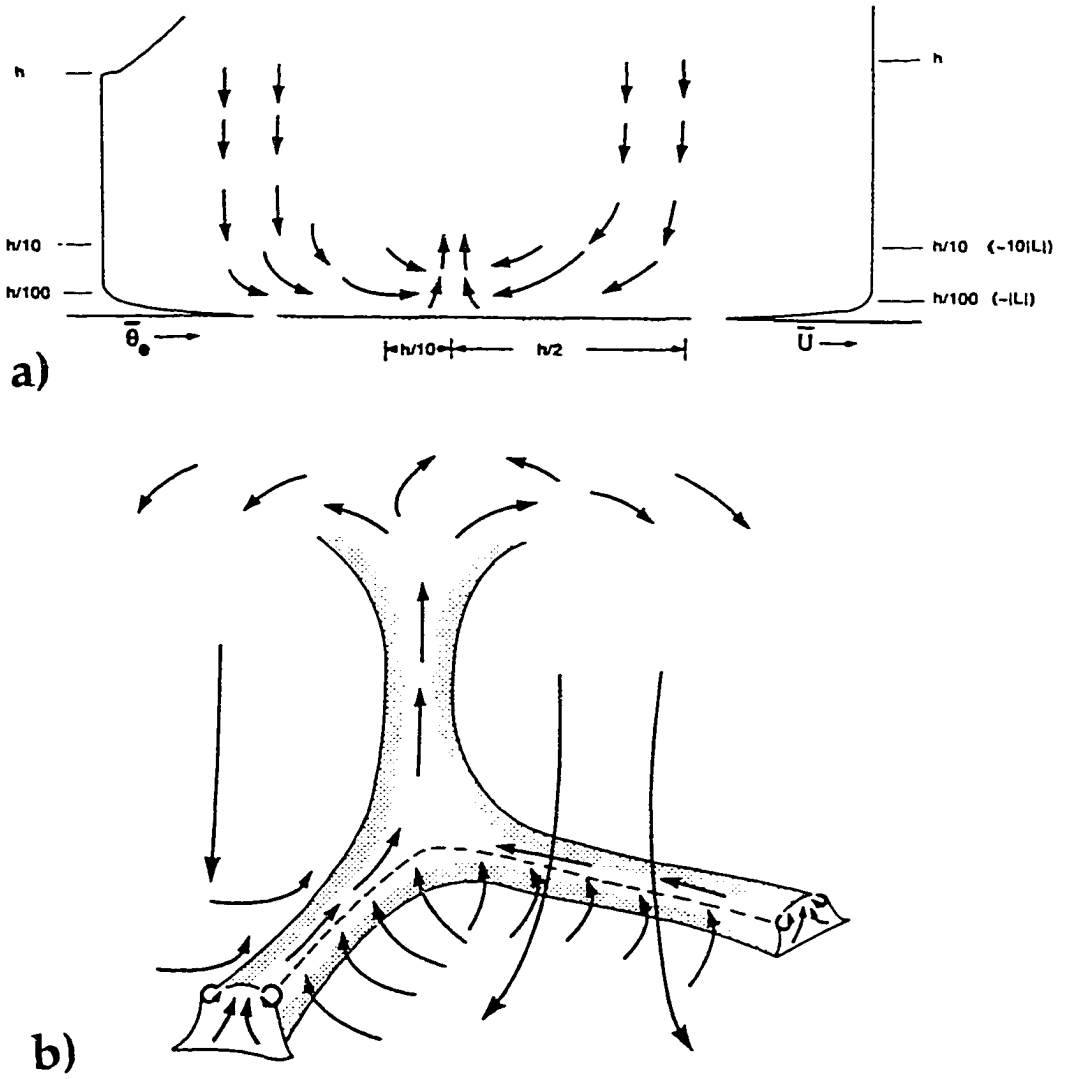

Fig. 3.7. Reproduced from Hess and Spillane (1990). Schematic diagram of the flow patterns for a strongly convective boundary layer. (Note that this has not been drawn to scale.) (a) Vertical cross-section. The horizontal and vertical dimensions of the convection cell are both approximately equal to h. Interactions between downdrafts and updrafts occur over horizontal and vertical dimensions of $\sim h/10 (\approx 10|L|)$ and an updraft wall of height $\sim h/10$ is formed. A layer of strong windshear and temperature lapse rate occurs between the surface and $\sim h/100 (\approx |L|) \sim h/100$. A temperature inversion layer caps the boundary layer. Vertical profiles of wind speed $\bar{U}$ and equivalent potential temperature $\bar{\theta}_e$ are shown. (b) A three-dimensional view of the general areas of downdrafts and the updraft walls. At the intersection of walls an updraft column is formed that extends to the top of the boundary layer (based on the measurements of Webb, 1977) (Adapted from the *J. Appl. Meteor.*)

3.3.2.2 Vertical Vortices

The most intriguing result of the current simulation is the presence of vertical vortices which form at or near the vertices of the convective rings. This was also observed in the laboratory experiments of Willis and Deardorff (1979). For simplicity, a vortex is defined here as a closed circulation in the horizontal velocity vectors. In this way, an attempt is made to distinguish between shear and curvature vorticity, the latter being required for existence of a vortex. [Although this definition may be rather arbitrary, it is a non-trivial task to rigorously define a vortex (see Lugt 1979)].

Figure 3.8 shows the horizontal velocity vectors (for all results presented, a vector at every other gridpoint is plotted) in the X-Y plane at the lowest simulation level, $z = \Delta z/2 = 5.3$ m at (a) t = 2000 s, (c) t = 3800 s, and (e) t = 4800 s and the associated vertical velocity contours in the X-Y plane at z = 5.3 m at (b) t = 2000 s, (d) t = 3800 s, and (f) t = 4800 s. These vortices are located at the intersections, or vertices, of convective rings where local maxima of vertical velocity are located. With time, the presence of a vortex modifies the updraft ring structure by broadening the updraft region. Sometimes a "wrapping up" of the updraft region occurs (e.g., Fig. 3.8 d) and this resembles, in some ways, the "hook echo" in supercell thunderstorms.

The vortices appear at the lowest simulation level as early as t = 1000 s with associated vertical vorticity magnitudes of about 0.04-0.05 s^{-1}. Figure 3.9 shows the domain maximum and minimum vertical vorticity as a function of time. It is clear that the magnitude of vertical vorticity increases with time, but less so after about 2000-2500 s. The local extrema in vertical vorticity correspond

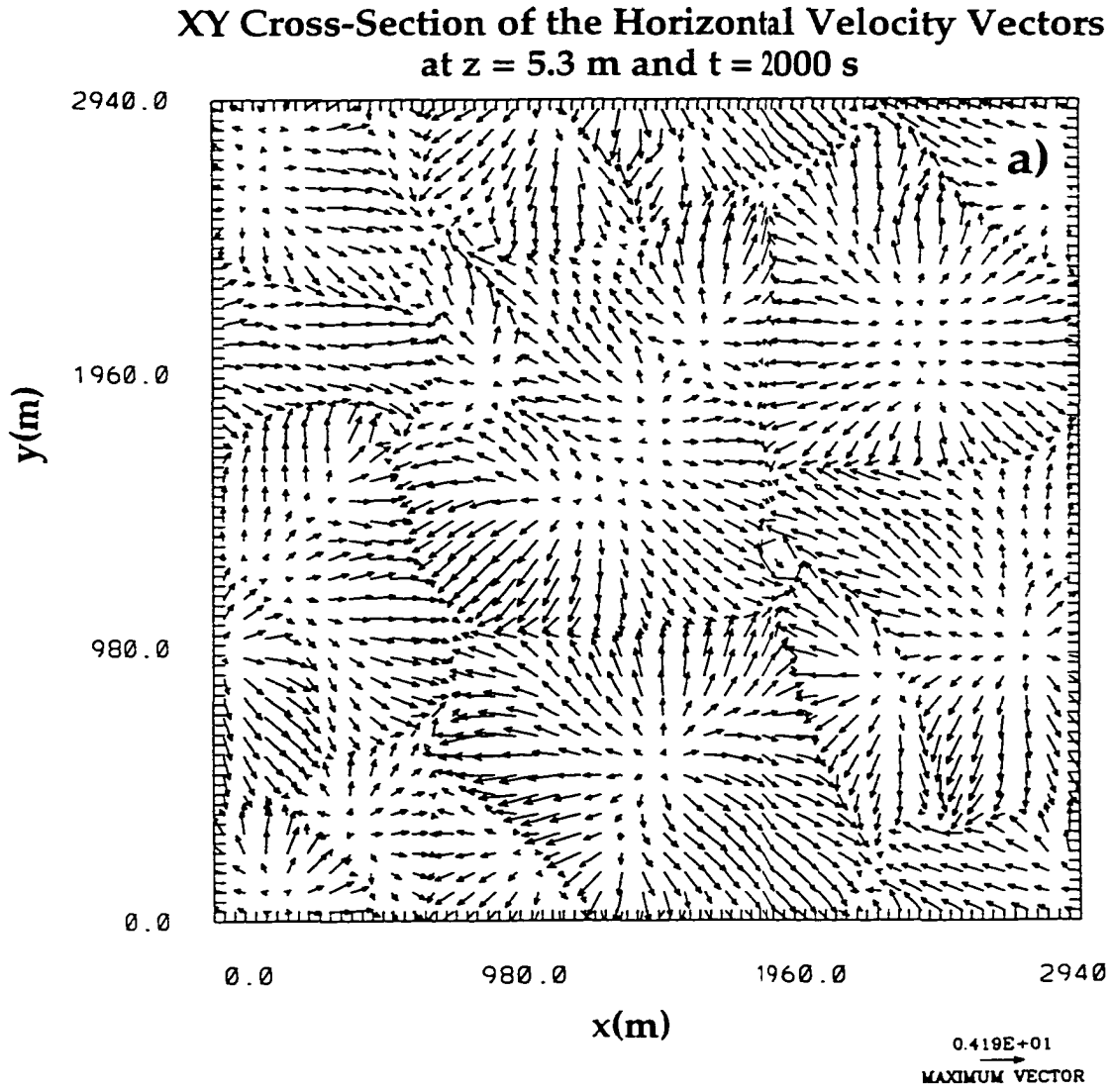

Fig. 3.8. (a) X-Y Cross-sections of horizontal velocity vectors at z = 5.3 m and t = 2000 s. Maximum vector length is 4.19 m s^{-1}.

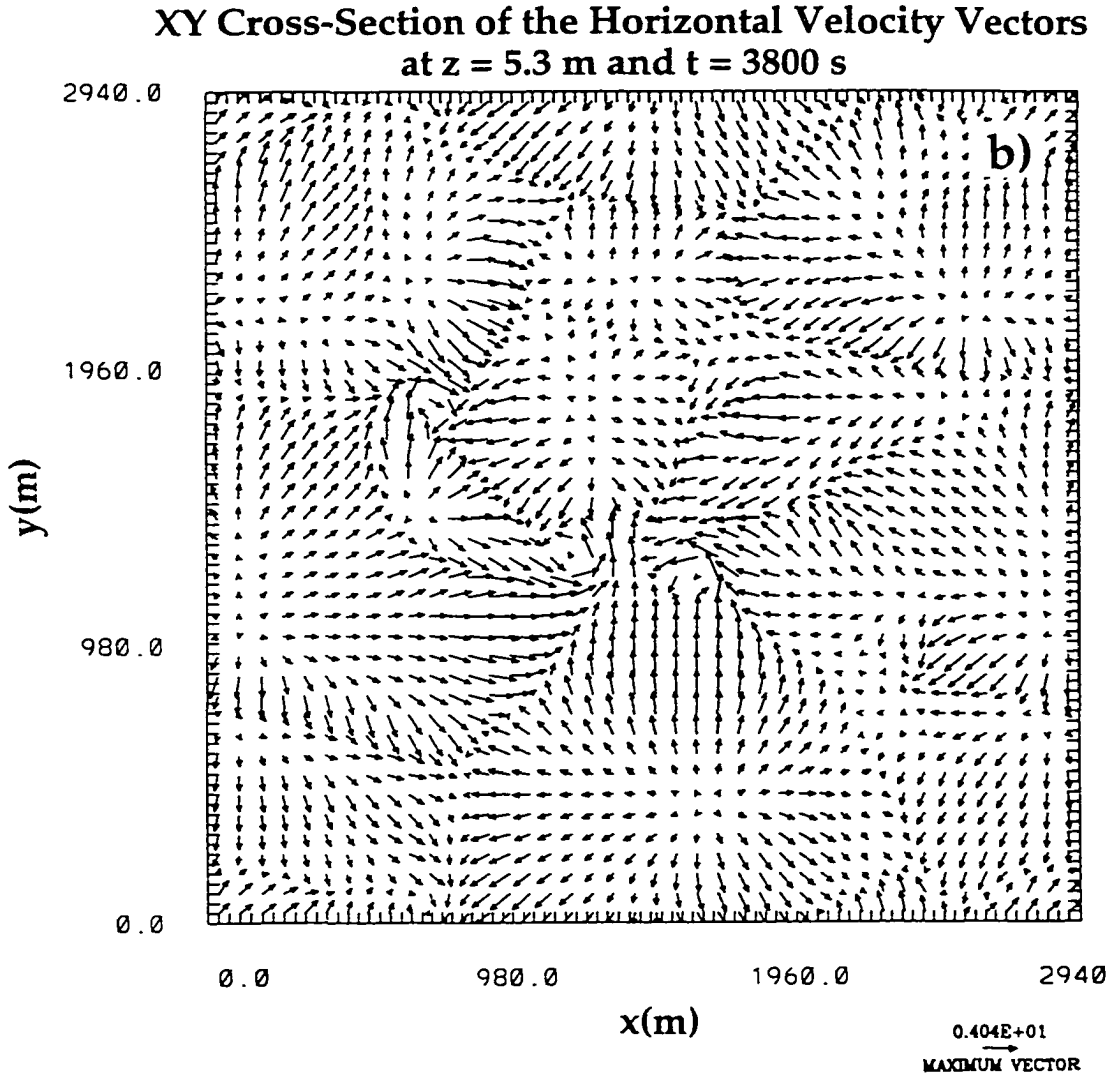

Fig. 3.8. *(continued).* (b) X-Y Cross-sections of horizontal velocity vectors at z = 5.3 m and t = 3800 s. Maximum vector length is 4.01 m s^{-1}.

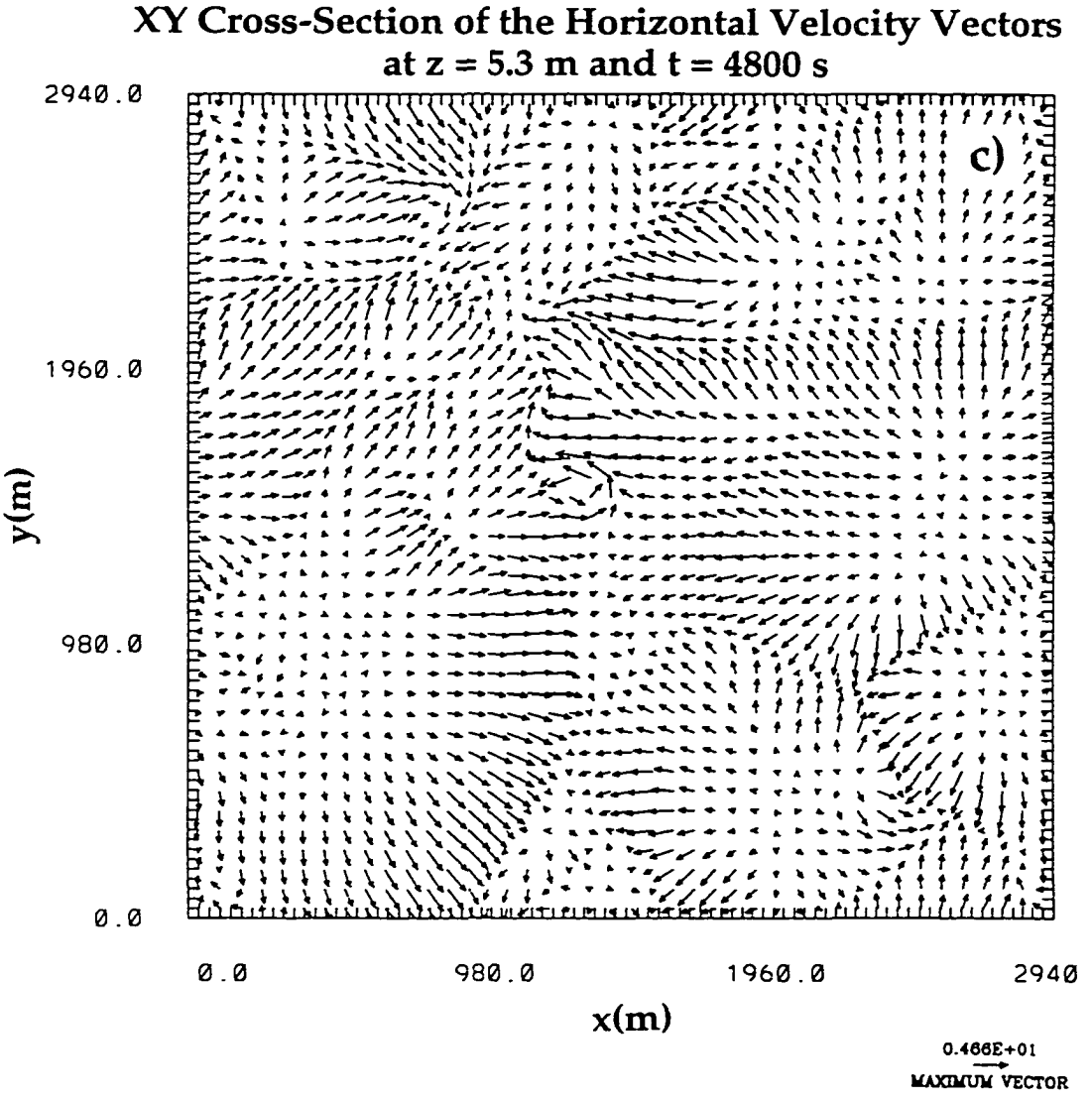

Fig. 3.8. *(continued).* (c) X-Y Cross-sections of horizontal velocity vectors at z = 5.3 m and t = 4800 s. Maximum vector length is 4.66 m s^{-1}.

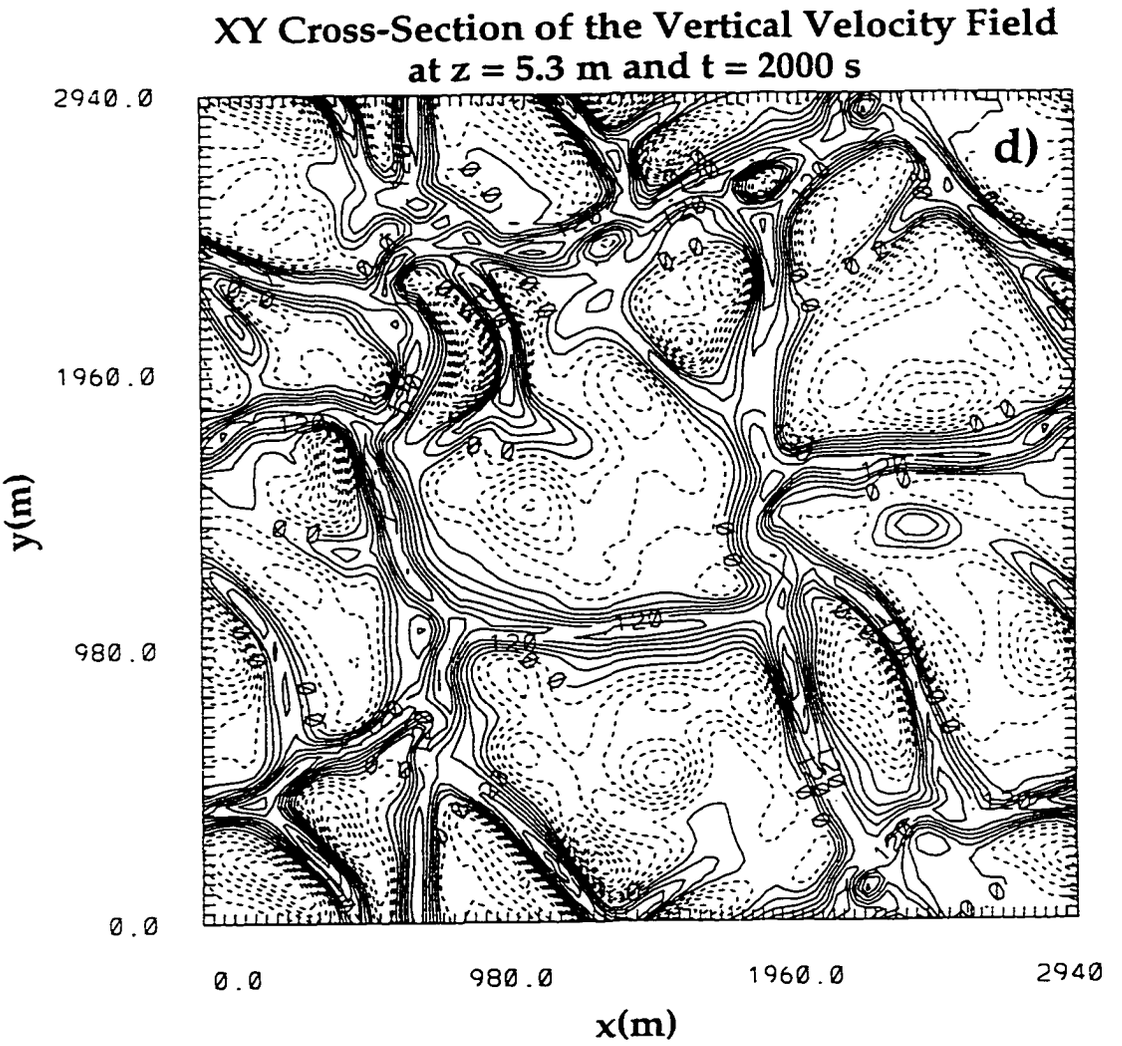

Fig. 3.8. *(continued)*. (d) X-Y Cross-sections of vertical velocity at z = 5.3 m and t = 2000 s. Contours from -0.27 to 0.24 by 0.03 m s^{-1}.

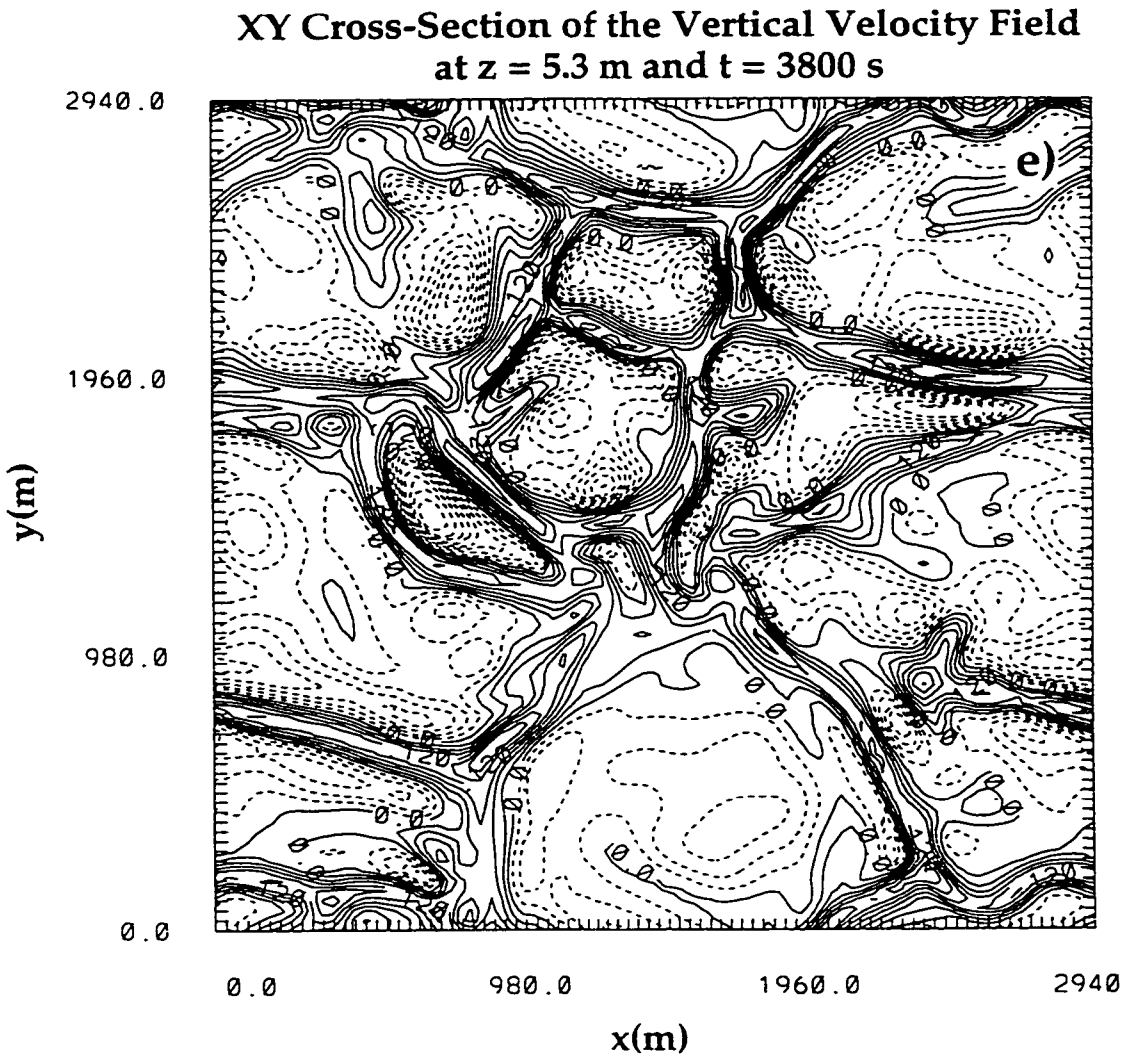

Fig. 3.8. *(continued)*. (e) X-Y Cross-sections of vertical velocity at z = 5.3 m and t = 3800 s. Contours from -0.24 to -0.24 by 0.03 m s^{-1}.

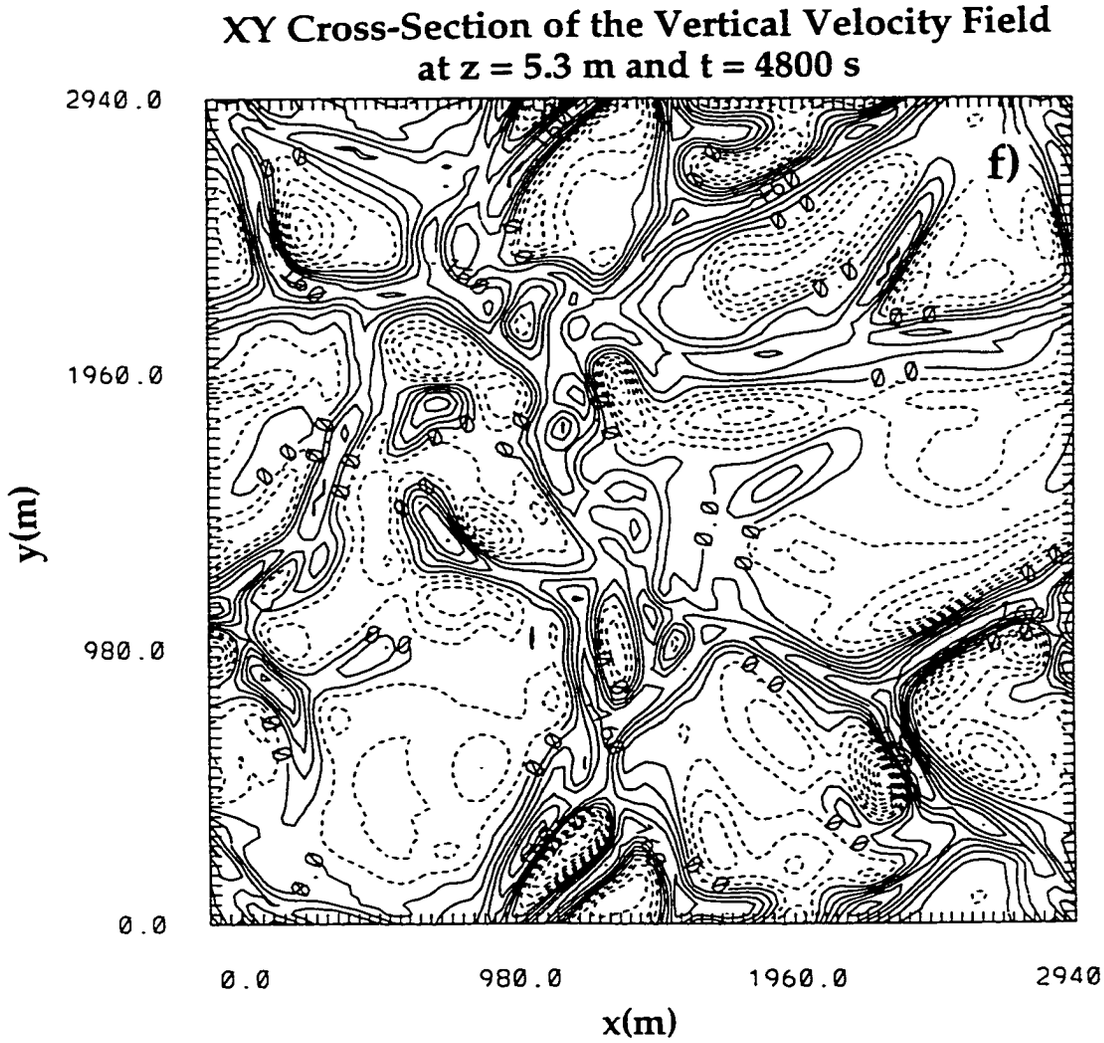

Fig. 3.8. *(continued).* (f) X-Y Cross-sections of vertical velocity at z = 5.3 m and t = 4800 s. Contours from -0.32 to 0.28 by 0.04 m s^{-1}.

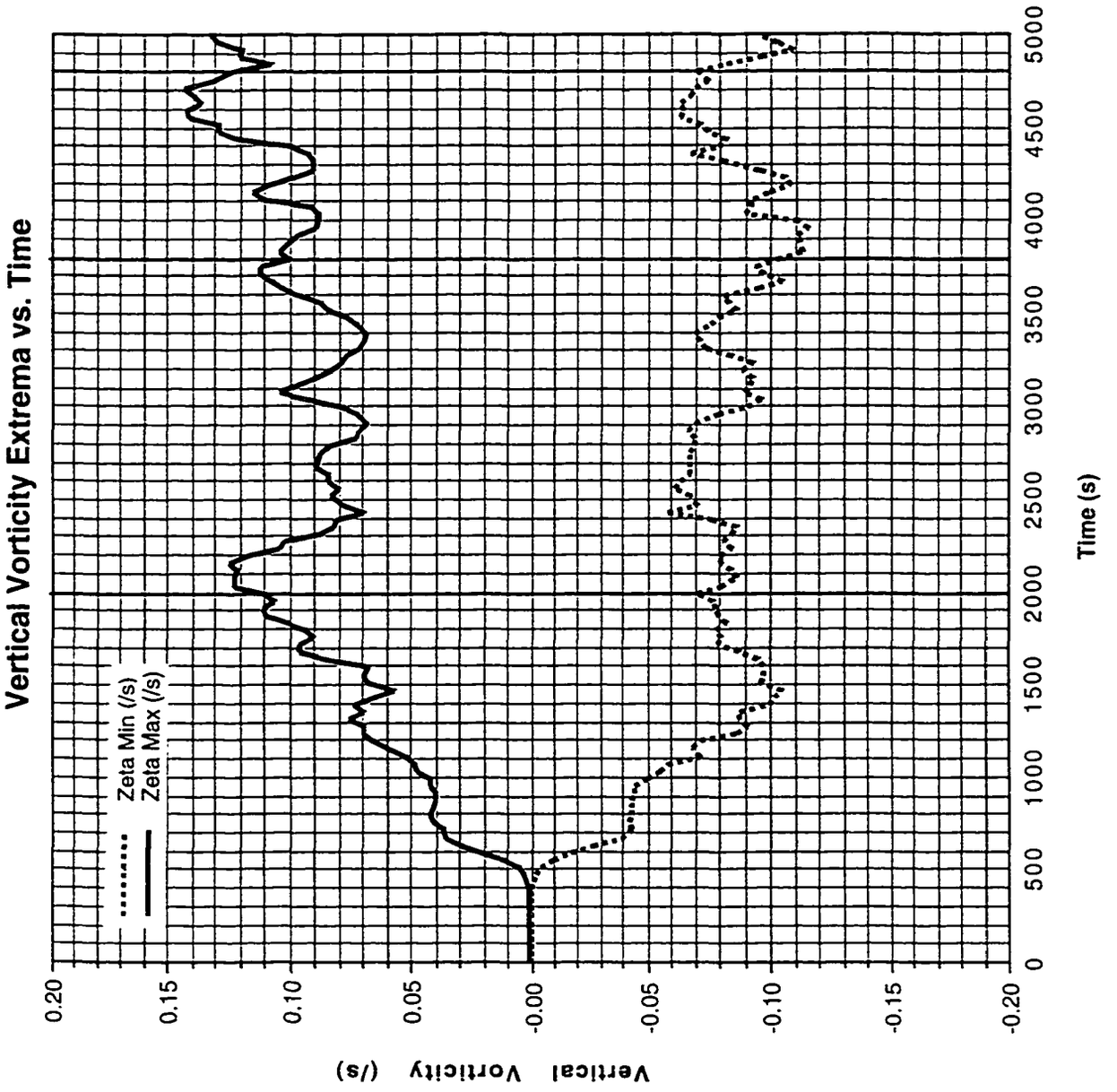

Fig. 3.9. Domain vertical vorticity (s^{-1}) maximum and minimum as a function of time (s).

to the established vortices shown in Fig. 3.8. At some times there are three or more vortices occurring simultaneously in the simulation, and in some cases vortices appear to form at higher levels before they appear at the lowest simulation level. This would be consistent with some of the proposed vorticity tilting mechanisms that would predict vertical vorticity first above the surface and subsequent evolution resulting in low-level vertical vorticity. The existence of these vortices in the current simulation offers support for the conclusion of Willis and Deardorff (1979) that surface roughness or inhomogeneities are not necessary for the formation of dust devils.

Figure 3.10 shows an estimate of the number of vortices occurring at each of the sampled times (every 100 s). These values were obtained by examining visually the horizontal velocity vector fields at z = 5.3 m. There is a slight decrease in the total number of simultaneously occurring vortices with time. One might expect that as the convective cells broaden, there are less cell intersection locations available as favored areas for vertical vortex formation. This result supports this contention.

The cyclonic vortex, which occurs at time t = 4800 s, has been selected for more in-depth examination. The vortex of interest is located at about x = 1313 m and y = 1558 m in Fig. 3.8 e. The vortex diameter at this height is about 250 m. Recall the size of the parent circulation observed using the mobile Doppler radar was about 1.5 km and that most observed dust devil diameters are on the order of tens of meters (Sinclair 1969). Therefore, the simulated circulation is of a size that lies between these two scales of motion. The horizontal wind speeds associated with the current simulated circulations are about 4-5 m s^{-1}. However, it is expected that the wind speeds will strengthen and that the circulation

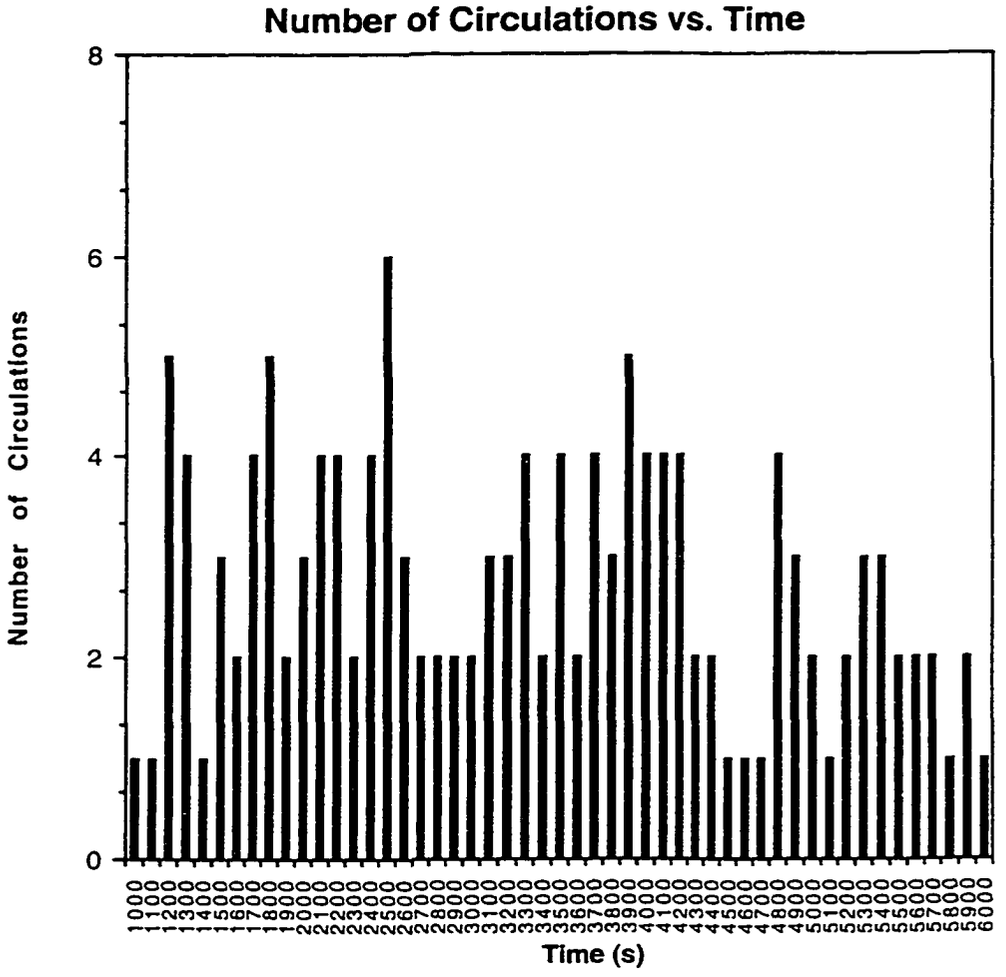

Fig. 3.10. Estimated number of vertical vortices occurring simultaneously at z = 5.3 m for times sampled every 100 s.

diameters will decrease with increased horizontal resolution. For example, the angular momentum associated with the circulation shown in Fig. 3.8 e is estimated to be about 500 m s^{-1}, where the angular momentum is found from multiplying the approximate radius of the circulation, 100 m, by the estimated azimuthal velocity, 5 m s^{-1}. If the horizontal resolution is reduced such that a vortex of radius 20 m can be resolved, by conservation of angular momentum, an associated azimuthal velocity of 25 m s^{-1} is expected.

Horizontal cross-sections of velocity vectors and vertical velocity at a higher level (z = 311.5 m) are shown in Fig. 3.11. The cyclonic circulation present at the lowest level (Fig. 3.8 e) is weaker at z = 311.5 m, but still clearly evident in Fig. 3.11 a and lies between two anticyclonic circulations. There are several more circulations at this height than at z = 5.3 m. Similar LES features were shown, but not discussed, in Mason (1989) and his Fig. 2 is included as Fig. 3.12 here. Figure 3.12 a and 3.12 b are X-Y cross-sections at z = 0.05 z_i, and Fig. 3.12 c and d are X-Y cross-sections at z = 0.4 z_i, at a selected time after the turbulence has become quasi-stationary. Figure 3.12 a and c show lines parallel to the instantaneous horizontal flow and Fig. 3.12 b and d show the associated vertical velocity contours. The apparent horizontal circulations simulated by Mason also occur at the vertices of the convective rings, with more swirling motion at the 0.4 z_i level than at the 0.05 z_i level. Mason used a horizontal resolution of 50 m and a vertically stretched coordinate. His convective cells (Fig. 3.12 b) are approximately 1-1.5 km in diameter at z = 0.05 z_i, which is quite similar to the diameter of the cells in the current study (Fig. 3.6 d).

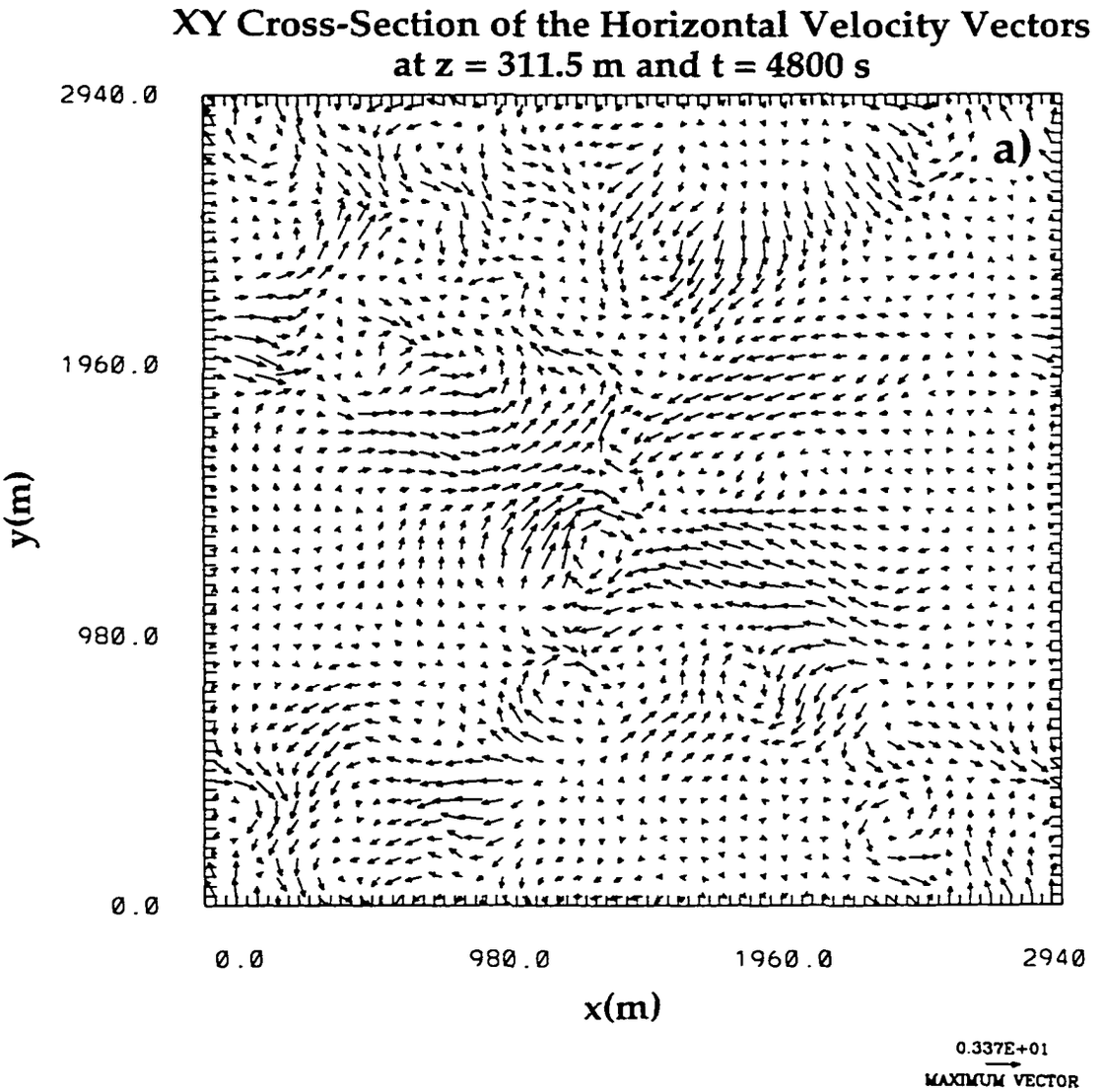

Fig. 3.11. (a) X-Y Cross-sections of horizontal velocity vectors at t = 4800 s and z = 311.5 m. Maximum vector length is 3.37 m s^{-1}.

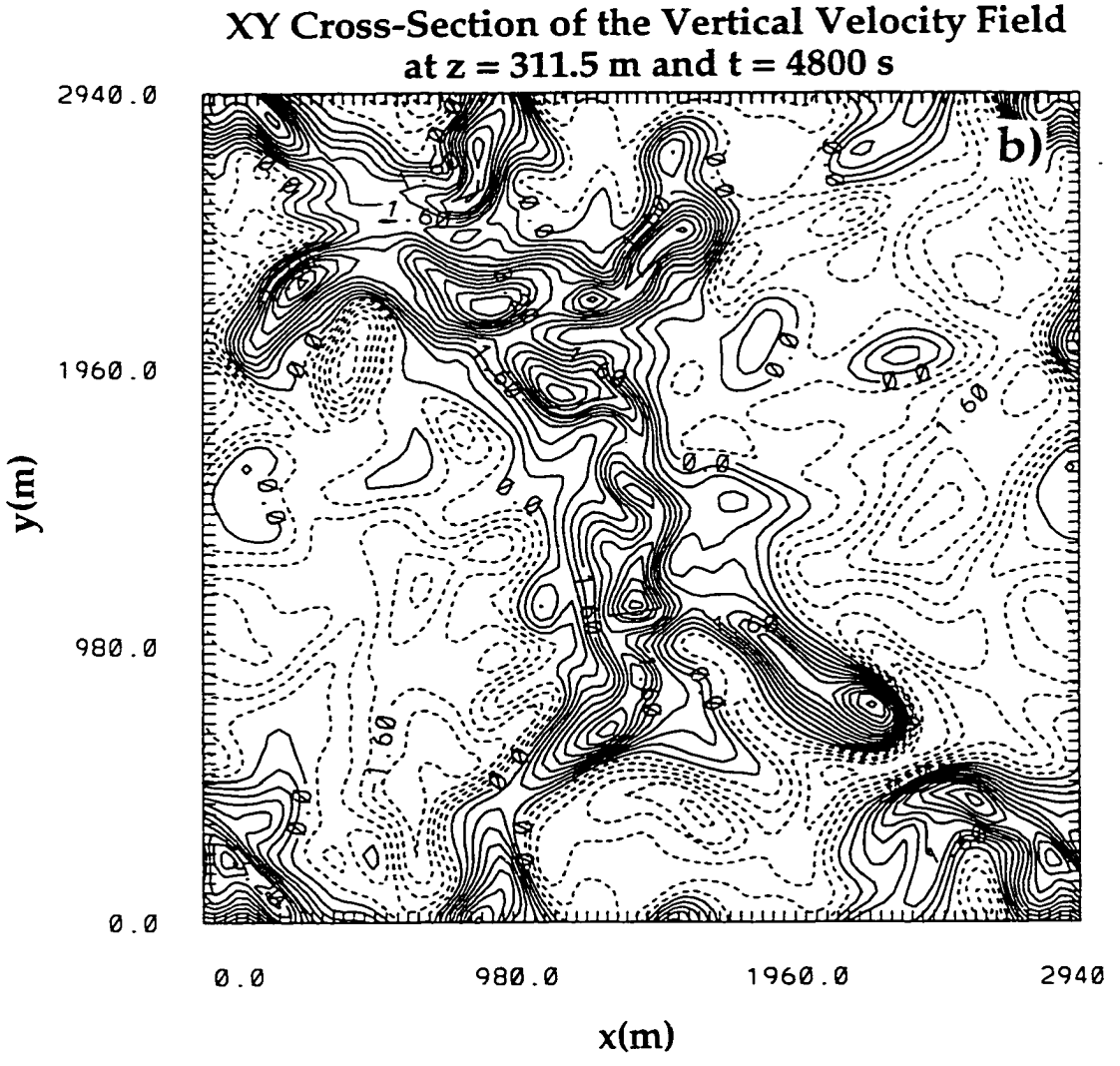

Fig. 3.11. *(continued).* (b) X-Y Cross-sections of vertical velocity at t = 4800 s and z = 311.5 m. Contours from -2.4 to 4.8 by 0.4 m s^{-1}.

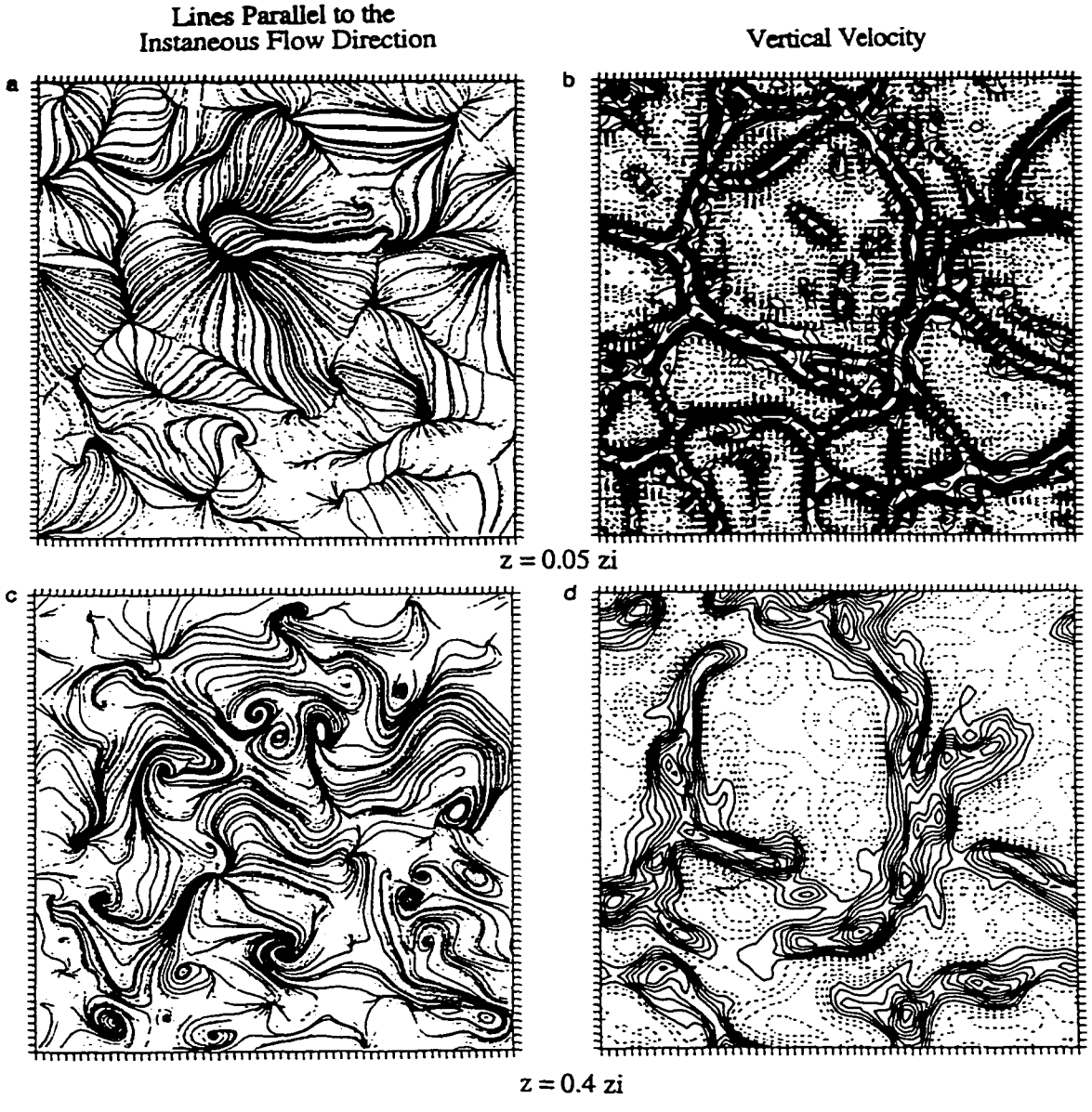

Fig. 3.12. From Mason (1989) X-Y Cross-sections. (a) Lines parallel to the instantaneous flow direction at z = 0.05 z_i. (b) Vertical velocity at z = 0.05 z_i. Maximum value is 1.1 w_* and contour interval is one-tenth of the maximum value. (c) Lines parallel to the instantaneous flow direction at z = 0.4 z_i. (d) Vertical velocity at z = 0.4 z_i. Maximum value is 2.1 w_* and contour interval is one-tenth the maximum value. (Adapted from *J. Atmos. Sci.*)

The vertical structure of the vortex shown in Fig. 3.8 e is displayed in Fig. 3.13, which contains cross-sections of various fields at y = 1557.5 m and t = 4800 s. A warm (Fig. 3.13 a) updraft (Fig. 3.13 c) is associated with the vortex (Fig. 3.13 e) and extends to a height of about 1500 m. Interestingly, the updraft is strongest and penetrates the highest in the region of the vortex. The inhibition of down-scale energy cascade in a helical flow (Lilly 1986) would be consistent with this result. The pressure field (Fig. 3.13 b) shows a definite pressure minimum near the surface of the vortex.

The eddy mixing coefficient K_m, is contoured in Fig. 3.13 d. The local K_m maxima (values > 2 $m^2 s^{-1}$) in the vicinity of the vertical vortex have been shaded for clarity. The turbulent mixing is maximized on the edges of the updraft where the gradients of vertical velocity are large. There is an embedded local mixing minimum that corresponds roughly with the center of the updraft. The variation in the height of the boundary layer can also be estimated using Fig. 3.13 d. The boundary layer height is estimated to be highest near the region where the vortex circulation is occurring at lower levels. If this occurs for many cases in the atmosphere, vortices such as dust devils could strongly influence the height of the boundary layer. Willis and Deardorff (1979) found in their laboratory simulation that the convective ring intersection points were associated with the locations of more energetic vertical updrafts, the strongest of which sometimes developed vertical vortices. These updrafts maintained their identity up to heights somewhat exceeding the mean inversion base height. Therefore, one could conclude that the existence of these intersection points may be more pertinent to the maximum boundary layer height than the existence of a vortex.

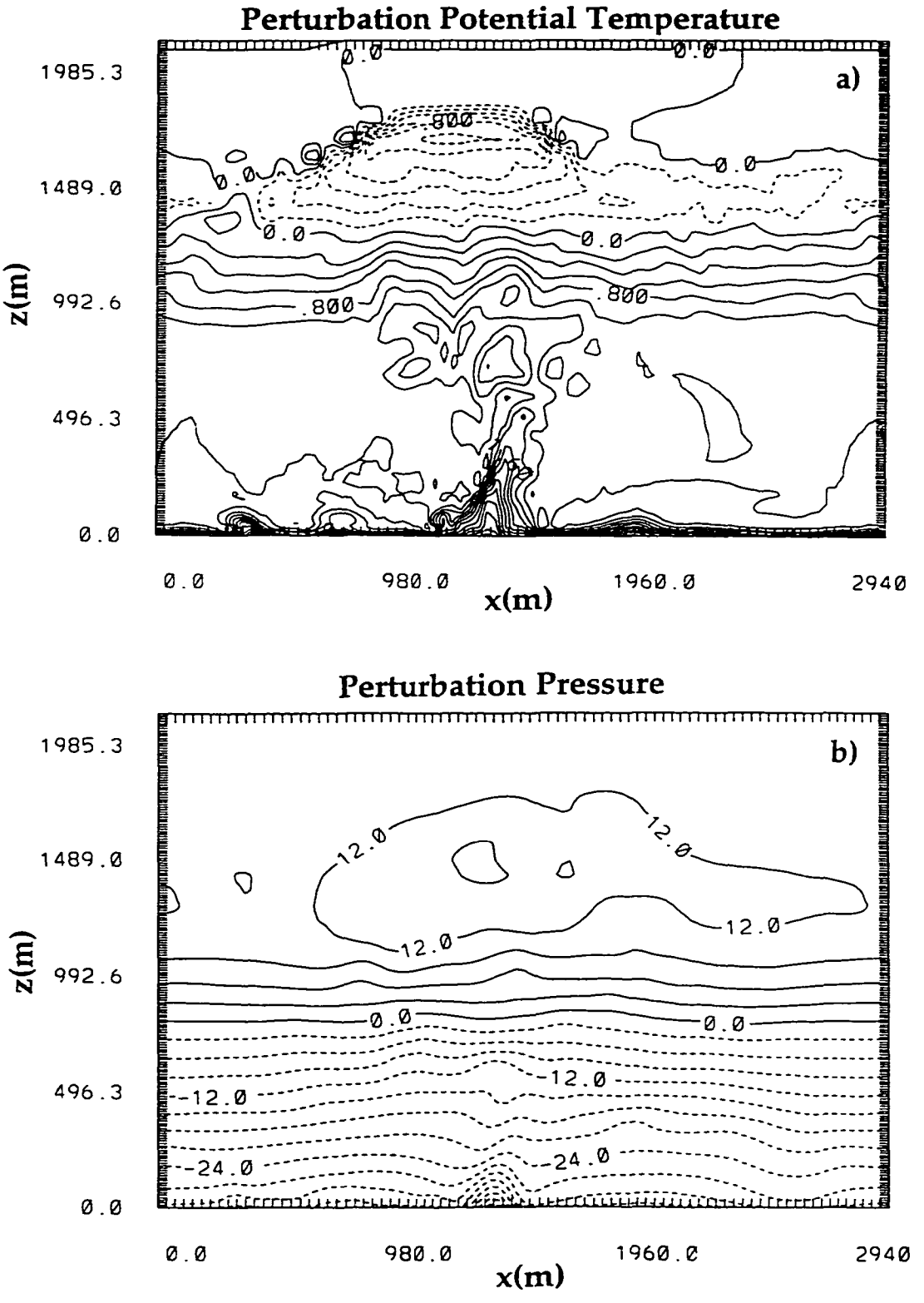

Fig. 3.13. X-Z Cross-sections at y = 1557.5 m at t = 4800 s. (a) Potential temperature with contours from -1.4 to 3.2 by 0.2 K. (b) Perturbation pressure with contours from -45.00 to 15.0 by 3.0 Pa.

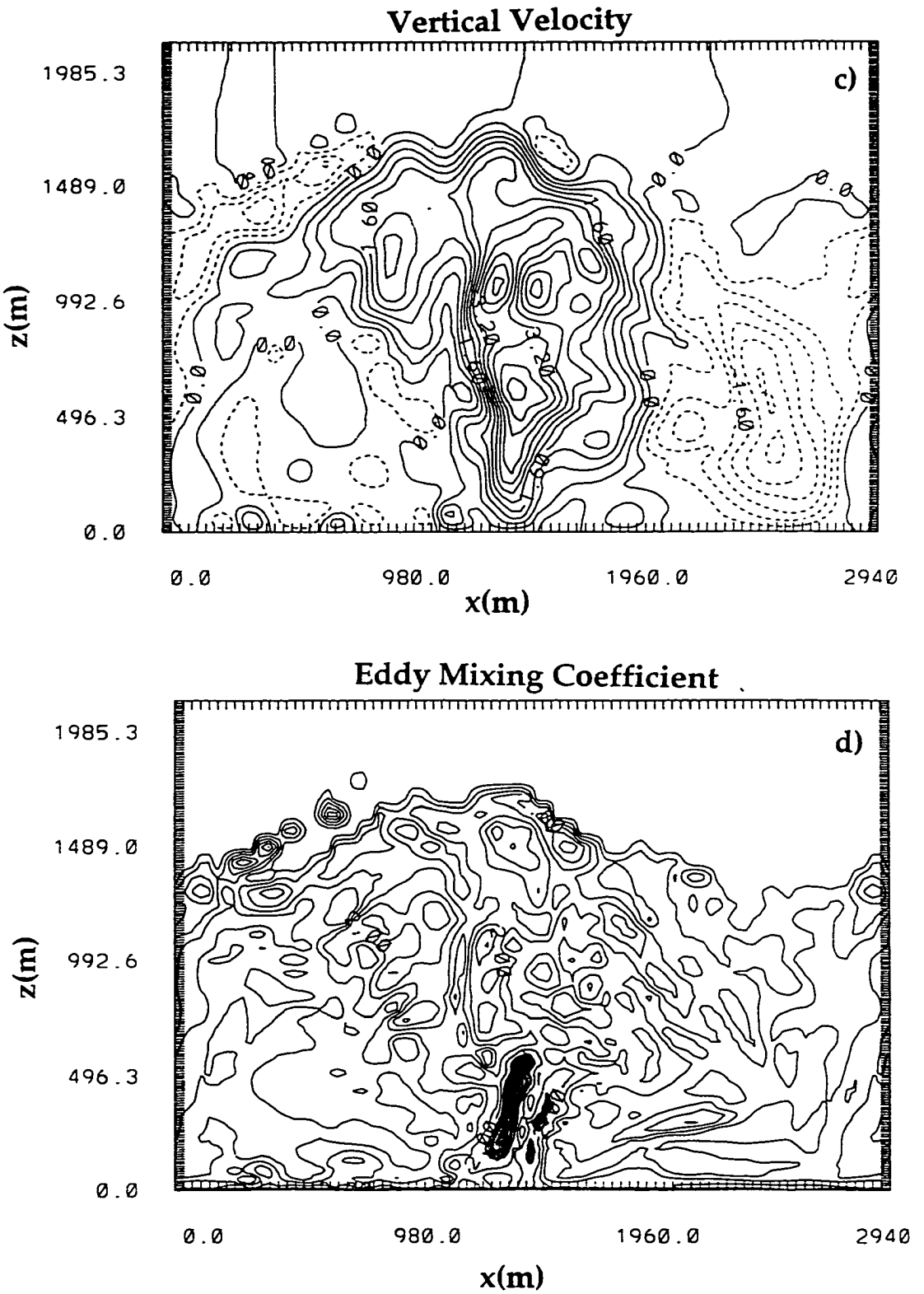

Fig. 3.13. *(continued).* X-Z Cross-sections at y = 1557.5 m at t = 4800 s. (c) Vertical velocity with contours from -2.4 to 4.4 by 0.4 m s^{-1}. (d) Eddy mixing coefficient, Km. Contours from 0.0 to 8.0 by 0.5 $m^2 s^{-1}$.

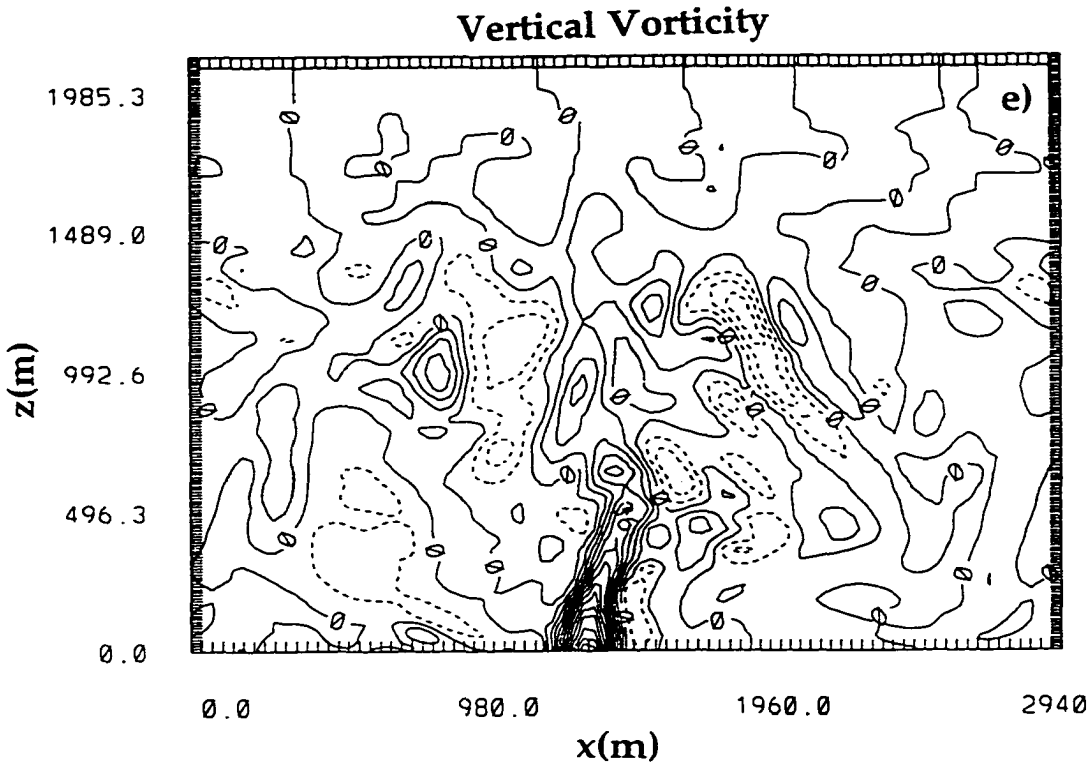

Fig. 3.13. *(continued).* X-Z Cross-sections at y = 1557.5 m at t = 4800 s. (e) Vertical vorticity with contours from -0.027 to 0.117 by 0.009 s^{-1}. Labels scaled by 1000.

But once a vortex is established at these locations, it may further enhance vertical transports of heat and momentum. The three main vortices depicted in Fig. 3.8 have mixed results (not shown) for the question of elevated boundary layer height over the location of vertical vortices.

The vertical vorticity field (Fig. 3.13 e) shows that the vortex column has a slight tilt to the east with height. The vertical vorticity column is about 300 m wide and is co-located with the updraft region up to ~ 600 m. Other vorticity maxima are located aloft and are co-located with positive vertical velocity. Anticyclonic vertical vorticity exists on either side of the vortex at low levels.

Despite the slight tilt with height, a local maximum in vertical velocity at z = 1684 m (Fig. 3.14) is approximately associated with the circulation at low-levels (Fig. 3.8 c). This is further indication that for this low-level vortex, the updraft penetrates higher in the vicinity of the vortex than at surrounding locations.

Transects at the lowest level (z = 5.3 m) were obtained and compared with observational data from instrumented observing systems over which dust devils passed (Sinclair 1973; Kaimal and Businger 1970). Transect data from the current simulation is shown in Fig. 3.15 and the center of the vortex is at approximately x = 1310 m. The potential temperature transect (Fig. 3.15 a) shows that the vortex core is relatively warmer than its surroundings and this is consistent with Sinclair's findings (1973, his Fig. 8, reproduced here as Fig. 3.16). As expected, the center also exhibits low pressure (Fig. 3.15 b). The vertical velocity transect (Fig. 3.15 c) shows that the central core updraft has a local minimum with downdrafts on either side, just outside the core (similar to Kaimal and Businger 1970, their Fig. 2, reproduced here as Fig. 3.17). The local minimum in vertical velocity at the vortex core is also identifiable in Sinclair's data (Fig. 3.16).

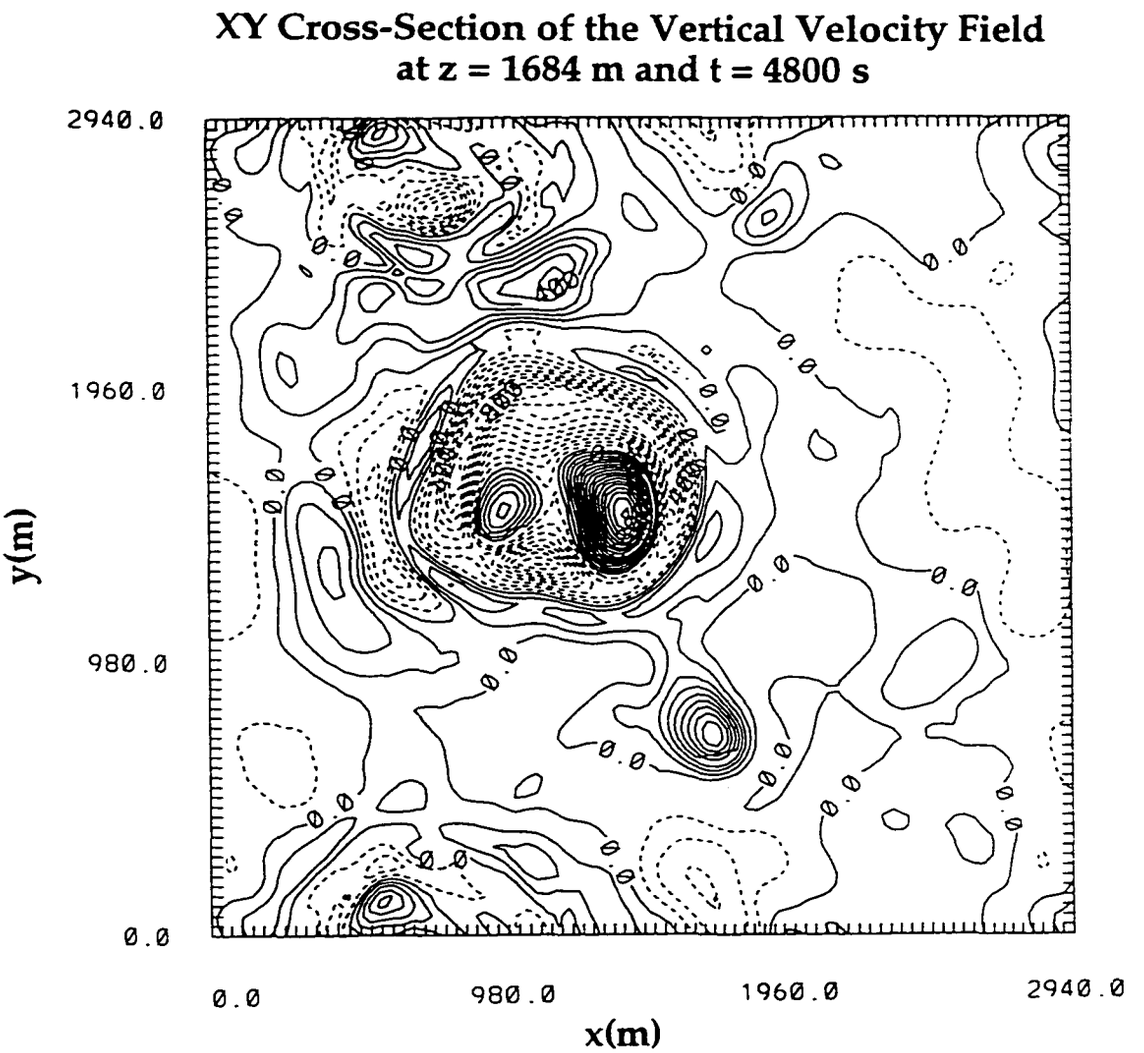

Fig. 3.14. X-Y Cross-section of the vertical velocity at z = 1684 m and t = 4800 s. Contours from –1.0 to 1.7 with interval 0.1 m s^{-1}.

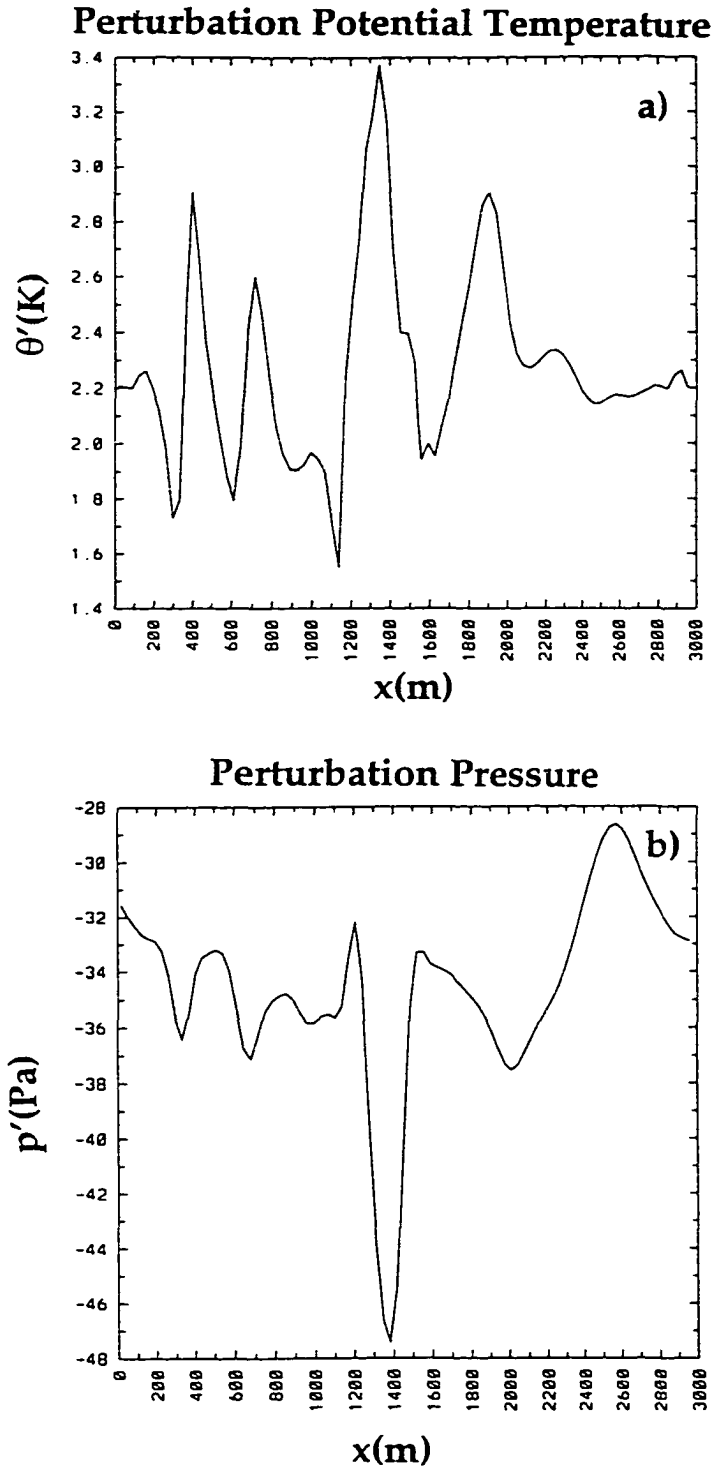

Fig. 3.15. Transects through the vortex along y = 1557.5 m and z = 5.3 m at t = 4800 s. (a) Potential temperature (K). (b) Perturbation pressure (Pa).

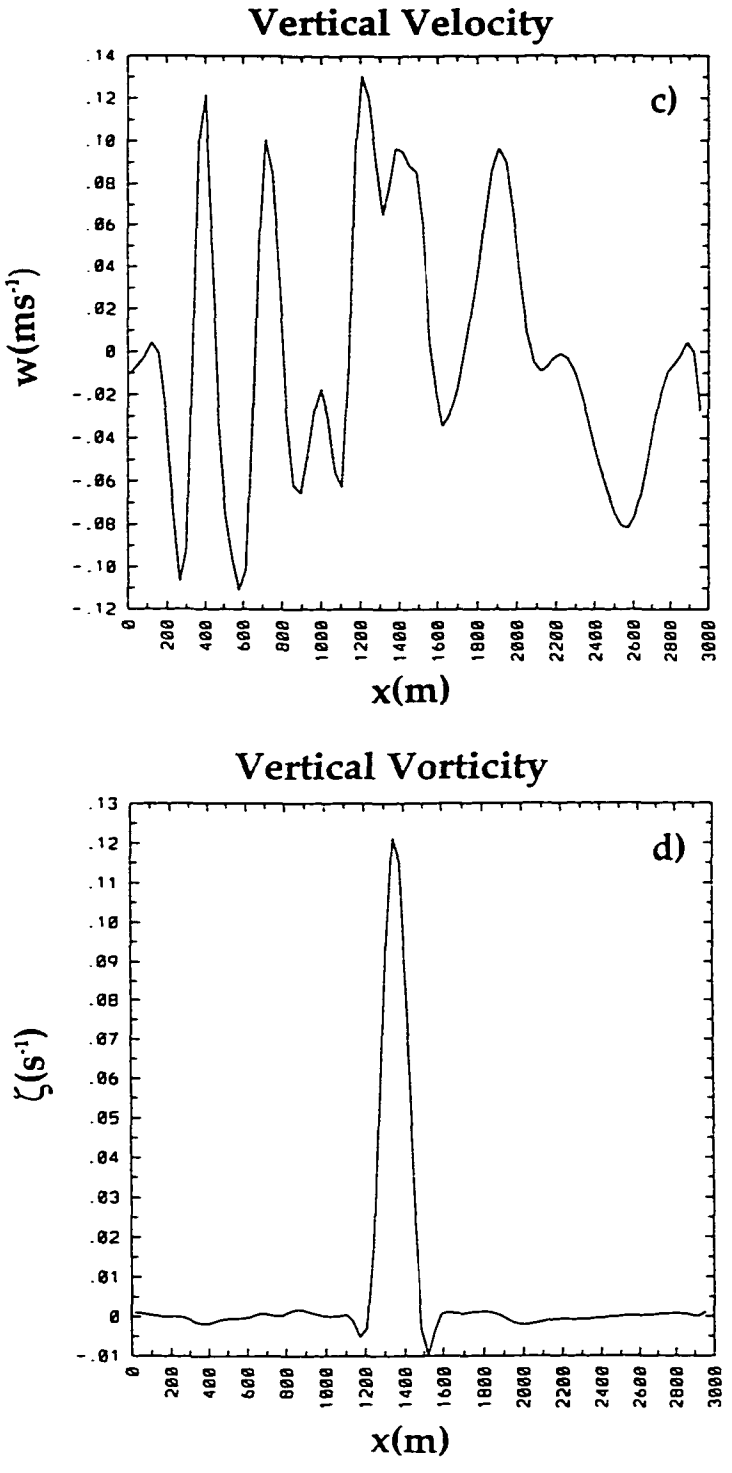

Fig. 3.15. *(continued)*. Transects through the vortex along y = 1557.5 m and z = 5.3 m at t = 4800 s. (c) Vertical velocity (m s^{-1}). (d) Vertical vorticity (s^{-1}).

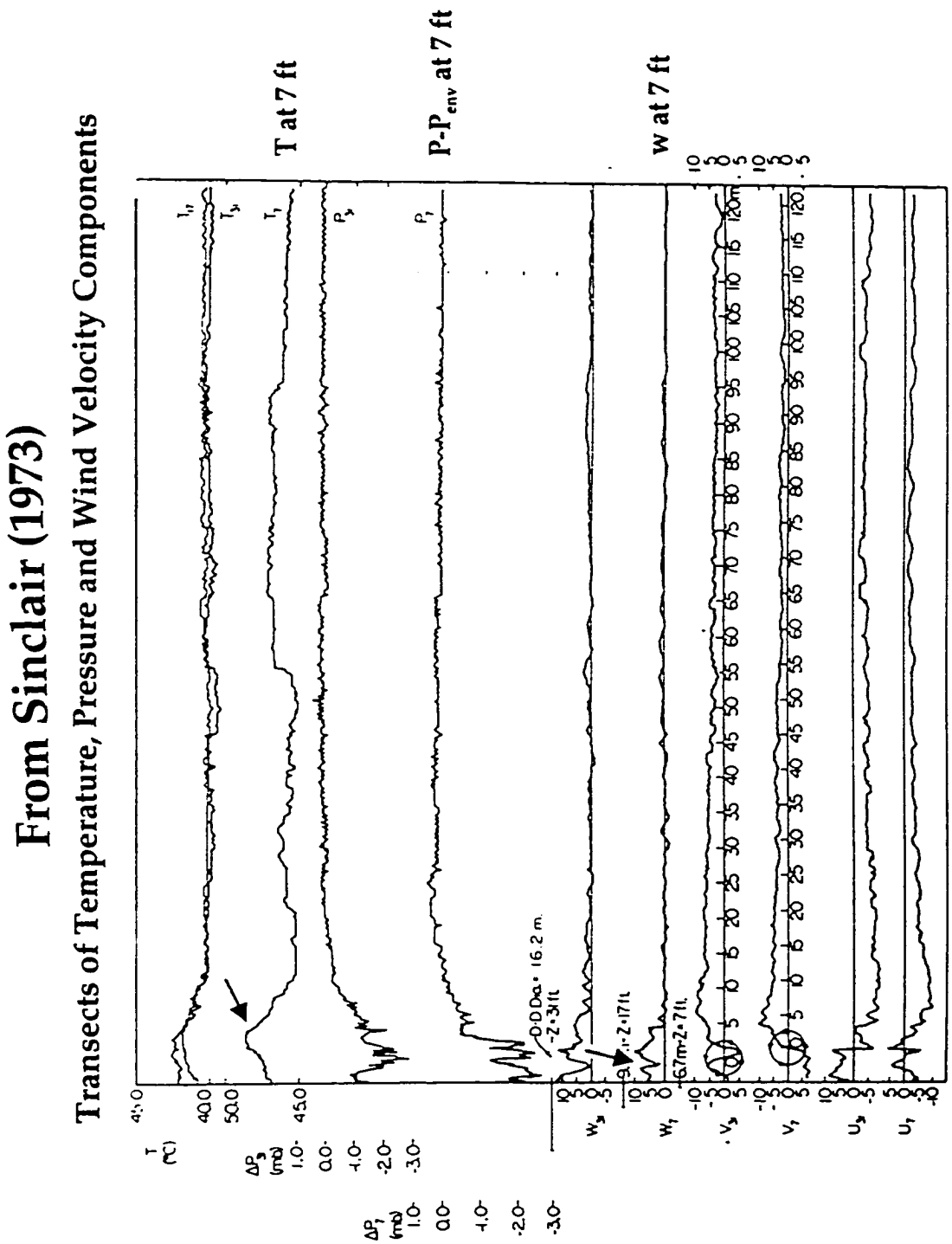

Fig. 3.16. Reproduced from Sinclair (1973). Temperature, pressure and wind velocity transects obtained by penetration of a dust devil with a mobile instrumented tower. The two temperature transects at the top were taken at heights of 7, 17, and 31 ft levels. Transects of pressure differences from environmental pressure were taken at heights of 7 and 31 ft. Wind velocities were taken at heights of 7 and 31 ft. The tangential (radial) velocity is represented by v (u) and the vertical velocity is denoted by w. The dust devil was moving to the left at4.5 m s^{-1}. (Adapted from the *J. Atmos.Sci.*)

From Kaimal and Businger (1970)

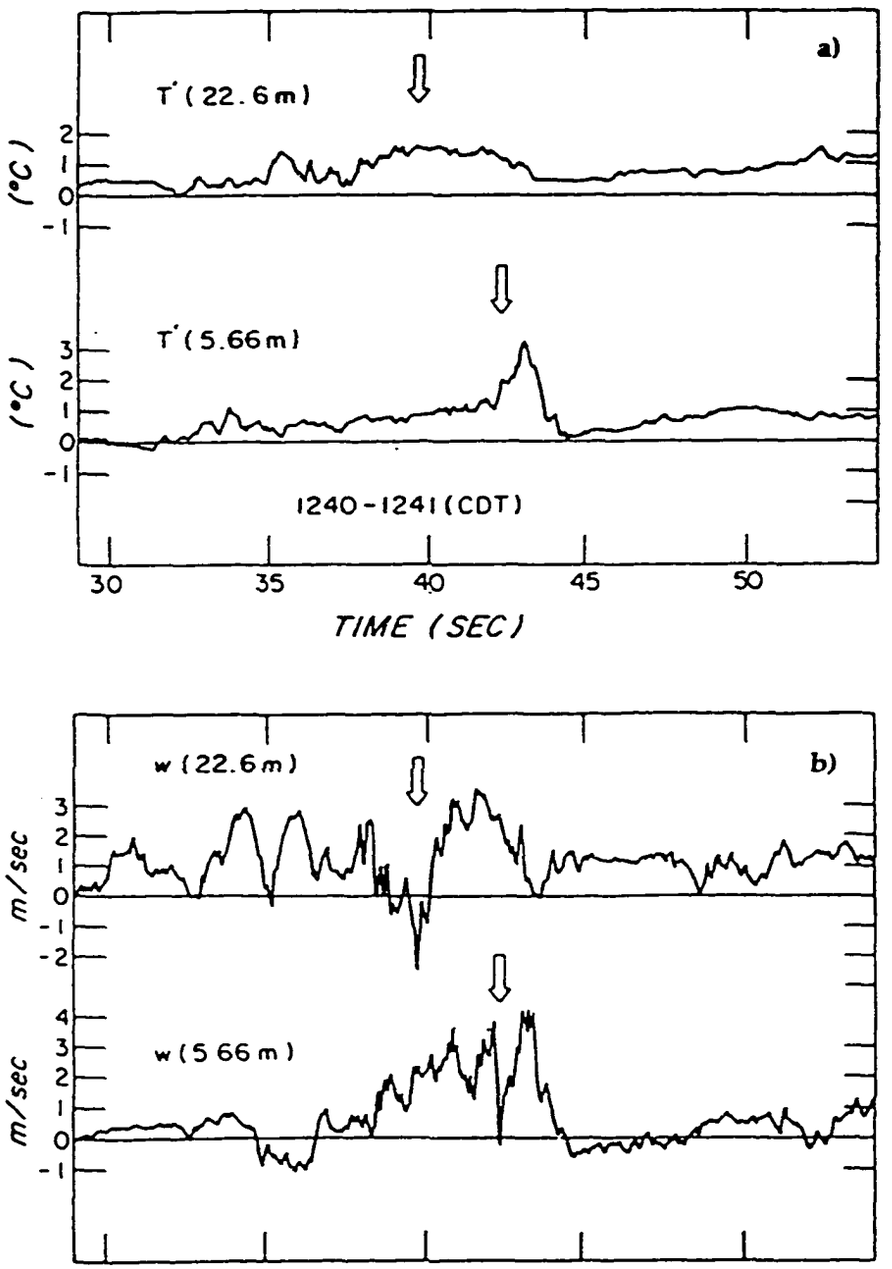

Fig. 3.17. Reproduced from Kaimal and Businger (1970). a) Temperature difference from the environmental temperature T′ transects at heights of 5.66 m and 22.6 m. b) Vertical velocity w transects at heights of 5.66 m and 22.6 m. Transects were obtained by passage of a dust devil over an instrumented tower. (Adapted from the *J. Appl. Meteor.*)

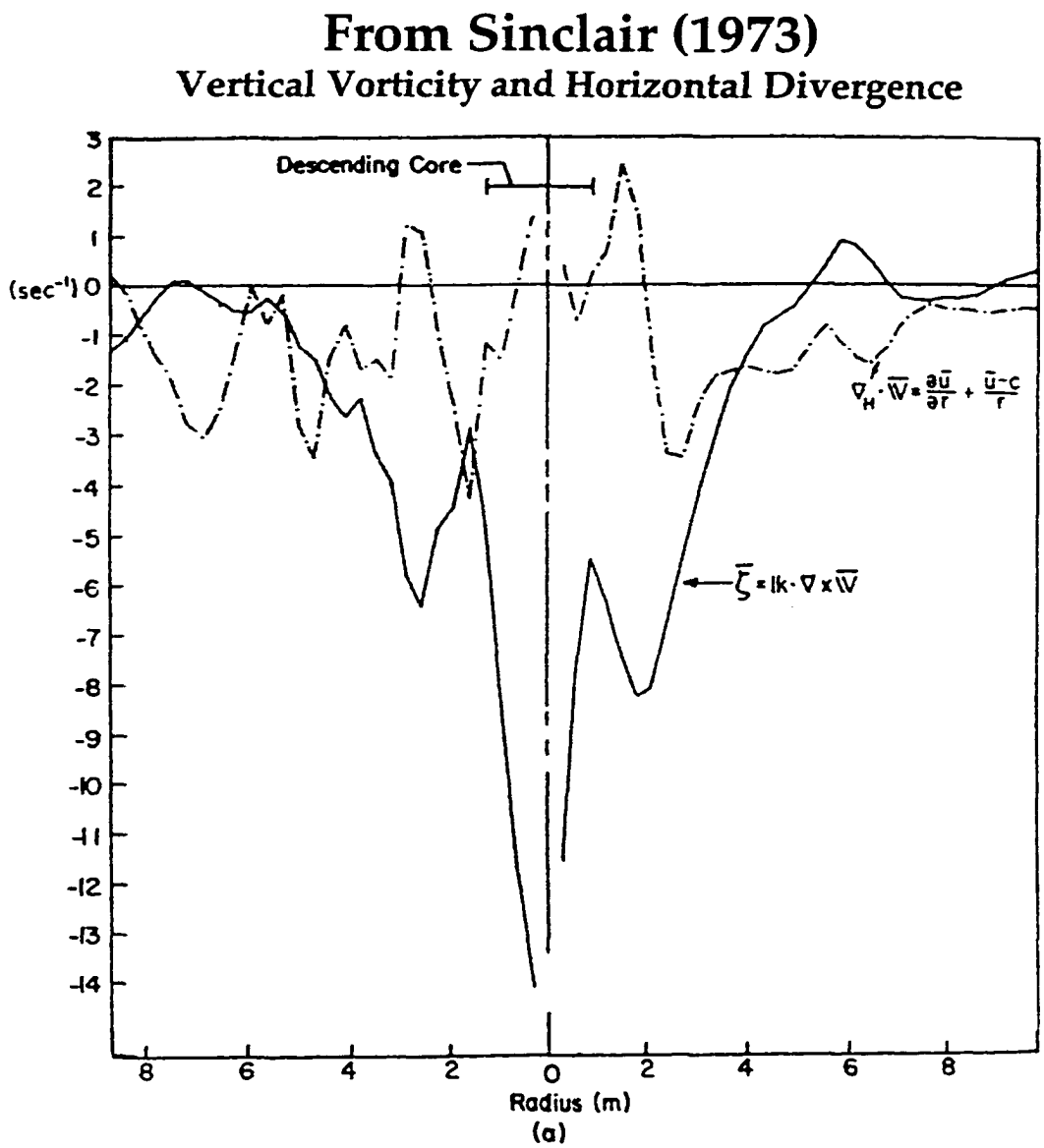

Fig. 3.18. Reproduced from Sinclair (1973). Vertical vorticity and horizontal divergence calculated assuming axial symmetry from wind velocity transects at a height of seven feet. Wind data were obtained by penetration of a dust devil with a mobile instrumented tower. (Adapted from the *J. Atmos.Sci.*)

Another feature is interest is the vertical vorticity transect (Fig. 3.15 d), which is again very similar to Sinclair's observations, except reversed in sign for his anticyclonic vortex (1973, his Fig. 13, reproduced here as Fig. 3.18). There are two local anti-cyclonic vorticity regions just outside the cyclonic vorticity core and such a s feature is evident in Sinclair's data (Fig. 3.18) as well. In addition, the vertical velocity maximum and vertical vorticity maximum (Fig. 3.15 c and d) are spatially well correlated at this level, which indicates a vertical helical flow. Based on this examination of the structure of the simulated circulations, it is concluded that they have general characteristics similar to dust devil vortices.

3.3.2.3. Other Comments

Some of the mechanistic theories described in Section 3.1.3 are briefly evaluated based on SIM1 results. The proposed criterion that – h /MO must be greater than 100 (Deardorff 1978) or 50 (Hess and Spillane 1990) is assessed. An estimate of –h/MO for SIM1 produces a value of 38. This value is even smaller than that proposed by Hess and Spillane for the existence of vertical vortices. Lilly (personal communication) proposed that the diameter of a vertical vortex divided by MO must be greater than unity for a dust devil-type vortex to exist. For SIM1, a value of 3.3 is approximated from $d_{vtx} / MO = 100m / 30m = 3.3$. Thus, this criterion holds for SIM1.

In addition, from an animation of the horizontal velocity vectors, it is apparent that the direction of vortex motion is along the branches of the polygonal convective rings, where horizontal convergence is strongest. This results leads to questions regarding the reported observed motion of dust devils relative to a ambient wind direction (e.g., Sinclair 1969). If a measurement of mean wind direction is obtained from a point measurement in a dust devil environment characterized by convective patterns as in Fig. 3.8 c, then the measured ambient wind could be from almost any direction. Therefore, it seems very difficult to make conclusions and dynamical inferences (e.g., Maxworthy 1973) about the direction of translation of a dust devil relative to a mean wind in such an environment.

3.4 Results from higher resolution simulations

A second simulation (SIM2) was performed using higher horizontal resolution. The number of gridpoints was 150 x 150 x 80 and in this case, no vertical stretch was used. The horizontal resolution was increased to $\Delta x = \Delta y = 20$ m and the vertical resolution was fixed $\Delta z = 15$ m. Therefore, the total height of the domain was reduced to 1200 m. The boundary depth increased such that the top of the domain inhibited the numerical solution and the simulation was terminated at time t = 4300 s. The Rayleigh damping layer was set at height $z = 1060$ m. All other model parameters and initial conditions were as in the first simulation. The parameters for SIM2 are summarized in Table 3.3.

Gridpts	L_x	L_y	L_z	Δx	Δy	Δz	Δt	T_{total}	Pr	Q_*
150 x 150x80	3 (km)	3 (km)	1.2 (km)	20 (m)	20 (m)	15 (m)	0.1 (s)	~1.5 hrs	0.4	0.24 Kms^{-1}

Table 3.3. Summary of simulation parameters for SIM2.

The cell broadening (as in SIM1) of the horizontal scale of the polygonal vertical velocity convective rings is shown in Fig. 3.19 for SIM2. At t = 4000 s the cells are about 1 km in diameter, while in SIM1 at t = 2800 s, the cells were already 1.5 km in diameter. Since the resolved cell size at any given time is smaller for SIM2, there are more cell intersection points, and thus more favored locations for vortex formation. Indeed, there are more simultaneously occurring vortices in SIM2. Figure 3.20 shows X-Y cross-sections horizontal velocity

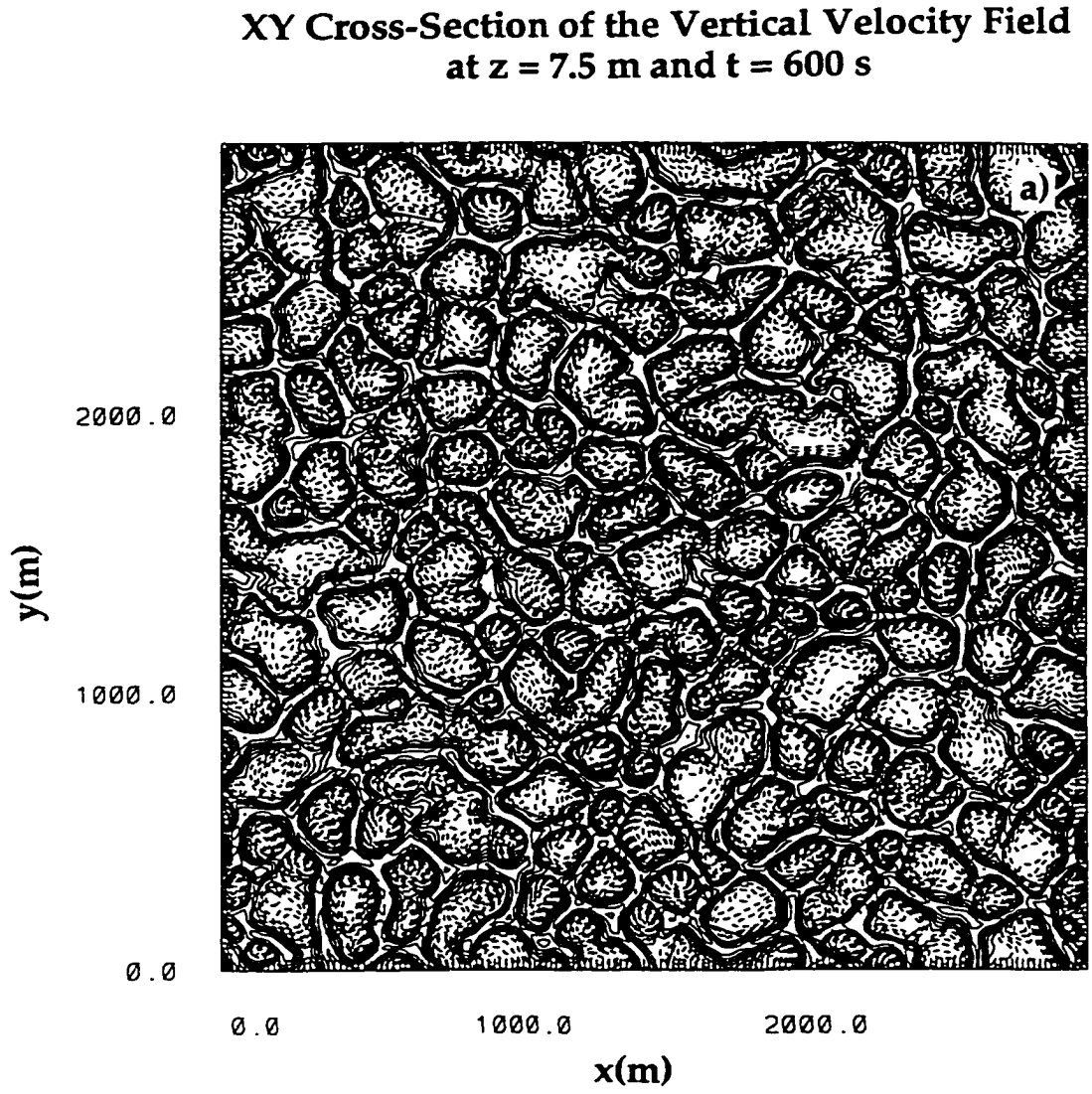

Fig. 3.19. X-Y Cross-section of the (a) vertical velocity at z = 7.5 m and t = 600 s. Contours from -0.32 to 0.28 with interval 0.04 m s^{-1}.

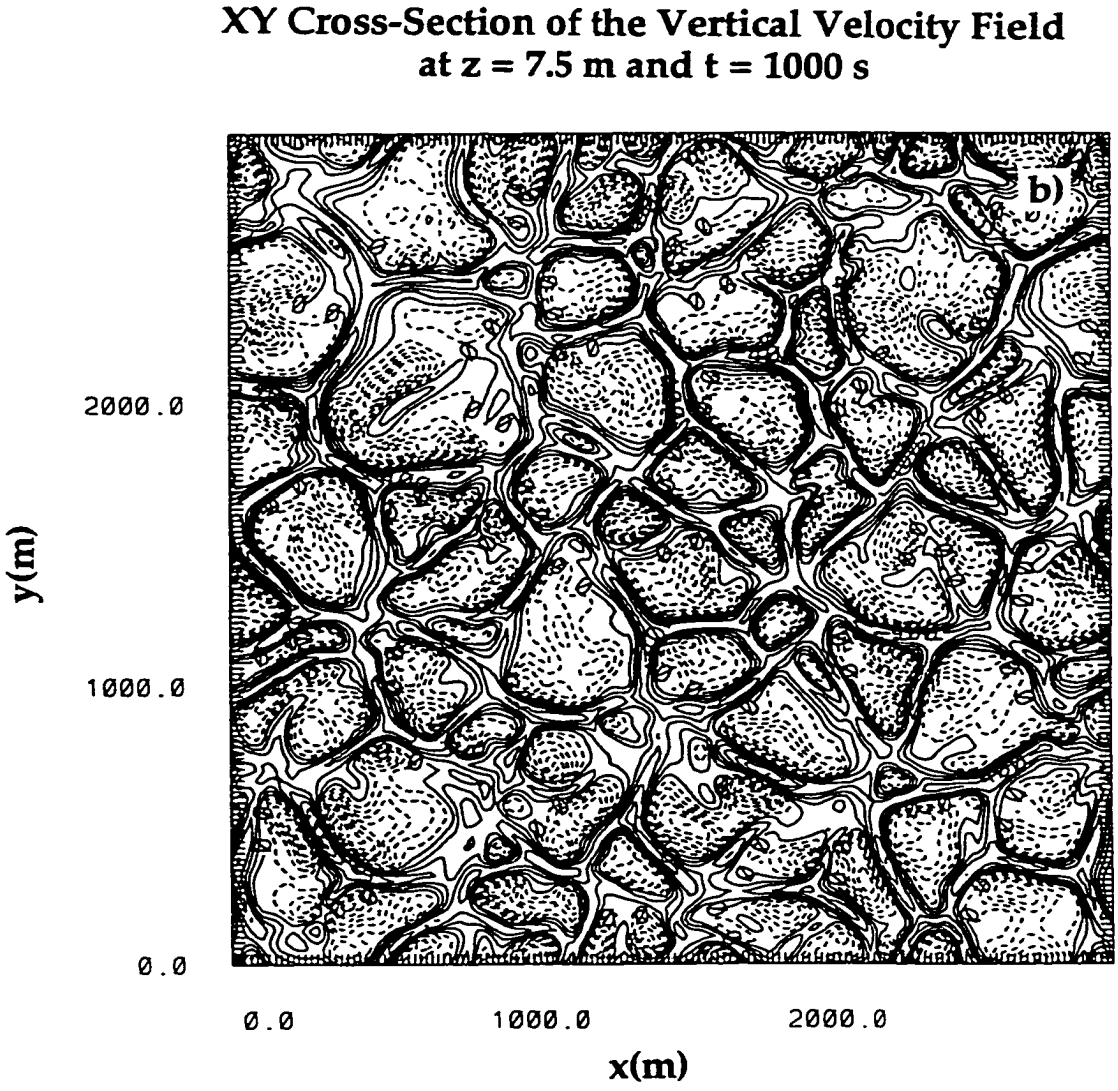

Fig. 3.19. (continued). (b) X-Y Cross-section of the vertical velocity at z = 7.5 m and t = 1000 s. Contours from -0.8 to 0.56 with interval 0.08 m s^{-1}.

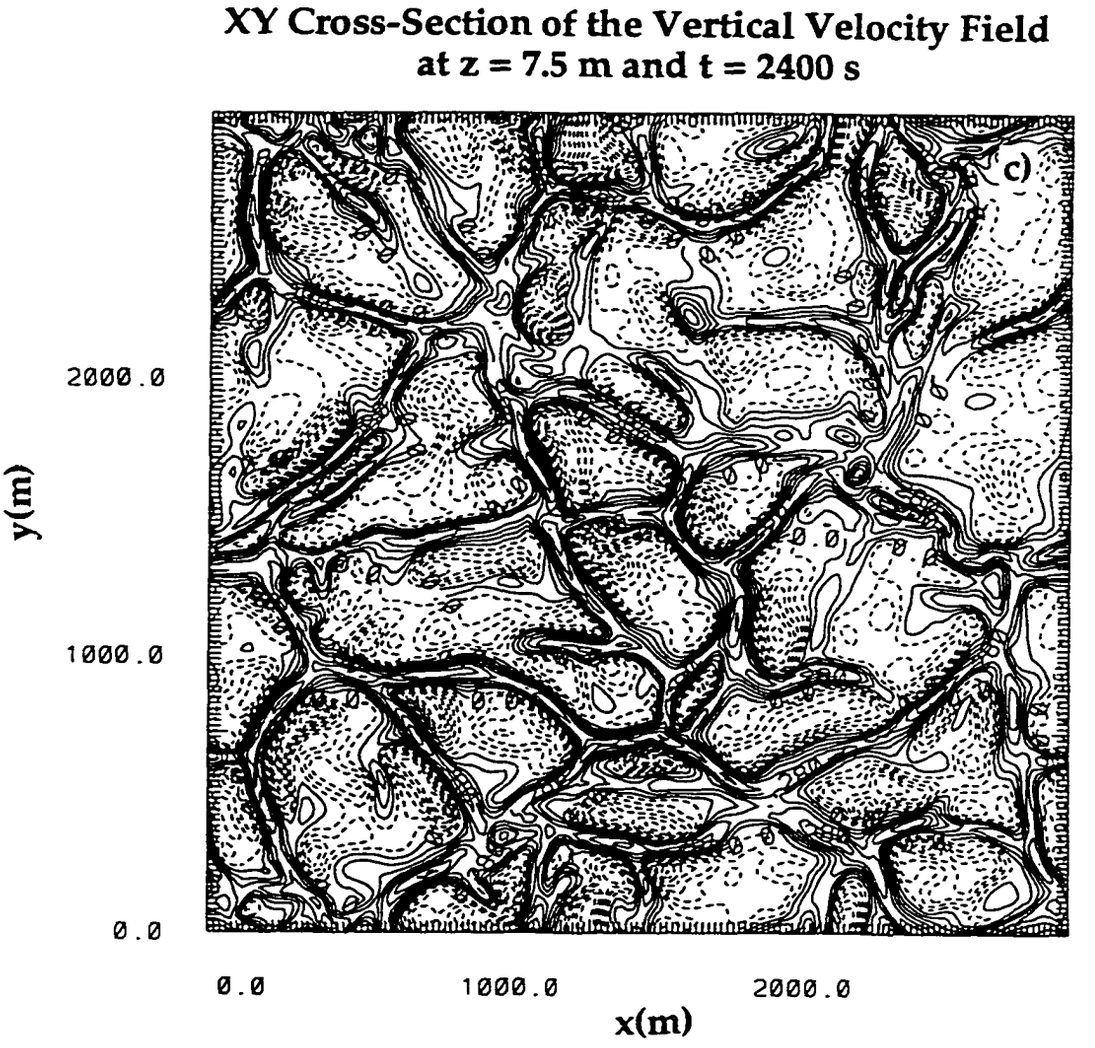

Fig. 3.19. (continued). (c) X-Y Cross-section of the vertical velocity at z = 7.5 m and t = 2400 s. Contours from -0.9 to 0.8 with interval 0.1 m s^{-1}.

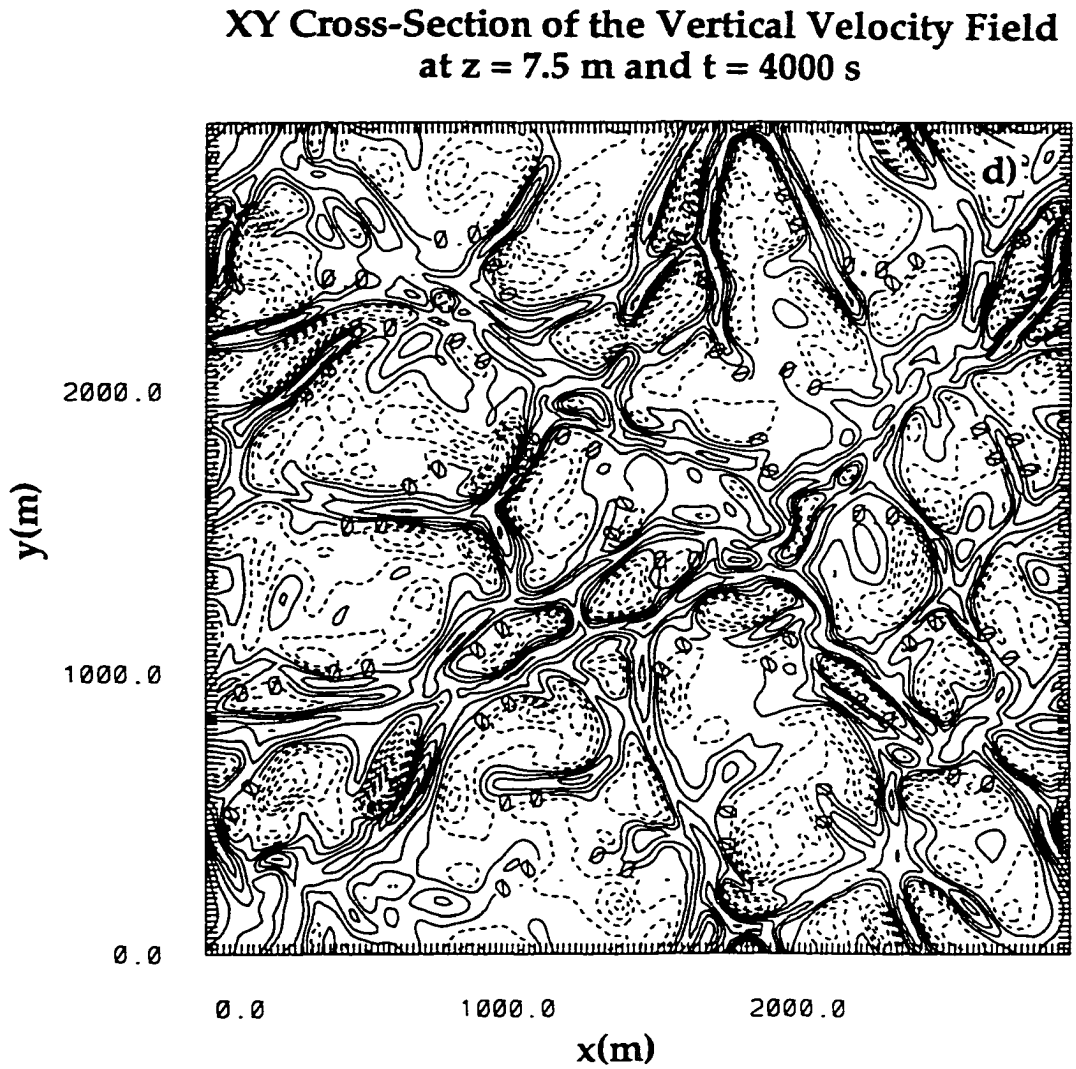

Fig. 3.19. (continued). (d) X-Y Cross-section of the vertical velocity at z = 7.5 m and t = 4000 s. Contours from -0.63 to 0.56 with interval 0.07 m s^{-1}.

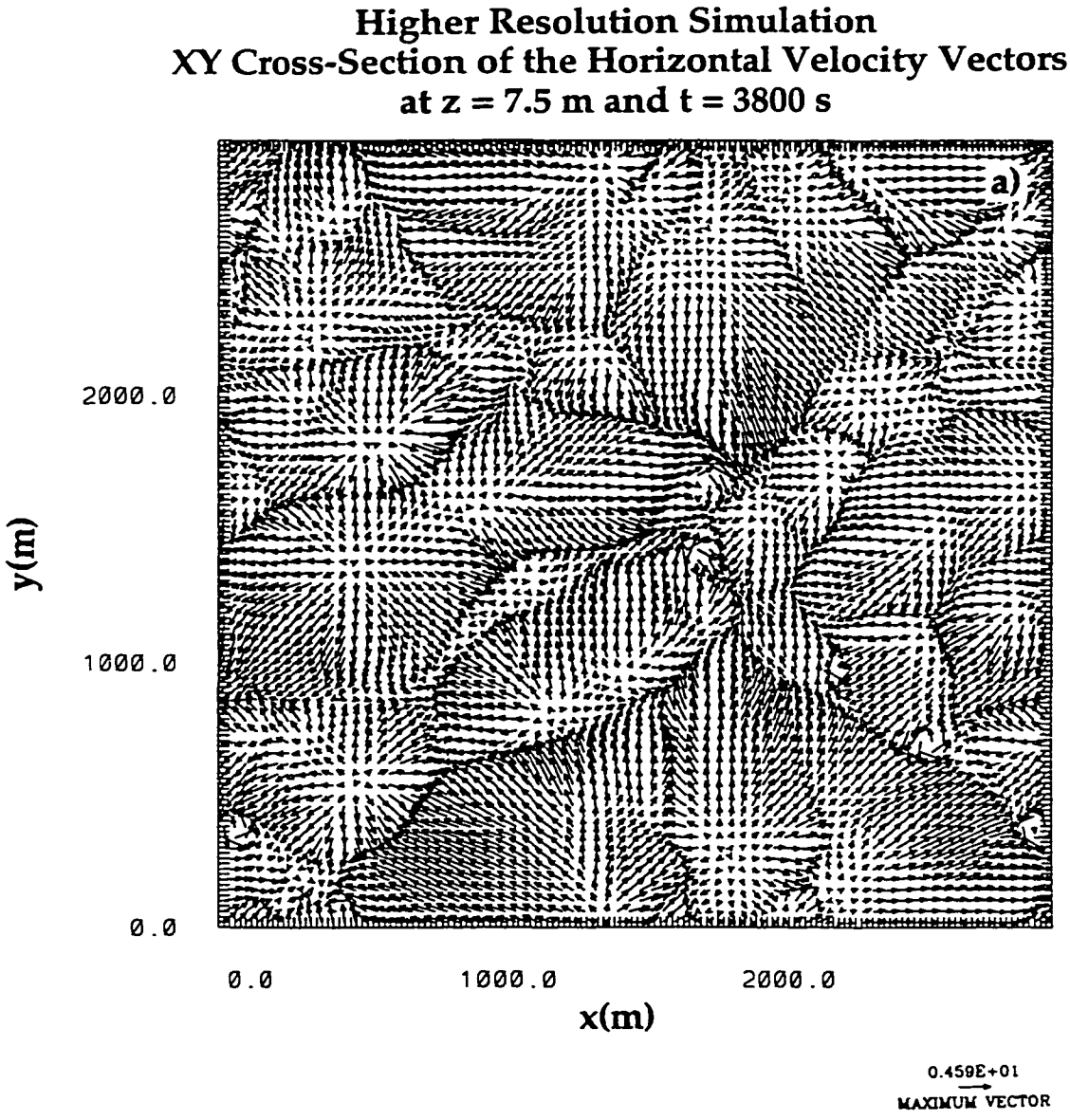

Fig. 3.20. (a) X-Y Cross-sections of horizontal velocity vectors at z = 7.5 m and t = 3800 s. Maximum vector length is 4.59 m s^{-1}.

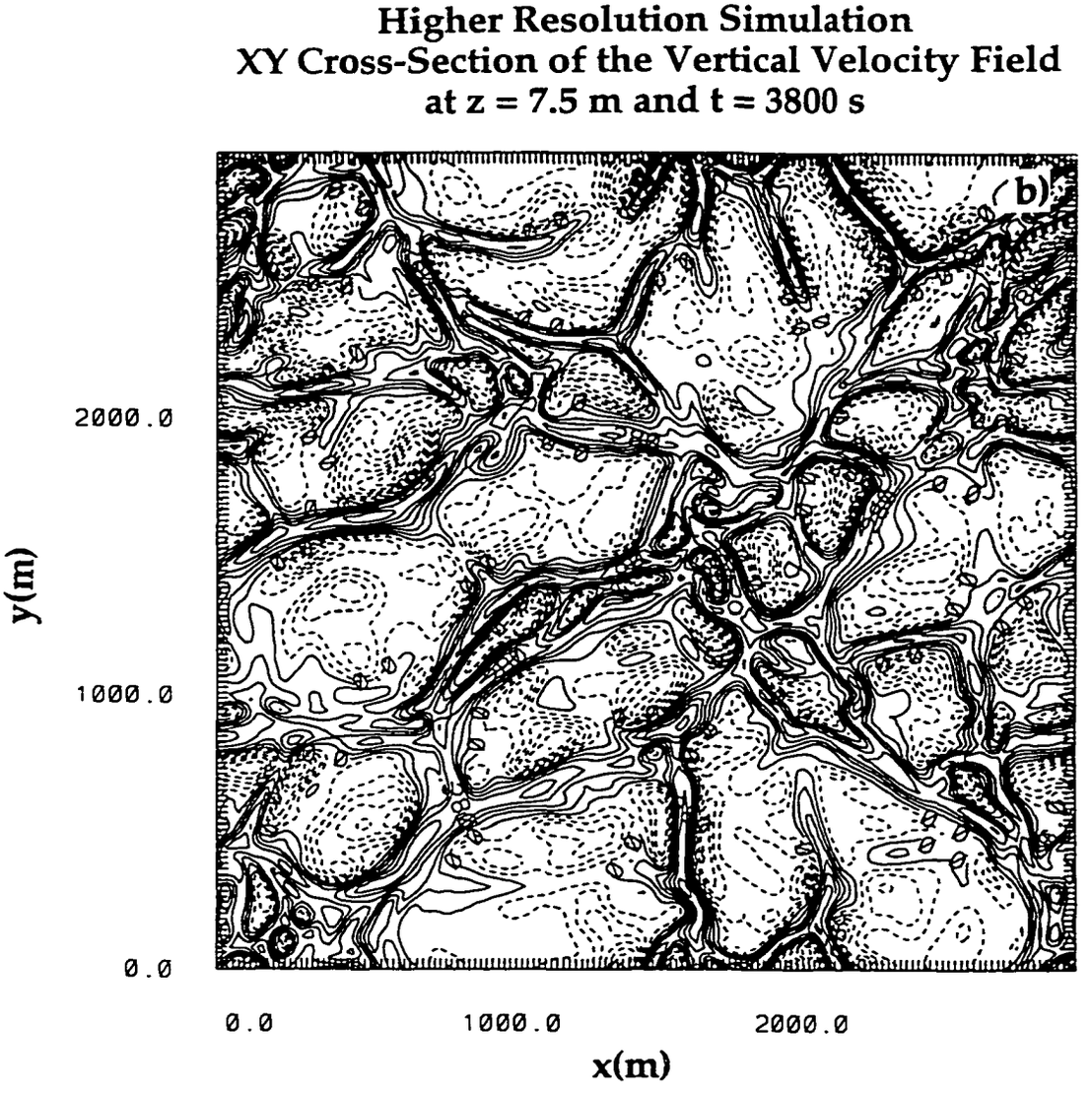

Fig. 3.20. (continued). (b) X-Y Cross-section of the vertical velocity at z = 7.5 m and t = 3800 s. Contours from -0.63 to 0.49 with interval 0.07 m s^{-1}.

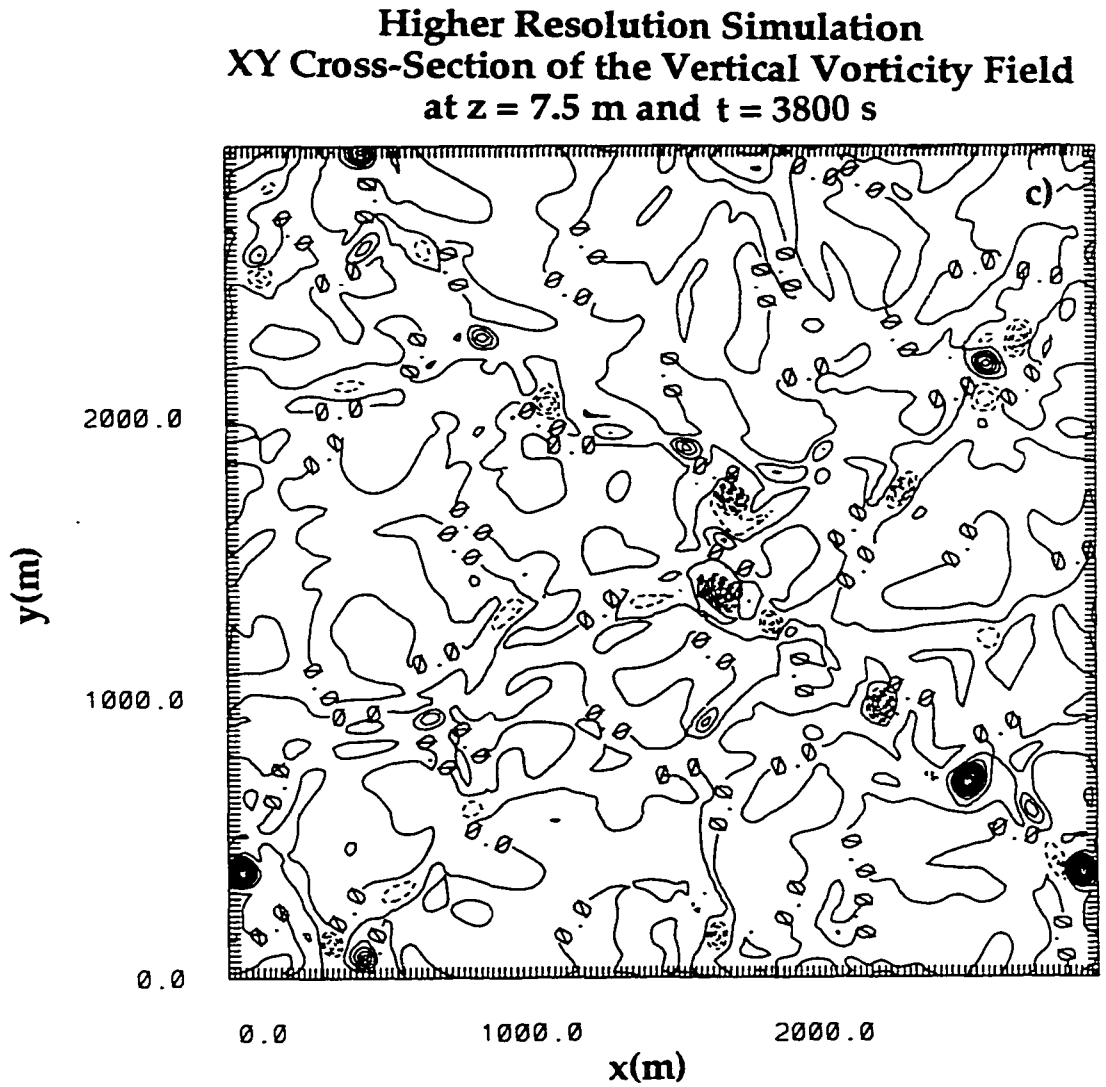

Fig. 3.20. (continued). (c) X-Y Cross-section of the vertical vorticity at z = 7.5 m and t = 3800 s. Contours from -0.2 to 0.24 by 0.02 s^{-1}.

vectors (Fig. 3.20 a), the vertical velocity field (Fig. 3.20 b), and the vertical vorticity field (Fig. 3.20 c) at a time when there are many vortices occurring. The vortices are approximately in a line, although of different senses of rotation (Fig. 3.20 c). Barcilon and Drazin (1972) report that dust devils have been observed to occur in lines, but that all these had the same sense of rotation. In Fig. 3.20 a, adjacent vortices have the same sense of rotation.

Vortices at two other times have been selected for further examination and are shown in Fig. 3.21 (t = 3200 s) and 3.22 (t = 4200 s). At both times, there are multiple vortices occurring. At t= 3200 s there are three vortices evident in Fig. 3.21 a that are located at approximately x = 1300 m and y = 1350 m. Two are cyclonic and these two are separated by an anticyclonic circulation. Figure 3.21 c, shows that there are two pairs of counter-rotating vorticity centers, but the anticyclonic member of the leftmost pair does not have a closed circulation in Fig. 3.21 a. The fact that vorticity center pairs are evident, even when there is a closed circulation of only one sign of rotation, suggests that the formation process for a single vortex may be preceded by the generation of a vorticity pair. Consequent evolution could then result in the dominance of one sign of vorticity over the other.

Similarly, Fig. 3.22 a shows a stronger vortex circulation (at about x= 2000 m and y = 1490 m) with an attendant vortex having the same sense of rotation. From Fig. 3.22 c, it is evident that these two anti-cyclonic circulations are in fact separated by a small cyclonic vorticity center that is not apparent in Fig. 3.22 a. The northernmost vortex has a maximum tangential velocity of 5.1 m s^{-1}. Both circulations are entirely embedded in the updraft region. From Fig. 3.22 b, it appears as if there is a "wrapping in" of the downdraft region to the west of the

circulation. This has qualitative similarities to the tornado vortex which is associated with the wrapping in of the "dry slot". The association of deformation of the updraft ring regions with the presence of a vortex is evident in both SIM1 and SIM2. .

X-Z Cross-sections of vortices at time t = 3200 s (t = 4200 s) and y = 1350 m (y = 1490 m) are shown in Fig. 3.23 (Fig. 3.24). The vertical coordinate is expanded by a factor of two for clarity. The two vortex pairs are clearly evident from Fig. 3.23 e. These are associated with warm (Fig. 3.23 a) low pressure (Fig. 3. 23 b) updrafts (Fig. 3.23 c). The updraft is highest over the region where the low-level vortices are occurring. The eddy mixing coefficient (Fig. 3.23 d) indicates that the boundary layer height may be elevated in the region at which the vortex near the surface is occurring. However, due to the proximity of the upper boundary of the model, the solutions there may be affected by the boundary condition and should be interpreted with caution. Note also that there are several mid-boundary layer vortices that do not extend to the surface (Fig. 3.23 e). Figure 3.23 f shows the vorticity vectors in the X-Z plane. The two cyclonic vortices are distinguished by the upward directed vorticity vectors over a depth of about 300 m.

At t = 4200 s the XZ cross-sections again show a warm (Fig 3.24 a), low-pressure (Fig. 3.24 b) updraft (Fig. 3.24 c) associated with the circulation. The eddy mixing coefficient (Fig. 3.24 d) does not show as distinct an elevation in boundary layer height in the vicinity of the low-level vortex in this cross-section. Fig. 3.24 e-f shows that the vortex at t = 4200 s is about twice as tall as those at t= 3200 s. This vortex is the strongest of the simulation and is associated with a vorticity value of about 0.23 s^{-1}. It is about 100 m in diameter. There is a slight

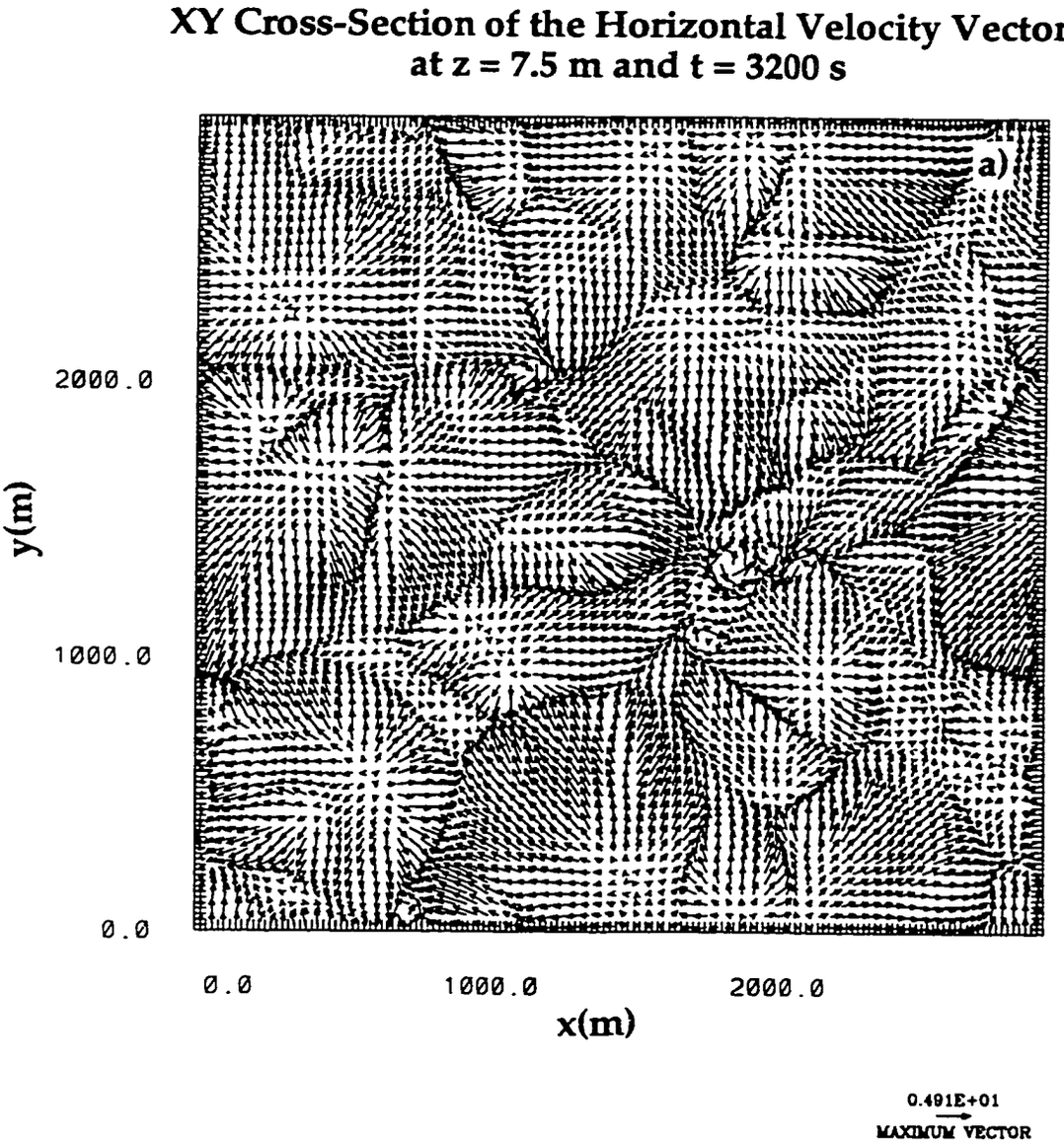

Fig. 3.21. (a) X-Y Cross-sections of horizontal velocity vectors at z = 7.5 m and t = 3200 s. Maximum vector length is 4.91 m s^{-1}.

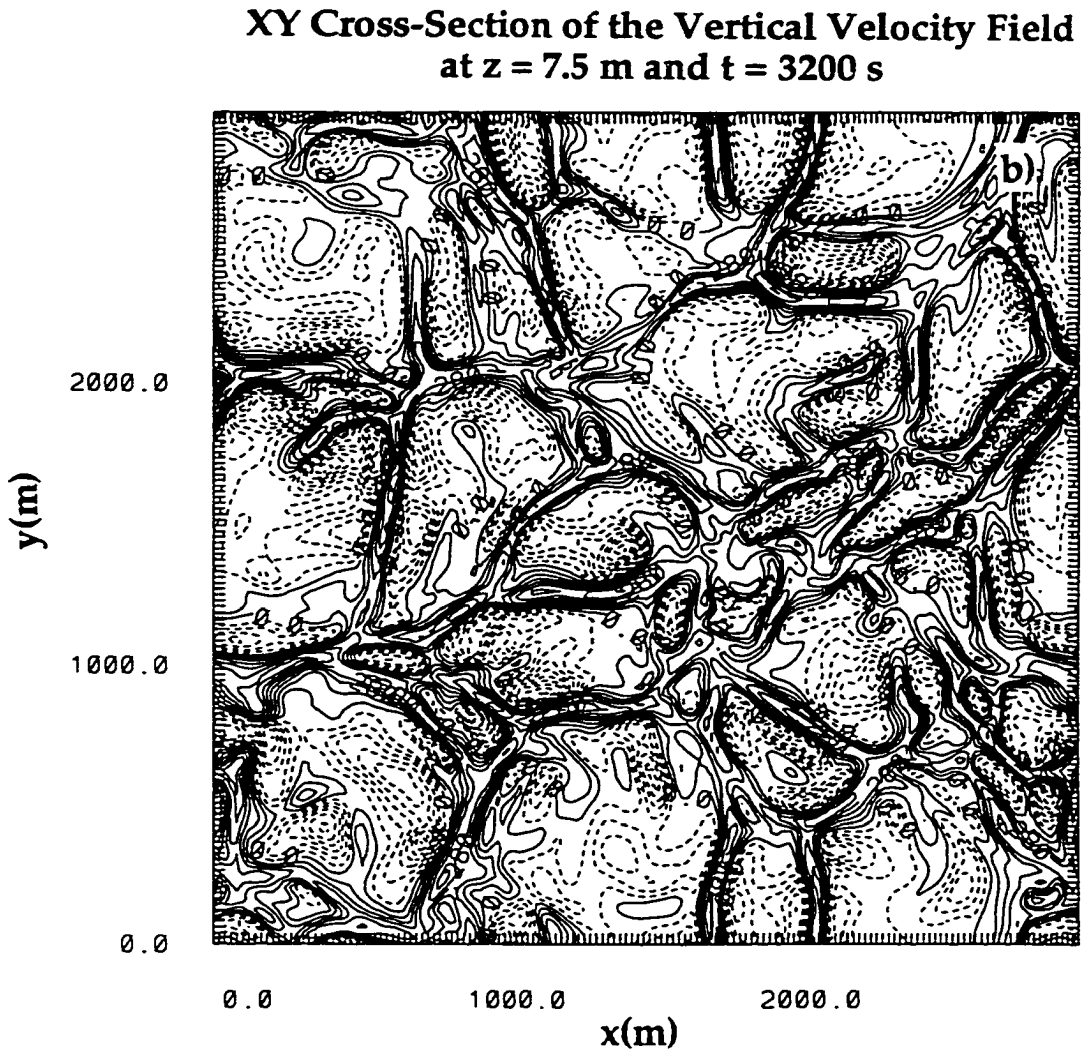

Fig. 3.21. (continued). (b) X-Y Cross-sections of vertical velocity at z = 7.5 m and t = 3200 s. Contours from -0.63 to 0.56 by 0.07 m s^{-1}.

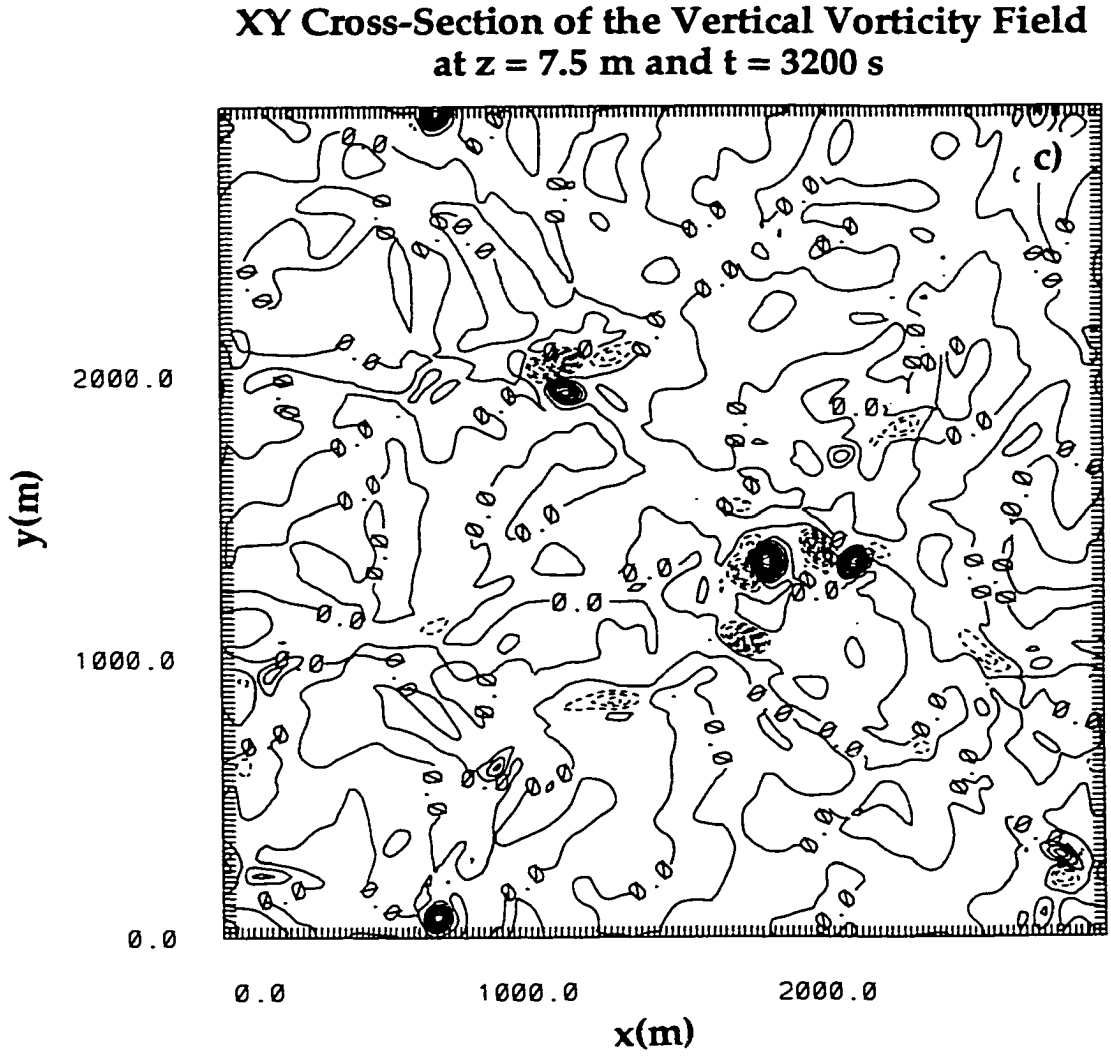

Fig. 3.21. (continued). (c) X-Y Cross-sections of vertical vorticity at z = 7.5 m and t = 3200 s. Contours from -0.14 to 0.2 by 0.02 s^{-1}.

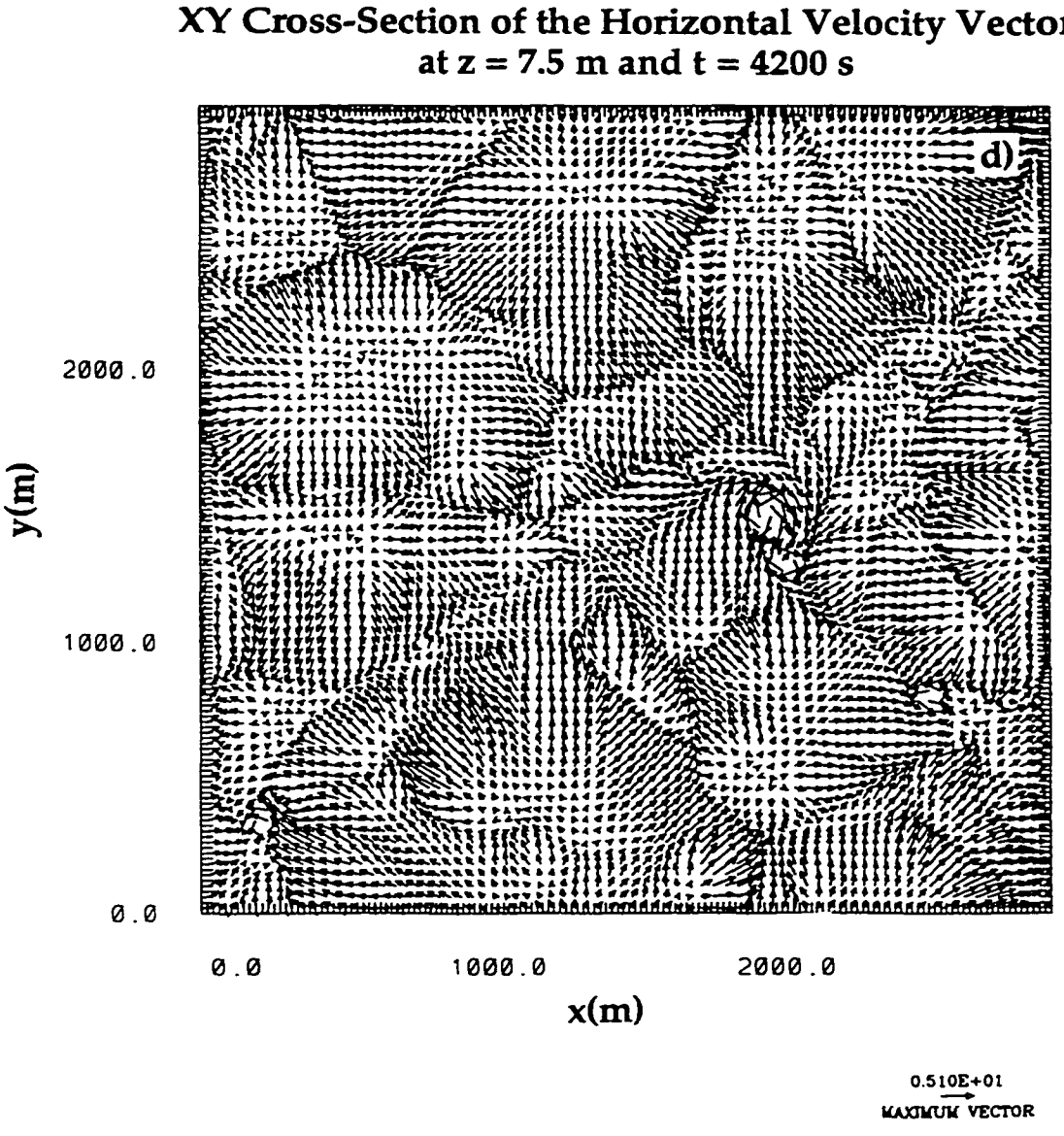

Fig. 3.22. (a) X-Y Cross-sections of horizontal velocity vectors at z = 7.5 m and t = 4200 s. Maximum vector length is 5.1 m s^{-1}.

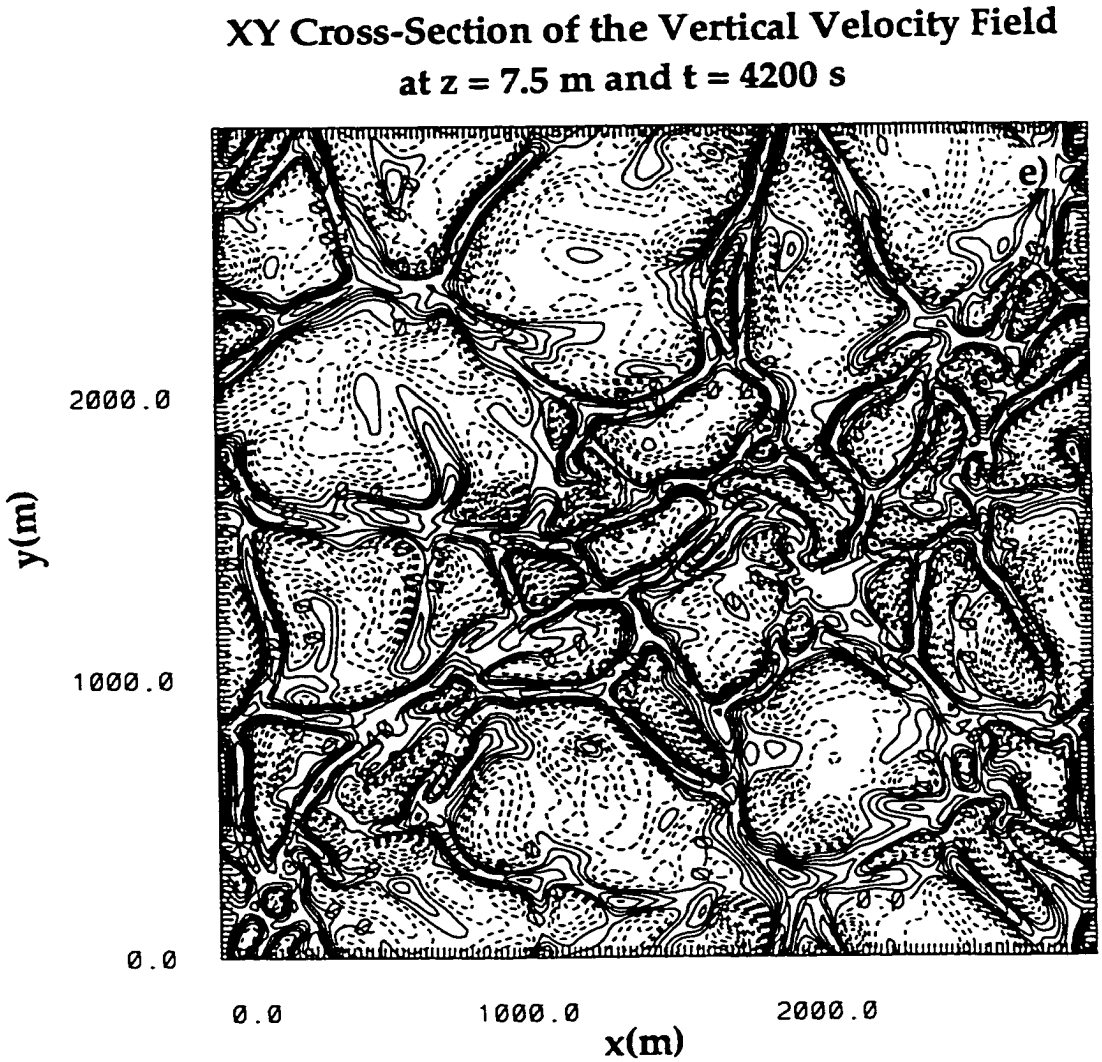

Fig. 3.22. (continued). (b) X-Y Cross-sections of vertical velocity at z = 7.5 m and t = 4200 s. Contours from -0.54 to -0.48 by 0.06 m s^{-1}.

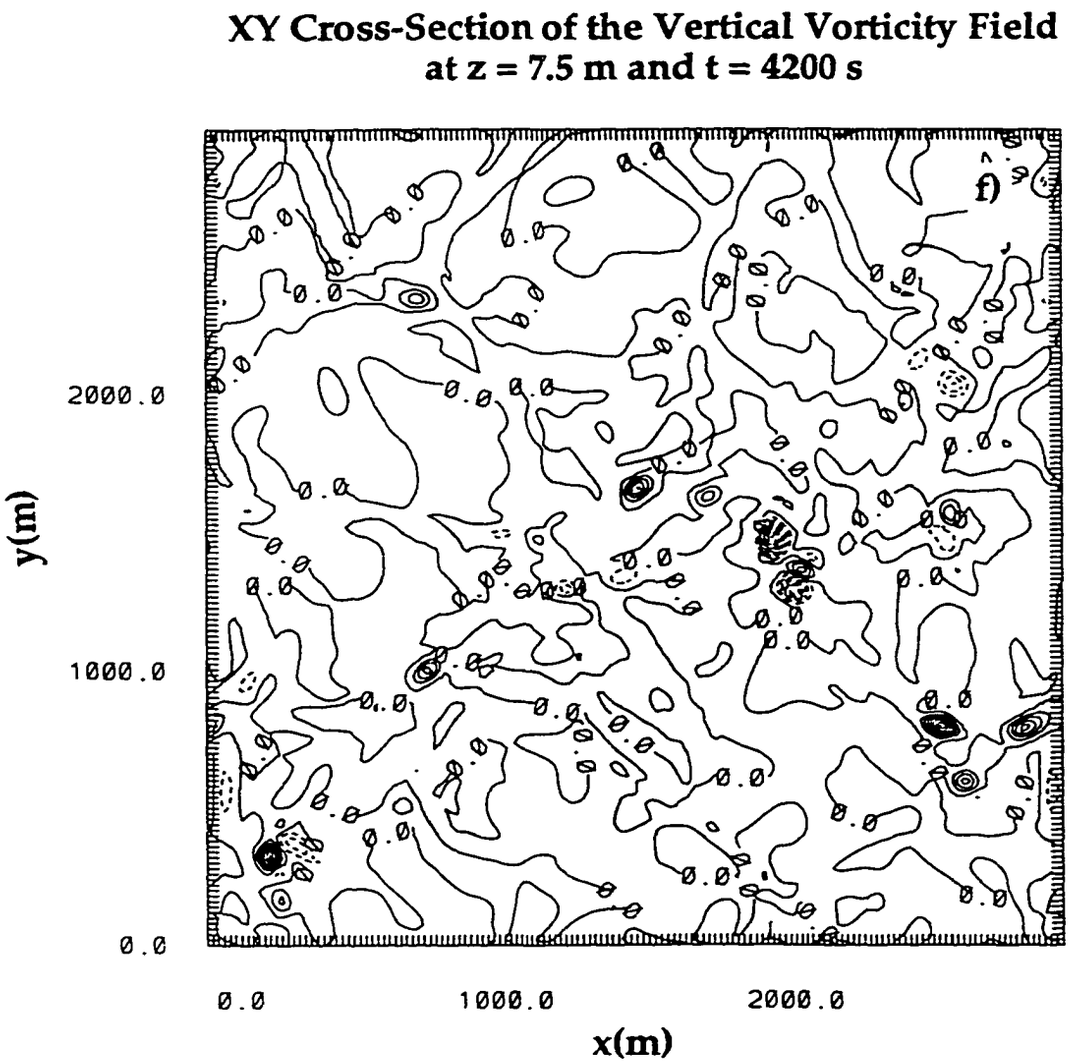

Fig. 3.22. (continued). (c) X-Y Cross-sections of vertical vorticity at z = 7.5 m and t = 4200 s. Contours from -0.27 to -0.21 by 0.03 s^{-1}.

indication that the anticyclonic vortex is surrounded by regions of positive vorticity. Figure 3.24 f clearly shows the downward directed vorticity vectors associated with the vortex.

Overall, the SIM2 resolved smaller-scale features than SIM1 and contained larger values of vorticity extrema. (In comparison, SIM1 maximum vertical vorticity value at t = 4600 s was 0.12 s^{-1}, while SIM2 had maximum vertical vorticity value of –0.29 s^{-1} at t = 4200 s.) The maximum horizontal velocity components however, where not significantly increased in SIM2. (e.g., SIM1 had total simulation horizontal velocity maximum of ~4.7 m s^{-1}, while SIM2 had total simulation horizontal velocity maximum of 5.33 m s^{-1}.) However, there were more vortices at a given time in SIM2 than in SIM1. If this trend continues for increasing resolution, it is possible that there may be a significant number of vortices resolvable for very high resolution. If so, it might be plausible that vertical vortices would have a even greater and more observable influence on the evolution of the simulated convective boundary layer.

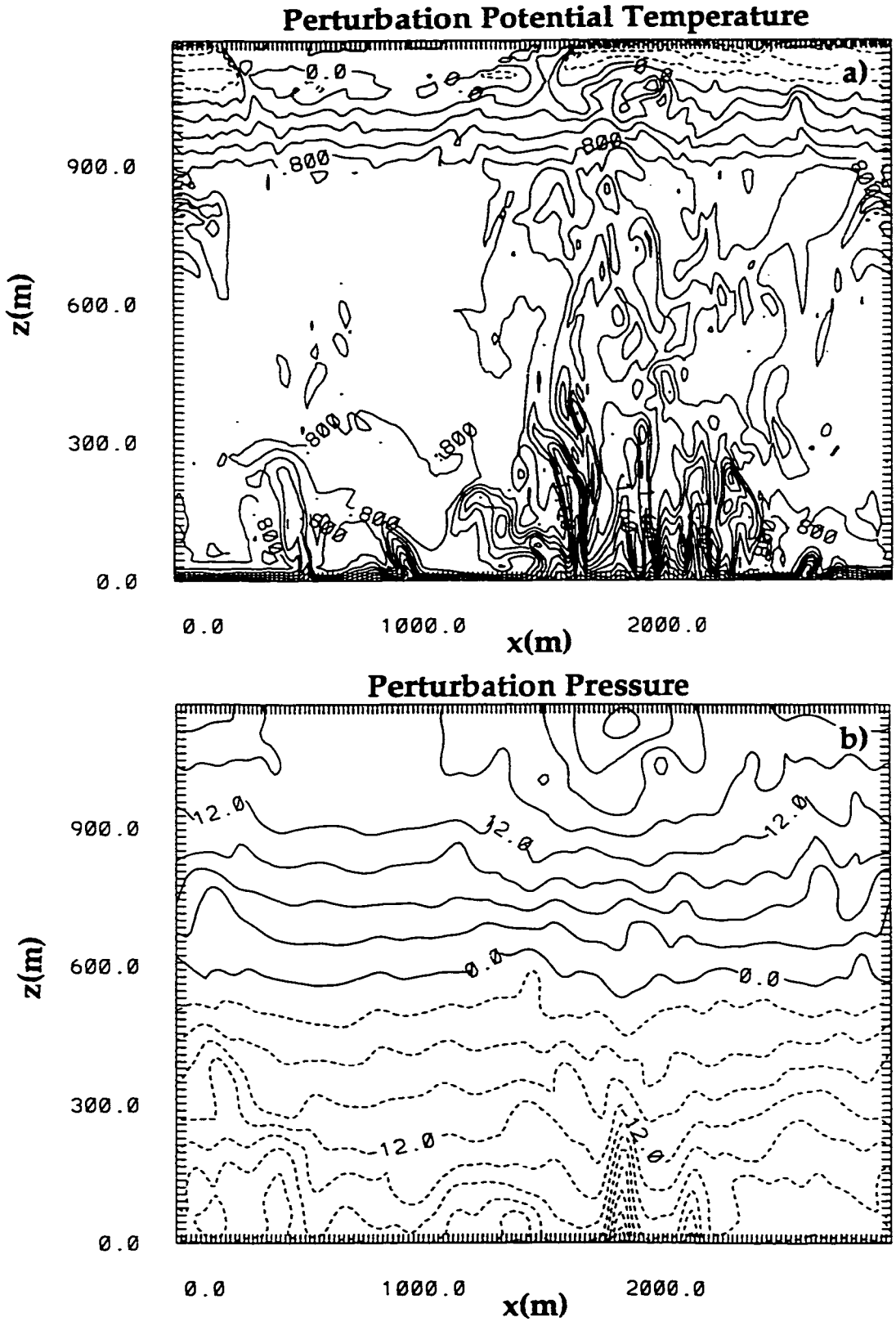

Fig. 3.23. X-Z Cross-sections at y = 1350 m at t = 3200 s. (a) Potential temperature with contours from –0.8 to 3.0 by 0.2 K. (b) Perturbation pressure with contours from -36.00 to 24.0 by 3.0 Pa.

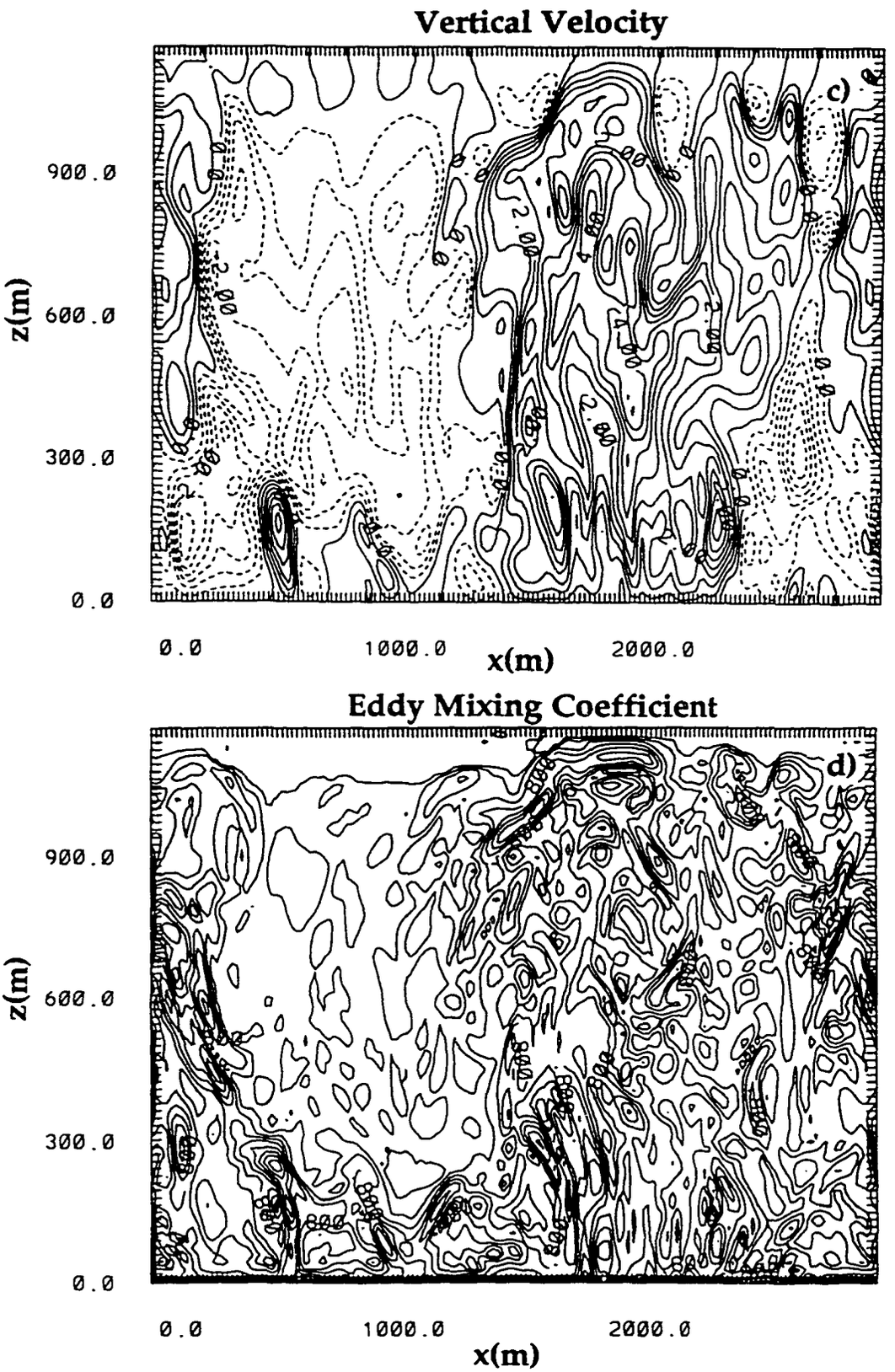

Fig. 3.23. (continued). X-Z Cross-sections at y = 1350 m at t = 3200 s. (c) Vertical velocity with contours from -3.0 to 4.5 by 0.5 m s^{-1}. (d) Eddy mixing coefficient, Km. Contours from 0.0 to 4.2 by 0.2 m^2 s^{-1}.

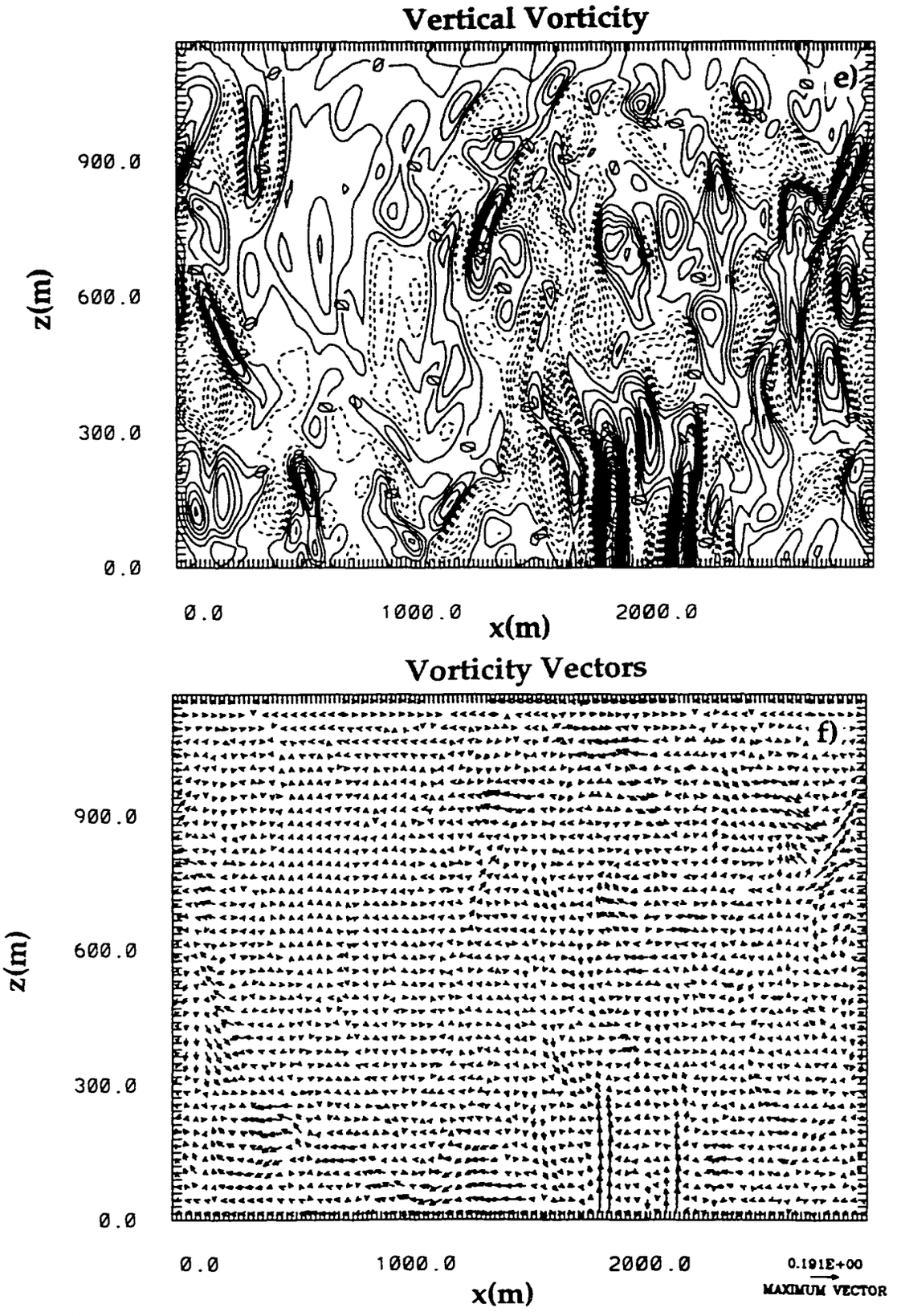

Fig. 3.23. (continued). X-Z Cross-sections at y = 1350 m at t = 3200 s. (e) Vertical vorticity with contours from -0.08 to 0.2 by 0.01 s^{-1}. Labels scaled by 1000. (f) Vorticity vectors. Maximum vector length is 0.191 s^{-1}.

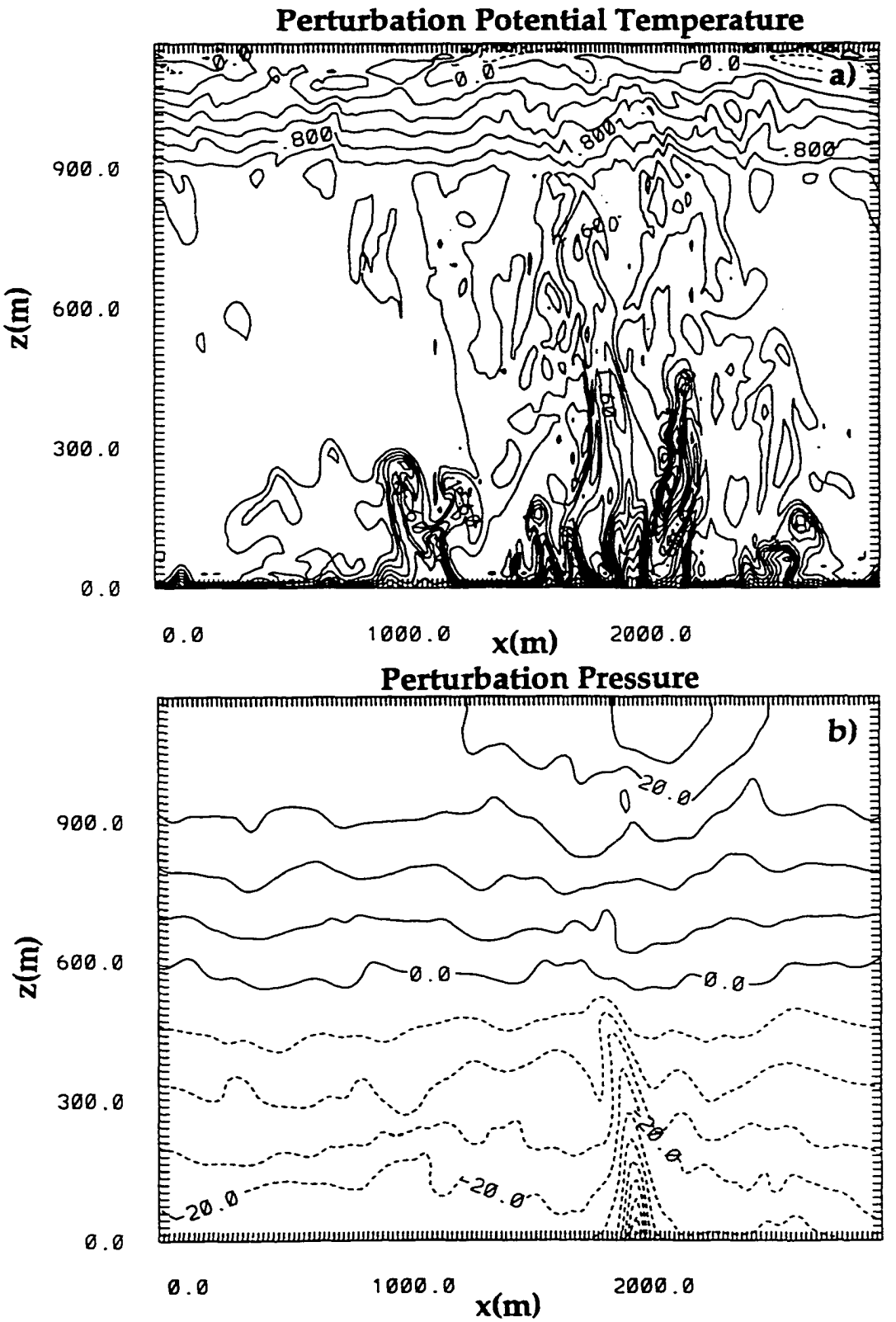

Fig. 3.24. X-Z Cross-sections at y = 1490 m at t = 4200 s. (a) Potential temperature with contours from –0.4 to 3.4 by 0.2 K. (b) Perturbation pressure with contours from -55.00 to 25.0 by 5.0 Pa.

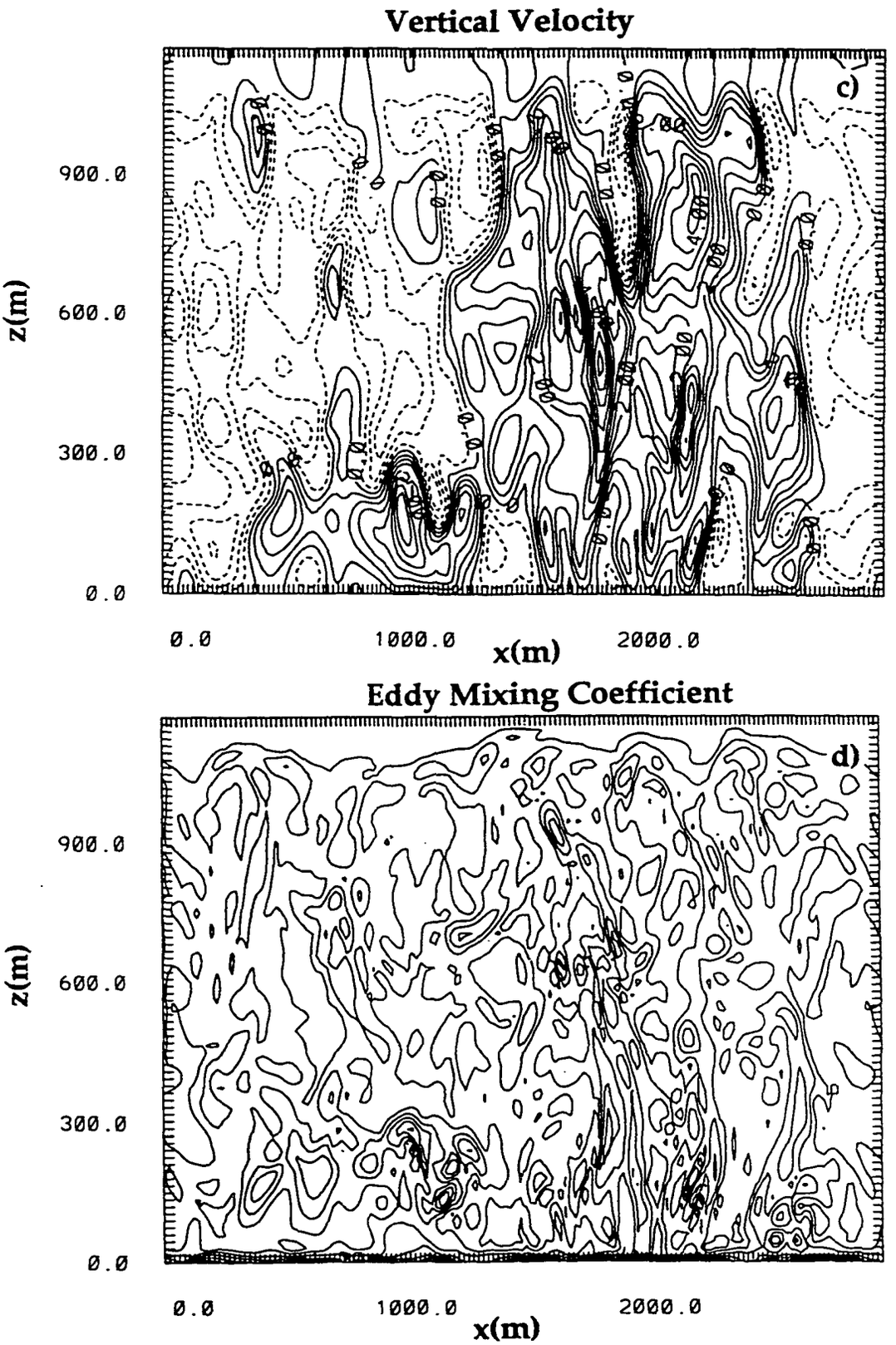

Fig. 3.24. (continued). X-Z Cross-sections at y = 1490 m at t = 4200 s. (c) Vertical velocity with contours from –2.5 to 5.5 by 0.5 m s^{-1}. (d) Eddy mixing coefficient, Km. Contours from 0.0 to 5.1 by 0.3 m^2 s^{-1}.

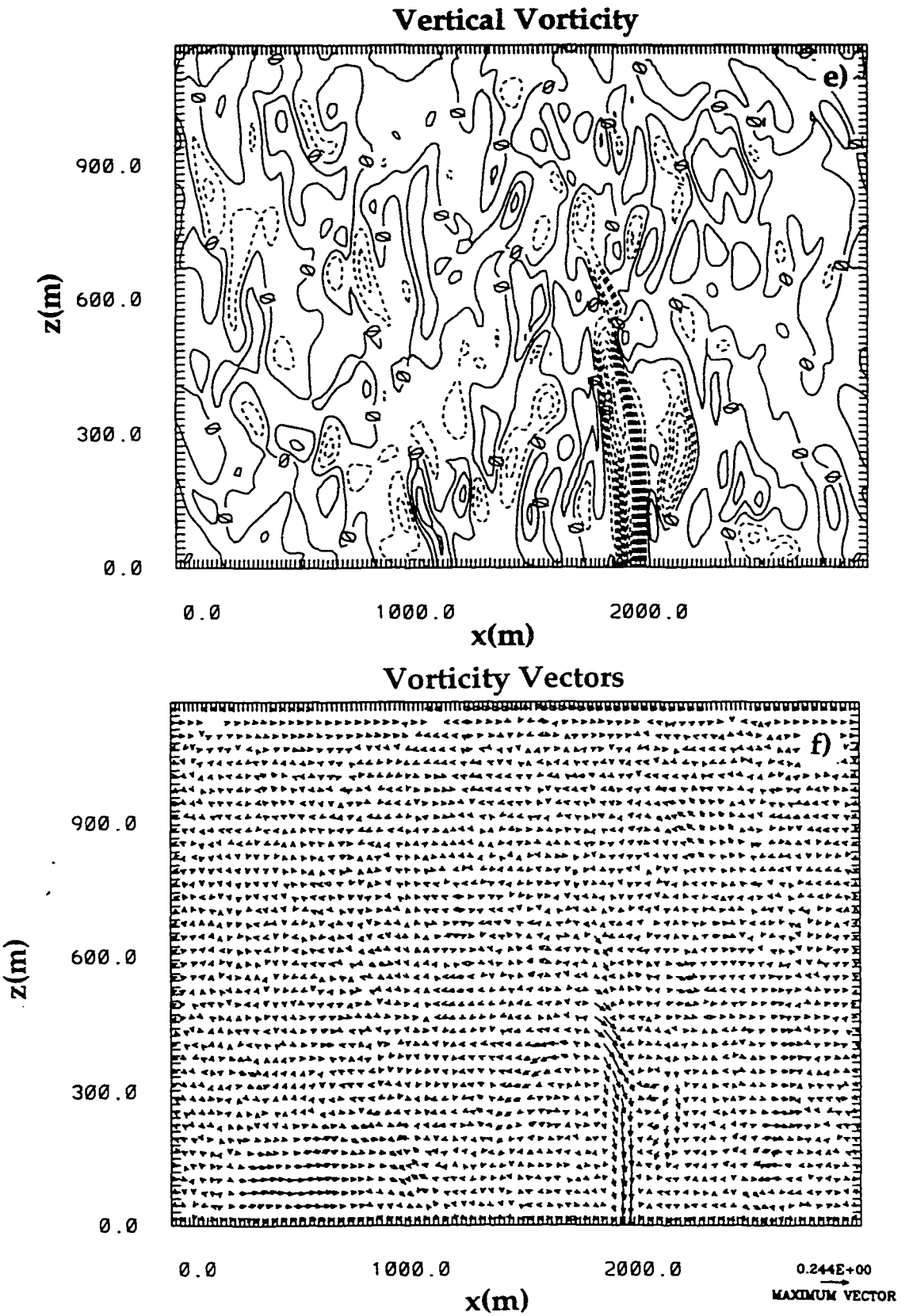

Fig. 3.24. (continued). X-Z Cross-sections at y = 1490 m at t = 4200 s. (e) Vertical vorticity with contours from -0.28 to 0.04 by 0.02 s^{-1}. Labels scaled by 1000. (f) Vorticity vectors. Maximum vector length is 0.244 s^{-1}.

3.5 Discussion – Possible sources of vorticity

After studying several other vortices that occurred in the simulations, and the evolution of the variable fields at times prior to their maximum intensity, the following conjectures with regard to formation processes have been developed.

Figure 3.25 shows a schematic diagram of the first proposed mechanism. Figure 3.25 a (b) shows a three-dimensional (two-dimensional, horizontal plane) schematic of the intersection region of the convective rings. A likely source of vorticity for these vortices, which occur in the absence of mean winds, is the larger convective cell circulations. These circulations create azimuthal horizontal vorticity rings (a portion of which is represented by the dashed line in Fig. 3.25 a) that are strongest near the updraft/downdraft intersections (where gradients of vertical velocity are largest). The vortex rings may be advected by the inflow toward the updraft regions. If the flow is stronger on one side of the updraft ring, the vortex line on that side may be advected into the middle of the updraft region (Fig. 3.25 b). There are often local updraft maxima at the vertices of the rings. These local vertical velocity maxima could tilt the vortex line and result in the formation of a vortex pair (Fig. 3.25 b) which would be embedded in the updraft region. A subsequent mechanism may lead to a vorticity center of either sign becoming co-located with the updraft maximum. The mechanism could be similar in concept to the supercell mechanism (Fig. 3.1) that explains the propagation of an updraft toward a vortex center.

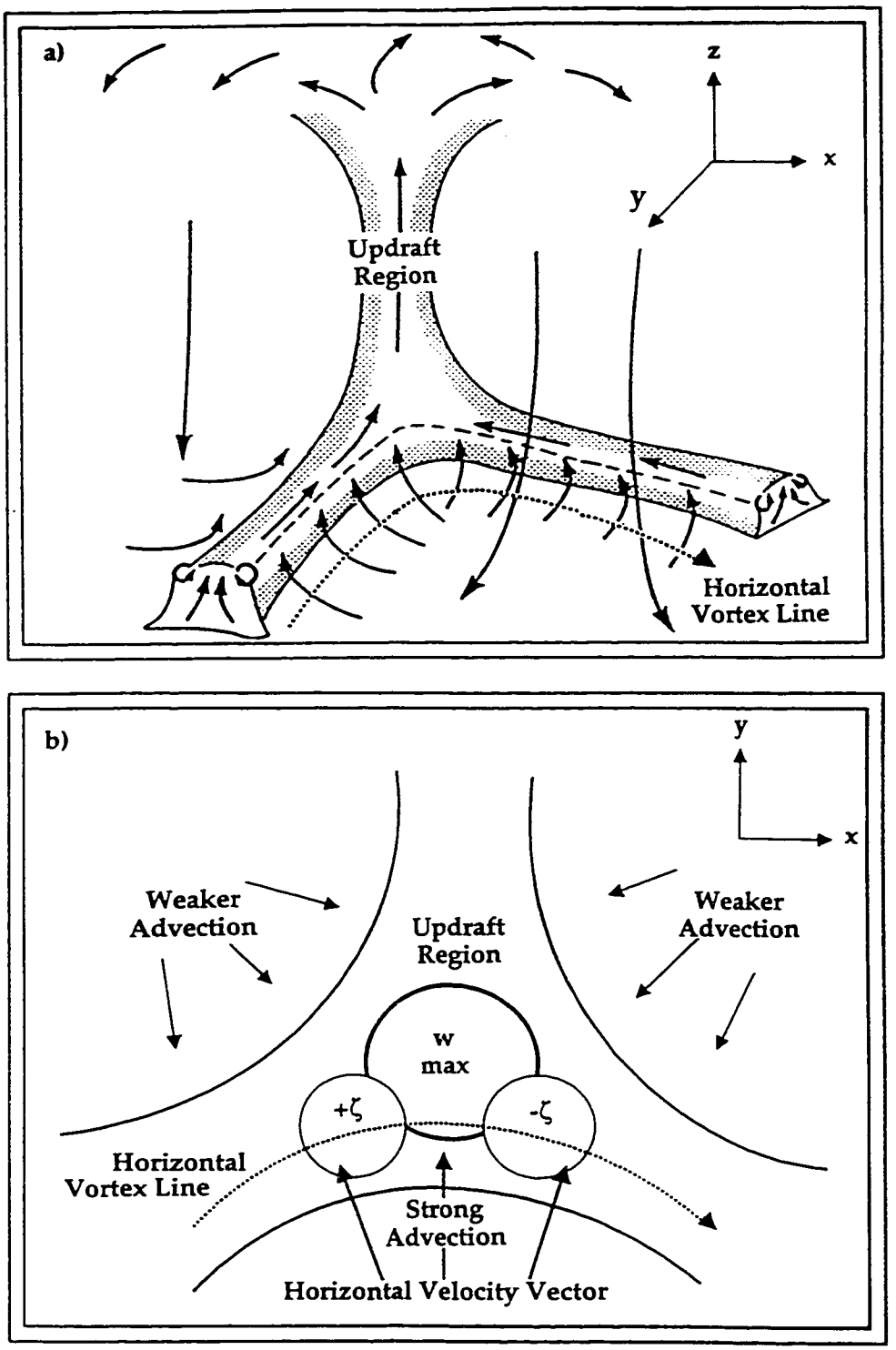

Fig. 3.25. Schematic diagram of the *first* proposed mechanism for the source of vertical vorticity for vertical vortices in pure convection. a) Three-dimensional schematic of a vertex (intersection region) of the polygonal convective rings. b) Two-dimensional, horizontal plane schematic of a vertex (intersection region) of the polygonal convective rings.

Some support for this mechanism can be seen by comparing Fig. 321 b and Fig. 3.21 c, where the largest valued vorticity centers lie entirely within the updraft ring regions. This feature is further demonstrated in Fig. 3.26 where the vertical vorticity pattern (Fig. 3.26 a) outlines the vertical velocity pattern (Fig. 3.26 b) and the local maxima of vertical vorticity lie at the vertices of the convective rings. This may be somewhat misleading however, since the values of vertical vorticity will obviously be largest in regions where vertical velocity is largest due to stretching. An attempt was made to adjust the contour interval of the vertical vorticity in order to discern a coherent pattern that might not lie along the convective ring branches, but no such pattern was identifiable.

Additional support for the proposed mechanism may be seen in the general pattern of vortex lines with respect to the convective cell pattern and these are shown for two arbitrary times in both SIM1 (Fig.3.27 a, b) and SIM2 (Fig.3.27 c, d). These times were selected because they most clearly illustrate the point. The horizontal vorticity vectors at the lowest level are strongest near the largest horizontal gradient of vertical velocity. They are frequently directed parallel to the updraft branches or rings. These vortex lines could then be advected at these low levels inward to the interior of the updraft branch where they may be tilted by local vertical velocity maxima at the updraft ring intersections.

It was often observed that vortices were preferred at locations where the updraft was separated by small distances. In other words, the angle between updraft branches near the intersection points tended to be small. This would be consistent with the fact that vorticity tilting terms would be strong where gradients in vertical velocity were large, such as in these regions.

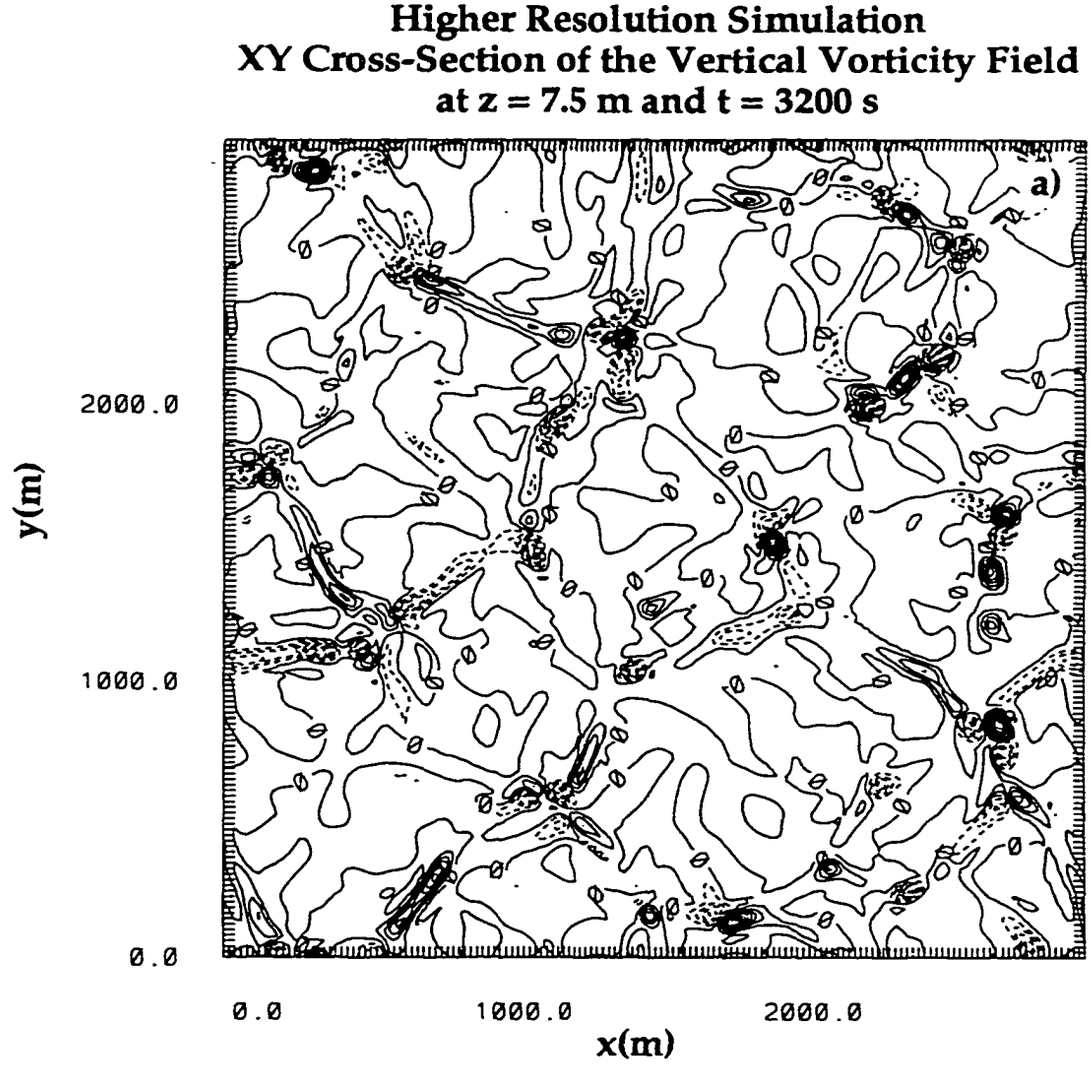

Fig. 3.26. X-Y Cross-sections of (a) vertical vorticity at z = 7.5 m and t = 3200 s. Contours from -0.14 to 0.1 by 0.01 s^{-1}.

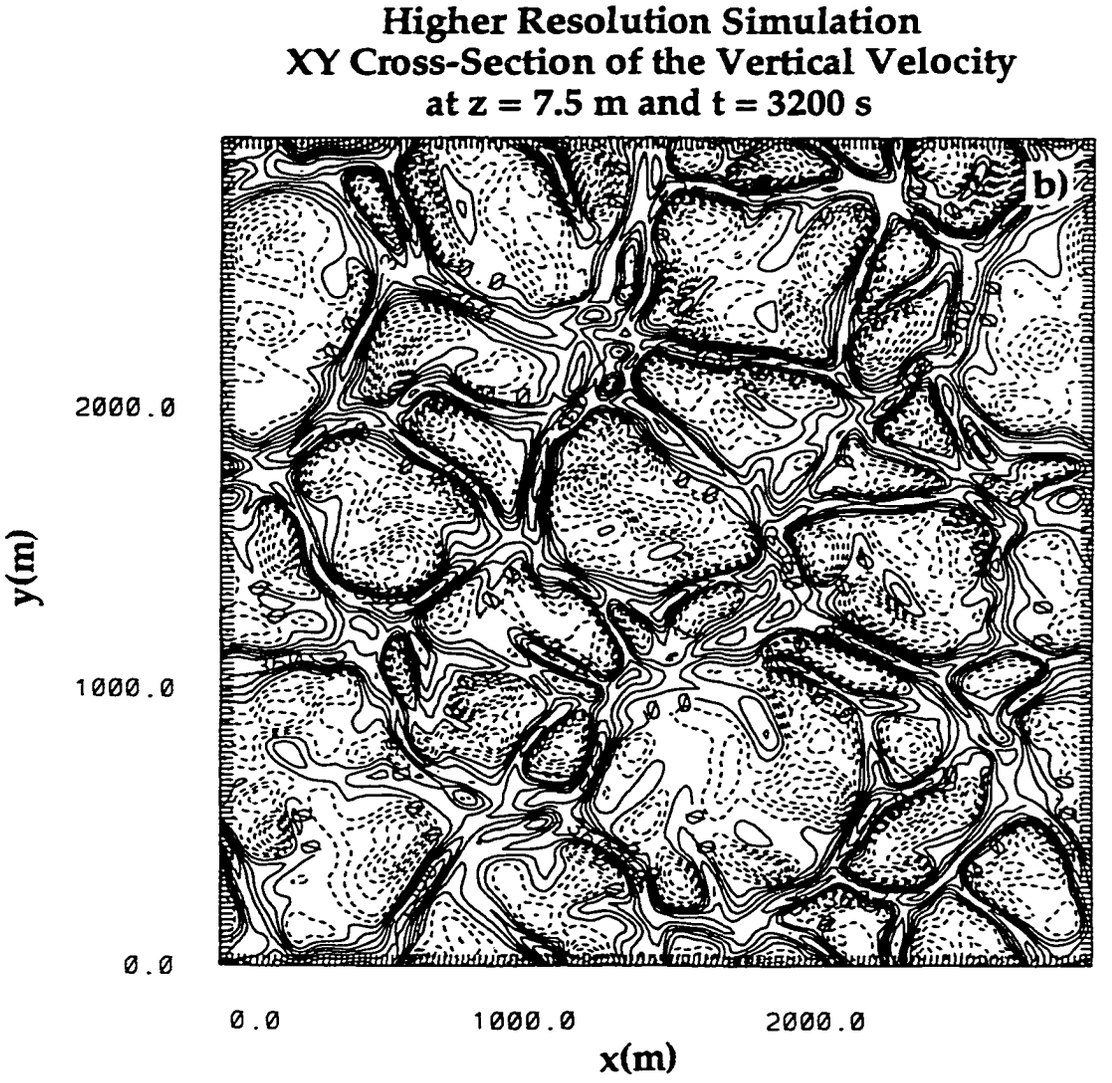

Fig. 3.26. (continued) (b) X-Y Cross-sections of vertical velocity at z = 7.5 m and t = 3200 s. Contours from -0.81 to 0.72 by 0.09 m s^{-1}.

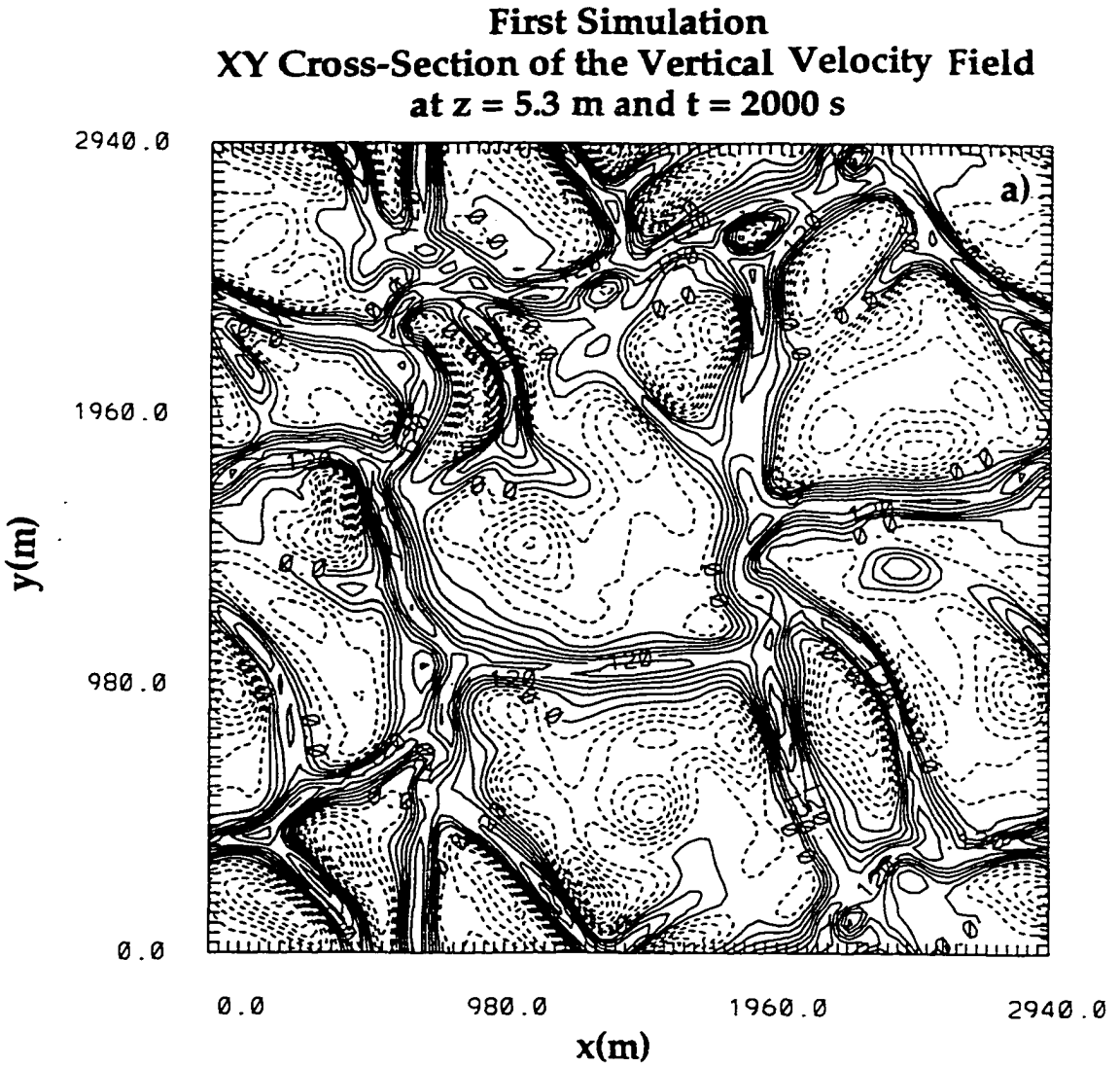

Fig. 3.27. (a) X-Y Cross-sections SIM1 at z = 5.3 m and t = 2000 s, vertical velocity, contours from –0.27 to 0.24 by 0.03 m s^{-1}.

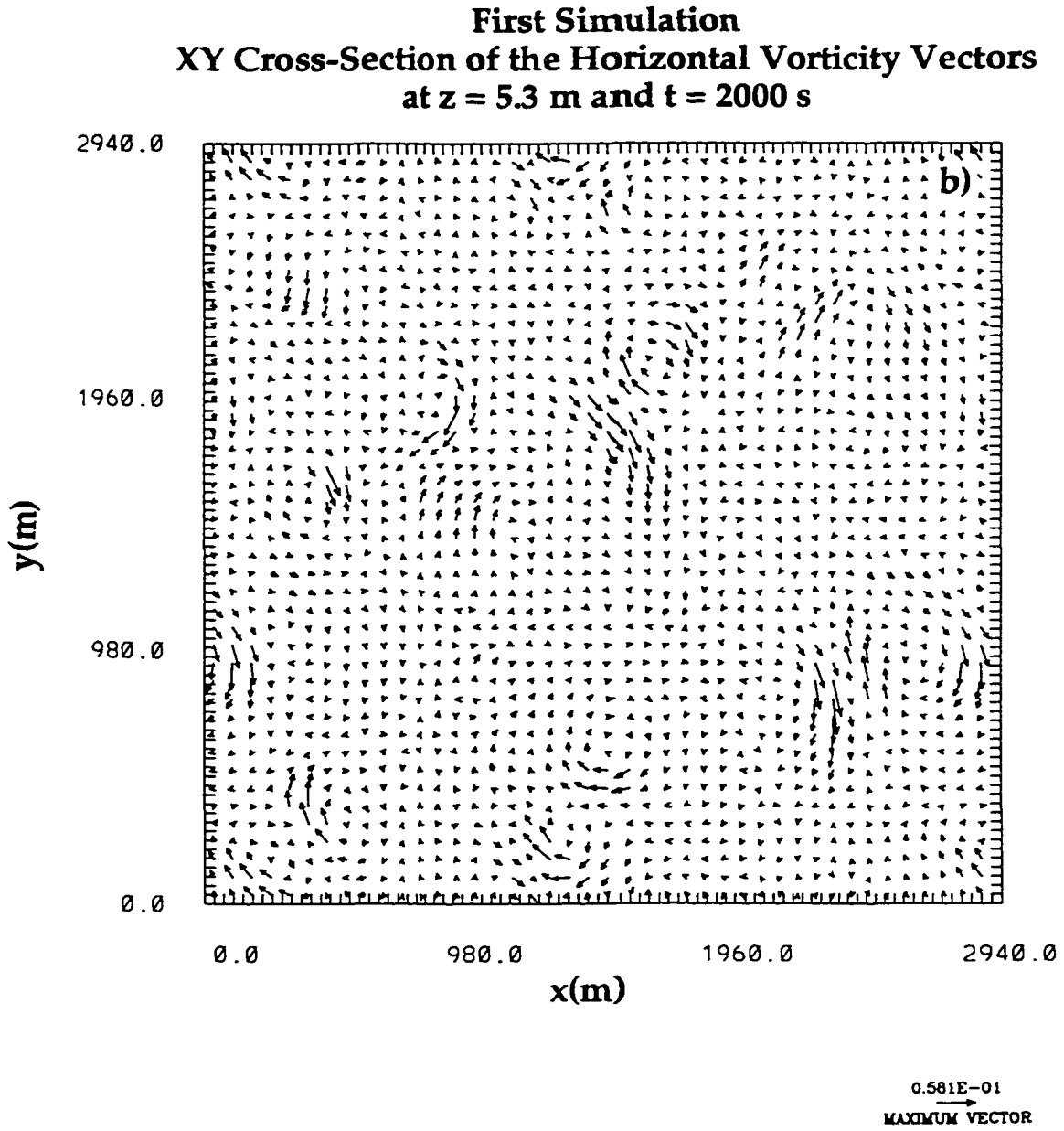

Fig. 3.27. (continued) (b) X-Y SIM1 Cross-sections of horizontal vorticity vectors at z = 5.3 m and t = 2000 s, maximum vector length .058 s^{-1}.

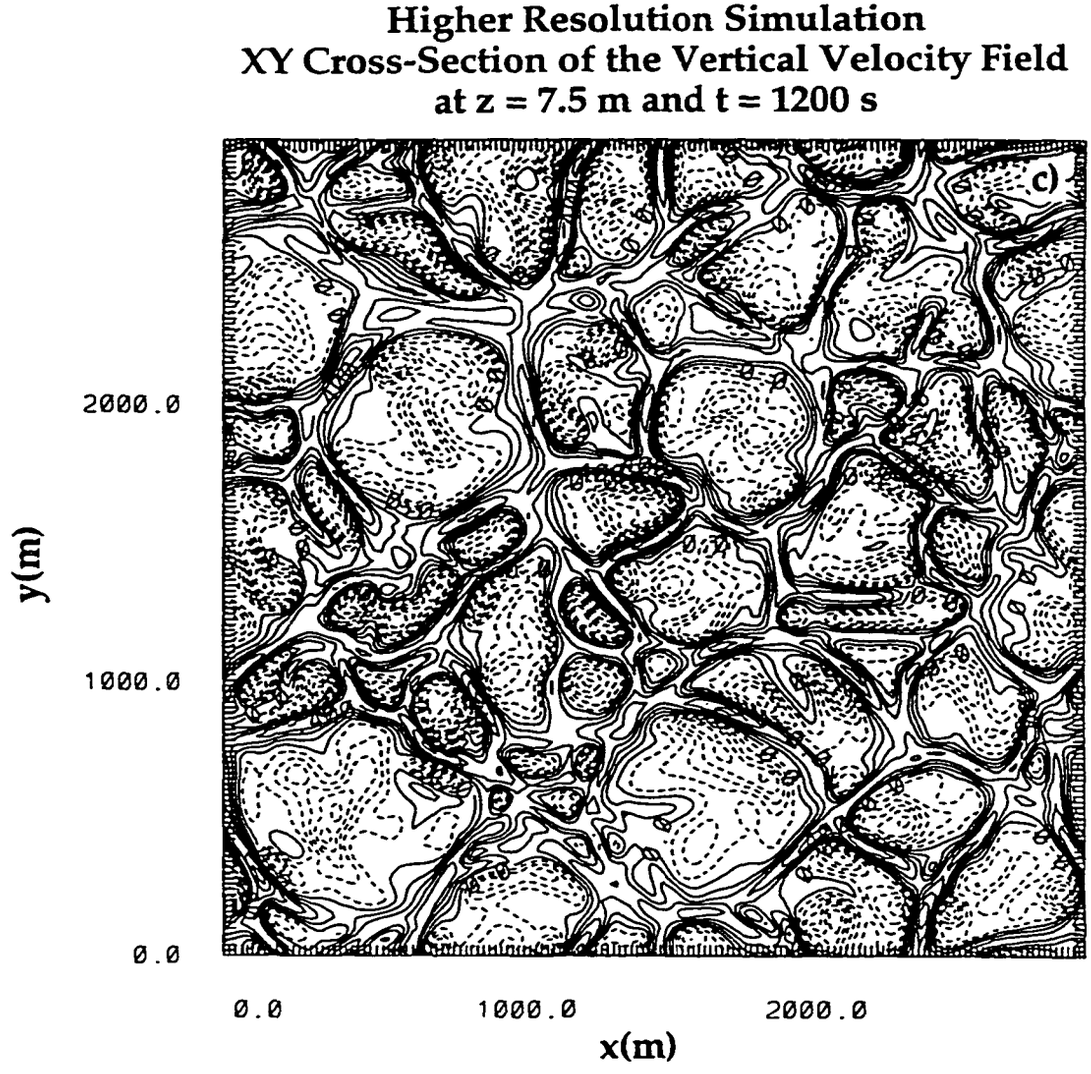

Fig. 3.27. (continued) (c) X-Y SIM2 Cross-sections of vertical velocity at z = 7.5 m and t = 1200s. Contours from –0.9 to 0.7 by 0.1 m s^{-1}.

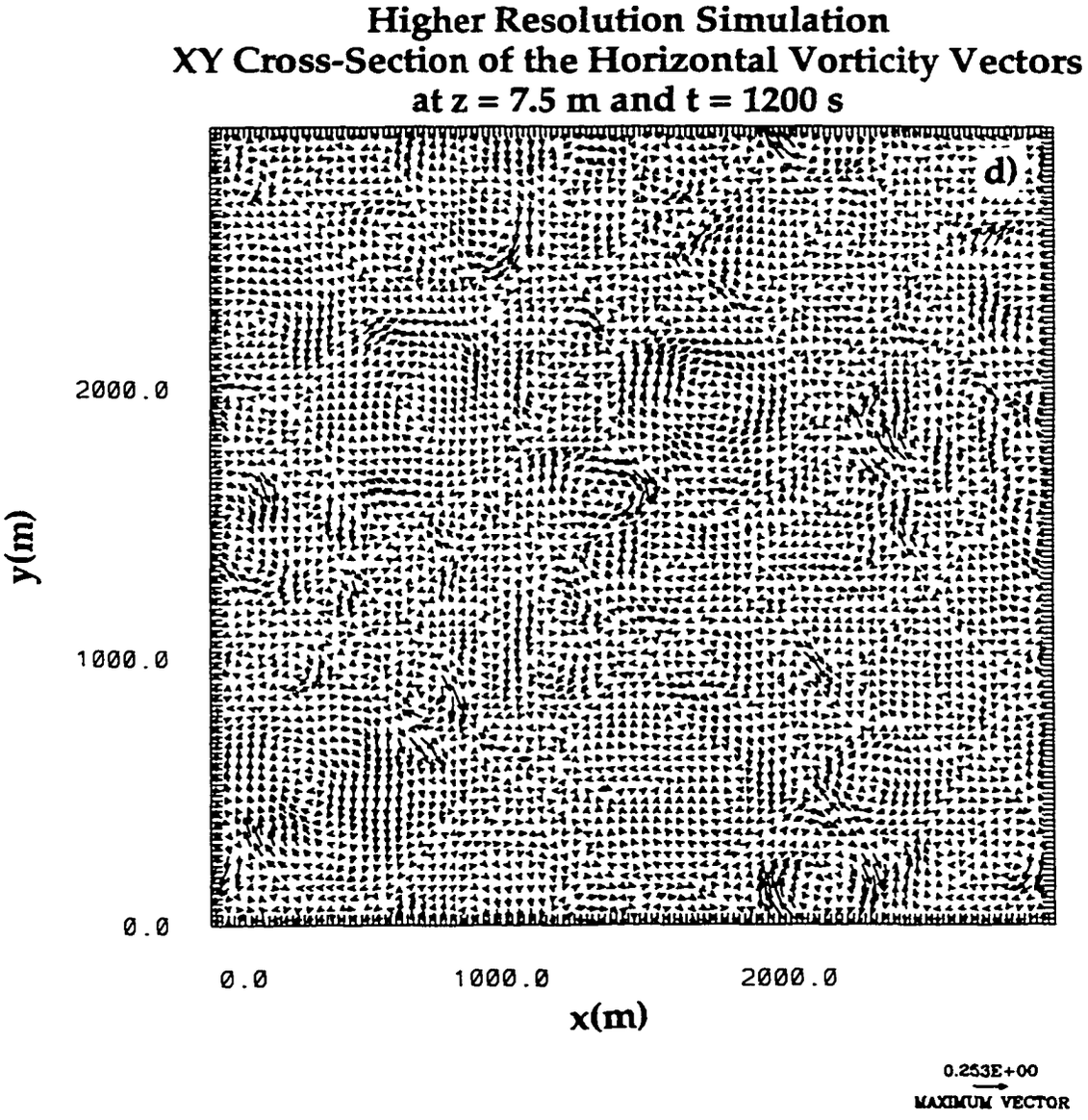

Fig. 3.27. (continued) (d) X-Y SIM2 Cross-sections of horizontal vorticity vectors at z = 7.5 m and t = 1200 s, maximum vector length .0253 s^{-1}.

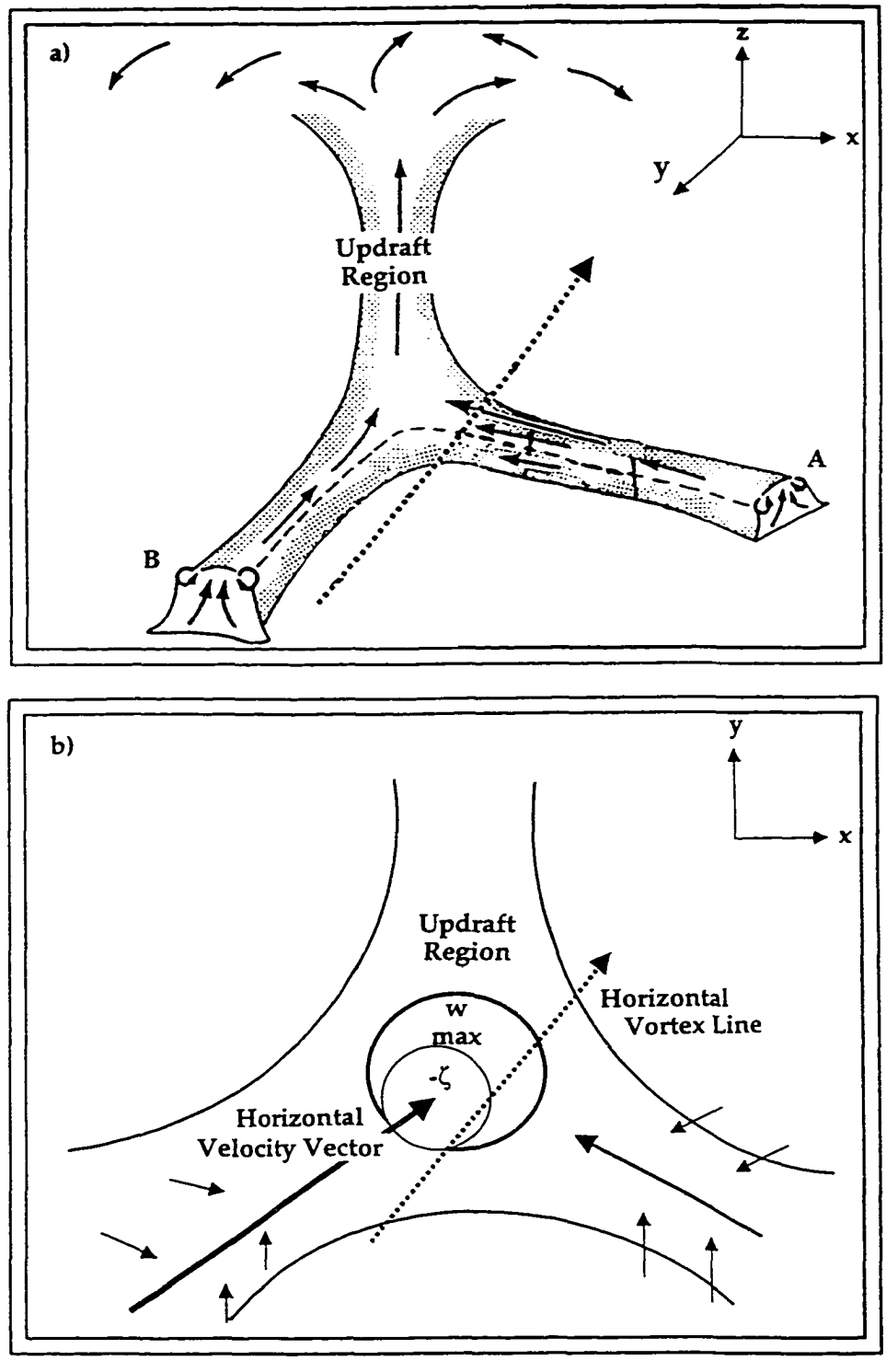

Fig. 3.28. Schematic diagram of the *second* proposed mechanism for the source of vertical vorticity for vertical vortices in pure convection. a) Three-dimensional schematic of a vertex (intersection region) of the polygonal convective rings. b) Two-dimensional, horizontal plane schematic of a vertex (intersection region) of the polygonal convective rings.

A second possible conjecture for vertical vortex formation that might reflect this dependence on angle is shown in Fig. 3.28. In this case, vertical shear of horizontal winds in one branch, denoted A (Fig. 3.28 a), would be associated with horizontal vorticity in the y-direction. Winds, flowing along and toward the updraft maximum at the intersection point from the south (updraft branch B), would then contain a streamwise component of vorticity. When tilted by the updraft, the vorticity would be immediately co-located with the vertical velocity local maximum and the updraft would acquire cyclonic rotation (Fig. 3.28 b). Future work will include more analysis to evaluate the plausibility of these and other conjectured mechanisms for vertical vortex formation in the convective boundary layer.

3.6 Summary

Large Eddy Simulations (LES's) of the convective boundary layer were carried out for the purpose of examining vertical vortex formation. In particular, a simulation (SIM1) having 35 m horizontal resolution and a simulation (SIM2) having 20 m horizontal resolution were performed.

The simulated open convective cells exhibit a cell broadening behavior with time that has been documented in prior studies of turbulent convection. It is suspected that a mechanism similar to the "updraft merger" process described by Shapiro and Kogan (1994) occurs in the current simulations. In the case of Shapiro and Kogan, the simulated updrafts were broad and the downdraft region between them was narrow. In our case, the mechanism would be

modified to explain the merger or broadening of downdrafts separated by narrow updraft regions.

The most interesting results show that vertical vortices form at the intersections of convective updraft rings and that these are locations of local maxima in vertical velocity. More vortices are evident above the lowest level. The vortices form in the absence of mean winds or surface inhomogeneities. There is inconclusive evidence that the height of the boundary layer is maximized in regions where vertical vortices exist. The structure of the simulated circulations is consistent with observational data of dust devil circulations.

Some limitations of this study include the fact that the mixing length in the subgrid-scale turbulence parameterization was not modified in the region of the potential temperature inversion. This is likely to have led to the "smearing out" of the temperature gradient in that region. Based on the comparison with the results of Mason (1989), in which mixing length adjustments were employed, it is not believed that this critically influences the processes responsible for the formation of vertical vortices.

Furthermore, as stated previously, the task has been divided into two parts, and this Chapter reports on first part, which includes the simulations designed to examine the suspected larger-convective scale vorticity generating motions. As a result, the strengths of the simulated circulations are not as strong as those observed with most dust devils. In addition, if very small-scale motions, especially in the lowest few meters near the surface, are critical to the generation of vertical vorticity and the subsequent alignment of a vortex center with an updraft, the horizontal and vertical resolution may have been insufficient to

represent vortex formation by these processes. If this is true, a more sophisticated surface flux parameterization may be also be required in higher resolution simulations.

In conclusion, the results of this work: 1) document the existence of these vertical boundary layer vortices; 2) suggest that these vortices may be much more common than prior work has implied; 3) show that vertical vortices can form in the absence of imposed sources of angular momentum, mean winds or surface inhomogeneities; and 4) provide guidance for the design of higher resolution experiments to further investigate boundary layer vertical vortex formation mechanisms.

Chapter 4

Dissertation Summary

This dissertation reports on two semi-independent studies of rotating atmospheric convection.

The first was an analytical investigation of the linear stability and structure of convection embedded in a mean shear flow with a circular hodograph which was performed as a contribution to the classical theory. This can be considered an extension of Asai's work, but with emphasis on the rotational and helicity features of the disturbances. It also examined the relevance of Beltrami flow solutions presented previously by Lilly and Davies-Jones, which could not be directly extended to consider the effects of buoyancy. The Boussinesq equations were applied to neutrally and unstably stratified fluids, with emphasis placed on the inviscid solutions. Upper and lower boundary conditions were free-slip and rigid. Lateral conditions were periodic, which allowed casting the disturbance equations into a horizontally periodic normal mode structure. The growth rates and disturbance forms were generally fairly similar to the results presented by Asai, except that the most unstable modes were nearly always oriented transverse to the shear component at the channel center. The most rapidly growing modes at small Richardson number were found to be highly helical, with the helicity obtained from the Beltrami mean state. The helicity transfer efficiency and disturbance relative helicity decreased rapidly, however, for negative Richardson numbers greater than about one.

The second study consisted of a numerical investigation of the formation mechanisms of vertical vortices in the convective boundary layer. Large Eddy Simulations (LES's) of the convective boundary layer were performed with the purpose of examining vertical vortex formation. The results of the study show that vertical vortices formed readily at the vertices of simulated Rayleigh-Benard-type convective cells. The formation of the vortices was independent of inhomogenieties in surface roughness or temperature. In addition, an imposed source of mean wind or angular momentum was not required for vortexgenesis. Vertical vortices in the atmosphere (and in LESs) may be much more common than prior work has implied and, if this is true, these vortices may play an important role in boundary layer transports and evolution. This would have impact on the design of boundary layer parameterizations in larger scale numerical models and possibly on the prediction of the location of convective thunderstorm initiation. Future work will include further investigation of the formation and maintenance of these convective boundary layer vertical vortices.

Chapter 5

Literature cited

References for Chapter 1

Asai, T., 1970a: Three-dimensional features of thermal convection in a plane Couette flow. *J. Meteor. Soc. Japan*, **48**, 18-29.

Asai, T., 1970b: Stability of a plane parallel flow with a variable vertical shear and unstable stratification. *J. Meteor. Soc. Japan*, **48**, 129-138.

Asai, T., 1972: Thermal instability of a shear flow turning the direction with height. *J. Meteor. Soc. Japan*, **50**, 525-532.

Barcilon, A., and P. Drazin, 1972: Dust devil formation. Geophysical Fluid Dynamics Institute, Tech. Rept. 35, Florida State University.

Brady, R. H., and E. J. Szoke, 1989: A case study of nonmesocyclone tornado development in Northeast Colorado: Similarities to waterspout formation., *Mon. Wea. Rev.*, **117**, 843-856.

Maxworthy T., 1973: A vorticity source for large scale dust devils and other comments on naturally occurring columnar vortices. *J. Atmos. Sci.*, **30**, 1717-1722.

Rotunno, R. and J. B. Klemp, 1982: The influence of shear-induced pressure gradient on thunderstorm motion. *Mon. Wea. Rev.*, **110**, 136-151.

Rotunno R. and J. B. Klemp, 1985: On the rotation and propagation of simulated supercell thunderstorms. *J. Atmos. Sci.*, **42**, 271-292.

Schlesinger, R. E. , 1980: A three-dimensional numerical model of an isolated deep thunderstorm. Part II: Dynamics of updraft splitting and mesovortex couplet evolution. *J. Atmos. Sci.*, **37**, 395-420.

Shapiro A., and Y. Kogan, 1994: On vortex formation in multicell convective clouds in a shear-free environment. *Atmos. Res.*, **33**, 125-136.

Sinclair, P. C., 1969: General characteristics of dust devils. *J. Appl. Meteor.*,**8**, 32-45.

Wu, W.-S., 1990: Helical buoyant convection. Ph. D. Dissertation, Univ. of Okla., Norman, OK.

References for Chapter 2

Asai, T., 1970a: Three-dimensional features of thermal convection in a plane Couette flow. *J. Meteor. Soc. Japan*, **48**, 18-29.

Asai, T., 1970b: Stability of a plane parallel flow with a variable vertical shear and unstable stratification. *J. Meteor. Soc. Japan*, **48**, 129-138.

Asai, T., 1972: Thermal instability of a shear flow turning the direction with height. *J. Meteor. Soc. Japan*, **50**, 525-532.

Barnes, S. L., 1968. On the source of thunderstorm rotation. ESSA Tech. Memo. ERLTM-NSSL 38, 28pp. Natl. Severe Storms Lab., Norman, OK.

Browning, K. A., and C. R. Landry, 1963: Airflow within a tornadic storm. *Preprints, 10th Weather Radar Conference*, pp. 116-122, American Meteorological Society, Boston, MA.

Davies-Jones, R. P., 1984: Streamwise vorticity: The origin of updraft rotation in supercell storms. *J. Atmos. Sci.*, **41**, 2991-3006.

Davies-Jones, R. P. , 1985: Dynamical interaction between an isolated convective cell and a veering environmental wind. *Preprints, 14th Conference on Severe Local Storms*, pp. 216-219, American Meteorological Society, Boston, MA.

Droegemeier, K. K., S. M. Lazarus, and R. Davies-Jones, 1993: The influence of helicity on numerically simulated convective storms. *Mon. Wea. Rev.*, **121**, 2005-2029.

Emanuel, K. A., 1994: *Atmospheric Convection*. Oxford University Press, 580 pp.

Hide, R., 1989: Superhelicity, helicity and potential vorticity. *Geophys. and Astrophys. Fluid Dyn.*, **48**, 68-79.

Kaufman, L., 1975: The LZ-algorithm to solve the generalized eigenvalue problem. *SIAM, J. Numer. Anal.*, **11**, 997-1024.

Klemp, J. B., and R. B. Wilhelmson, 1978a: The simulation of three-dimensional convective storm dynamics. *J. Atmos. Sci.*, **35**, 1070-1096.

Klemp, J. B. and R. B. Wilhelmson, 1978b: Simulations of right- and left-moving storms produced through storm splitting. *J. Atmos. Sci.*, **35**, 1097-1110.

Klemp, J. B., R. B. Wilhelmson, and P. S. Ray, 1981: Observed and numerically simulated structure of a mature supercell thunderstorm. *J. Atmos. Sci.*, **38**, 1558-1580.

Lemone M. A., 1983: Momentum transport by a line of cumulonimbus. *J. Atmos. Sci.*, **40**, 1815-1834.

Lemone, 1984: Momentum flux by lines of cumulonimbus over the tropical oceans. *J. Atmos. Sci.*, **41**, 1914-1932.

Lilly, D. K., 1982: The development and maintenance of rotation in convective storms. *Intense Atmospheric Vortices*. L. Bengtsson and J. Lighthill, Eds., Springer-Verlag, 149-160.

Lilly, D. K., 1986a. The structure, energetics and propagation of rotating convection storms. Part I: Energy exchange with the mean flow. *J. Atmos. Sci.*, **43**, 113-125.

Lilly, D. K., 1986b. The structure, energetics and propagation of rotating convection storms. Part II: Helicity and storm stabilization. *J. Atmos. Sci.*, **43**, 126-40.

Lilly D. K. and B. F. Jewett, 1990. Momentum transport and kinetic energy budgets of simulated supercell thunderstorms. *J. Atmos. Sci.*, **47**, 707-726.

McCaul, E. W., Jr., 1993: Observations and simulations of hurricane-spawned tornadic storms. *The Tornado: Its Structure, Dynamics, Prediction and Hazards.* Geophysical Monograph 79, American Geophysical Union, Washington, DC.

Maddox, R.A., 1976: An evaluation of tornado proximity wind and stability data. *Mon. Wea. Rev.*, **104**, 133-142.

Rotunno, R. and J. B. Klemp, 1982: The influence of shear-induced pressure gradient on thunderstorm motion. *Mon. Wea. Rev.*, **110**, 136-151.

Rotunno R. and J. B. Klemp, 1985: On the rotation and propagation of simulated supercell thunderstorms. *J. Atmos. Sci.*, **42**, 271-292.

Rasmussen, E. N., and R. B. Wilhelmson, 1983: Relationships between storm characteristics and 1200 GMT hodograph, low level shear, and stability. *Preprints, 13th Conference on Severe Local Storms*, pp. J5-J8, American Meteorological Society, Boston, MA.

Schlesinger, R. E. , 1980: A three-dimensional numerical model of an isolated deep thunderstorm. Part II: Dynamics of updraft splitting and mesovortex couplet evolution. *J. Atmos. Sci.*, **37**, 395-420.

Shapiro, A., 1993: The use of an exact solution of the Navier-Stokes equations in a validation test of a three-dimensional nonhydrostatic numerical model., *Mon. Wea. Rev.*, **121**, 2420-2425.

Truesdell, C. 1954: *The kinematics of vorticity*. Indiana University Press, 232 pp.

Weisman, M. L. and J. B. Klemp, 1982: The dependence of numerically simulated convective storms on vertical wind shear and buoyancy. *Mon. Wea. Rev.*, **110**, 504-520.

Wilhelmson, R. B., and J. B. Klemp, 1981: A three-dimensional analysis of splitting severe storms on 3 April 1964. *J. Atmos. Sci.*, **38**, 1581-1600.

Wu, W.-S., 1990: Helical buoyant convection. Ph. D. Dissertation, Univ. of Okla., Norman, OK.

Wu, W.-S., D. K. Lilly, and R. M. Kerr, 1992: Helicity and thermal convection with shear. *J. Atmos. Sci.*, **49**, 1800-1809.

References for Chapter 3

Agee, E. and A. Gluhovsky, 1999: LES model sensitivities to domains grids, and large-eddy timescales. *J. Atmos. Sci.*, **56**, 599-604.

Anderson, J. R., K. K. Droegemeier, R. B. Wilhelmson, 1985: Simulation of the thunderstorm subcloud environment. *Preprints, 14th Conference on Severe Local Storms* . AMS. p147.

Andre, J. C., and M. Lesieur 1977: Influence of helicity on high Reynolds number isotropic turbulence. *J. Fluid Mech.*, **81**, 187-207.

Asselin, R. 1972: Frequency filter for time integrations. *Mon. Wea. Rev.* , **100**, 487-490.

Barcilon, A., and P. Drazin, 1972: Dust devil formation. Geophysical Fluid Dynamics Institute, Tech. Rept. 35, Florida State University.

Battan, L., J., 1958: Energy of a dust devil. *J. Meteorol.*, **15**, 235.

Bluestein , H. B., 1985: The formation of a "landspout" in a "broken line" squall line in Oklahoma. Preprints, 14th Conference on Severe Local Storms, Indianapolis, Amer. Meteor. Soc., 312-315.

Brady, R. H., and E. J. Szoke, 1989: A case study of nonmesocyclone tornado development in Northeast Colorado: Similarities to waterspout formation., *Mon. Wea. Rev.*, **117**, 843-856.

Busse, F. H., 1972: The oscillatory instability of convection rolls in a low Prandtl number fluid. *J. Fluid. Mech.*, **52**, 97-112.

Businger, J. A., 1972: The atmospheric boundary layer. Chapter 6 in Remote sensing of the Troposphere, US DOC NOAA and Univ. of Colorado, pp. 6-1 to 6-51.

Carroll, J. J., and J. A. Ryan, 1970: Atmospheric vorticity and dust devil rotation. *J. Geophys. Res.*, **75**, 5179-5184.

Cooley, J. R., 1971: Dust devil meteorology. NOAA Tech. Memo. NWS CR-42.

Cortese, T., and S. Balachandar, 1993: Vortical nature of thermal plumes in turbulent convection. *Phys. Fluids*, **A5**, 3226-3232.

Crozier, W. D., 1970: Dust devil properties. *J. Geophys. Res.*, **75**, 4583-4585.

Davies-Jones, R. P. 1982: A new look at the vorticity equation with application to tornadogenesis. *Preprints, 12th Conference on Severe Local Storms*, pp. 249-252. American Meteorological Society, Boston, Mass.

Davies-Jones, R. P. 1984: Streamwise vorticity: The origin of updraft rotation in supercell storms. *J. Atmos. Sci.*, **41**, 2991-3006.

Deardorff, J. W., 1972: Numerical investigation of neutral and unstable planetary boundary layers. *J. Atmos. Sci.*, **29**, 91-115.

Deardorff, J. W., 1978: Observed characteristics of the outer layer. Unpublished lectures notes. *Short course on the Planetary Boundary Layer*, Boulder, AMS. 101 pp.

Dörnbrack, A., 1997: Broadening of convective cells. *Quart. J. Roy. Meteor. Soc.*, **123**, 829-847.

Droegemeier, K. K. and R. Davies-Jones, 1987: Simulation of thunderstorm microbursts with a supercompressible numerical model. *Proceedings of the 5th International Conference on Numerical Methods in Laminar and Turbulent Flow.* Montreal, Canada.

Droegemeier, K. K. and R. B. Wilhelmson, 1987: Numerical simulation of thunderstorm outflow dynamics. Part I: Outflow sensitivity experiments and turbulence dynamics. *J. Atmos. Sci.*, **44**, 1180-1210.

Durward, J., 1931: Rotation of dust devils. *Nature*, **128**, 412.

Emanuel, K. A., 1988. Toward a general theory of hurricanes. *Amer. Sci.*, **76**,371-379.

Fiedler, B. H., and M. Khairoutdinov, 1994: Cell broadening in three-dimensional thermal convection between poorly conducting boundaries: Large eddy simulations. *Beitr. Phys. Atmosph.*, **67**, 235-241.

Fitzjarrald, D. E., 1973: A field investigation of dust devils. *J. Appl. Meteor.*, **12**, 808-813.

Flower, W. D., 1936: Sand devils. Gr. Brit. Meteorol. Off. Prof. Note 71.

Fujita, T., 1971: Proposed mechanism of suction spots accompanied by tornadoes. *Preprints, 7th Conference on Severe Local Storms 5-7 Oct. 1971, Kansas City, MO.* AMS. Boston, MA p208-213.

Goody, R. and P. Gierasch, 1974: The influence of vorticity on free convection. *J. Atmos. Sci.*, **31**, 1021-1027.

Grant, C. G., 1949: Dust devils in the sub-Arctic. *Weather*, **4**,402-403.

Hallet, J. and T. Hoffer, 1971: Dust devil systems. *Weather*, **26**, 247-250.

Hess, G. D., K. T. Spillane, and R. S. Lourensz, 1988: Atmospheric vortices in shallow convection. *J. Appl. Meteor.*, **27**, 305-317.

Hess, G. D., and K. T. Spillane, 1990: Characteristics of dust devils in Australia. *J. Appl. Meteor.*, **29**, 498-507.

Ives, R. L. 1947: Behavior of dust devils. *Bull. Amer. Meteor. Soc.*, **28**, 168-174.

Kaimal, J. C. and J. A. Businger, 1970: Case studies of a convective plume and a dust devil. *J. Appl. Meteor.*, **9**, 612-620.

Kanak, K. M., 1996: (Informal presentation) Preliminary radar observations of dust devils. *Eighteenth Conference on Severe Local Storms. Feb. 19-23, 1996, San Francisco, CA.*

Kanak, K. M., and D. K. Lilly, 1996: The linear stability and structure of convection in a mean circular shear. *J. Atmos. Sci.*, **53**, 2578-2693.

Klemp, J. B., 1987: Dynamics of tornadic thunderstorms. *Ann. Rev. Fluid Mech.*, **19**, 369-402.

Klemp, J. B., and D. K. Lilly, 1978: Numerical simulation of hydrostatic mountain waves. *J. Atmos. Sci.*, **35**, 78-107.

Klemp, J. B., and R. B. Wilhelmson, 1978: The simulation of three-dimensional convective storm dynamics. *J. Atmos. Sci.*, **35**, 1070-1096.

Kogan and Shapiro, 1996: The simulation of a convective cloud in a 3D model with explicit microphysics. Part II: Dynamical and microphysical aspects of cloud merger. *J. Atmos. Sci.*, **53**, 2525-2545.

Kurihara, Y., and J. L. Holloway, 1967: Numerical integration of the nine-level global primitive equations model formulated by the box method. *Mon. Wea. Rev.*, **95**, 509-530.

Lamberth, R. L., 1966: On the measurement of dust devil parameters. *Bull. Amer. Meteor. Soc.*, **47**, 522-526.

LeMone, M. A., 1990: Some observations of vertical velocity skewness in the convective planetary boundary layer. *J. Atmos. Sci.*, **47**, 1163-1169.

Leonard, B. P., 1991: The ULTIMATE conservative difference scheme applied to unsteady one-dimensional advection. *Comp. Meth. in Appl. Mech. and Engineering*, **88**, 17-74.

Lilly, D. K. 1962: On the numerical simulation of buoyant convection. *Tellus*, **14**, 168-172.

Lilly, D. K., 1982: The development and maintenance of rotation in convective storms. *Intense Atmospheric Vortices*, L. Bengtsson and J. Lighthill, Eds., Springer-Verlag, 149-160.

Lilly, D. K., 1986. The structure, energetics and propagation of rotating convection storms. Part I: Energy exchange with the mean flow. *J. Atmos. Sci.*, **43**, 113-125.

Lilly, D. K., 1999: Helical buoyant convection. Geophysical and Astrophysical Convection. To be published.

Ludlum, F. H., and R. S. Scorer, 1953: Convection in the atmosphere. *Quart. J. Roy. Meteor. Soc.*, **79**, 317-341.

Lugt, H. J., 1979: The dilemma of defining a vortex. *Recent developments in theoretical and experimental fluid mechanics*. Springer-Verlag, p. 309.

MacPherson, J. I., and A. K. Betts, 1997: Aircraft encounters with strong coherent vortices over the boreal forest. *J. Geophys. Res.*, **102, D24**, 29231-29234.

McGinnigle, J. B., 1970: A note on observed dust-whirl damage at Nicosia, Cyprus. *Meteor. Mag.*, **99**, p118-122.

Mason, P. J., 1989: Large-eddy simulation of the convective atmospheric boundary layer. *J. Atmos. Sci.*, **46**, 1492-1516.

Maxworthy T., 1973: A vorticity source for large scale dust devils and other comments on naturally occurring columnar vortices. *J. Atmos. Sci.*, **30**, 1717-1722.

Moeng, C. -H., and R. Rotunno 1990: Vertical-velocity skewness in the buoyancy-driven boundary layer. *J. Atmos. Sci.*, **47**, 1149-1162.

Moeng, C.-, H., and P. P. Sullivan, 1994: A comparison of shear- and buoyancy-driven planetary boundary layer flows. *J. Atmos. Sci.*, **51**, 999-1022.

Morton, 1966: Geophysical Vortices. Progress in Aeronautical Sciences, Vol. 7, Pergamon Press, 145-193.

Nieuwstadt, F.T.M., P.J. Mason, C.-H. Moeng, and U. Schumann, 1991: Large eddy simulation of the convective boundary layer: A comparison of four computer codes. *Turbulent Shear Flows* 8, F. Durst et al., Eds., Springer-Verlag, 343-367.

Porch, W. M., 1974: Fast-response light scattering measurements of aerosol suspension in a desert area. *Atmos. Environ.*, **8**, 897-904.

Rotunno, R., and J. B. Klemp, 1982: The influence of the shear-induced pressure gradient on thunderstorm motion. *Mon. Wea. Rev.*, **110**, 136-151.

Rotunno, R., and J. B. Klemp, 1985: On the rotation and propagation of simulated supercell thunderstorms. *J. Atmos. Sci.*, **42**, 271-292.

Ryan, J. A., and J. J. Carroll, 1970: Dust devil wind velocities: mature state. *J. Geophys. Res.*, **75(2)**, 431-542.

Shapiro A., and Y. Kogan, 1994: On vortex formation in multicell convective clouds in a shear-free environment. *Atmos. Res.*, **33**, 125-136.

Sinclair, P. C., 1964: Some preliminary dust devil measurements. *Mon. Wea. Rev.*, **92**, 363.

Sinclair, P. C., 1965: On the rotation of dust devil. *Bull. Amer. Meteor. Soc.*, **46**, 388.

Sinclair, P. C., 1969: General characteristics of dust devils. *J. Appl. Meteor.*, **8**, 32-45.

Sinclair, P. C., 1973: The lower structure of dust devils. *J. Atmos. Sci.*, **30**, 1599-1619.

Smagorinsky, J. 1963: General circulation experiments with the primitive equations. I. The basic experiment. *Mon. Wea. Rev.*, **91**, 99-164.

Smith, R. L., and D. W. Holmes, 1961: Use of Doppler radar in meteorological observations. *Mon. Wea. Rev.*, **89**, 1-7.

Smith, R. K. and L. M. Leslie, 1976: Thermally driven vortices: A numerical study with application to dust-devil dynamics. *Quart. J. Roy. Meteor. Soc.*, **102**, 791-804.

Snow, J. T., and T. M. McClelland, 1990: Dust devils at white sands missile range, New Mexico. 1. Temporal and spatial distributions. *J. Geophys. Res.*, **95**, 13707-13721.

Taylor, G. I. 1916: Conditions at the surface of a hot body exposed to the wind. *Brit. Adv. Com. Aero. Rep. and Memor.*, 272.

Tremback, C. J., J. Powell, W. R. Cotton, and R. A. Pielke, 1987: The forward-in-time upstream advection scheme: Extension to higher orders. *Mon. Wea. Rev.*, **115**, 540-555.

Wakimoto and Wilson, 1989: Non-supercell tornadoes, *Mon. Wea. Rev.*, **117**, 1113-1140.

Walko, R. L. 1993: Tornado spin-up beneath a convective cell: Required basic structure of the near-field boundary layer winds. *The Tornado: Its Structure, Dynamics, Prediction, and Hazards.* C. Church, Ed., American Geophysical Union, 89-95.

Webb, E. K., 1963. Sink vortices and whirlwinds. *Proceedings of the 1st Australian Conference on Hydraulics and Fluid Mechanics.* Pergamon Press. Oxford.

Webb, E. K., 1977: Convection mechanism of atmospheric heat transfer from surface to global scales. *Proc. Second Australasian Conf. Heat and Mass Transfer*, Univ. of Sydney, 523-529.

Webb, E. K., 1984: Temperature and humidity structure in the lower atmosphere. *Geodetic Refraction - Effects of Electromagnetic Wave propagation through the atmosphere.*, F. K. Brunner, Ed., Springer, 56 pp.

Weisman, M. L. and J. B. Klemp, 1982: The dependence of numerically simulated convective storms on vertical wind shear and buoyancy. *Mon. Wea. Rev.*, **110**, 504-520.

Willis, G. E., and J. W. Deardorff, 1979: Laboratory observations of turbulent penetrative convection planforms. *J. Geophys. Res.*, **84**, 296-301.

Xue, M., K. K. Droegemeier, V. Wong, A. Shapiro, and K. Brewster, 1995: The ARPS version 4.0 users guide. Center for Analysis and Prediction of Storms. University of Oklahoma. Norman, Oklahoma.

References for Appendix A (not listed in Chapter 3 references)

Arakawa, A. and V. R. Lamb, 1977: Computational design of the basic dynamical processes of the UCLA general circulation model. *Methods in Computational Physics*, **17**, Academic Press, 174-265.

Lilly, D. K. 1965: On the computational stability of numerical solutions of time-dependent non-linear geophysical fluid dynamics problems. *Mon. Wea. Rev.*, 93,11-26.

Purser, R. J., 1987: The filtering of Meteorological Fields., *J. of Clim. and Appl. Meteor.*, **26**, 1764-1769.

Robert, A. J., 1966: The integration of a low order spectral form of the primitive meteorological equations. *J. Meteor. Soc. Japan*, **44**, 237-245.

References for Appendix B (not listed in Chapter 3 references)

Straka, J. M. and K. K. Droegemeier, 1991: Some test problems for the Advanced Regional Prediction System (Unpublished, Univ. of Oklahoma).

Straka, J. M., R. B. Wilhelmson, L. J. Wicker, J. R. Anderson, and K. K. Droegememeier 1993: Numerical solutions of a non-linear density current: A benchmark solution and comparisons. *Intl. J. Num. Meth. Fluids.* **17**, 1-22.

APPENDIX A

Finite Difference Form of the Equations

A.1. The numerical grid

An Arakawa-C grid (Arakawa and Lamb 1977) is used in which the thermodynamic variables are solved at points that are staggered from the points at which velocity is calculated (Fig. A.1). The boundaries are occupied by the velocity points. This grid is convenient for the calculation of divergence, and certain terms in the subgrid turbulence parameterization in that minimal averaging of thermodynamic variables is required.

The following notation (Lilly 1965) will be used to present the spatial discretization,

$$\overline{\phi}^{nx} = \frac{1}{2}\left[\phi\left(x + n\frac{\Delta x}{2}\right) + \phi\left(x - n\frac{\Delta x}{2}\right)\right] \tag{A. 1}$$

and

$$\delta_{nx}\phi = \frac{1}{n\Delta x}\left[\phi\left(x + n\frac{\Delta x}{2}\right) - \phi\left(x - n\frac{\Delta x}{2}\right)\right] \tag{A. 2}$$

where, ϕ is a dependent variable, x is one of the independent variables, x, y, or z, Δx is an interval over which the operation is taken, and n is an integer.

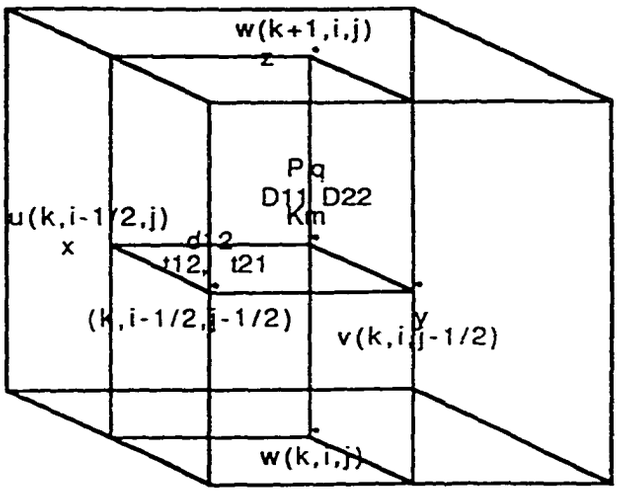

Fig. A.1. Three-dimensional schematic diagram of the finite difference grid and the locations of variables.

A.2. Time integration of the supercompressible equations

Although the efficiency of integrating the equations is improved by the supercompressible approximation, through the reduction of the sound speed, model performance can be further enhanced. This is done by employing the time-splitting technique (Klemp and Wilhelmson 1978), in which the terms associated with the generation of sound waves are integrated on a "small" timestep, while all other terms are integrated on a "large" timestep.

The large timestep integration scheme is centered-in-time (leapfrog) and may be written for any variable,

$$\phi^{t+\Delta t} = \phi^{t-\Delta t} + 2(\Delta t)F^{t}, \tag{A. 3}$$

to which a time filter (Robert 1966; Asselin 1972) is applied to prevent the possibility of solution decoupling at odd and even timesteps,

$$\left.\begin{aligned} \phi^{t^{*}+\Delta t} &= \phi^{t-\Delta t} + 2(\Delta t)F^{t^{*}} \\ \phi^{t} &= \phi^{t^{*}} + \alpha\left(\phi^{t^{*}+\Delta t} - 2\phi^{t^{*}} + \phi^{t-\Delta t}\right) \end{aligned}\right\}. \tag{A. 4}$$

The first equation in (A.4) denotes a leapfrog step with the asterisk denoting the terms which have not yet been smoothed by the second step. The two equations may be combined and written using, $\alpha = 0.1$ as

$$\phi^{t^*} = (1-2\alpha)\phi^t + \alpha\left(\phi^{t+\Delta t} - \phi^{t-\Delta t}\right). \qquad \text{(A. 5)}$$

The small timestep integration is the explicit forward-backward scheme (Klemp and Wilhelmson 1978). The terms of (3.8) and (3.10) that are evaluated on the small timestep are on the left hand side of the following:

$$\left.\begin{aligned} \frac{\partial u_i}{\partial t} + \frac{1}{\bar{\rho}}\frac{\partial p'}{\partial x_i} &= F_{u_i} \\ \frac{\partial p'}{\partial t} + c_s^2 \frac{\partial\left(\bar{\rho} u_i\right)}{\partial x_i} &= F_p \end{aligned}\right\}, \qquad \text{(A. 6)}$$

where, F_{ui} and F_p include the advective, buoyancy, subgrid-scale mixing, and filter terms that are computed on the large timestep. The terms included in F_p are small and are neglected as in Klemp and Wilhelmson (1978).

The finite difference form of these equations using the forward-backward scheme is given by,

$$\delta_\tau u + \frac{1}{\bar{\rho}}\left(\delta_x p\right)^\tau = F_u^t; \quad \delta_\tau v + \frac{1}{\bar{\rho}}\left(\delta_y p\right)^\tau = F_v^t; \quad \delta_\tau w + \frac{1}{\bar{\rho}^z}\left(\delta_z p\right)^\tau = F_w^t, \qquad \text{(A. 7)}$$

and

$$\delta_\tau p' + c^2\bar{\rho}\left(\delta_x u + \delta_x v\right)^{\tau+\Delta\tau} + c^2\left(\delta_z \bar{\rho}^z v\right) = 0 \quad . \qquad \text{(A. 8)}$$

The time interval of the small timesteps is $\Delta\tau$ and there are $n = 2\Delta t/\Delta\tau$ small steps for each large timestep of interval Δt.

A.3. Spatial discretization of the advective and buoyancy terms

Terms F_U, F_V, and F_W consist of the advective, buoyancy, subgrid scale mixing, and filter terms, all of which are evaluated on the large timestep, with mixing and filter terms lagged in time for numerical stability; that is,

$$F_{u_i}^t = adv(t) + mix(t-\Delta t) + filt(t-\Delta t) + \delta_{i3} buoy(t). \qquad \text{(A. 9)}$$

In addition, equation (3.2) is evaluated entirely on the large timestep. First the advective and buoyancy forcing terms for (3.10) are considered, which are also written as (A.7).

For equations (A.7) the advective and buoyant terms are discretized using the quadratic conserving "Box" method (Kurihara and Holloway 1967)

$$F_u = \overline{\overline{u}^x \delta_x u}^x + \overline{\overline{v}^x \delta_y u}^y + \overline{\overline{w}^x \delta_z u}^z \qquad \text{(A. 10)}$$

$$F_v = \overline{\overline{u}^y \delta_x v}^x + \overline{\overline{v}^y \delta_y v}^y + \overline{\overline{w}^y \delta_z v}^z \qquad \text{(A. 11)}$$

$$F_w = \overline{\overline{u}^z \delta_x w}^x + \overline{\overline{v}^z \delta_y w}^y + \overline{\overline{w}^z \delta_z w}^z + g\left(\frac{\overline{\theta}^z}{\overline{\theta}} - \frac{c_v}{c_p}\frac{\overline{p}^z}{\overline{p}}\right) \qquad \text{(A. 12)}$$

Potential temperature advective terms are discretized using either the Box method, centered-in-time, or the 6th-order, flux conservative Crowley scheme

(Tremback et al. 1987) with a forward timestep. Note that when the Crowley scheme is used, the subgrid mixing and filter terms for potential temperature are calculated using the variables defined at the current time level. The advective term of (3.2) can be written as

$$-u_j \frac{\partial \theta}{\partial x_j} = -\frac{\partial (u_j \theta)}{\partial x_j} + \theta \frac{\partial u_j}{\partial x_j} \quad . \tag{A. 13}$$

The first term on the right hand side can be discretized and written as,

$$\frac{\Delta t}{\Delta x_i}\left[F_{j+1/2} - F_{j-1/2}\right] \quad , \tag{A. 14}$$

where, the 6th-order Crowley scheme is used to define,

$$\begin{aligned}
F_{i+1/2}\frac{\Delta t}{\Delta x_i} = {} & \frac{\alpha}{60}\left(-\theta_{i-2} + 8\theta_{i-1} - 37\theta_i - 37\theta_{i+1} + 8\theta_{i+2} - \theta_{i+3}\right) \\
& + \frac{\alpha^2}{360}\left(-2\theta_{i-2} + 25\theta_{i-1} - 245\theta_i + 245\theta_{i+1} - 25\theta_{i+2} + 2\theta_{i+3}\right) \\
& + \frac{\alpha^3}{48}\left(\theta_{i-2} - 7\theta_{i-1} + 6\theta_i + 6\theta_{i+1} - 7\theta_{i+2} + 1\theta_{i+3}\right) \\
& + \frac{\alpha^4}{144}\left(\theta_{i-2} - 11\theta_{i-1} + 28\theta_i - 28\theta_{i+1} + 11\theta_{i+2} - \theta_{i+3}\right) \\
& + \frac{\alpha^5}{240}\left(-\theta_{i-2} + 3\theta_{i-1} - 2\theta_i - 2\theta_{i+1} + 3\theta_{i+2} - \theta_{i+3}\right) \\
& + \frac{\alpha^5}{720}\left(-\theta_{i-2} + 5\theta_{i-1} - 10\theta_i + 10\theta_{i+1} - 5\theta_{i+2} + \theta_{i+3}\right)
\end{aligned} \tag{A. 15}$$

where α is $u_i = \Delta t / \Delta x_i$. At three points from the boundary, the fourth-order Crowley advection is used and at two points from the boundary, the second-order Crowley advection scheme is used.

In association with the Crowley scheme, a monotonic flux corrector (Leonard 1991; Straka personal communication), a high-order operator that guarantees monotonicity, is used for potential temperature.

A.4. Finite difference form of the subgrid turbulence parameterization

To maintain numerical stability the subgrid mixing terms are evaluated using the previous time level.

Figure A.1 shows that the locations of τ_{11}, τ_{22}, τ_{33}, D_{11}, D_{22}, D_{33}, K_m and K_h are defined at the potential temperature point at the grid box center. H_1 is defined at the u point, H_2 at the v point, and H_3 at the w point. Discretization of the turbulent subgrid mixing terms for velocity is as follows:

- Deformation terms, D_{ij}:

$$
\begin{aligned}
D_{11} &= 2\frac{\partial u}{\partial x} = 2\delta_x u \qquad D_{12} = \frac{\partial u}{\partial y} + \frac{\partial v}{\partial x} = \delta_y u + \delta_x v \\
D_{22} &= 2\frac{\partial v}{\partial y} = 2\delta_y v \qquad D_{13} = \frac{\partial w}{\partial x} + \frac{\partial u}{\partial z} = \delta_x w + \delta_z u \\
D_{33} &= 2\frac{\partial w}{\partial z} = 2\delta_z w \qquad D_{23} = \frac{\partial w}{\partial y} + \frac{\partial v}{\partial z} = \delta_y w + \delta_z v
\end{aligned}
\tag{A. 16}
$$

- Stress tensor components (tensor is symmetric for a regular Cartesian grid), τ_{ij}:

$$\begin{aligned} \tau_{11} &= K_m\left(D_{11} - \frac{2}{3}\frac{\partial u_i}{\partial x_i}\right), & \tau_{12} &= \overline{K_m}^{xy} D_{12} \\ \tau_{22} &= K_m\left(D_{22} - \frac{2}{3}\frac{\partial u_i}{\partial x_i}\right), & \tau_{13} &= \overline{K_m}^{xz} D_{13} \\ \tau_{33} &= K_m\left(D_{33} - \frac{2}{3}\frac{\partial u_i}{\partial x_i}\right), & \tau_{23} &= \overline{K_m}^{yz} D_{23} \end{aligned} \qquad \text{(A. 17)}$$

- The turbulent mixing terms for potential temperature are computed using,

$$H_1 = \overline{K_h}^{x}\delta_x\theta; \qquad H_2 = \overline{K_h}^{y}\delta_y\theta; \qquad H_3 = \overline{K_h}^{z}\delta_z\theta \qquad \text{(A. 18)}$$

A.5. Finite difference form of the numerical filters

To maintain computational stability the numerical filtering terms are also evaluated using the previous time level.

The fourth-order numerical filter used follows that of Purser (1987),

$$D_f = -K_D\left(\delta_{xxxx}\phi + \delta_{yyyy}\phi\right), \qquad \text{(A. 19)}$$

where K_D is found from $(K_D\Delta t/(\Delta x)^4) = 0.0025$ (Klemp and Wilhelmson 1978). The template for the fourth-order derivative is

$$\delta_{xxxx}\phi = \phi_{i+2} - 4\phi_{i+1} + 6\phi_i - 4\phi_{i-1} + \phi_{i-2} \tag{A. 20}$$

Near the boundary, the second-order filter is used,

$$D_f = -K_D\left(\delta_{xx}\phi + \delta_{yy}\phi\right), \tag{A. 21}$$

which can be written as

$$\delta_{xx}\phi = \phi_{i+1} - 2\phi_i + \phi_{i-1}. \tag{A. 22}$$

APPENDIX B

Model Validation

Validation tests have been performed for KANSAS including a series of simple flow tests for symmetry and spurious solutions. KANSAS has also been benchmarked against the SAM [Straka's Atmospheric Model, Straka et al. (1993)] for a simulation of a simple rising bubble, with and without mean wind shear. Lastly, the results of a LES simulation are compared with those of Nieuwstadt et al. (1991).

B.1. Uniform and oblique flow tests

A series of simple flow tests (described in Straka and Droegemeier 1991, unpublished) were performed and consist of initial conditions using combinations of u and/or v = ± 10 ms^{-1}. These tests were designed to help to insure that loop indexing and boundary conditions are handled properly in the numerical model. All the runs were performed with 40 x 40 x 40 gridpoints, $\Delta x = \Delta y = 1000$m, Δt = 6 s and the total number of timesteps of integration was 200. Lateral boundary conditions were open / radiative and rigid vertical conditions were used. These simulations were run on the ECAS CrayJ90 and are expected to be accurate to 64 bit precision. The model is successful is there were no differences between the initial and final fields after 200 timesteps of integration.

B.2. Single buoyant thermal

Next a simple simulation of a rising bubble was performed using KANSAS for benchmark and symmetry tests. The results were compared with those of the SAM for the same simulation.

In this test, a simple rising thermal specified as the initial condition in Klemp and Wilhelmson (1978; hereafter KW78)

$$\Delta\theta = \Delta\theta_o \cos^2\left[\frac{\pi r}{2}\right] \qquad r < 1 \tag{B. 1}$$

where,

$$r = \sqrt{\left(\frac{x - x_c}{x_r}\right)^2 + \left(\frac{y - y_c}{y_r}\right)^2 + \left(\frac{z - z_c}{z_r}\right)^2} \tag{B. 2}$$

was simulated. The subscript c refers to the location of the center of the thermal and subscript r denotes the radial dimensions of the thermal in each Cartesian direction. The thermal strength, $\Delta\theta_o$, was set to 2 °C. The initial bubble parameters were $xc = yc = 12500$ m, $zc = 1250$m, $xr = yr = 3000$ m and $zr = 1000$ m. Boundary conditions were open lateral conditions with gravity wave speed set to 12 ms^{-1}. Rigid semi-slip upper and lower boundary conditions were prescribed. The domain size was 26 x 26 x 13 gridpoints, and resolution is $\Delta x = \Delta y = 1000$m, $\Delta z = 500$m , with $\Delta t = 6$s. The number of small timesteps was set to

12 and the sound speed was reduced to 150 ms^{-1}. The base-state surface potential temperature was 305 K and the base state surface pressure was set to 97500 Pa. The base-state potential temperature profile was very similar to that of KW78 and is shown in Table B. 1.

p (mb)	θ (K)
948	305
895	305
844	305
796	307
750	309
706	311
664	313
624	315
587	317
551	319
517	323
485	329
455	337

Table B. 1. Initial Base State Potential Temperature Profile

Several experiments using different model configurations were performed and the variable domain extrema at time = 1800 seconds are summarized in Table B.2. The vapor variable was included in the tests here, but was not used in the dry dissertation simulations. These runs were designed to test mainly the turbulence closure in the presence of mean static stability changes and mean shear. The performance of the boundary conditions was also considered in the cases with mean shear. All Cases shown use the sounding shown in Table B. 1 except Case A. Cases A and B are dry and have the Smagorinsky turbulence closure. Case C is the same as B except with a mean shear with u=-20ms^{-1} near the surface to u = 20 ms^{-1} at the top of the domain. Case D (E) is the same as Case

KANSAS

	CASE A		CASE B		CASE C		CASE D	
	Min	Max	Min	Max	Min	Max	Min	Max
θ'	-0.057863	2.155786	-0.246244	2.366313	-0.302958	2.757188	-0.000055	1.816457
q_v	0.0	0.0	0.0	0.0	0.0	0.0	-3.3635	M
p'	-11.016190	13.3492355	-95.1575	51.5034	-99.5113	60.3936	-54.7195	70.1524
u	-7.8787127	7.8787127	-6.113561	18.716982	-6.189371	19.620908	-9.487383	9.487383
v	-7.8787098	7.8787098	-8.572634	8.572634	-9.165696	9.165696	-9.481575	9.481575
w	-3.6282795	5.8387909	-3.769457	16.522141	-4.149321	18.129393	-4.003019	16.400047
K_m	0.0	594.55211	0.0	65.5589599	0.0	505.401764	0.0	147.824722

SAM

	CASE A		CASE B		CASE C		CASE D	
	Min	Max	Min	Max	Min	Max	Min	Max
θ'	-.1174622	.4300842	-0.6437988	0.6647949	-2.151001	4.481079	-1.882935	1.921051
q_v	0.0	0.0	0.0	0.0	0.0	0.0	-3.369792	4.996581
p'	-11.4025	12.3039	-2.2268	2.1224	0.0	3212.3993	-4.2865	4.2133
u	-7.974189	7.974189	-0.686720	0.686720	-16.320023	-18.38964	-1.684766	1.684766
v	-7.974187	7.974187	-0.686720	0.686720	-0.762780	0.762780	-1.684839	1.684839
w	-3.620363	6.002355	-0.444436	0.950582	-0.717385	0.972906	-1.123266	2.101229
K_m	0.0	610.0125	0.0	65.23405	0.0	512.7020	-0.37417	147.3903

Table B.2. Comparison of variables extrema for KANSAS and SAM for simulation of a buoyant thermal with variable base state potential temperature.

KANSAS

	CASE E		CASE F		CASE G			
	Min	Max	Min	Max	Min	Max		
θ'	-1.8694153	4.50140381	-1.1650696	0.59252930	-549987793	0.43081665		
q_v	-0.5017857	M	-4.834203	M	0.0	0.0		
p'	0.0	5449.23535	-13.582806	16.0772724	-6.7721820	11.0923004		
u	-24.910713	23,05086	-23.036306	23.0444756	-19.929466	21.4838123		
v	-2.1382169	2.13821269	-3.8585782	3.8585782	-1.0615584	1.06155837		
w	-1.1655247	1.23252082	-3.4099793	4.03110743	-0.6446258	0.54984957		
K_m	0.0	506.556641	0.0	0.0	0.0	0.0		

SAM

	CASE E		CASE F		CASE G			
	Min	Max	Min	Max	Min	Max		
θ'	-2.014709	4.5600591	-1.163879	0.5927124	-.546521	0.4319153		
q_v	-7.145969	3.376306	-4.831864	6.905262	0.0	0.0		
p'	0.0	3933.8062	-13.7344	15.9266	-6.7946	11.0771		
u	-16.448467	19.068415	-3.983488	4.092145	-2.635054	1.481197		
v	-0.910067	0.910067	-3.853786	3.853786	-1.062726	1.062726		
w	-0.957574	1.174168	-3.407076	4.027468	-0.644684	0.54984957		
K_m	-5.303372	484.9965	0.0	0.0	0.0	0.0		

Table B.2 Continued.: Comparison of variables extrema for KANSAS and SAM for simulation of a buoyant thermal with variable base state potential temperature.

B (C) except including vapor. Case F (G) is the same as E (C), but without the Smagorinsky turbulence closure.

A second set of tests was performed to test the 6th-order Crowley scheme for scalars and the 4th-order numerical filter. In this set 26 x 26 x 26 gridpoints were used. The potential temperature was constant with height and set to 300 K. The surface pressure was 96500. The resolution was $\Delta x = \Delta y = 1000$m, $\Delta z = 500$m, with $\Delta t = 6$s. The initial bubble parameters were $xc = yc = 12500$ m, $zc = 1750$m, $xr = yr = 10800$ m and $zr = 2000$ m. Boundary conditions were open lateral conditions with gravity wave speed set to 30 m/s. Rigid semi-slip upper and lower boundary conditions were prescribed. The variable extrema are shown in Table B.3 at time t = 1080 s or about 180 timesteps.

Case H included the Smagorinsky closure and no mean wind shear. Case I was the same as H except with a mean wind in the x-direction that varies from 0 ms^{-1} near the surface to 10 ms^{-1} at the top of the domain. Case J is like Case I except that instead of the turbulence closure, a 4th-order numerical filter is used. Case G is like Case A in that it has no mean wind shear, but it does not use the turbulence closure. However, it includes the 6th-order Crowley numerical scheme for scalars instead of the box scheme.

The variable extrema of KANSAS and SAM compare very well for most cases. There are as many as seven matching digits (e.g. Case K). There are about two matching digits for some of the runs using the Smagorinsky diffusion and this is likely due to the significantly increased number of calculations and the associated truncation error. Note also that the values of maximum K_m calculated

KANSAS

	CASE H		CASE I		CASE J		CASE K	
	Min	Max	Min	Max	Min	Max	Min	Max
θ′	-0.057863	2.155786	-0.246244	2.366313	-0.302958	2.757188	-0.000055	1.816457
p′	-48.7623	66.2078	-95.1575	51.5034	-99.5113	60.3936	-54.7195	70.1524
u	-8.910837	8.910837	-6.113561	18.716982	-6.189371	19.620908	-9.487383	9.487383
v	-8.910837	8.910837	-8.572634	8.572634	-9.165696	9.165696	-9.481575	9.481575
w	-3.373961	15.407157	-3.769457	16.522141	-4.149321	18.129393	-4.003019	16.400047

SAM

	CASE H		CASE I		CASE J		CASE K	
	Min	Max	Min	Max	Min	Max	Min	Max
θ′	-0.060610	2.163421	-.2476391	2.379751	-0.302957	2.757385	-0.000055	1.816457
p′	-48.9438	66.5930	-96.9389	51.3527	-99.5164	60.4142	-54.7194	70.124
u	-8.957682	8.957682	m	m	M	m	-9.487382	9.487382
v	-8.957682	8.957682	-8.599605	8.599605	-9.165836	9.165836	-9.481574	9.481575
w	-3.383658	15.465333	-3.795500	16.570355	-4.149824	18.129571	-5.003018	16.400048

Table B.3 Comparison of variables extrema for KANSAS and SAM for simulation of a buoyant thermal with constant base state potential temperature to test the Smagorinsky turbulence closure.

by each of the models for Case A (Case B) were 368.12 m^2s^{-1} (358.27 m^2s^{-1}) for KANSAS and 366.69 m^2s^{-1} (358.59 m^2s^{-1}) for SAM.

Other similar tests (not shown) were performed for the stretched coordinate options, Rayleigh damping, and surface flux portions of the models and similar comparisons were achieved.

B.3. LES test problem

In this test, we compared results of the KANSAS model with the results of Nieuwstadt et al. 1991 (N91). Their paper compared four simulations of the convective boundary layer. Descriptions of each of the four and that of the KANSAS models and the simulation parameters are listed in Table B.4. KANSAS and Mason use the Smagorinsky closure. All other models use higher order turbulence closures. A major difference between KANSAS and the other models is that KANSAS uses the supercompressible form of the equations of motion while all the other models are Boussinesq models. The second main difference is that KANSAS has no modification of the mixing length near the surface or the inversion.

The initial condition is the same as that described in Chapter 3 for the simulation of the convective boundary layer. However, the constant surface heat flux is set to Q = 0.06 K ms-1.in N91. All other simulation parameters are listed in Table B.4. Calculation of the horizontally averaged heat flux, vertical velocity variance and horizontal u-velocity variance are averaged over a time interval of 1

Comparison of LES Parameters

			Mason	Moeng	Nieuwstadt	Schumann	KANSAS
Equations			Boussinesq	Boussinesq	Boussinesq	Boussinesq	Super-Compressible
Domain	Size		6.4 x 6.4 x 8 km	6.4 x 6.4 x 2.4 km	6.4 x 6.4 x 2.4 km	6.4 x 6.4 x 2.4 km	6.4 x 6.4 x 8 km
	Gridpts		40 x 40 x 68	40 x 40 x 48	40 x 40 x 40	40 x 40 x 40	46 x 46 x 40
	$\Delta x\ \Delta y\ \Delta z$		160, 160, 20-80 m	160, 160,50 m	160, 160, 60 m	160, 160, 60 m	160, 160, 60 m
	Δt		0.65 s	3.0 s	4.48 s	10.96 s	2.0 s
	Base State θ		θ= 300 K up to 1350 m and then dtdz=.003Km^{-1}	θ= 300 K up to 1350 m and then dtdz=.003Km^{-1}	θ= 300 K up to 1350 m and then dtdz=.003Km^{-1}	θ= 300 K up to 1350 m and then dtdz=.003Km^{-1}	θ= 300 K up to 1350 m and then dtdz=.003Km^{-1}
Numerics	Grid		Vel Staggered T@P	Staggered in z only ; T@P	Staggered T@W	Staggered T@P	Staggered T@P
	Time Scheme		Leapfrog/ Forward on Diffus	Adams-Bashforth	Leapfrog/ Forward on Diffus	Adams-Bashforth	Leapfrog/ Forward on Diffus
	Spatial Scheme		2nd-order Variance Conserving	Pseudo-Spectral	2nd-order Variance Conserving	2nd-orderVariance Conserving/θ upwd	2nd-order Variance Conserving
	P solver		FFT	FFT	FFT	FFT	Prognostic
	B.C.	Later	Periodic	Periodic	Periodic	Periodic	Periodic
		Top	Rigid & Damping Layer	Open with Radiation BC	Rigid & Damping Layer	Open with Radiation BC	Rigid & Damping Layer
		Sfc	W=0 Const Heat flux	W=0 Const Heat flux	W=0 &Const Γ=0.16 K/hr	W=0 Const Heat flux	W=0 Const Heat flux
Turbulence Closure	Type		Smagorinsky	1.5 Order	1.5 Order	2nd Order	Smagorinsky
	Cs		0.32	0.18	0.18	0.165	0.21
	Pr		0.46	0.33	0.33	0.42	0.4
	Δ		Non-uniform	$(\Delta x\ \Delta y\ \Delta z)^{1/3}$	$(\Delta x\ \Delta y\ \Delta z)^{1/3}$	$1/3(\Delta x\ \Delta y\ \Delta z)$	$(\Delta x\ \Delta y\ \Delta z)^{1/3}$
	l, near sfc		$l \alpha z$			$l \alpha z$	constant
	l and static stability		reduced in statically stable regions	reduced in statically stable regions	reduced in statically stable regions		constant

Table B.4. Comparison of LES models of Nieuwstadt et al. (1991) and KANSAS for simulation of a convective boundary layer.

τ = 1096 s in N91 over 10 τ -11 τ. These figures from N91 are reproduced here as Fig. B.1a-c. The corresponding values from KANSAS are shown in Fig. B.1d-f.

The heat flux profile Fig. B.1a and B.1d compare well. Differences near to surface might be explained by the fact that KANSAS does not modify the mixing length as proportional to height above the surface as the other models do. Otherwise KANSAS' heat flux profile most closely resembles Mason's. This would be consistent with the fact that both KANSAS and Mason models utilize the Smagorinsky closure.

Fig. B.1.b and B.1.e show the vertical velocity variance profiles. Here the maximum for KANSAS lies at about 0.3 z_i as in Nieuwstadt's and Schumann's models. The variance of the u-velocity fluctuations is shown in Fig B.1c and B.1f. Here the KANSAS profile most closely resembles Mason's, except near the surface where it is more like Schumann's. KANSAS' value at the surface is less than the other models. All of the statistical profiles compare reasonably well for KANSAS and the other LES models.

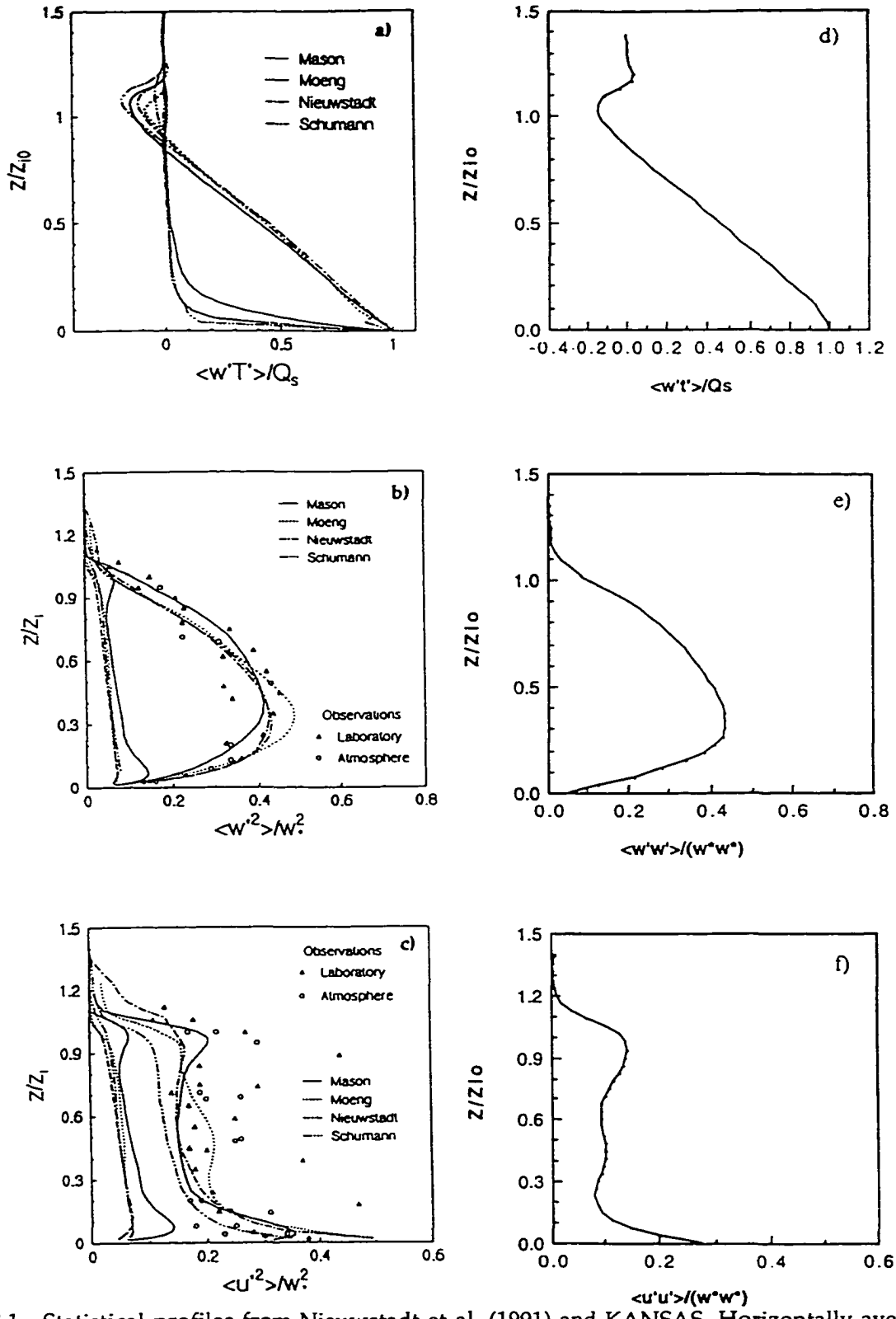

Fig. B.1. Statistical profiles from Nieuwstadt et al. (1991) and KANSAS. Horizontally averaged and temporally averaged (over the period of t = 10τ-11τ) profiles of: a) total (resolved-scale plus SGS) potential temperature flux, $\langle w'\theta' \rangle / Q_*$; b) total vertical velocity fluctuation variance, $\langle w'w' \rangle / w_*^2$; c) total u-velocity fluctuation variance, $\langle u'u' \rangle / w_*^2$